

On the Implications of Stellar Evolution and Stellar Interiors from
White Dwarf Seismology

by

Morgan T. Chidester

A Dissertation Presented in Partial Fulfillment
of the Requirement for the Degree
Doctor of Philosophy

Approved June 2023 by the
Graduate Supervisory Committee:

F.X. Timmes, Chair
Patrick Young
Mingming Li
Sanchayeeta Borthakur
Michael Line

ARIZONA STATE UNIVERSITY

August 2023

ABSTRACT

White Dwarf stars are the stellar remnants of low mass stars which have completed their evolution. Nearly all stars will become white dwarfs. The interior of a white dwarf encapsulates its evolution history: unraveling a white dwarf's internal structure constrains the physical events which occurred to construct its composition. Variable, or pulsating, white dwarfs emit pulsations which are sensitive to their internal stratification. Just as seismology reveals Earth's interior, asteroseismology can reveal stellar interiors. The standard approach to construe an observed white dwarf's chemical makeup is to match observed pulsation properties to theoretical stellar models. Observed white dwarf pulsation data has reached 6-7 significant digits of precision. As such, it is important for computational modeling to consider systematic offsets from initial conditions and theoretical uncertainties that are within the detectable threshold. By analyzing the magnitude of pulsation differences among various uncertainties from white dwarf models, one can place constraints on important theoretical uncertainties.

In this thesis, I explore impacts on white dwarf pulsations that result from accounting for various uncertainties in computational models. I start by showing the importance of ^{22}Ne , and its impact on the pulsations in Helium atmosphere white dwarfs. Next, I discuss how certain trapped modes of white dwarfs may yield a signal for the $^{12}\text{C}(\alpha, \gamma)^{16}\text{O}$ reaction rate probability distribution function. This reaction occurs during the Helium core burning phase in stellar evolution, and chiefly determines the Carbon and Oxygen abundance of white dwarfs. Following this work, I show how overshooting impacts the pulsation signatures of the $^{12}\text{C}(\alpha, \gamma)^{16}\text{O}$ reaction rate. I then touch on the analytical work I've done regarding educational research in the HabWorlds course offered at Arizona State University (ASU). I then summarize my conclusions from these efforts.

DEDICATION

To my husband, family, friends, colleagues, previous professors, advisor F.X. Timmes, and Savior, Jesus Christ. I wouldn't have been able to achieve this if it weren't for them.

ACKNOWLEDGEMENTS

My family has always encouraged me to accomplish my goals. There were a few phone calls with my siblings (each, but especially my brother, John Taylor) that distinctively motivated me to persevere. My parents never doubted my ability to accomplish this dream. My Grandpa Bodily consistently called me each week and asked about my research. He made sure I was staying on track to complete my degree. My Grandmother passed away before I started graduate school, but she left a legacy of perseverance and work ethic, as well as incredible kindness, charity and love. Memories of her inspired me when things got difficult. I want my family to know how much I appreciate their support during this journey.

I want to thank Lindsey Stirling, the Piano Guys, Helen Jane Long, Dua Lipa, Lauren Diagle, and Benjamin Taylor for providing music that helped me focus and stay motivated to work. It made the “grind” much more enjoyable.

My husband Arthur has constantly supported me the last 4 years; I was never alone through this journey. I encountered a few personal battles during my P.h.D experience that I never thought I would face. He was always someone I could talk to, and I never felt embarrassed or belittled by my shortcomings with him. He encouraged me to keep going, and continue to move forward even through challenging times.

My advisor F.X. Timmes is an exceptional person. He supported me during the entire graduate experience. He is a true expert in the field, and a very wise and considerate person. He offered care, support, guidance, and continual mentorship. It's been one of my greatest privileges to work with him these past 4 years.

Finally, I would feel ashamed if I did not acknowledge the hand of my Heavenly Father and His Son, Jesus Christ in all of this. I relied on much prayer and faith, and I can't deny Their help through this process, even when I least deserved it. I can attest to the mercy and grace given to those who put their faith in Jesus Christ.

The research in chapter 2 was supported by the National Science Foundation (NSF) under the Software Infrastructure for Sustained Innovation program grants (ACI-1663684, ACI-1663688, ACI-1663696). It was also supported by the NSF under grant PHY-1430152 for the Physics Frontier Center “Joint Institute for Nuclear Astrophysics - Center for the Evolution of the Elements” (JINA-CEE). A.T. is a Research Associate at the Belgian Scientific Research Fund (F.R.S-FNRS).

I’d like to thank James Deboer for sharing the $^{12}\text{C}(\alpha, \gamma)^{16}\text{O}$ probability distribution function, Josiah Schwab for sharing `wd_builder`, and Pablo Marchant for sharing `mkipp`. This research in chapter 3 was supported by NASA under the Astrophysics Theory Program grant NNH21ZDA001N-ATP, by the NSF under grant PHY-1430152 for the “Joint Institute for Nuclear Astrophysics - Center for the Evolution of the Elements”, and by the NSF under the Software Infrastructure for Sustained Innovation grants ACI-1663684, ACI-1663688, and ACI-1663696 for the `MESA` Project.

I acknowledge using ChatGPT (OpenAI, 2023) to polish the language of one paragraph (Vishniac, 2023) in Chapter 4. The research in chapter 4 as supported by NASA under the Astrophysics Theory Program grant NNH21ZDA001N-ATP.

I acknowledge useful discussions at virtual Sky House 2020. This thesis made extensive use of the SAO/NASA Astrophysics Data System (ADS).

TABLE OF CONTENTS

	Page
LIST OF TABLES	x
LIST OF FIGURES	xi
CHAPTER	
1 INTRODUCTION	1
1.1. Overview	1
1.2. Evolutionary Phases of Low-Mass Stars	3
1.2.1 Pre-Main Sequence	3
1.2.2 The Main Sequence	6
1.2.3 H Shell Burning	9
1.2.4 Core He-Burning	9
1.2.5 The AGB and Thermal Pulses (TPs)	12
1.2.6 The Fate of Low Mass Stars	13
1.3. WDs & Chandrasekar Limit	14
1.4. Asteroseismology	15
1.4.1 Notation	16
1.4.2 Gaining Insight to Stellar Interiors and Evolution	17
1.5. Motivating Problems to Explore with WD Seismology	18
1.5.1 Inclusion of ^{22}Ne	18
1.5.2 The $^{12}\text{C}(\alpha, \gamma)^{16}\text{O}$ Reaction Rate	19
1.5.3 Overshooting	20
1.6. Computational Tools and Methods	20
1.6.1 Modules for Experiments in Stellar Astrophysics - MESA	21
1.6.2 wd_builder for Ab Initio Modeling	24
1.6.3 GYRE	24

CHAPTER	Page
1.7. Learning Analytics in the Online Habworlds Course	24
1.8. Outline	24
2 THE IMPACT OF ^{22}Ne on	
WD PULSATIONS	25
2.1. Abstract	25
2.2. Introduction	26
2.3. A Baseline WD Model	29
2.3.1 Input Physics	29
2.3.2 Mass Fraction Profiles	30
2.3.3 Constructing Ab Initio White Dwarf Models	31
2.3.4 Pulsation Periods of the Baseline Model	36
2.4. The Impact Of ^{22}Ne	40
2.4.1 Putting the ^{22}Ne Into ^{14}N	43
2.4.2 Zero-Metallicity and Super-Solar Metallicity	47
2.5. Trends in the Period Changes with the White Dwarf Mass	49
2.6. Discussion	54
3 PROBING $^{12}\text{C}(\alpha, \gamma)^{16}\text{O}$	
WITH TRAPPED MODES IN WDs	59
3.1. Abstract	59
3.2. Introduction	60
3.3. Models	63
3.3.1 Updated $^{12}\text{C}(\alpha, \gamma)^{16}\text{O}$ Reaction Rates	63
3.3.2 MESA <code>wd_builder</code> , and GYRE	63
3.4. Results	66

CHAPTER	Page
3.4.1 Evolutionary DAVs	66
3.4.2 Variations	78
3.5. Sensitivities	79
3.5.1 Width of the O→C Transition	80
3.5.2 3α Reaction Rate Probability Distribution Function	80
3.5.3 Mixing During Core He-Depletion	81
3.5.4 Number of Thermal Pulses	83
3.6. Summary	84
4 HOW OVERSHOOTING IMPACTS	
WD PULSATION SIGNATURES OF $^{12}\text{C}(\alpha, \gamma)^{16}\text{O}$	88
4.1. Abstract	88
4.2. Introduction	89
4.3. Stellar Evolutionary Models	92
4.3.1 Core Overshooting Prescription During the CHeB	95
4.4. Results	97
4.4.1 Evolution of Composition Profiles	97
4.4.2 Evolutionary Differences After the Main-Sequence	100
4.4.3 WD Adiabatic Pulsation Analysis	101
4.4.4 NOV Set vs. C22	103
4.4.5 Detailed Analysis of Differences	105
4.5. Discussion	111
4.6. Summary	115
4.7. Acknowledgements	116

CHAPTER	Page
5 HOW SPREADSHEET AND GRAPH COACHING IMPACTS STUDENT PERFORMANCE IN HABWORLDS COURSE.....	117
5.1. Abstract	117
5.2. Introduction	118
5.2.1 The Learning Analytics↔Learning Design Connection	118
5.2.2 Related Work	119
5.2.3 A Simplified Framework	122
5.2.4 Novelty of this Work	124
5.2.5 Research Questions	125
5.3. Methodology.....	126
5.3.1 Course Context	126
5.3.2 Learning Design Objective: Better Teaching of 21st Century Skills.....	127
5.3.3 Summary of LA↔LD Collaboration	128
5.3.4 Initial Spreadsheet LD Modifications	129
5.3.5 Graph LD Implementations Post-Fall 2019	130
5.3.6 Additional LD Modifications Post-Spring 2020	132
5.3.7 Categorizing LD Change Types	132
5.3.8 Population and Sample Sizes.....	133
5.3.9 Data Sources and Statistical Analyses	133
5.3.10 Statistical Analysis.....	134
5.4. Results	136
5.4.1 Spreadsheet Changes and Their Effect Sizes.....	136
5.4.2 Graph Changes and Their Effect Sizes	139

CHAPTER	Page
5.4.3 Application Scores	139
5.5. Discussion and Conclusions.....	140
5.5.1 Demonstrating LA↔LD Partnership	140
5.5.2 Spreadsheet LD Changes Analysis.....	141
5.5.3 Graph LD Changes Analysis	142
5.5.4 Application Scores	143
5.5.5 Limitations	143
5.5.6 Conclusions	145
5.5.7 Future Work.....	146
5.6. List of Abbreviations	148
5.7. Declarations	148
5.7.1 Availability of Data and Materials	148
5.7.2 Competing Interests.....	148
5.7.3 Funding	148
5.7.4 Authors' Contributions	149
5.8. Acknowledgements	149
6 SUMMARY	152
REFERENCES	154
APPENDIX	
A CO-AUTHOR PERMISSIONS	178
B APPENDIX FOR CHAPTER 2	179
C APPENDIX FOR CHAPTER 4	185
D APPENDIX FOR CHAPTER 5	189

LIST OF TABLES

Table	Page
4.1 g_2 Weight Function Percentages Per WD Region	108
4.2 g_6 Weight Function Percentages Per WD Region	109
5.1 Categorization of LD Changes Studied.....	150
5.2 Regression Output.	151
D.1 Detailed Spreadsheet LD Changes.	190
D.2 Detailed Graph LD Changes.	191

LIST OF FIGURES

Figures	Page
1.1 Life Cycles of Stars. Stars with lower masses end their lives as WDs while massive stars end their lives as black holes or neutron stars. Figure taken from https://www.schoolsobservatory.org/learn/astro/stars/cycle	3
1.2 Typical evolutionary path for a low mass star. The path shown is from a full evolutionary MESA stellar model.	4
1.3 Left: Eagle nebula. A well known molecular cloud. Bright areas represent star formation (stellar nurseries). Figure taken from https://www.space.com/16396-eagle-nebula-m16-hubble-images-pillars-of-creation.html . Right: The pre-main sequence evolution for a sun-like star. Image taken from https://www.e-education.psu.edu/astro801/content/15_p5.html	5
1.4 Stellar Tracks for various stellar masses on the Hertzsprung-Russel (HR) diagram. The red lines indicate the boundaries for the MS. This figure was taken from Taghiniyarami (2016).	8
1.5 Typical evolution of ^{12}C and ^{16}O mass fractions as a function of the ^4He mass fraction at constant temperature and density. The oxygen mass fraction rises above the carbon mass fraction only when the helium abundance is relatively small.	12
1.6 Observed variable WDs on the $T_{\text{eff}} - \log(g)$ plane, taken from the Montreal White Dwarf Database. The instability strip lines are described in the figure.	16

Figure	Page
1.7 Left: Same is Figure 1.2. Right: Mass fraction profiles showcasing the WD model’s interior stratification.	17
2.1 Mass fraction profiles of the $0.56 M_{\odot}$ DB WD resulting from the evolution of the $2.1 M_{\odot}$, $Z=0.02$, ZAMS model.	29
2.2 Evolution of baseline model’s photon luminosity L and neutrino luminosity L_{ν} (left top), effective temperature T_{eff} and radius R (left middle), central temperature T_c and central density ρ_c (left bottom). Time begins a few thermal timescales after the ab initio WD is released. Gray bands show the luminosity and T_{eff} range of currently observed DBV WD (Montreal White Dwarf Database, Dufour <i>et al.</i> , 2017). Mass fraction profiles are shown at $T_{\text{eff}} = 30,039$ K (right top), $15,012$ K (right middle), and $12,092$ K (right bottom) and at the end of the evolution. Initial mass fraction profiles are shown as solid curves and the diffusing mass fraction profiles are shown as dotted curves. . . .	32
2.3 Propagation diagram for the dipole $\ell=1$ (top) and quadrupole $\ell=2$ (bottom) g-modes at $L=0.01 L_{\odot}$ for the baseline WD model. The Lamb frequency (S_{ℓ} , orange), Brunt-Väisälä frequency (N , blue), radial order $n=1,2,3,10$ eigenfrequencies (dotted black lines), nodes in the radial eigenfunction (filled circles), and g-mode period of each radial order are labeled.	33
2.4 Comparison of the approximation for N^2 (blue curve) in Equation (2.6) and the full calculation of N^2 from MESA (green curve).	38

Figure	Page
2.5 Mass-radius relation of the baseline DB WD model at $\log(L/L_{\odot}) = -2.5$ with key features located: the transition from $X(^{16}\text{O})$ to $X(^{12}\text{C})$ dominated, the rise of $X(^4\text{He})$, the $X(^{12}\text{C})$ bump, where $S_{\ell} < N$ occurs, the transition to $X(^4\text{He})$ dominated, and where $N^2 < 0$	39
2.6 Period evolution of the $\ell=1$ (purple) and $\ell=2$ (green) g-modes at radial orders $n=1,2,3,10$ as the baseline model cools. Each point represents a timestep in MESA where the g-mode was calculated by GYRE. The gray band show the T_{eff} range of observed DBV WD.....	40
2.7 Top to Bottom: Relative period differences of the $g_{1,1}$, $g_{1,2}$, $g_{2,1}$, $g_{2,2}$, $g_{10,1}$ and $g_{10,2}$ modes between the baseline model, P_B , and a model where the ^{22}Ne has been replaced with ^{14}N , $P_{14\text{N}}$. We use the notation $g_{n,\ell}$ for a g-mode of order n and degree ℓ . Gray bands show the T_{eff} range of currently observed DBV WDs.	41
2.8 Top to Bottom: Relative differences in the H^2 , μ_I Γ_1 , χ_{ρ} , and T contributions to N^2 in Equation 2.6. Subscript B represents the baseline model, and subscript ^{14}N represents and a model where ^{22}Ne has been replaced with ^{14}N	42
2.9 Weight functions of the low-order g-modes for baseline model with ^{22}Ne (black curves) and a baseline model where ^{22}Ne has been replaced with ^{14}N (green curves). Subpanels show the relative percent differences between the two curves. The profiles shown are when the two models have cooled to $\log(L/L_{\odot}) = -2.5$. Nodes in the radial eigenfunctions are marked by filled circles.	43

Figure	Page
2.10 Top to Bottom : Relative period differences of the $g_{1,1}$, $g_{1,2}$, $g_{2,1}$, $g_{2,2}$, $g_{10,1}$ and $g_{10,2}$ modes between the baseline model, P_B , a zero-metallicity WD model (gray curves) where the ^{14}N and ^{22}Ne have been put into ^4He and ^{12}C respectively, and a super-solar metallicity model (green curves) where the ^{14}N and ^{22}Ne of the baseline model are doubled.	44
2.11 Top to Bottom: Relative differences in the H^2 , μ_I , Γ_1 , χ_ρ , and T contributions to N^2 in Equation 2.6. Subscript B represents the baseline model, and subscript Z represents the zero-metallicity models (gray curves) and super-solar metallicity models (green curves).	45
2.12 Top Panels: Mass fraction profiles for $0.56 M_\odot$ baseline (colored curves) and zero metallicity (black dashed curves) models at $T_{\text{eff}} \simeq 30,000$ K, 15,000 K, and 12,100 K. <i>Middle Panels</i> : Relative differences in mass fraction profiles, where we have zeroed out the ^{22}Ne and ^{14}N offsets from ^{12}C and ^4He respectively. <i>Bottom Panel</i> : Relative differences in μ_I	50
2.13 Top to Bottom: Relative period differences of the $g_{1,1}$, $g_{1,2}$, $g_{2,1}$, $g_{2,2}$, $g_{10,1}$ and $g_{10,2}$ modes between the baseline model, P_B , and the zero-metallicity WD model, P_Z , with diffusion turned off.	51
2.14 Mass fractions profiles for $0.52 M_\odot$ (left column) and $0.73 M_\odot$ (right column) ab initio DB WD models at $T_{\text{eff}} \simeq 30,000$ K (top), 15,000 K (middle), and at the end of the evolution (bottom). Initial mass fraction profiles are shown as solid curves and the diffusing mass fraction profiles are shown as dotted curves.	52

Figure	Page
2.15 Relative period differences of the $g_{1,1}$, $g_{1,2}$, $g_{2,1}$, $g_{2,2}$, $g_{10,1}$ and $g_{10,2}$ modes for $0.526 M_\odot$ (left column) and $0.729 M_\odot$ (right column). Differences are between the baseline model, P_B , a zero-metallicity WD model (gray curves) where the ^{14}N and ^{22}Ne have been put into ^4He and ^{12}C respectively, and a super-solar metallicity model (green curves) where the ^{14}N and ^{22}Ne of the baseline model are doubled.	53
3.1 Left: $^{12}\text{C}(\alpha, \gamma)$ reaction rate ratios, σ_i/σ_0 , as a function of temperature. For our models, σ_i spans -3.0 to 3.0 in 0.5 step increments, with σ_0 being the current nominal rate. Negative σ_i are gray curves and positive σ_i are green curves. The $\pm 1, 2, 3 \sigma_i$ curves are labeled. The blue band show the range of temperatures encountered during core and shell He burning. Right: Mass fraction profiles of the evolutionary DAV models resulting from the $^{12}\text{C}(\alpha, \gamma)$ reaction rate uncertainties σ_i after each model has cooled to $T_{\text{eff}}=11,500 \text{ K}$. The nominal $\sigma=0$ reaction rate is the black curve, negative σ_i are gray curves and positive σ_i are green curves. Solid curves are for ^{12}C and ^{16}O , dashed curves are for ^1H and ^4He . The trace isotopes ^{14}N , ^{20}Ne , ^{22}Ne , and ^{56}Fe are labeled. Key regions and transitions are also labeled (see text).	64
3.2 Kippenhahn diagram near core He depletion for the $\sigma=0$ evolutionary DAV model. Blue shading represents convective regions, gray the radiative regions, green the H envelope, and the red line marks core He depletion. Labeled are the eventual WD mass and the edges of radiative He burning region R2. Also shown is the evolution of the central ^4He , ^{12}C , and ^{16}O mass fractions.	66

Figure	Page
3.3 Mass-radius relation with key regions and chemical transitions annotated for the $\sigma = 0$ evolutionary DAV model when it has cooled to $T_{\text{eff}} = 11,500$ K. The shaded interiors highlight the regions that can most directly probe the $^{12}\text{C}(\alpha, \gamma)$ reaction rate.	68
3.4 Top: Brunt-Väisälä frequency profiles as a function of fractional radius for the evolutionary DAVs after they have cooled to $T_{\text{eff}} = 11,500$ K. As in Figure 3.1 the nominal $\sigma = 0$ reaction rate is the black curve, positive σ_i are green curves, and negative σ_i are gray curves. Blue bands mark the O→C and C→He transition regions for all σ_i . Bottom: The Ledoux B term in Equation 3.1 as a function of fractional radius. An enlarged view of the first peak in B at the O→C transition is shown in the inset plot.	70
3.5 Top: Kinetic energy of adiabatic g-modes for radial orders $n = 1-19$ and harmonic degree $\ell = 1$ after the evolutionary DAVs have cooled to $T_{\text{eff}} = 11,500$ K. The colors are as in Figure 3.1. Local minima identify trapped modes. The g_5 and g_{10} trapped modes are highlighted with blue bands. Bottom: Period spacing diagram with the local minima at g_5 and g_{10} highlighted by blue bands. The mean period spacing for $\sigma = 0$ model is marked by the dashed line.	72
3.6 Weight functions of the g_4 , g_5 , g_6 , and g_{10} modes for the $\sigma = 0$ model after it cools to $T_{\text{eff}} = 11,500$ K. Trapped modes are in bold font. Weight functions returned by GYRE are normalized to have unit area under their curve. The fractional area under the curve of region R1, the O→C transition, region R2, and the sum of R3 and R4 are given.	74

Figure	Page
3.7 Integer multiples q of the radial wavelength λ_r profiles versus radius for the g_5 , and g_{10} modes, for σ_0 . The trapped g_5 mode is shown by the dark blue solid line, and the dotted curves depict the trapped g_{10} mode. Solid black segments depict the width of the regions R1, R2, R3, and R4, as defined by distance between labeled chemical transitions.	75
3.8 Top panels: Relative period differences from $\sigma = 0$ for the g_5, g_6 , and g_{10} modes as the evolutionary DAVs cool. Colors for the σ_i follow Figure 3.1. The range of T_{eff} in observed DAV WDs is marked, with the vertical dashed black line selecting the $T_{\text{eff}} = 11,500$ K midpoint. Bottom panel: Relative period differences for g_5 versus the $^{12}\text{C}(\alpha, \gamma)^{16}\text{O}$ reaction rate uncertainties σ_i at $T_{\text{eff}} = 11,500$ K. Scatter points are the raw data values and the curve is a polynomial fit.	76
3.9 Relative period differences for model sequences of varying WD masses, shell masses, and classes. The <code>wd_builder</code> DAVs were measured at $T_{\text{eff}} = 11,500$ K for the <code>wd_builder</code> DBVs were measured at $T_{\text{eff}} = 25,000$ K. Labeled are the $\pm 3\sigma$ uncertainties on the experimental $^{12}\text{C}(\alpha, \gamma)^{16}\text{O}$ reaction rate in steps of 0.5σ , the trapped g-mode that most distinctly probes the radiatively-formed, carbon-rich region R2, and the mean relative period difference for each sequence.	77

Figure	Page
4.1 Top: Mass fraction profiles without overshooting (NOV) during the CHeB phase. Left: Mass fraction profiles after core He-depletion, terminated prior to the first thermal pulse at $\log(L/L_\odot) > 3.0$. Middle: Mass Fraction profiles at the first <code>wd_builder</code> model step. These profiles have been shaved of their excess H envelope prior to running on the WD cooling track. These are the initial hot WD profiles. Right: Mass fraction profiles when the models have cooled to $T_{\text{eff}} = 10,000$ K. The smoothness in the profiles reflects the element diffusion processes included in the calculation. Bottom: Mass fraction profiles with core overshooting (OV) during the CHeB phase, in the same format as above. Green curves represent positive $\sigma_i {}^{12}\text{C}(\alpha, \gamma){}^{16}\text{O}$ reaction rates, grey curves represent negative $\sigma_i {}^{12}\text{C}(\alpha, \gamma){}^{16}\text{O}$ reaction rates. For both positive and negative σ_i , the shading grows fainter the further σ is from the standard rate ($\sigma = 0$; black curve).	93
4.2 Composition profiles after the NOV (top) and OV (bottom) models cool to $T_{\text{eff}} = 10,000$ K. Region boundaries are indicated by vertical blue lines, and the σ_i colors are the same as in Figure 4.1.	97

Figure	Page
4.3 Kippenhahn diagrams for the NOV (left) and OV (right) $\sigma = 0.0$ models. The x-axis is the respective stellar model's age, the left y-axis is the mass coordinate, the right y-axis is the central mass fraction of the isotopes. Bright green areas represent convection, blue shaded regions depict nuclear burning (see colorbar), white areas represent radiation, and yellow-gold areas represent overshooting (right figure). The light green area shows the hydrogen envelope. The solid pink curve is the central ^4He mass fraction, the solid dark blue curve is the central ^{16}O mass fraction, and the dark yellow curve is the central ^{12}C mass fraction. The dashed line shows core helium depletion. The evolution was terminated when $\log(L/\text{L}_\odot) > 3.0$ for all stellar models, and the figures are plotted until that point. Annotated is the radiative R2 region's edges and widths. An interactive figure is provided in the online version. Its functionality compares the NOV and OV Kippenhahn diagrams for any given $\sigma_i \ ^{12}\text{C}(\alpha, \gamma)^{16}\text{O}$ reaction rate. To use the interactive figure, click on the 'sigma' slider at the top, and slide through the indices 0 through 12. Sliding through each index provides the user the side by side comparison of the Kippenhahn diagrams for the respective $\sigma_i \ ^{12}\text{C}(\alpha, \gamma)^{16}\text{O}$ reaction rate used in the evolution. Index 0 starts at $\sigma_{-3.0}$ and index 12 ends at $\sigma_{3.0}$	98

Figure	Page
4.4 Top two: NOV set's signature adiabatic pulsation modes shown at $T_{\text{eff}} = 11,500$ (bright green), and $T_{\text{eff}} = 10,000$ (blue) K respectively. The first panel shows the signal from the g_2 mode; the second shows the signal from the g_6 trapped mode. Bottom: The kinetic energy diagrams for all σ_i at $T_{\text{eff}} = 11,500$ K (left) and $T_{\text{eff}} = 10,000$ K (right) respectively. The green dots/lines represent E_{kin} for $\sigma_i > 0$; grey for $\sigma_i < 0$; black for $\sigma = 0$. The shading of color gets fainter the further away from $\sigma = 0$.	102
4.5 Pulsation periods as function of T_{eff} for the NOV (black) and OV (grey) model sets.	103
4.6 Top to bottom: Mass fractions of ^{12}C and ^{16}O ; B profile; normalized weight function profile for the g_6 mode; normalized weight function profile for the g_2 mode. The left column shows the NOV results and the right column shows the OV results. Both figures are for $\sigma = 0.0$, $T_{\text{eff}} = 10,000$ K. The R1-R4 region boundaries are indicated by dashed vertical lines. An interactive figure is provided in the online version. Its functionality compares the NOV and OV diagrams, as structured in this figure, for any given σ_i $^{12}\text{C}(\alpha, \gamma)^{16}\text{O}$ reaction rate. To use the interactive figure, click on the ‘sigma’ slider at the top, and slide through indices 0 through 12. Sliding through each index provides the user the side by side comparison of the diagrams for the respective σ_i $^{12}\text{C}(\alpha, \gamma)^{16}\text{O}$ reaction rate used in the evolution.	106

Figure	Page
4.7 Integer multiples of the local radial wavelengths $q \cdot \lambda_r$ for g_2 and g_6 as a function of the star's radius R . Mode resonance occurs when $q \cdot \lambda_r$ closely matches the width of a certain region(s) in the star. The left panel is the NOV set's mode resonance and the right panel is the OV set's mode resonance. In both panels, the black horizontal lines mark the respective region widths. Blue curves show $q \cdot \lambda_r$ for g_2 and maroon curves show $q \cdot \lambda_r$ for g_6 . The q values are stated in the legend.	110
4.8 Adiabatic g_2 (left) and g_6 (right) mode signatures for the NOV and OV sets, at $T_{\text{eff}} = 11,500$ (bright green) and $T_{\text{eff}} = 10,000$ K (blue) respectively.	110
5.1 General framework to successfully unite LD with LA, aimed to enhance student learning and performance.	123
5.2 Top: Fall 2019 question in <i>R*1: Calculate Distance</i> lesson that suggests ease of spreadsheet use for computation in the left help button. Bottom: Same question in the post-Fall 2019 semesters (through Spring 2021), modified to give support for spreadsheet use in the prompt. The help buttons were also removed. Note that the numerical values shown are randomly generated for each student to prevent cheating. The underlying calculation shown was not modified as part of the LD changes.	131

Figure	Page
5.3 A: Wilcox Effects for screens with spreadsheet changes. Effects with error bars indicate screens with split screens. B: Wilcox Effect sizes for screens with graph changes. For both panels, blue circles are the weighted means of the Spring 2020, Fall 2020, and Spring 2021 semesters. Orange circles are for Spring 2020 only, while the purple circles are the weighted means of Fall 2020 and Spring 2021 effect sizes. The x-axis is categorized by the type of change as indexed in Table 5.1. Please refer to Table 5.1 for the detailed descriptions.	138
5.4 Mean scores on application lessons (quizzes) following each lesson. The x-axis is the lesson name and the y axis is the mean percentage score. Black dots represent the Fall 2019 mean percentage scores; gold dots are the weighted mean values of the post-Fall 2019 semester percentage scores. Error bars show one standard error and represent the variability among the three treatment semesters.	140
B.1 Relative differences in the $g_{1,1}$, $g_{1,2}$, $g_{2,1}$, $g_{2,2}$, $g_{10,1}$, $g_{10,2}$ pulsation periods for different minimum mass resolutions as the baseline WD models cool. We use the notation $g_{n,\ell}$ for a g-mode of order n and degree ℓ . The minimum mass resolution of 5,000 cells, used for all the results reported, is shown by the black horizontal lines.	183
B.2 Relative differences in the $g_{1,1}$, $g_{1,2}$, $g_{2,1}$, $g_{2,2}$, $g_{10,1}$, and $g_{10,2}$ pulsation period for different temporal resolutions as the baseline WD models cool. The largest change in the central temperature allowed over a timestep, <code>delta_lgT_cntr_limit = 0.001</code> , used for all the results reported, is shown by the black horizontal lines.	184

Figure	Page
C.1 Mass fraction profiles for at the completion of CHeB for a 30 isotope (solid) and 23 isotope nuclear reaction network (dotted). Shown are the 5 most abundant isotopes for both networks.	186
C.2 Left: Evolution of central mass fractions during CHeB until $\log(L/L_{\odot}) = 3.0$ at three resolutions. Middle: Mass fraction profiles at $\log(L/L_{\odot}) = 3.0$ for the three resolutions. Right: Middle figure zoom-in to show differences.	188

Chapter 1

INTRODUCTION

1.1 Overview

The constituents of life were formed in the interiors of stars, ergo, “*we are made of star stuff*” (Carl Sagan). To better understand the origins of life, one must become acquainted with studying stars.

The fate of 98% of stars, including the Sun, is to become a White Dwarf (WD) (Fontaine *et al.*, 2001). WDs are the stellar corpses of low mass ($M \lesssim 8 M_{\odot}$) stars. Broadly, they are simplified as solid Carbon-Oxygen (CO) cooling embers with a thin gaseous shell. The basic structure of WDs are simple to understand compared to other stars and are among the most well understood class of stars. They set a lower bound for the age of our universe, help estimate the initial to final mass function, are common progenitors of type Ia supernova explosions, and, as we’ll see, serve as probes of their evolutionary past (Kalirai *et al.*, 2008; Moll *et al.*, 2014). Due to their abundance in the universe, there are $\sim 72,000$ cataloged WDs in the *Montreal White Dwarf Database* (MWDD, Dufour *et al.* (2016)) alone, making them prime candidates for such areas of study.

The internal structure of a star encapsulates its evolution history. Stellar interiors are elusive from direct observation. A popular technique to probe the interiors of stars is asteroseismology, the study of pulsating stars. Just as seismology has revealed much of Earth’s interior composition and structure, asteroseismology can extract information of stellar interiors. This, in turn, can reveal information about stellar evolution.

Stars are known to pulsate at various times in their evolution. For WDs, there are two main variable (pulsating) classes. The first are known as DAV WDs and have hydrogen (H) atmospheres. The second main class are DBV WDs and have helium (He) atmospheres. The physical reason behind why these stars pulsate will be addressed later.

The standard practice to unravel a WD's interior is by tuning the properties of a computational WD model until its ensuing pulsations match the observed variable WD's. Computational modelling is naturally subject to uncertainties. Often, modelling uncertainties are assumed to be insignificant, or are simply overlooked. Observational pulsation data has reached 6-7 significant figures of precision. As such, seemingly insignificant theoretical considerations may be more important than expected because the results can qualitatively differ within the degree of discernability, depending on what is (or isn't) accounted for in the modelling process.

In this Thesis, I show the importance of accounting for such theoretical considerations and uncertainties regarding WD seismology. I will show how the presence/absence of ^{22}Ne alters the pulsation results within the detectable limit, how certain trapped modes from WD pulsations are potential tracers of the $^{12}\text{C}(\alpha, \gamma)$ reaction rate, and how the $^{12}\text{C}(\alpha, \gamma)$ reaction rate's signature from certain modes change when accounting for an additional theoretical uncertainty known as overshooting. This thesis informs modelers of the sensitivities that WD seismology should consider, furthers our fundamental understanding of stellar evolution, and captures important information regarding the chemical evolution of stars. This work is a small contribution to the ongoing effort to better understand stellar evolution for low mass stars, and the processes that ultimately form life.

1.2 Evolutionary Phases of Low-Mass Stars

Figure 1.1 is a simplified overview of the life cycle for stars, categorized into low and high mass stars (average and massive stars in figure). All stars come from a stellar nebula, spend most of their lives illuminating their environments via H burning (fusion), then undergo the relative processes to become either a WD (low mass stars) or a black hole/neutron star (high mass stars). We will concern ourselves with the top branch of Figure 1.1 as we seek to understand more about the stellar evolution history for WDs.

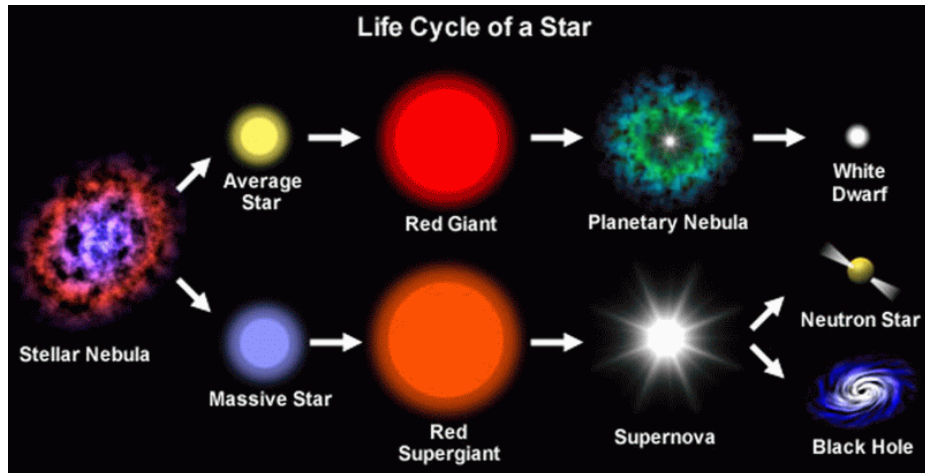


Figure 1.1: Life Cycles of Stars. Stars with lower masses end their lives as WDs while massive stars end their lives as black holes or neutron stars. Figure taken from <https://www.schoolsobservatory.org/learn/astro/stars/cycle>.

Figure 1.2 shows the evolutionary path for a low mass star, and is a version of a Hertsprung-Russell (HR) diagram. HR diagrams depict the temperature-luminosity relation for stars, and they are useful for referencing various stages of evolution.

1.2.1 Pre-Main Sequence

The pre-Main Sequence (pre-MS) is the star formation period prior to stellar burning. This corresponds to the grey portion in Figure 1.2, from points 0 to 1.

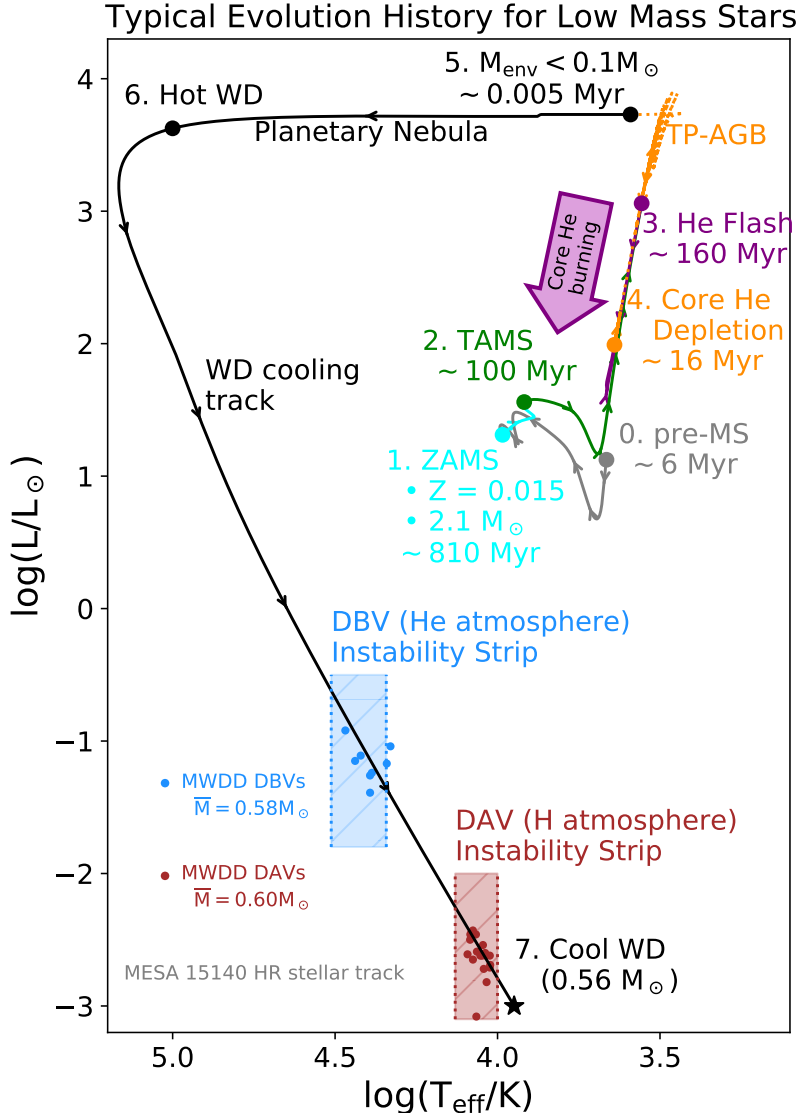


Figure 1.2: Typical evolutionary path for a low mass star. The path shown is from a full evolutionary MESA stellar model.

Figure 1.1 shows that all stars come from a stellar nebula, which are the overdense, cool regions in molecular clouds. The left of Figure 1.3 is a well known molecular cloud, the Eagle nebula. The columns of gas and dust provide material to promote star formation. The overdense regions are subject to gravitational contraction; the material begins to shrink in on itself, forming a protostar. The right side of Figure 1.3 shows the HR portion of the pre-MS for a Sun-like star (red/yellow track). The

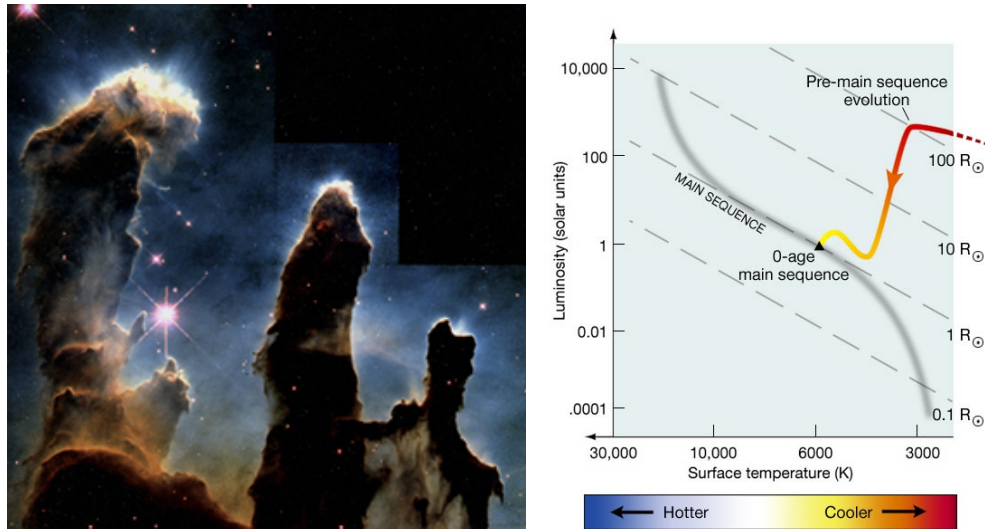


Figure 1.3: Left: Eagle nebula. A well known molecular cloud. Bright areas represent star formation (stellar nurseries). Figure taken from <https://www.space.com/16396-eagle-nebula-m16-hubble-images-pillars-of-creation.html>. Right: The pre-main sequence evolution for a sun-like star. Image taken from https://www.e-education.psu.edu/astro801/content/15_p5.html

protostar begins to collapse from $\sim 100R_{\odot}$ (100 times the Sun's radius) to $\sim 1R_{\odot}$. The luminosity drops during this phase, while the temperature heats only slightly. This is because the star is too cool for any internal energy sources to illuminate the protostar (aside from its blackbody radiation), so all the energy is supplied by gravitational potential energy from contraction.¹ The contraction process is rather slow, so excess heat gradually radiates outward, keeping the protostar relatively cool. For low mass stars, this process is characterized by the “Hayashi track”, which is the steep descent in the right of Figure 1.3. During this time, the star is fully convective. At the bottom of the Hayashi track, there’s a turning point, and the luminosity begins to increase. Here, the star is compact and hot enough to become radiative, and may even start deuterium burning. It ascends in luminosity for a bit, before settling on

¹Equating luminosity to the power from contraction: $L = -\frac{dW}{dt} \sim -\frac{GM^2}{R^2} \frac{dR}{dt}$. Further, blackbody luminosity is defined as $L = 4\pi\sigma_B R^2 T_{\text{eff}}^4$. As R decreases, and T_{eff} changes little, the overall L also decreases during gravitational contraction.

what is known as the zero-age main sequence (ZAMS), defined as the initial start of H fusion ².

1.2.2 The Main Sequence

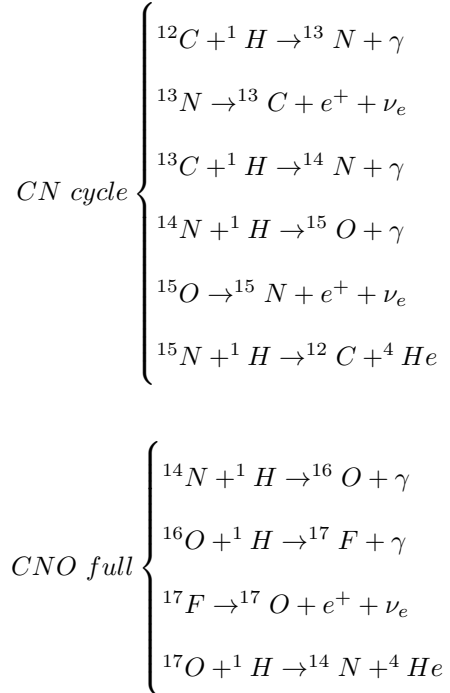
From ZAMS, stars spend the majority of their lives burning H in their cores under hydrostatic equilibrium (HSE) ³. This phase of evolution is the main sequence (MS) and is the cyan portion of the stellar track in Figure 1.2, from points 1 to 2. There are two main H burning mechanisms: the proton-proton (PP) chain and the CNO cycle. These are listed below (Kawaler, 1995). Proton-Proton Chains:

$$\begin{aligned}
 PP - I & \left\{ \begin{array}{l} {}^1H + {}^1H \rightarrow {}^2H + e^+ + \nu_e \\ {}^2H + {}^1H \rightarrow {}^3He + \gamma \\ {}^3He + {}^3He \rightarrow {}^4He + {}^1H + {}^1H \end{array} \right. \\
 PP - II & \left\{ \begin{array}{l} {}^3He + {}^4He \rightarrow {}^7Be + \gamma \\ {}^7Be + e^- \rightarrow {}^7Li + \nu(+\gamma) \\ {}^7Li + {}^1H \rightarrow {}^4He + {}^4He \end{array} \right. \\
 PP - III & \left\{ \begin{array}{l} {}^7Be + {}^1H \rightarrow {}^8B + \gamma \\ {}^8B \rightarrow {}^8Be + e^+ + \nu_e \\ {}^8Be \rightarrow {}^4He + {}^4He \end{array} \right.
 \end{aligned}$$

²The information in this paragraph can be found from many sources, but I'll state Hansen and Kawaler (1994a); Young (2020) as two examples.

³The state when external forces (gravity) is balanced by a pressure gradient force. For stars, the pressure gradient force comes from fusion processes. Nuclear burning supports stars against gravitational collapse.

CNO cycle reactions:



Stars with $M \lesssim 1.1M_\odot$ dominantly burn H via the PP chains, and their cores are purely radiative. The CNO cycle dominates H-burning for stars with $M \gtrsim 1.1 \sim 8.0M_\odot$, and have convective cores (Young, 2020).

The end product for both chains is ${}^4\text{He}$, a He (or α) particle. Any beginning or intermediate reactants (i.e. the Be, B, C, N, O , and F isotopes) are merely catalysts that promote the net conversion of 4 protons into a He particle. There is no substantial net creation or destruction of these catalyst reactants, and the abundance of these isotopes is a gauge of the star's initial metallicity ⁴ that it was bestowed from the parent molecular cloud. This has important implications on subsequent stages of stellar evolution.

The H-burning phase is on the order of $\tau_{MS} \sim 10^{10}$ years for low-intermediate mass stars (Iben, 1967; Hansen and Kawaler, 1994a). When a star's core is deplete of its H fuel, it has reached the end of the MS phase, known as the terminal age MS

⁴any element/isotope above He on the periodic table

(TAMS), point 2 in Figure 1.2. Figure 1.4 shows an HR diagram for various stellar masses. Each curve represents the evolutionary track for a respective mass. The solid red line indicates the ZAMS starting point, and the dashed red line indicates the TAMS. During the MS, the star will evolve along a similar track between these red lines, depending on its mass. For lower mass stars, the placement of its overall evolutionary track is lower in both temperature and luminosity.

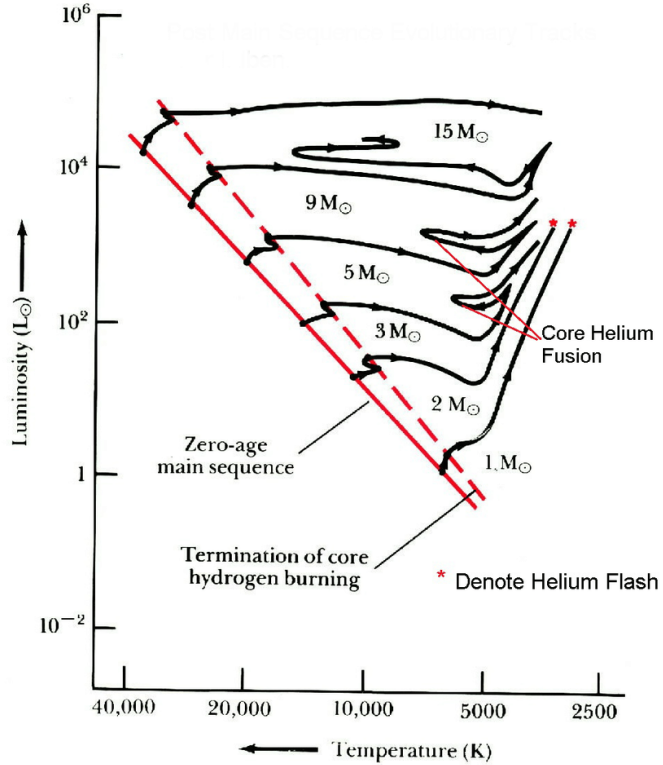


Figure 1.4: Stellar Tracks for various stellar masses on the Hertzsprung-Russel (HR) diagram. The red lines indicate the boundaries for the MS. This figure was taken from Taghiniyarami (2016).

The stellar tracks with $M > 1M_{\odot}$ show a hook-like feature at the TAMS, where the star rises in both luminosity and temperature. This is a result of H exhaustion. For stars with convective cores, H is depleted out to a stellar radius of $r = r_{convective\ core}$. The temperature in the H shell surrounding the core is lower than the required temperature to burn H in the shell, and the star contracts under

the force of gravity. The contraction happens for a brief time, on a Kelvin-Helmholtz timescale,⁵ and the star briefly increases in luminosity and moves “blueward,” rising in temperature⁶. This is depicted in Figure 1.4, where all stellar tracks with $M > 1 M_{\odot}$ (all stars with convective cores) increase in both luminosity and temperature along the TAMS line. For radiative cores (i.e. the $1 M_{\odot}$ star in Figure 1.4), H is depleted only in the center, out until $r = 0 + \delta$, and gradually increases in mass fraction to the surface of the star. For these stars, there is a smooth transition to H shell burning, and there isn’t the featuristic Kelvin-Helmholtz jag at the TAMS.

1.2.3 H Shell Burning

At the TAMS, the star is left with a predominately He core, with a surrounding H-rich atmosphere. The temperature of the core isn’t sufficiently high enough to proceed to He burning, but is now sufficiently high for H burning to take place in a thin layer just outside the inert He core (H shell burning). Shellular burning is the source of the observable luminosity at this time (points 2 to 3 in Figure 1.2).

With no fusion happening in the core, the only power source available to support the core is its gravitational potential energy. The core begins to contract until the conditions for core He burning are reached.

1.2.4 Core He-Burning

The temperature condition at which core helium burning (CHeB) can begin is when $T_{core} \gtrsim 10^8$ K (Young, 2020; Pinsonneault and Ryden, 2023; Kawaler, 1995; Burbidge *et al.*, 1957a). For stars with $M_* \gtrsim 2.3 M_{\odot}$, this condition is met before

⁵the timescale in which contraction is solely responsible for a star’s luminosity:
 $t_{KH} \sim 2 \times 10^7 \left(\frac{M}{M_{\odot}}\right)^2 \left(\frac{L}{L_{\odot}}\right)^{-1} \left(\frac{R}{R_{\odot}}\right)^{-1} (yrs)$ (Hansen and Kawaler, 1994b)

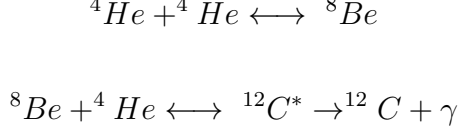
⁶Hotter stars are “bluer” than cooler stars, which appear more “red”. Temperature is a gauge for color, and often the HR diagram is plotted on a color index on the x-axis. The temperature-color reasoning comes from Blackbody radiation.

the inert core becomes degenerate⁷, and He burning occurs naturally as soon as the temperature condition is reached. For stars with masses between $\sim 0.4M_{\odot} - \sim 2.3M_{\odot}$, the conditions in the core are far different. Stars in this range have degenerate inert cores that are extremely dense, to the point that the pressure law the core obeys, its equation of state (EOS), is almost entirely dependent on the density ($P_{deg} \propto \rho^{5/3}$) rather than an ideal gas ($P \propto \rho T$). As such, any temperature increase has no significant effect on the local pressure and density conditions. When $T_{core} \gtrsim 10^8$ K for these stars, He burning begins under a brief positive feedback loop: the burning heats the plasma, increases the temperature leading to a faster burning rate, which increases temperature again, which increases the burning rate again, etc. The loop ends when the temperature is sufficiently high to lift the degeneracy pressure law and restore the gas law EOS. This thermonuclear runway is relatively brief, and is known as the He flash (point 3 in Figure 1.2). After the He flash, the EOS stabilizes and core He burning proceeds (Hansen and Kawaler, 1994a; Young, 2020; Pinsonneault and Ryden, 2023).

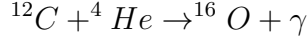
The first He burning reaction is known as the triple alpha process, where a net input of 3 He (α) particles produce ^{12}C . The first step of the process is the combination of 2 α particles to form 8Be . This is an endothermic process, requiring an energy input of ~ 92 keV. The lifetime of 8Be is 10^{-16} s. During CHeB, the temperature and density is high enough for a 8Be nucleus moving at $\sim 0.01c$ to travel $\sim 10^5$ times the length of its diameter prior to decaying. This makes for a larger probabalistic encounter with another α particle to then form ^{12}C (Pinsonneault and Ryden, 2023).

⁷or before the inert core reaches a central density larger than $\sim 10^5 \text{ g cm}^{-3}$

Following Burbidge *et al.* (1957a), the full 3- α process⁸ is then



As carbon production increases, helium burning proceeds with a subsequent α capture to form ${}^{16}O$:



These two reactions compete with one another as He depletes in the core.

Figure 1.5 shows the evolution of the central ${}^{12}C$ and ${}^{16}O$ creation with respect to 4He depletion. The annotated \dot{Y}_x equations relate the respective isotope derivatives to the abundances and rates of creation/depletion of the other main isotopes during CHeB. The main reactions during CHeB are the 3- α process and ${}^{12}C(\alpha, \gamma){}^{16}O$. There is also a subsequent reaction in the α burning sequence of ${}^{16}O(\alpha, \gamma){}^{20}Ne$. This process is relatively slow at typical He burning temperatures in relation to 3- α process and ${}^{12}C(\alpha, \gamma){}^{16}O$.

For low mass stars, the competition between 3- α and ${}^{12}C(\alpha, \gamma){}^{16}O$ during CHeB will ultimately determine the inner CO core structure that the ensuing WD will end up with. Another process during CHeB has important implications on the star's initial metallicity. During core H burning, the slowest step in the CNO cycle is ${}^{14}N(p, \gamma){}^{15}O$. At the end of core H burning, there is a piled up pool of ${}^{14}N$, which is converted to ${}^{22}Ne$ during CHeB via ${}^{14}N(\alpha, \gamma){}^{18}F(e^+\nu_e){}^{18}O(\alpha, \gamma){}^{22}Ne$. Thus, at the end of CHeB, the resulting amount of ${}^{22}Ne$ is a reflection of the minimum metallicity the star was born with. Further, the amount of ${}^{22}Ne$ at the end of CHeB sets the ${}^{22}Ne$ abundance for the forthcoming WD. In the following chapters, we will see that WD pulsations are

⁸Fred Hoyle found that significant carbon production would only occur if the fusion of 4He with 8Be went to an excited state of ${}^{12}C$. This is based on energy resonance (Burbidge *et al.*, 1957a; Pinsonneault and Ryden, 2023)

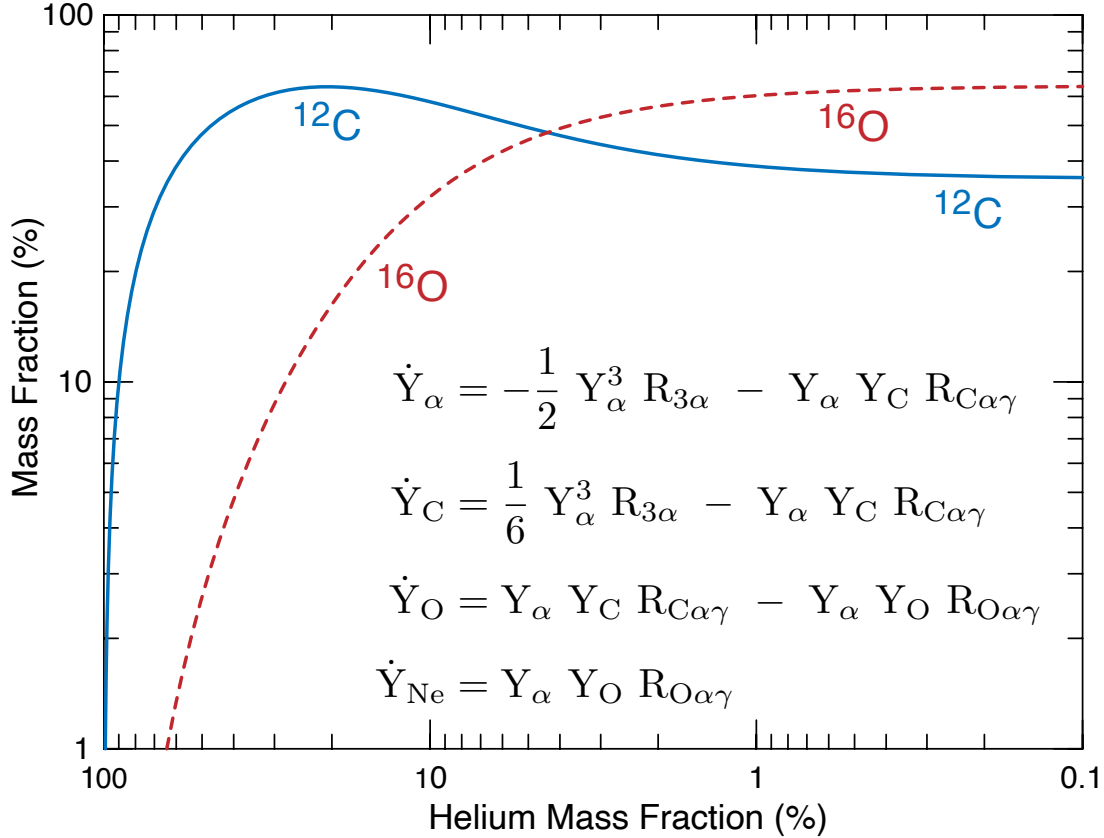


Figure 1.5: Typical evolution of ^{12}C and ^{16}O mass fractions as a function of the ^{4}He mass fraction at constant temperature and density. The oxygen mass fraction rises above the carbon mass fraction only when the helium abundance is relatively small.

sensitive to both ^{22}Ne and CO abundances; processes during CHeB directly impact WD composition profiles and WD pulsations. I will discuss the importance of the CHeB phase of stellar evolution in the upcoming sections and chapters.

1.2.5 The AGB and Thermal Pulses (TPs)

Point 4 in Figure 1.2 marks core He depletion. The core contracts, and the star is illuminated via shell burning in a surrounding layer. The outer layers expand and cool, and the overall luminosity ascends up the active giant branch (AGB) in the HR diagram.

The CO core is surrounded by a He shell, which is topped with a H envelope. Burning occurs in both shells, but they are out of phase with each-other; He burning has a shorter timescale than H burning, causing thermal instabilities, and drives thermal pulses, or TPs. This phase can be thought of as “double shell burning”. In stellar modeling, TPs are easily detected by the drastic rise and fall in surface luminosity, “pulsing” up and down on the HR diagram for $\sim 10^5$ years. These pulses can drive mass loss of the star. The details of TPs are not well understood (Gautschy, 2023), but this phase of evolution has important impacts on a star’s host galaxy and ISM (Rosenfield *et al.*, 2016), as well as a low mass star’s future WD atmosphere and its WD pulsations. I will show some consequences of the latter in chapter 4.

1.2.6 The Fate of Low Mass Stars

During and after the AGB (points 4-6 in Figure 1.2), the core continues to contract, becoming increasingly dense. When the TPs cease, the star moves to the next phase of evolution known as the Planetary Nebula. There is extreme mass loss of the exterior layers, however the processes are not fully understood⁹. With the core contracting, the star is seen to slide rapidly from the right of the HR diagram to the left. The luminosity remains relatively constant while the temperature gets much hotter. This is understood from the surface luminosity equation $L = 4\pi R^2 T^4 \sigma_B$, where σ_B is the Boltzman constant, and R, T are the surface radius and temperature respectively. As the core shrinks, it heats up. The drastic heating is the combined effect of shrinking and revealing the near core-temperature, which is much hotter than the previous stratified envelope temperature. At the end of the “slide”, the remnant star is a hot white dwarf.

⁹It is thought that some combination of variability, thermal pulses, and “superwinds” are responsible for the substantial mass loss (Kawaler, 1995).

1.3 WDs & Chandrasekar Limit

WDs, points 6 to 7 in Figure 1.2, are supported by electron degeneracy pressure, the pressure of rapidly moving electrons which prevents gravitational collapse. This EOS requires WDs to be extremely compact objects, with $\rho \sim 10^6 \text{ g cm}^{-3}$.

WDs are also characterized by a limiting mass for which they cannot exceed. In 1931, Chandrasekhar famously derived this maximum mass to be $\sim 1.4M_\odot$ for non-rotating, non-magnetic (ideal) WDs¹⁰ (Chandrasekhar, 1931). Any remnant core above the limiting mass cannot be supported by electron degeneracy pressure and proceeds to later burning stages and phases of evolution. This corresponds to stars born at a ZAMS mass above $\sim 9M_\odot$.

The focus of this paper studies WD stars, so I will mention a few reasons why they are of special interest. As mentioned, the fate of nearly all stars ($\sim 98\%$) will become WDs, including our Sun. Naturally, this gives an abundant supply of observed WD data, making them an easily accessible class of stellar candidates to study. The Chandrasekhar mass limit for WDs places constraints on early evolutionary stages, and on the evolution of WDs (Kawaler, 1995). For example, as pointed out in Kawaler (1995), there is a cutoff luminosity of $L \approx 10^{-4.5}L_\odot$ where no WD has been observed in the solar neighborhood, reflecting the finite age of the disk of our galaxy.

WDs are relatively simple objects to understand. They are degenerate cooling CO embers, veiled by a gaseous atmosphere of H and/or He. They simply radiate away until they become too dim to detect. The well-understood nature of WDs helps constrain prior stages in stellar evolution.

¹⁰In cases considering large magnetic fields, or noncommutativity, the mass limit may be larger (Das and Mukhopadhyay, 2013; Kalita *et al.*, 2021)

1.4 Asteroseismology

Most of the observable properties available to us can only inform us of stellar atmospheres. This limits what we can truly know about stellar interiors and their evolution.

There is potential to probe deeper into stellar interiors through asteroseismology, the study of pulsating stars. In general, this is because pulsations are sensitive to the medium they travel through¹¹. Seismology of the earth has given us information of earth's interior structure. Likewise, asteroseismology can inform us of stellar interiors.

Most stars pulsate. The most common pulsations are known as p-modes and g-modes. p-modes are caused by pressure disturbances, and g-modes are caused by gravitational disturbances.

This thesis explores WD seismology. Observationally, variable WDs have multi-periodic oscillations with periods in the range $P \sim 100 - 1000$ s. There are two main variable WD groups, known as DAVs (or ZZ-ceti variables), and DBVs (or V777 Her), where 'V' stands for variable. Observed DAVs and DBVs are shown in the red and blue shaded areas in Figure 1.2. Figure 1.6 also shows the $T_{\text{eff}} - \log(g)$ (surface gravity) plane for observed variable WDs, taken from *MWDD*. The lines outline two ranges of "instability strips" where observed pulsating WDs are generally located. The hotter, left region represents the observed DBV WDs, and the cooler, right region represents the observed DAV WDs. The DAV WDs have H atmospheres and are observed to pulsate within $13000 \pm 500 \gtrsim T_{\text{eff}} \gtrsim 11000 \pm 500$ K. The DBV WDs have a He surface, with an instability pulsation range of $24,000 \gtrsim T_{\text{eff}} \gtrsim 21500$ K (Kawaler, 1995). The variability during these instability periods come from the

¹¹Examples: waves on a string have a faster frequency for light-weight strings and a slower frequency for heavier strings; guitar has a higher pitch (frequency) when string is tightened (greater tension); dropping a pebble in water creates more ripples than dropping a pebble in sand. Frequency properties like these can be traced back to the medium the waves travel through.

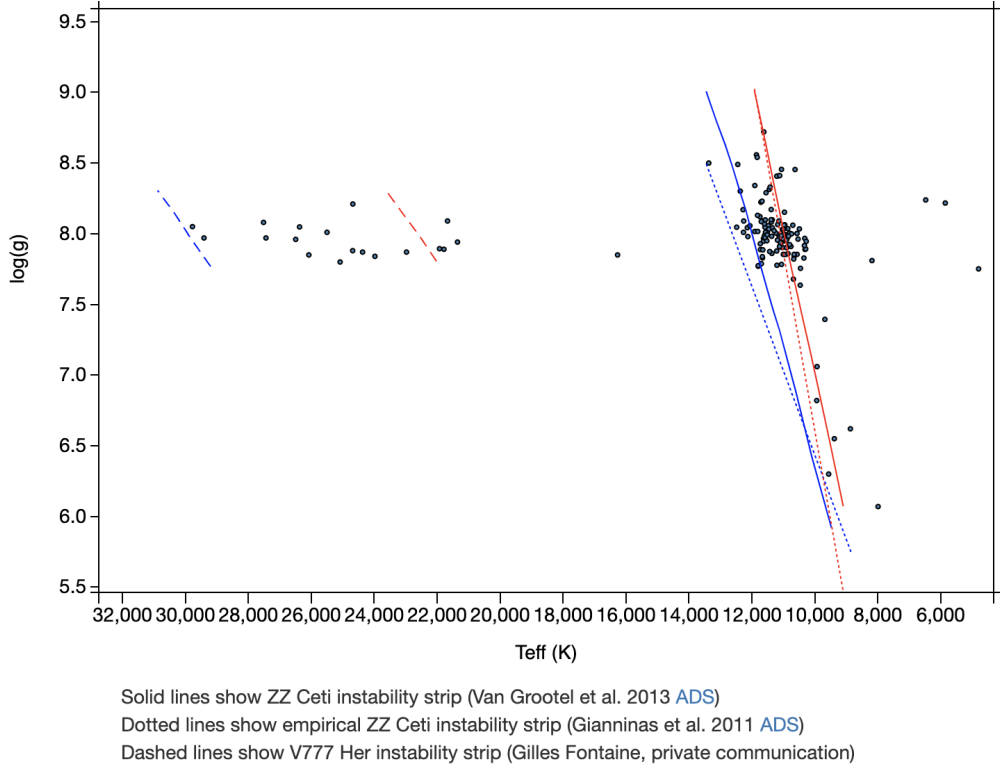


Figure 1.6: Observed variable WDs on the $T_{\text{eff}} - \log(g)$ plane, taken from the Montreal White Dwarf Database. The instability strip lines are described in the figure.

partial recombination of the H and He atoms, for DAV and DBV WDs respectively. Recombination for H occurs at $T_{\text{eff}} \sim 12,000\text{K}$ and He recombination occurs at $T_{\text{eff}} \sim 22,000\text{K}$. This increases the envelope opacity, decreasing the flow of radiation, which leads to pulsational instabilities and hence g-mode oscillations (Van Grootel, V. et al. (2012) and references therein).

1.4.1 Notation

Details of non-radial oscillation theory can be found in Unno et al. (1989). At large, these oscillations come from spherical harmonics. On a piano, each piano key has a unique pitch that is identified by its assigned note and octave. In a WD, the g-modes can be thought of as piano keys, and are identified by the harmonic degree ℓ ,

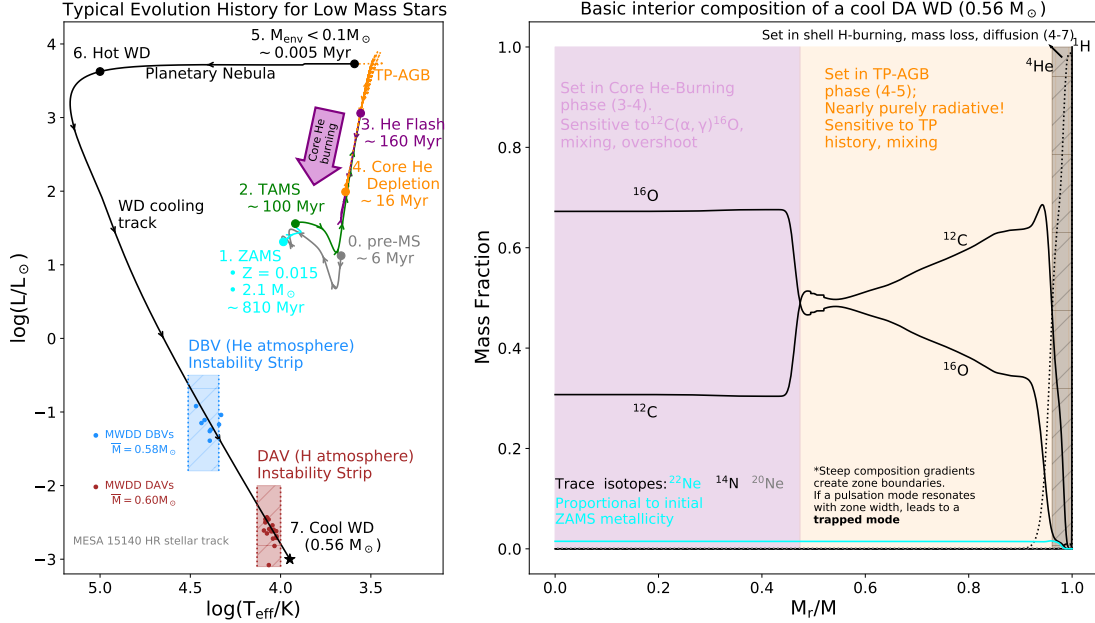


Figure 1.7: Left: Same is Figure 1.2. Right: Mass fraction profiles showcasing the WD model’s interior stratification.

azimuthal orders m , and radial order n . The radial order is the number of nodes in the radial direction of the WD. The combination of these properties are the identifying “notes” of the WD’s oscillations. I will often only refer to g-modes with n , and assume $\ell = 1$ and $m = 0$ in this thesis.

1.4.2 Gaining Insight to Stellar Interiors and Evolution

The goal of asteroseismology is to gain information about stellar interiors, and in turn, their evolution history. Figure 1.7 helps shed light on how a WD interior relates back to its evolutionary past. The left of Figure 1.7 is a repeated HR diagram of Figure 1.2. The right side of Figure 1.7 shows the mass fraction profiles of the resulting WD model, with respect to fractional mass.

The purple shaded area represents the CO remnant inner core region. Here, the abundances and structure of the ^{12}C and ^{16}O profiles are determined during core He burning (stages 3-4 in the left plot). As annotated in the figure, the resulting profiles

here are sensitive to the prescribed $^{12}\text{C}(\alpha, \gamma)^{16}\text{O}$ reaction rate, mixing processes, and overshooting. The presence of trace isotopes are proportional to the initial ZAMS metallicity.

The light-orange shaded area represents the carbon-rich outer core of this WD model. As annotated, the structure of the ^{12}C and ^{16}O profiles are determined along the TP-AGB (points 4-5 in the left), and the result is sensitive to the TP history accounted for and mixing.

The grey-shaded area shows the thin He/H atmosphere. This is determined from points 4-7 on the left figure and the result depends on shell H-burning, the mass loss mechanisms, and diffusion down the WD cooling track.

The asterisk in Figure 1.7 explains that sharp composition gradients - such as those seen at the purple/orange and orange/grey interfaces - create zone boundaries. These boundaries can be thought of as ‘walls’ within the WD. If pulsation modes resonate with one or more zones, they become ‘trapped’. This occurs when the local wavelength for a given mode nearly matches the width of the local zone.

1.5 Motivating Problems to Explore with WD Seismology

1.5.1 Inclusion of ^{22}Ne

As mentioned in Section 1.2.4, the amount of ^{22}Ne a WD ends up with sets the minimum birth metallicity the star was given. Often, modelers do not include trace elements such as ^{22}Ne when fitting to observed WD pulsations. This trace element is directly proportional to the star’s birth metallicity. Chapter 2 answers whether or not including ^{22}Ne in WD models significantly impacts WD pulsations.

1.5.2 The $^{12}\text{C}(\alpha, \gamma)^{16}\text{O}$ Reaction Rate

The formation of the elements in the Universe come from nucleosynthesis, the creation of new atomic nuclei from nuclear fusion and fission reactions (Bethe, 1939; Burbidge *et al.*, 1957b; Descouvemont, 2020). Most of the Universe’s composition is from the primordial hydrogen and helium from the Big Bang. Essentially all other “heavy” elements were made in stellar interiors or in the explosion processes of high mass stars (Descouvemont, 2020).

Stellar modeling relies heavily on nuclear inputs, namely, the nuclear reactions to account for, and their corresponding reaction rates. Determining reaction rates can be challenging; it is difficult to replicate stellar conditions on Earth for experimentation, thus, nuclear reaction rates often depend on theoretical models or extrapolation (Fields, 2021).

Thousands of nuclear reactions take place in a star’s life. But only a few markedly impact stellar evolution (deBoer *et al.*, 2017). As described in Section 1.2.4, the 3- α and $^{12}\text{C}(\alpha, \gamma)^{16}\text{O}$ reactions occur during CHeB, and create carbon and oxygen in the stellar interior - both of which are essential elements for biological life. Not only do these reactions compete during CHeB to construct the CO for WDs, but they are also the reactions ultimately responsible for determining the C/O ratio of the Universe. Nobel prize winner Willy Fowler said “*The human body is 65% oxygen... and 18% carbon... Oxygen and carbon are the most abundant elements heavier than hydrogen and helium in the Sun and similar main-sequence stars. It is little wonder that the determination of the ratio of $^{12}\text{C}/^{16}\text{O}$ produced during helium burning is a problem of paramount importance in nuclear astrophysics.*”

The 3- α reaction rate is known within $\sim 10\%$. The $^{12}\text{C}(\alpha, \gamma)^{16}\text{O}$ reaction rate has improved over the years, but the current rate is known within $\sim 50\%$. The

desired level is to be compatible with the $3\text{-}\alpha$ rate uncertainty, near the $\sim 10\%$ level. deBoer *et al.* (2017) describes the complexity in determining the rate of $^{12}\text{C}(\alpha, \gamma)^{16}\text{O}$ both experimentally and theoretically. There are numerous efforts seeking to further constrain the uncertainty, and chapters 3 and 4 in this Thesis discuss the potential to use WD seismology to contribute to this effort.

1.5.3 Overshooting

Convective mixing is another uncertainty in computational stellar modeling (Herwig, 2000; Salaris and Cassisi, 2017; Jermyn *et al.*, 2022; Anders *et al.*, 2022; Blouin *et al.*, 2023). Modeling with the classic mixing length theory (MLT), rising parcels supposedly stop at the convective-radiative interface, and do not penetrate into the layer above. But realistically, some fluid elements might “overshoot” into the above layer (Hansen and Kawaler, 1994a). Likewise, at the base of convective regions, sinking parcels may surpass into the layer below. One way to account for this is to include overshooting in computational modeling.

Including convective overshooting in modeling can mix the composition at convective-radiative interfaces, and transport heat. Further, additional He fuel added to the convective core can impact the $3\text{-}\alpha$ and $^{12}\text{C}(\alpha, \gamma)^{16}\text{O}$ reactions, enhancing energy production near the ingestion, and lead to an overall increase of the ^{16}O mass fraction in the core (De Gerónimo *et al.*, 2017). Chapter 4 in this Thesis looks at some impacts of overshooting in greater detail, specifically on the effects that overshooting has on $^{12}\text{C}(\alpha, \gamma)^{16}\text{O}$ reaction rate signature WD pulsation modes.

1.6 Computational Tools and Methods

This Thesis relied primarily on the open-source stellar evolution toolkit Modules for Experimentation in Stellar Astrophysics (**MESA**) (Paxton *et al.*, 2011, 2013,

2015, 2018, 2019). Some of our WD models used the ab-initio capability in `MESA`, `wd_builder` (Schwab *et al.*, 2020). We also used the `GYRE` stellar oscillation code to compute WD pulsations (Townsend and Teitler, 2013; Townsend *et al.*, 2018).

1.6.1 Modules for Experiments in Stellar Astrophysics - `MESA`

In broad scope, `MESA` is a 1D stellar evolution code that can model and evolve very low mass to massive stars through advanced evolutionary phases. It began by improving on the EZ stellar evolution code (Eggleton, 1972; Paxton, 2004). `MESA` solves the fully coupled structure and composition equations simultaneously (Paxton *et al.*, 2011) to model spherically symmetric stellar models. The code is capable of evolving very low mass stars, brown dwarfs, and gas giant planets to old ages, sunlike stars from the pre-MS to a cool WD, intermediate-mass stars through CHeB and thermal pulses, and massive stars from the pre-MS to the onset of core collapse (MESA Paxton *et al.*, 2011, 2013, 2015, 2018, 2019; Jermyn *et al.*, 2023)

The `MESA` EOS is a blend of the OPAL (Rogers and Nayfonov, 2002a), SCVH (Saumon *et al.*, 1995), FreeEOS (Irwin, 2004), HELM (Timmes and Swesty, 2000), PC (Potekhin and Chabrier, 2010a), and Skye (Jermyn *et al.*, 2022) EOSes.

Radiative opacities are primarily from OPAL (Iglesias and Rogers, 1996, 1993), with low-temperature data from Ferguson *et al.* (2005a) and the high-temperature, Compton-scattering dominated regime by Poutanen (2017). Electron conduction opacities are from Cassisi *et al.* (2007) and Blouin *et al.* (2020).

Nuclear reaction rates are from JINA REACLIB (Cyburt *et al.*, 2010), NACRE (Angulo *et al.*, 1999) and additional tabulated weak reaction rates Fuller *et al.* (1985); Oda *et al.* (1994); Langanke and Martínez-Pinedo (2000). Screening is included via the prescription of Chugunov *et al.* (2007). Thermal neutrino loss rates are from Itoh *et al.* (1996).

The models that **MESA** builds and evolves are divided into cells, and the structure equations and composition equations are solved for all cells at the same time, for a given time-step. The equations are stated in the **MESA** I instrument paper, but I will show how the density, pressure, temperature, energy, and isotope species is determined from the conservation of mass, momentum and energy equations.

The density of a cell k is found from the re-written form of the finite volume mass conservation equation

$$\ln r_k = \frac{1}{3} \ln[r_{k+1}^3 + \frac{3}{4\pi} \frac{d(r_k)}{\rho_k}]$$

Here, r_{k+1} is the radius of the inner cell boundary, r_k is the radius of the outer cell boundary, ρ_k is the density of cell k , dm_k is the mass contained in cell k .

The pressure P_k is found from momentum conservation at the interior cell boundary

$$P_{k-1} - P_k = \bar{dm}_k \left[-\frac{Gm_k}{4\pi r_k^4} - \frac{a_k}{4\pi r_k^2} \right]$$

where G is the gravitational constant, $\bar{dm}_k = 0.5(dm_{k-1} - dm_k)$, and a_k is the Lagrangian acceleration at the k boundary¹². The first term in the brackets comes from hydrostatic equilibrium, and the second is the hydrodynamic component.

The temperature T_k for a cell is found by

$$T_{k-1} - T_k = \bar{dm}_k [\nabla_{T,k} \left(\frac{dP}{dm} \right)_{hydrostatic} \frac{\bar{T}_k}{\bar{P}_k}]$$

where $\nabla_{T,k} = d\ln T / d\ln P$ at boundary k , \bar{T}_k is the temperature interpolated by mass at k , \bar{P}_k is the pressure interpolated by mass at k .

The finite volume form of energy conservation for a given cell is

$$L_k - L_{k+1} = dm_k (\epsilon_{nuc} - \epsilon_{\nu, thermal} + \epsilon_{grav})$$

¹² a_k is evaluated by the change in velocity over the evolution time step. This is zero if hydrodynamics is turned off

where ϵ_{nuc} is the specific net nuclear reaction energy rate, $\epsilon_{\nu,thermal}$ is the specific thermal neutrino-loss rate, and ϵ_{grav} is the specific rate of change of gravitational energy from contraction or expansion.

Finally, the mass species for isotope i moving across face k is

$$F_{i,k} = (X_{i,k} - X_{i,k-1} \frac{\sigma_k}{dm_k})$$

where $X_{i,k}$ is the mass fraction for isotope i in cell k , and σ_k is the Lagrangian diffusion coefficient from the mixing prescription.

The above equations are solved fully coupled and simultaneously with a first-order backward differencing time integration.

MESA solves for the isotope species of each cell during a given time-step by tracking the rate of change from nuclear reactions (burning) plus the change from mixing. The nuclear reactions come from built in libraries in the **MESA** modules, such as **net** or **jina**. The libraries contain tabulated reaction rates as functions of temperature. These tables are interpolated on to give a rate per isotope per cell, at the cell's temperature. When initializing an evolutionary run, the user specifies a nuclear reaction network, which tells **MESA** which isotopes to keep track of and their associated nuclear reactions. Users may also specify a nuclear reaction rate library. For instance, in chapters 3 and 4, I used the updated $^{12}\text{C}(\alpha, \gamma)^{16}\text{O}$ reaction rate tables comprised by deBoer *et al.* (2017).

The full computational details are explained in the **MESA** I - **MESA** V instrument papers (Paxton *et al.*, 2011, 2013, 2015, 2018, 2019) and the **MESA** documentation.

In this Thesis, **MESA** version 15140 was used for all stellar evolutionary models.

1.6.2 `wd_builder` for *Ab Initio* Modeling

Some models in this Thesis used the WD ab-inito capability in `MESA`, the `wd_builder` module. This module constructs a WD model at the start of the WD cooling track from a user-provided template composition file, initial mass, and approximate central temperature. `wd_builder` then converges via the Newton-Raphson method to construct the WD model, and further evolves the model through the WD cooling track. (Schwab *et al.* (2020))

1.6.3 `GYRE`

This Thesis used the `GYRE` stellar oscillation code to compute and track the WD pulsation history for our models (Townsend and Teitler (2013), Townsend *et al.* (2018)). `GYRE` solves the dimensionless separated oscillation equations from linear perturbation theory, as described in Dziembowski (1971).

1.7 Learning Analytics in the Online Habworlds Course

1.8 Outline

Much of the information we want to know from the stars is hidden within their interiors. As asteroseismology probes stellar interiors, this Thesis largely explores various stellar evolution and modeling questions with WD seismology. Chapter 2 explores the impact that ^{22}Ne has on WD pulsations, chapter 3 looks at how certain trapped modes in WDs may serve as probes for the $^{12}\text{C}(\alpha, \gamma)^{16}\text{O}$ reaction rate, chapter 4 investigates the impact that overshooting has on $^{12}\text{C}(\alpha, \gamma)^{16}\text{O}$ signature modes, chapter 5 discusses some educational research work done during my P.h.D, and chapter 6 summarizes the take-aways of this Thesis.

Chapter 2

THE IMPACT OF ^{22}Ne ON WD PULSATIONS

Below is the published work of Morgan T. Chidester et al 2021 ApJ 910 24.

2.1 Abstract

We explore changes in the adiabatic low-order g-mode pulsation periods of 0.526, 0.560, and $0.729 M_{\odot}$ carbon-oxygen white dwarf models with helium-dominated envelopes due to the presence, absence, and enhancement of ^{22}Ne in the interior. The observed g-mode pulsation periods of such white dwarfs are typically given to 6–7 significant figures of precision. Usually white dwarf models without ^{22}Ne are fit to the observed periods and other properties. The root-mean-square residuals to the $\simeq 150$ –400 s low-order g-mode periods are typically in the range of $\sigma_{\text{rms}} \lesssim 0.3$ s, for a fit precision of $\sigma_{\text{rms}}/P \lesssim 0.3\%$. We find average relative period shifts of $\Delta P/P \simeq \pm 0.5\%$ for the low-order dipole and quadrupole g-mode pulsations within the observed effective temperature window, with the range of $\Delta P/P$ depending on the specific g-mode, abundance of ^{22}Ne , effective temperature, and mass of the white dwarf model. This finding suggests a systematic offset may be present in the fitting process of specific white dwarfs when ^{22}Ne is absent. As part of the fitting processes involves adjusting the composition profiles of a white dwarf model, our study on the impact of ^{22}Ne can provide new inferences on the derived interior mass fraction profiles. We encourage routinely including ^{22}Ne mass fraction profiles, informed by stellar evolution models, to future generations of white dwarf model fitting processes.

2.2 Introduction

Photons emitted from stellar surfaces and neutrinos released from stellar interiors may not directly reveal all that we want to know about the internal constitution of the stars. For example, a direct view of the chemical stratification from the core to the surface is hidden. These interior abundance profiles matter: they impact a star’s opacity, thermodynamics, nuclear energy generation, and pulsation properties. The stellar models, in turn, are used to interpret the integrated light of stellar clusters and galaxies (e.g., Alsing *et al.*, 2020), decipher the origin of the elements (e.g., Arcones *et al.*, 2017; Placco *et al.*, 2020), predict the frequency of merging neutron stars and black holes (Giacobbo and Mapelli, 2018; Farmer *et al.*, 2020; Marchant and Moriya, 2020; Abbott *et al.*, 2020), and decipher the population(s) of exploding white dwarfs that underlay Type Ia supernova cosmology (e.g., Miles *et al.*, 2016; Rose *et al.*, 2020).

Neutrino astronomy, in concert with stellar models, can probe the isotopic composition profiles in energy producing regions of the Sun (Borexino Collaboration *et al.*, 2018, 2020) and nearby ($d \lesssim 1$ kpc) presupernova massive stars up to tens of hours before core-collapse (e.g., Patton *et al.*, 2017; Simpson *et al.*, 2019; Mukhopadhyay *et al.*, 2020). Stellar seismology, also in concert with stellar models, can probe the elemental composition profiles in pulsating stars from the upper main-sequence (e.g., Simón-Díaz *et al.*, 2018; Pedersen *et al.*, 2019; Balona and Ozuyar, 2020) through the red-giant branch (e.g., Hekker and Christensen-Dalsgaard, 2017; Hon *et al.*, 2018) to white dwarfs (WDs, e.g., Hermes *et al.*, 2017; Giammiceli *et al.*, 2018; Córscico *et al.*, 2019; Bell *et al.*, 2019; Bischoff-Kim *et al.*, 2019; Althaus *et al.*, 2020).

Most of a main-sequence star’s initial metallicity Z comes from the carbon-nitrogen-oxygen (CNO) and ^{56}Fe nuclei inherited from its ambient interstellar medium. All of the CNO piles up at ^{14}N when H-burning on the main-sequence is

completed because the $^{14}\text{N}(p,\gamma)^{15}\text{O}$ reaction rate is the slowest step in the H-burning CNO cycle. During the ensuing He-burning phase, all of the ^{14}N is converted to ^{22}Ne by the reaction sequence $^{14}\text{N}(\alpha,\gamma)^{18}\text{F}(,e^+\nu_e)^{18}\text{O}(\alpha,\gamma)^{22}\text{Ne}$. The abundance of ^{22}Ne when He-burning is completed is thus proportional to the initial CNO abundance of the progenitor main-sequence star. The weak reaction in this sequence powers the neutrino luminosity during He-burning (e.g., Serenelli and Fukugita, 2005; Farag *et al.*, 2020) and marks the first time in a star’s life that the core becomes neutron rich. For zero-age main sequence (ZAMS) masses between $\simeq 0.5 \text{ M}_\odot$ (Demarque and Menzel, 1971; Prada Moroni and Straniero, 2009; Gautschy, 2012) and $\simeq 7 \text{ M}_\odot$ (Becker and Iben, 1979, 1980; García-Berro *et al.*, 1997), depending on the treatment of convective boundary mixing (Weidemann, 2000; Denissenkov *et al.*, 2013; Jones *et al.*, 2013; Farmer *et al.*, 2015; Lecoanet *et al.*, 2016; Constantino *et al.*, 2015, 2016, 2017), the $^{14}\text{N}(\alpha,\gamma)^{18}\text{F}(,e^+\nu_e)^{18}\text{O}(\alpha,\gamma)^{22}\text{Ne}$ reaction sequence determines the ^{22}Ne content of a resulting carbon-oxygen white dwarf (CO WD). We follow the convention that ^{22}Ne is the “metallicity” of the CO WD.

Camisassa *et al.* (2016) analyze the impact of ^{22}Ne on the sedimentation and pulsation properties of H-dominated atmosphere WDs (i.e., the DAV class of WD) with masses of 0.528, 0.576, 0.657, and 0.833 M_\odot . These WD models result from $Z=0.02$ non-rotating evolutionary models that start from the ZAMS and are evolved through the core-hydrogen and core-helium burning, thermally pulsing asymptotic giant branch (AGB), and post-AGB phases. At low luminosities, $\log(L/\text{L}_\odot) \lesssim -4.5$, they find that ^{22}Ne sedimentation delays the cooling of WDs by 0.7 to 1.2 Gyr, depending on the WD mass. They also find that ^{22}Ne sedimentation induces differences in the periods that are larger than the present observational uncertainties.

Giambicchele *et al.* (2018) analyze in their supplemental material the effect of ^{22}Ne on the pulsation periods of a 0.570 M_\odot template-based model for the DB WD

KIC 08626021. They considered a model consisting of pure oxygen core surrounded by a pure helium envelope with the same mass and effective temperature equal to those inferred for KIC 08626021. Next, they considered a model that replaces the pure oxygen core with an oxygen-dominated core plus a trace amount of ^{22}Ne . They find that the model with ^{22}Ne has, on average, shorter pulsation periods.

This article is novel in three ways. One, we explore the impact of ^{22}Ne on the adiabatic low-order g-mode pulsation periods of CO WD models with a He-dominated atmosphere (i.e., the DBV class of WD) as the models cool through the range of observed DBV effective temperatures. Two, we derive an approximation formula for the Brunt-Väisälä frequency in WDs that allows new physical insights into why the low-order g-mode pulsation periods change due to the presence, and absence, of ^{22}Ne . Three, we analyze how the ^{22}Ne induced changes in the pulsation periods depend on the mass and temporal resolutions of the WD model. Our explorations can help inform inferences about the interior mass fraction profiles derived from fitting the observed periods of specific DBV WDs (e.g., Metcalfe *et al.*, 2002; Fontaine and Brassard, 2002; Metcalfe, 2003; Metcalfe *et al.*, 2003; Hermes *et al.*, 2017; Giammichele *et al.*, 2017a, 2018; Charpinet *et al.*, 2019; De Gerónimo *et al.*, 2019; Bischoff-Kim *et al.*, 2019).

In Section 2.3 we summarize the input physics, and discuss in detail the chemical stratification, cooling properties, and g-mode pulsation periods of one DBV WD model. In Section 2.4 we present our results on changes to the low-order g-mode pulsation periods due to the presence, or absence, of ^{22}Ne from this model. In Section 2.5 we study changes in the g-mode pulsation periods due to ^{22}Ne from a less massive and a more massive WD model. In Section 2.6 we summarize and discuss our results. In Appendix B we study the robustness of our results with respect to

mass and temporal resolution, and in Appendix B we discuss in more depth some of the input physics.

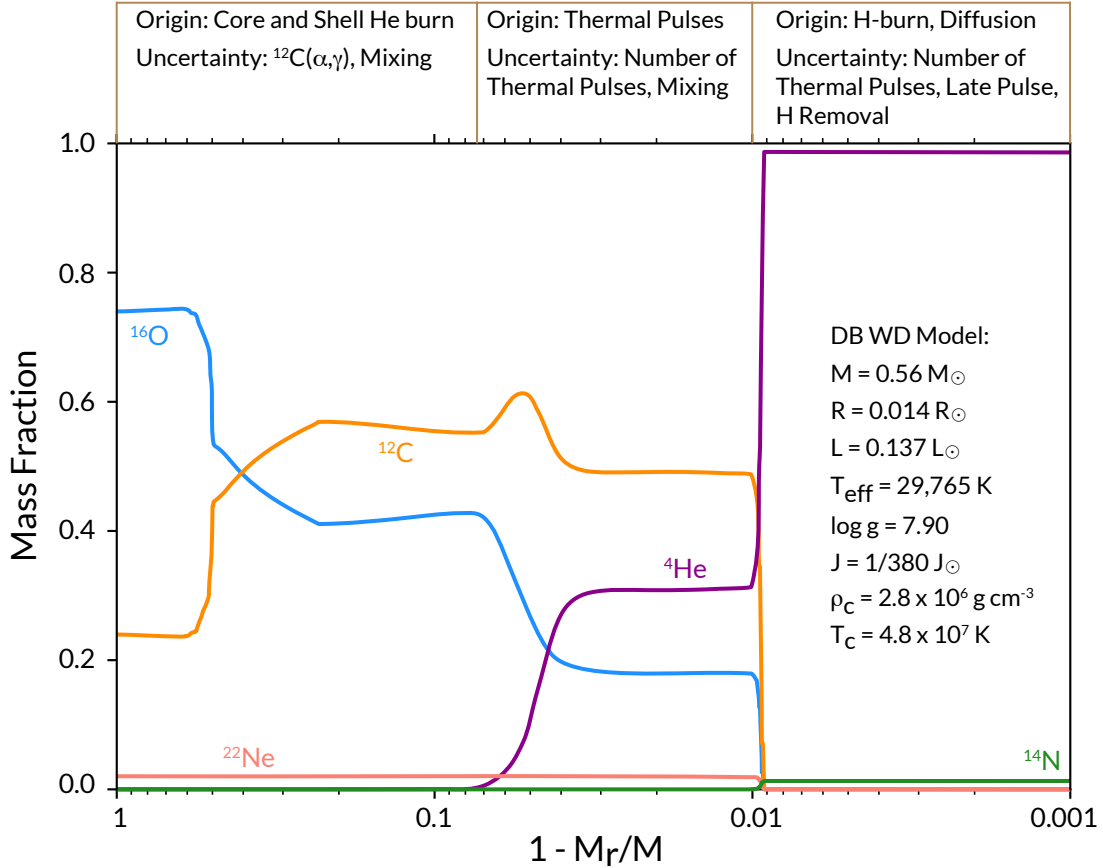


Figure 2.1: Mass fraction profiles of the 0.56 M_\odot DB WD resulting from the evolution of the 2.1 M_\odot , $Z=0.02$, ZAMS model.

2.3 A Baseline WD Model

2.3.1 Input Physics

We use **MESA** version r12115 (Paxton *et al.*, 2011, 2013, 2015, 2018, 2019) to evolve a 2.1 M_\odot , $Z=0.02$ metallicity model from the ZAMS through core H-burning and core He-burning. After winds during the thermal pulses on the AGB have reduced the H-rich envelope mass to 0.01 M_\odot , the remaining hydrogen is stripped from the surface to form a young, 0.56 M_\odot DB WD. This model is tuned to match the observed

and inferred properties of KIC 08626021 (Bischoff-Kim *et al.*, 2014a; Giammiceli *et al.*, 2018; Timmes *et al.*, 2018a; Charpinet *et al.*, 2019; De Gerónimo *et al.*, 2019). Additional details of the input physics are given in Appendix B, and the MESA r12115 files to reproduce our work are available at

<https://doi.org/10.5281/zenodo.4338180>

2.3.2 Mass Fraction Profiles

Figure 2.1 shows the mass fraction $X(^A Z)$ profiles of the resulting $0.56 M_\odot$ DB WD model, where A is the number of nucleons and Z is the number of protons. Brown boxes divide the mass fraction profiles into three regions according to their origins and uncertainties. The $X(^{12}\text{C})$ and $X(^{16}\text{O})$ profiles in the innermost $\simeq 90\%$ by mass region are determined during core and shell He-burning. The main uncertainties in this region are the $^{12}\text{C}(\alpha, \gamma)^{16}\text{O}$ reaction rate (e.g., deBoer *et al.*, 2017), and the treatment of convective mixing boundaries during core H-and He-burning (e.g., Constantino *et al.*, 2015, 2016, 2017).

The CO and $X(^4\text{He})$ profiles between $\simeq 1\%$ and $\simeq 10\%$ of the exterior WD mass originate from shell He-burning during the thermal pulse phase of evolution on the AGB. Most of the total He mass is held in this region. The primary uncertainties in this region are the number of thermal pulses and convective boundary layer mixing. The number of thermal pulses a model undergoes is sensitive to the mass resolution, time resolution, mass loss rate, and the treatment of convective boundaries (Iben and Renzini, 1983; Herwig, 2005; Karakas and Lattanzio, 2014). The sharp change in all the mass fractions at $\simeq 1\%$ of the exterior WD mass marks the extent reached by the convective boundary during the last thermal pulse.

CO profiles in this region may also be subject to other mixing processes. For example, the magnitude of the $X(^{12}\text{C})$ “bump” is subject to the strength and duration

of the thermohaline instability, which occurs when material is stable to convection according to the Ledoux criterion, but has an inverted molecular weight gradient (Baines and Gill, 1969; Brown *et al.*, 2013; Garaud, 2018; Bauer and Bildsten, 2018).

The $X(^4\text{He})$ profile of the outer $\simeq 0.1\%$ to 1% of the WD mass is determined by shell H-burning. All of the initial CNO mass fractions have been converted to ^{14}N . The main uncertainties in this region are the number of thermal pulses during the AGB phase of evolution, late or very late thermal pulses (Bloecker, 1995b,a; Blöcker, 2001), and mechanisms to remove the residual high entropy, H-rich layer to produce a DB WD from single and binary evolution (e.g., D'Antona and Mazzitelli, 1990; Althaus and Benvenuto, 1997; Parsons *et al.*, 2016).

The $X(^{22}\text{Ne})$ profile is essentially flat and spans the inner $\simeq 99\%$ by mass. As discussed in Section 2.2, $X(^{22}\text{Ne})$ is created from ^{14}N during He-burning.

2.3.3 Constructing *Ab Initio* White Dwarf Models

Starting from a set of pre-main sequence (pre-MS) initial conditions, accurate predictions for the properties of the resulting WD model, especially the mass fraction profiles, do not exist due to the nonlinear system of equations being approximated. In addition, evolving a stellar model from the pre-MS to a WD can be resource intensive. It can thus be useful for systematic studies to build ab initio WD models (e.g., WDEC, Bischoff-Kim and Montgomery, 2018). By ab initio we mean calculations that begin with a WD model, as opposed to a WD model that is the result of a stellar evolution calculation from the pre-MS. A potential disadvantage (or advantage) of ab initio WD models is the imposed initial mass fraction profiles may not be attainable by a stellar model evolved from the pre-MS. Throughout the remainder of this article we

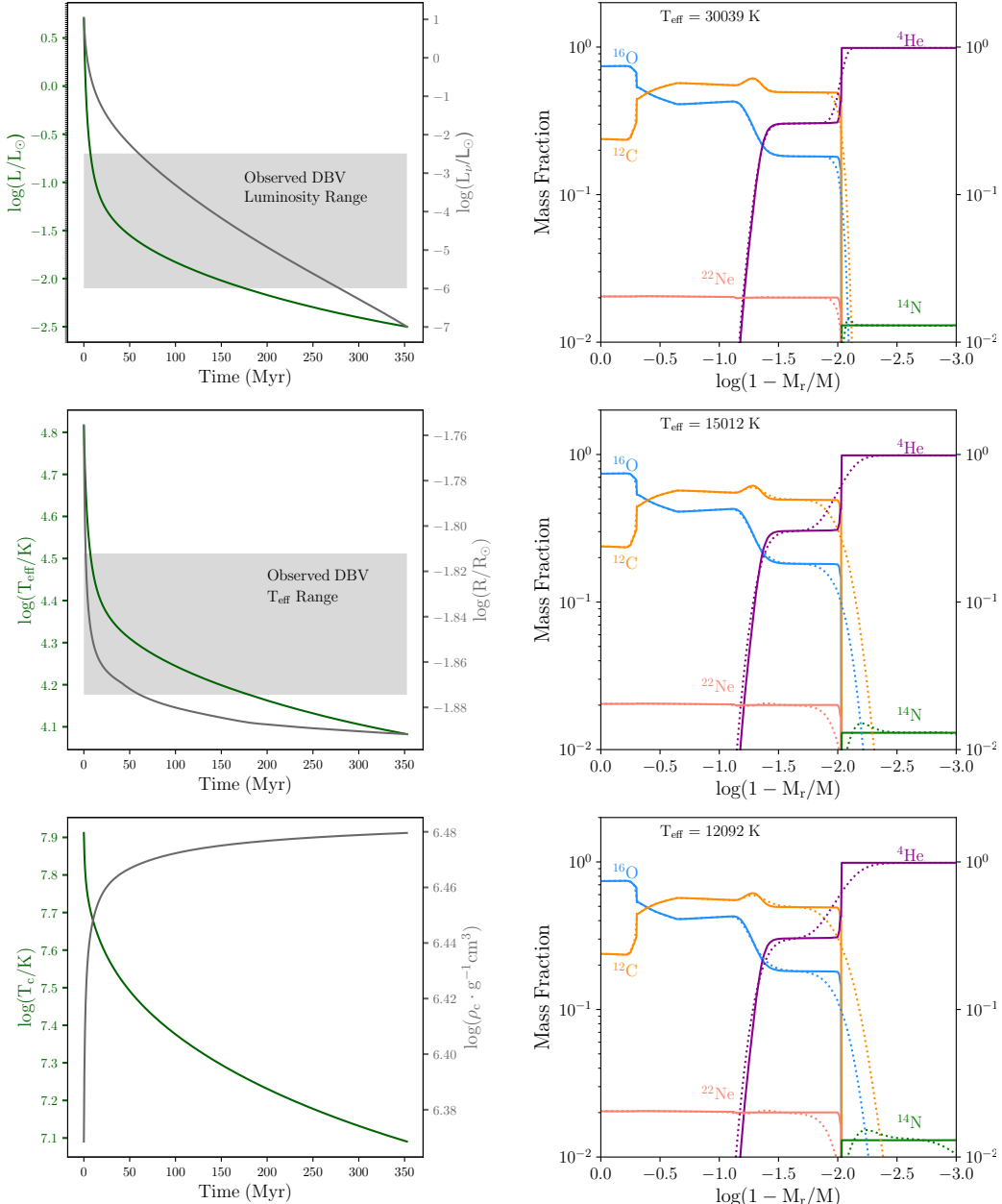


Figure 2.2: Evolution of baseline model’s photon luminosity L and neutrino luminosity L_ν (left top), effective temperature T_{eff} and radius R (left middle), central temperature T_c and central density ρ_c (left bottom). Time begins a few thermal timescales after the ab initio WD is released. Gray bands show the luminosity and T_{eff} range of currently observed DBV WD (Montreal White Dwarf Database, Dufour *et al.*, 2017). Mass fraction profiles are shown at $T_{\text{eff}} = 30,039 \text{ K}$ (right top), $15,012 \text{ K}$ (right middle), and $12,092 \text{ K}$ (right bottom) and at the end of the evolution. Initial mass fraction profiles are shown as solid curves and the diffusing mass fraction profiles are shown as dotted curves.

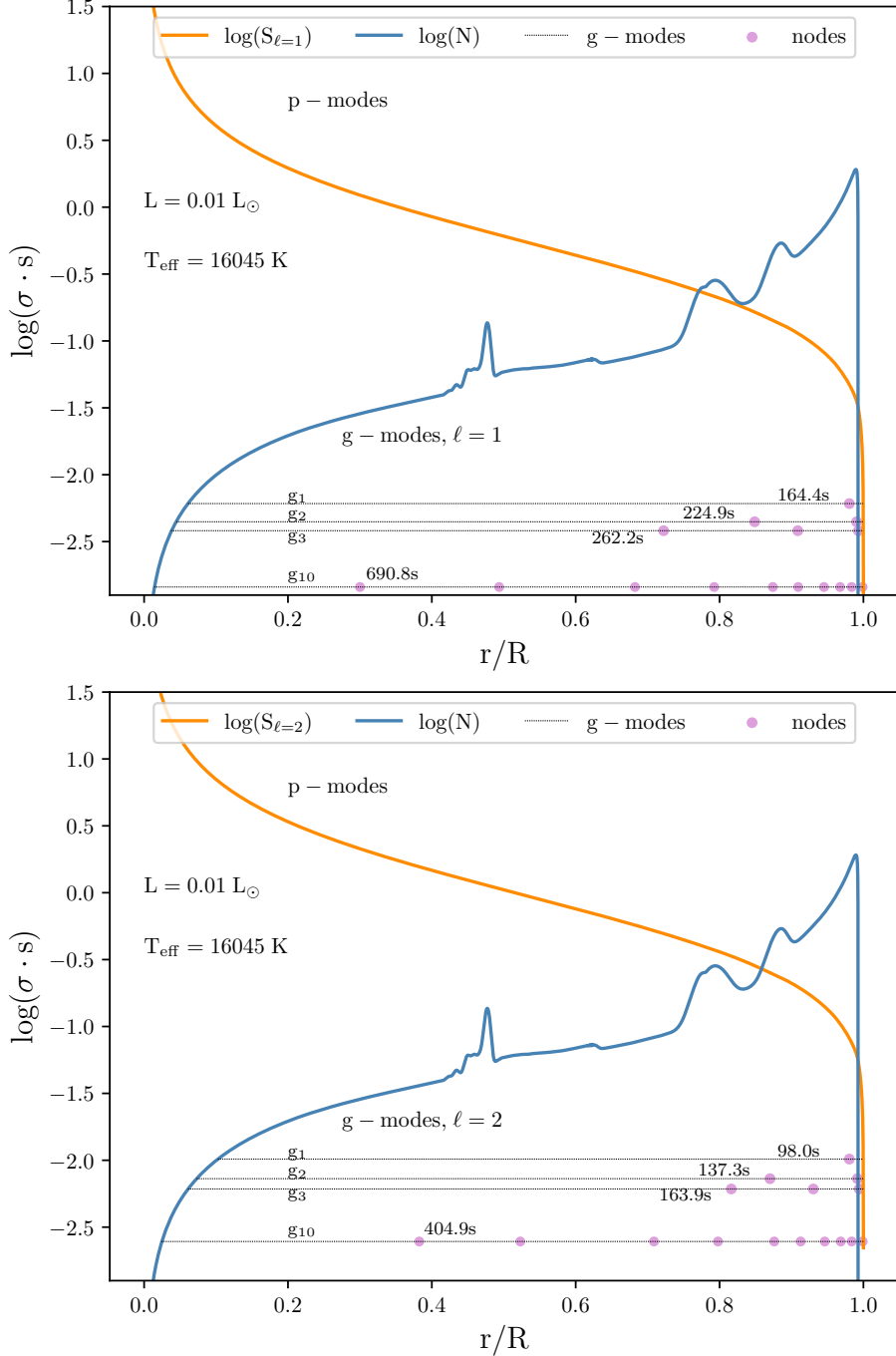


Figure 2.3: Propagation diagram for the dipole $\ell=1$ (top) and quadrupole $\ell=2$ (bottom) g-modes at $L=0.01 L_{\odot}$ for the baseline WD model. The Lamb frequency (S_{ℓ} , orange), Brunt-Väisälä frequency (N , blue), radial order $n=1,2,3,10$ eigenfrequencies (dotted black lines), nodes in the radial eigenfunction (filled circles), and g-mode period of each radial order are labeled.

use a new capability, `wd_builder`, to construct ab initio WD models in `MESA` of a given mass and chemical stratification.

The initial structure of an ab initio WD model is approximated as an isothermal core and a radiative envelope in hydrostatic equilibrium. Here we specify an initial WD mass of $0.56 M_{\odot}$, the same WD mass as produced by the stellar evolution calculation. The imposed $X(^4\text{He})$, $X(^{12}\text{C})$, $X(^{14}\text{N})$, $X(^{16}\text{O})$, and $X(^{22}\text{Ne})$ profiles are taken from the stellar evolution derived mass fraction profiles of Figure 2.1 and normalized to sum to unity in each cell. Henceforth we refer to this ab initio WD model as the “baseline model”.

For ab initio WD models we use He-dominated, $\log(\text{H}/\text{He}) = -5.0$, model atmosphere tables spanning $5,000 \text{ K} \leq T_{\text{eff}} \leq 40,000 \text{ K}$ that were provided by Odette Toloza (2019, private communication) using the Koester WD atmosphere software instrument (Koester, 2010). These tabulated atmospheres for DB WDs are publicly available as a standard atmosphere option as of `MESA` r12115. In addition, we use five element classes for the diffusion classes – ^4He , ^{12}C , ^{14}N ^{16}O , and ^{22}Ne . Otherwise, all of the physics implementations and modeling choices are as described in Section 2.3.1.

The initial baseline model is then evolved with `MESA`. As the model is not in thermal equilibrium, there is an initial transient phase lasting a few thermal timescales that is disregarded. The thermal timescale is $\tau_{\text{th}} \simeq E_{\text{th}}/L_{\text{tot}} \simeq 0.67 \text{ Myr}$, where E_{th} is the thermal energy of the WD and L_{tot} is the photon plus neutrino luminosity. Specifically, we set the zero point to be 1.5 thermal timescales ($\simeq 1 \text{ Myr}$) after the transient reaches its peak luminosity. The evolution terminates when L_{tot} falls below $\log(L/L_{\odot}) = -2.5$.

Figure 2.2 shows the cooling properties of the baseline model. Plasmon neutrino emission dominates the energy loss budget at $T_{\text{eff}} \gtrsim 25,000 \text{ K}$ (e.g., Vila, 1966; Cuttler and Savedoff, 1969; Winget *et al.*, 2004; Bischoff-Kim and Montgomery, 2018).

Photons leaving the WD surface begin to dominate the cooling as the electrons transition to a strongly degenerate plasma (van Horn, 1971). The luminosity becomes proportional to the enclosed mass, $L_r \propto M_r$, in this model only when $T_{\text{eff}} \lesssim 20,000$ K (Timmes *et al.*, 2018a). Energy transport in the interior is dominated by conduction, driven primarily by electron-ion scattering. Energy transport in the outer layers is dominated by radiation or convection associated with the partial ionization of He at $T_{\text{eff}} \simeq 30,000$ K.

Figure 2.2 also shows the diffusion of the initial mass fractions as the baseline WD model cools to $T_{\text{eff}} = 30,000$ K, 15,000 K and 12,138 K (corresponding to the termination at $\log(L/L_{\odot}) = -2.5$). Element diffusion of ^{22}Ne is modest for the baseline $0.56 M_{\odot}$ DB WD model. Depletion of the ^{22}Ne mass fraction at $\log(1 - M_r/M) \simeq -1.9$ has occurred by the time the model has cooled to $T_{\text{eff}} \simeq 30,000$ K. As the model cools further, the surface regions in the tail of the He-dominated layer further deplete and a small ^{22}Ne bump forms and propagates inwards toward the center. The timescale for ^{22}Ne to travel from near the surface to the center of this WD model is $\tau_D \simeq 2\bar{Z}\Gamma^{1/3}\rho_6^{-1/2}$ Gyr $\simeq 30$ Gyr (Isern *et al.*, 1991; Bravo *et al.*, 1992; Bildsten and Hall, 2001; Deloye and Bildsten, 2002; Camisassa *et al.*, 2016), where \bar{Z} is the mean charge of the material, Γ is the electrostatic to thermal energy ratio, and ρ_6 is the baryon mass density in units of 10^6 g cm^{-3} . Thus, the $X(^{22}\text{Ne})$ profile does not significantly change as the $0.56 M_{\odot}$ baseline model evolves to $\log(L/L_{\odot}) = -2.5$ in $\simeq 350$ Myr. More massive WDs show larger amounts of ^{22}Ne sedimentation over the same time period (Camisassa *et al.*, 2016). WD cooling data suggests a significant enhancement due to ^{22}Ne diffusion (Cheng *et al.*, 2019; Bauer *et al.*, 2020), but does not effect the baseline model until it cools to effective temperatures lower than considered here ($T_{\text{eff}} \lesssim 10,000$ K).

2.3.4 Pulsation Periods of the Baseline Model

Having established the structural and composition profiles of a cooling baseline WD model, we now consider the g-mode pulsation periods. Some of the material is classic (e.g., Unno *et al.*, 1989; Fontaine and Brassard, 2008), but we also derive and verify the accuracy of an approximation formula for the Brunt-Väisälä frequency in WDs that allows physical insights into why the low-order g-mode pulsation periods change due to variations in the mass fraction of ^{22}Ne . This material is essential for establishing that the baseline model, before introducing any modifications to the chemical profiles, produces pulsation periods that are commensurate with the observations of DBV WDs.

Figure 2.3 shows the propagation diagram (e.g., Unno *et al.*, 1989) for the baseline WD model after it has cooled to $T_{\text{eff}} = 16,045$ K and dimmed to $L = 0.01 L_{\odot}$, within the DBV WD observation window. Adiabatic pulsation frequencies are calculated using release 5.2 of the GYRE software instrument (Townsend and Teitler, 2013; Townsend *et al.*, 2018). For a fixed radial overtone number, the $\ell = 1$ periods are $\sim \sqrt{3}$ longer than the $\ell = 2$ periods, due to the local dispersion relation for low-frequency g-modes σ_g scaling as

$$\sigma_g^2 \simeq \ell(\ell + 1)N^2/(k_r^2 r^2) , \quad (2.1)$$

where k_r is the radial wave number. The Brunt-Väisälä frequency N is

$$N^2 = \frac{g^2 \rho}{P} \frac{\chi_T}{\chi_\rho} (\nabla_{\text{ad}} - \nabla_T + B) , \quad (2.2)$$

where g is the gravitational acceleration, ρ is the mass density, P is the pressure, T is the temperature, χ_T is the temperature exponent $\partial(\ln P)/\partial(\ln \rho)|_{T,\mu_I}$, χ_ρ is the density exponent $\partial(\ln P)/\partial(\ln T)|_{\rho,\mu_I}$, ∇_{ad} is the adiabatic temperature gradient, ∇_T

is the actual temperature gradient, and B accounts for composition gradients (e.g., Hansen and Kawaler, 1994a; Fontaine and Brassard, 2008). Bumps in the N profile of Figure 2.3 correspond to transitions in the $X(^{16}\text{O})$, $X(^{12}\text{C})$, and $X(^4\text{He})$ profiles. The implementation of Equation 2.2 in **MESA** is described in Section 3 of Paxton *et al.* (2013).

An approximation for N^2 in the interiors of WDs that yields physical insights begins by assuming ∇_{ad} is much larger than ∇_T and B . Then

$$N^2 = \frac{g^2 \rho}{P} \frac{\chi_T}{\chi_\rho} \nabla_{\text{ad}} . \quad (2.3)$$

In the interior of a WD the ions are ideal and dominate the temperature derivatives of an electron degenerate plasma. Substituting the pressure scale height $H = P/(\rho g)$ and equation 3.110 of Hansen and Kawaler (1994a)

$$\chi_T = \frac{\rho}{P} \frac{k_B T}{\mu_I m_p} \quad (2.4)$$

into Equation 2.3 gives

$$N^2 = \frac{1}{H^2 \chi_\rho} \frac{k_B T}{\mu_I m_p} \nabla_{\text{ad}} , \quad (2.5)$$

where k_B is the Boltzmann constant, $\mu_I = 1/(\sum_i X_i/A_i)$ is the ion mean molecular weight, and m_p is the mass of the proton. Equation 3.90 of Hansen and Kawaler (1994a) shows $\nabla_{\text{ad}} = (\Gamma_3 - 1)/\Gamma_1$, where Γ_1 is the first adiabatic index and $\Gamma_3 \rightarrow k_B/(\mu_I m_p c_v)$ is the third adiabatic index, where in the gas phase the ideal specific heat capacity is $c_v = 3k_B/(2\mu_I m_p)$. The sentence beneath equation 3.112 of Hansen and Kawaler (1994a) thus notes that $\Gamma_3 - 1 = 2/3$ for the ions in the gas phase ($\Gamma_3 - 1 = 1/3$ in the liquid phase). Combining these expressions, yields the approximation

$$N^2 = \frac{2}{3\Gamma_1\chi_\rho H^2} \frac{k_B T}{\mu_I m_p} . \quad (2.6)$$

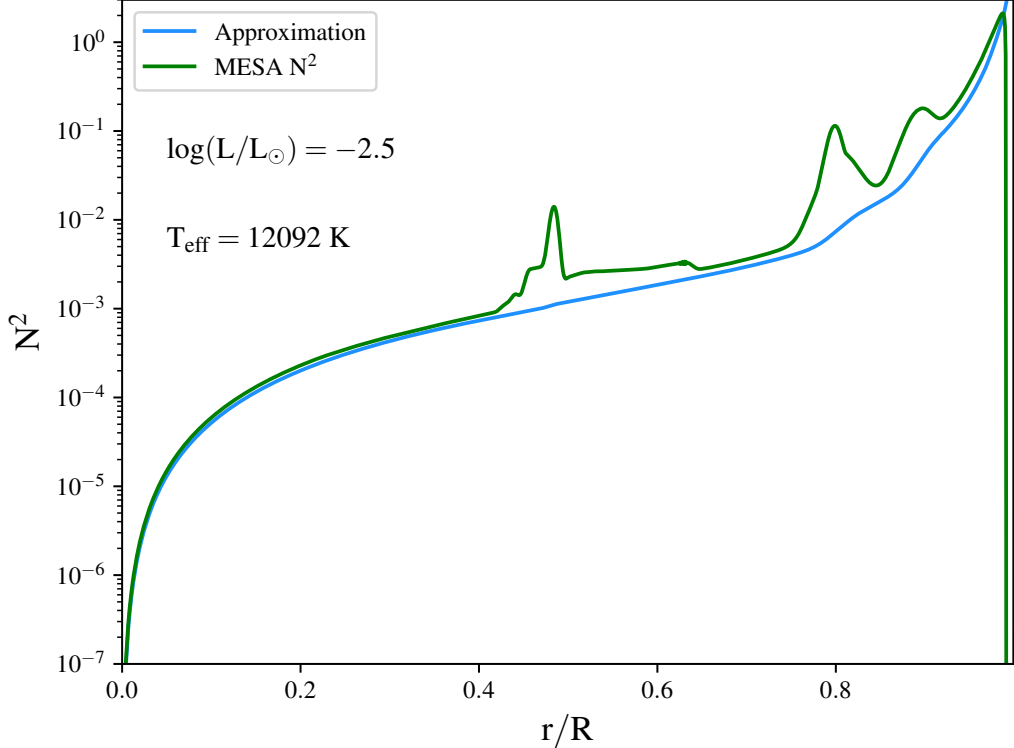


Figure 2.4: Comparison of the approximation for N^2 (blue curve) in Equation (2.6) and the full calculation of N^2 from **MESA** (green curve).

Figure 2.4 compares the approximation in Equation (2.6) with the full N^2 calculation from **MESA**. The difference at $r/R \simeq 0.5$ corresponds to the $X(^{16}\text{O}) \rightarrow X(^{12}\text{C})$ transition, at $r/R \simeq 0.8$ to the ^{12}C bump, and at $r/R \simeq 0.9$ to the transition to a He dominated atmosphere. Except for the outermost layers and regions where the composition gradients are significant, the agreement is sufficient to use Equation (2.6) as a scaling relation for building physical insights. We always use, however, the full N^2 calculation from **MESA** for any quantitative analysis.

It is useful to reference features of the baseline model with respect to mass or radius. Figure 2.5 thus shows the mass-radius relation of the baseline model at $\log(L/L_\odot) = -2.5$ with key transitions labeled.

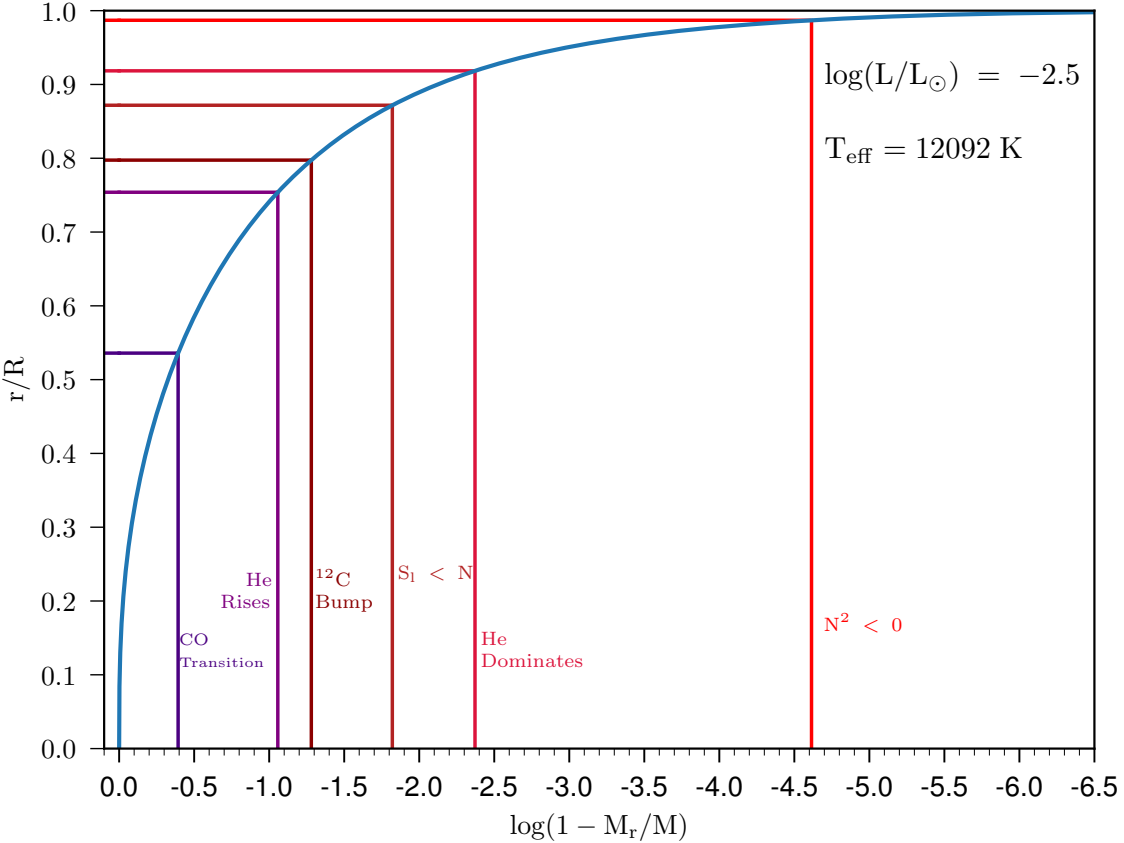


Figure 2.5: Mass-radius relation of the baseline DB WD model at $\log(L/L_{\odot}) = -2.5$ with key features located: the transition from $X(^{16}\text{O})$ to $X(^{12}\text{C})$ dominated, the rise of $X(^4\text{He})$, the $X(^{12}\text{C})$ bump, where $S_{\ell} < N$ occurs, the transition to $X(^4\text{He})$ dominated, and where $N^2 < 0$.

Figure 2.6 shows the low-order g-mode pulsation periods as the baseline WD model cools. The periods increase due to N^2 decreasing as the cooling progresses, per Equation 2.6. Higher radial orders have steeper slopes due to the periods scaling with k_r in Equation 2.1. The increase in number of MESA models at $T_{\text{eff}} \simeq 30,000$ K is due to the partial ionization of He, which leads to envelope convection in relatively hot DBV WDs. The change in slope at $T_{\text{eff}} \simeq 20,000$ K is due to the luminosity becoming proportional to the enclosed mass, $L_r \propto M_r$, as the plasmon neutrino emission becomes insignificant.

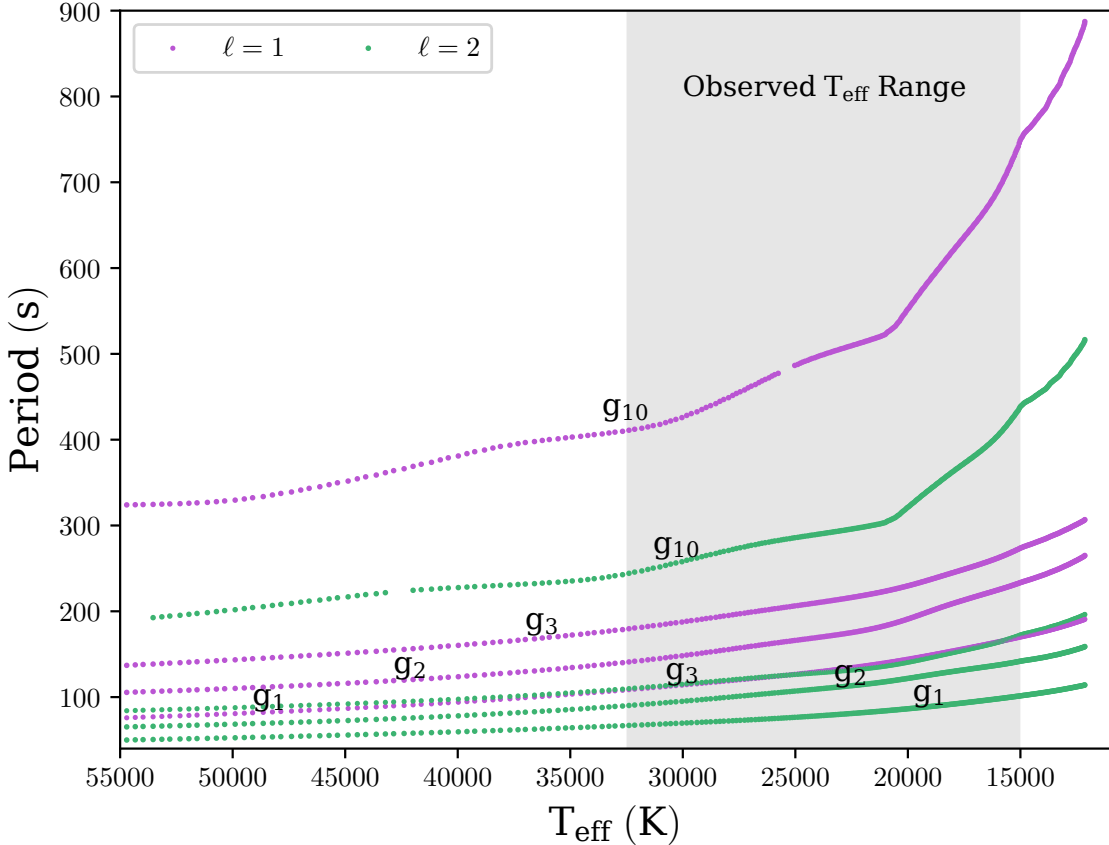


Figure 2.6: Period evolution of the $\ell = 1$ (purple) and $\ell = 2$ (green) g-modes at radial orders $n=1,2,3,10$ as the baseline model cools. Each point represents a timestep in MESA where the g-mode was calculated by GYRE. The gray band shows the T_{eff} range of observed DBV WD.

In Appendix B we show that the low-order g-mode pulsation periods of the baseline model calculated with GYRE are only weakly dependent on the mass and temporal resolution of the MESA calculations.

2.4 The Impact Of ^{22}Ne

Having established the cooling properties and g-mode pulsation periods of a baseline model whose mass fraction profiles are from a stellar evolution model, we now explore changes in the g-mode pulsation periods due to changes in the ^{22}Ne mass

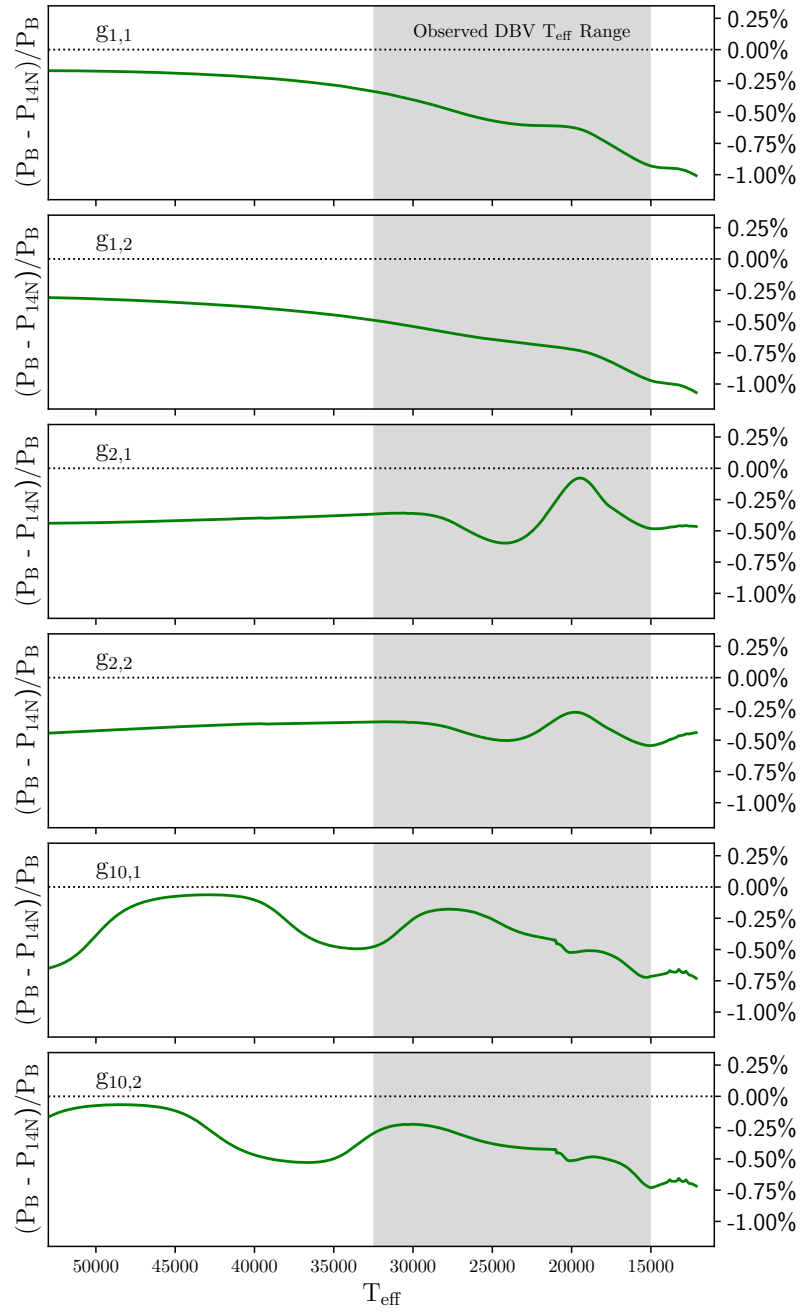


Figure 2.7: Top to Bottom: Relative period differences of the $g_{1,1}$, $g_{1,2}$, $g_{2,1}$, $g_{2,2}$, $g_{10,1}$ and $g_{10,2}$ modes between the baseline model, P_B , and a model where the ^{22}Ne has been replaced with ^{14}N , $P_{14\text{N}}$. We use the notation $g_{n,\ell}$ for a g-mode of order n and degree ℓ . Gray bands show the T_{eff} range of currently observed DBV WDs.

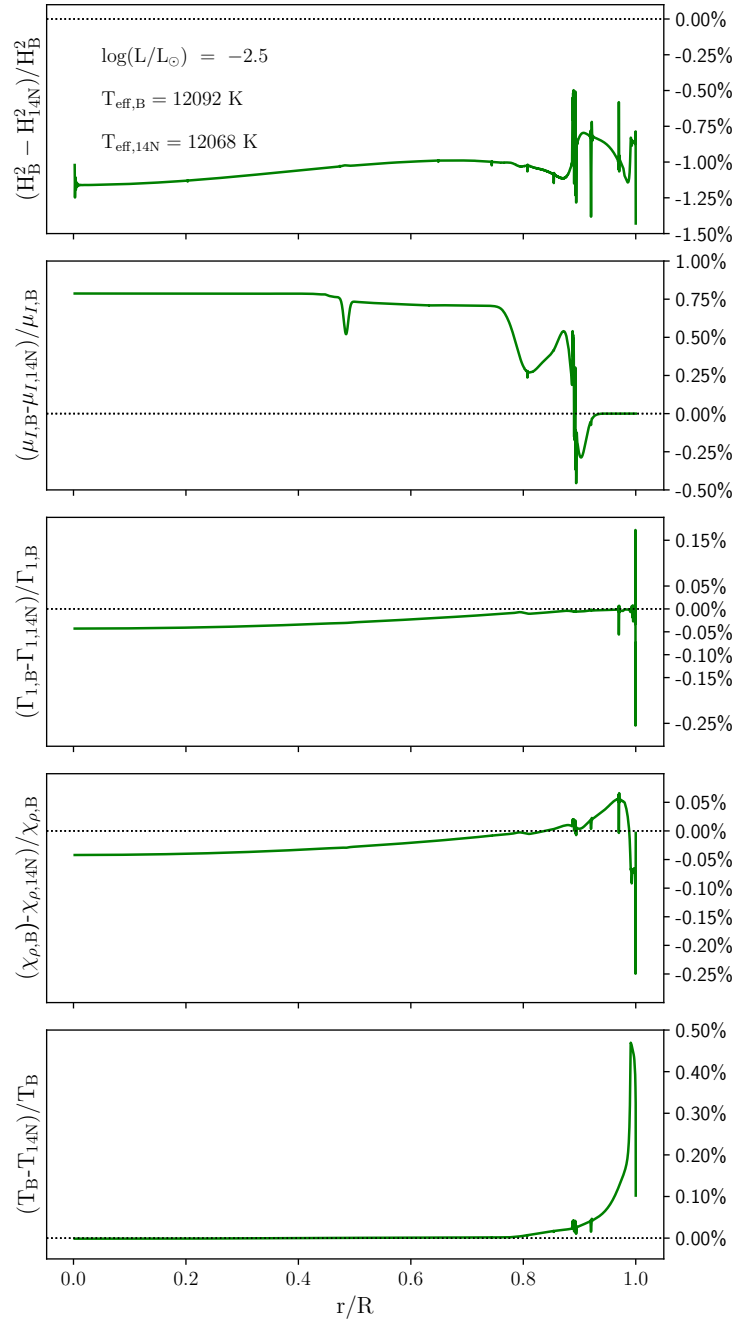


Figure 2.8: Top to Bottom: Relative differences in the H^2 , μ_I , Γ_1 , χ_ρ , and T contributions to N^2 in Equation 2.6. Subscript B represents the baseline model, and subscript ^{14}N represents a model where ^{22}Ne has been replaced with ^{14}N .

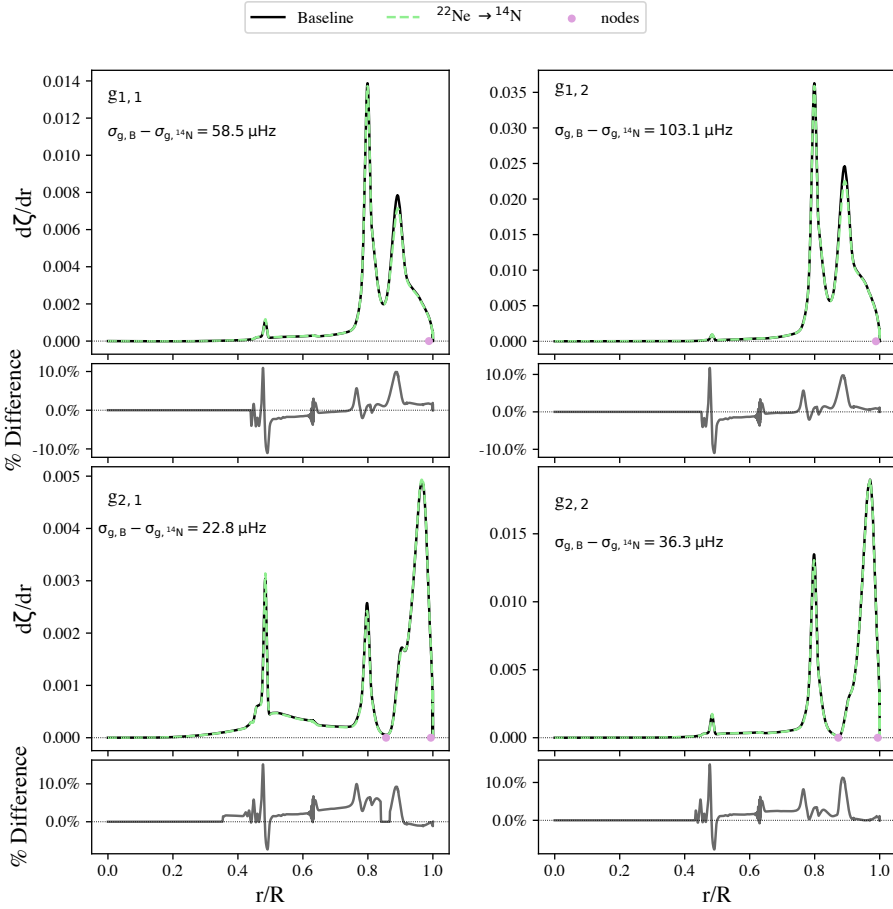


Figure 2.9: Weight functions of the low-order g-modes for baseline model with ^{22}Ne (black curves) and a baseline model where ^{22}Ne has been replaced with ^{14}N (green curves). Subpanels show the relative percent differences between the two curves. The profiles shown are when the two models have cooled to $\log(L/L_{\odot}) = -2.5$. Nodes in the radial eigenfunctions are marked by filled circles.

fraction profile shown in Figure 2.1. We consider three modifications: replacing ^{22}Ne with ^{14}N , a metal-free model, and a super-solar metallicity model.

2.4.1 Putting the ^{22}Ne Into ^{14}N

Replacing $X(^{22}\text{Ne})$ with $X(^{14}\text{N})$ is a model for the reaction sequence $^{14}\text{N}(\alpha, \gamma)^{18}\text{F}(, e^+ \nu_e)^{18}\text{O}(\alpha, \gamma)^{22}\text{Ne}$ either physically not occurring or being ignored. Figure 2.7 shows the relative differences in the low-order g-mode pulsation periods from

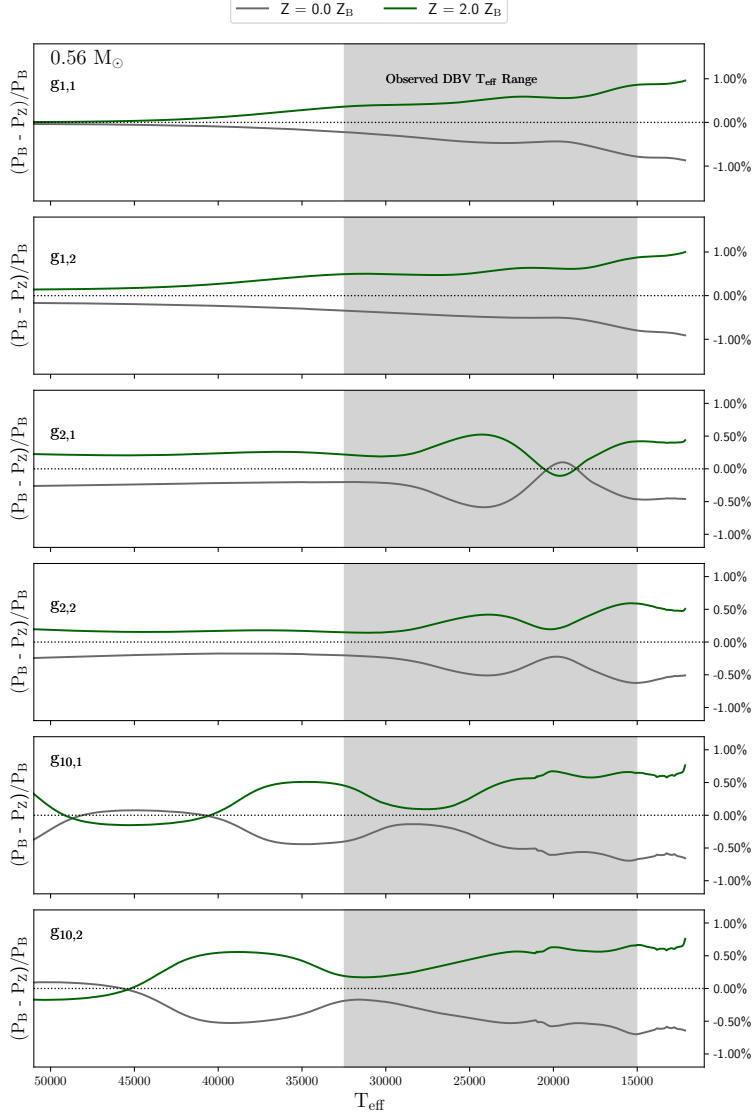


Figure 2.10: Top to Bottom : Relative period differences of the $g_{1,1}$, $g_{1,2}$, $g_{2,1}$, $g_{2,2}$, $g_{10,1}$ and $g_{10,2}$ modes between the baseline model, P_B , a zero-metallicity WD model (gray curves) where the ^{14}N and ^{22}Ne have been put into ^4He and ^{12}C respectively, and a super-solar metallicity model (green curves) where the ^{14}N and ^{22}Ne of the baseline model are doubled.

this composition change. All of the relative differences are negative, implying the pulsation periods in models that exclude ^{22}Ne are longer than the corresponding pulsation periods in models that include ^{22}Ne . The magnitude of the relative period differences span $\simeq 0.25\%-1\%$ over the range of currently observed DBV WDs, with the $g_{1,1}$ and $g_{1,2}$ modes showing the largest differences at cooler T_{eff} . The change in the

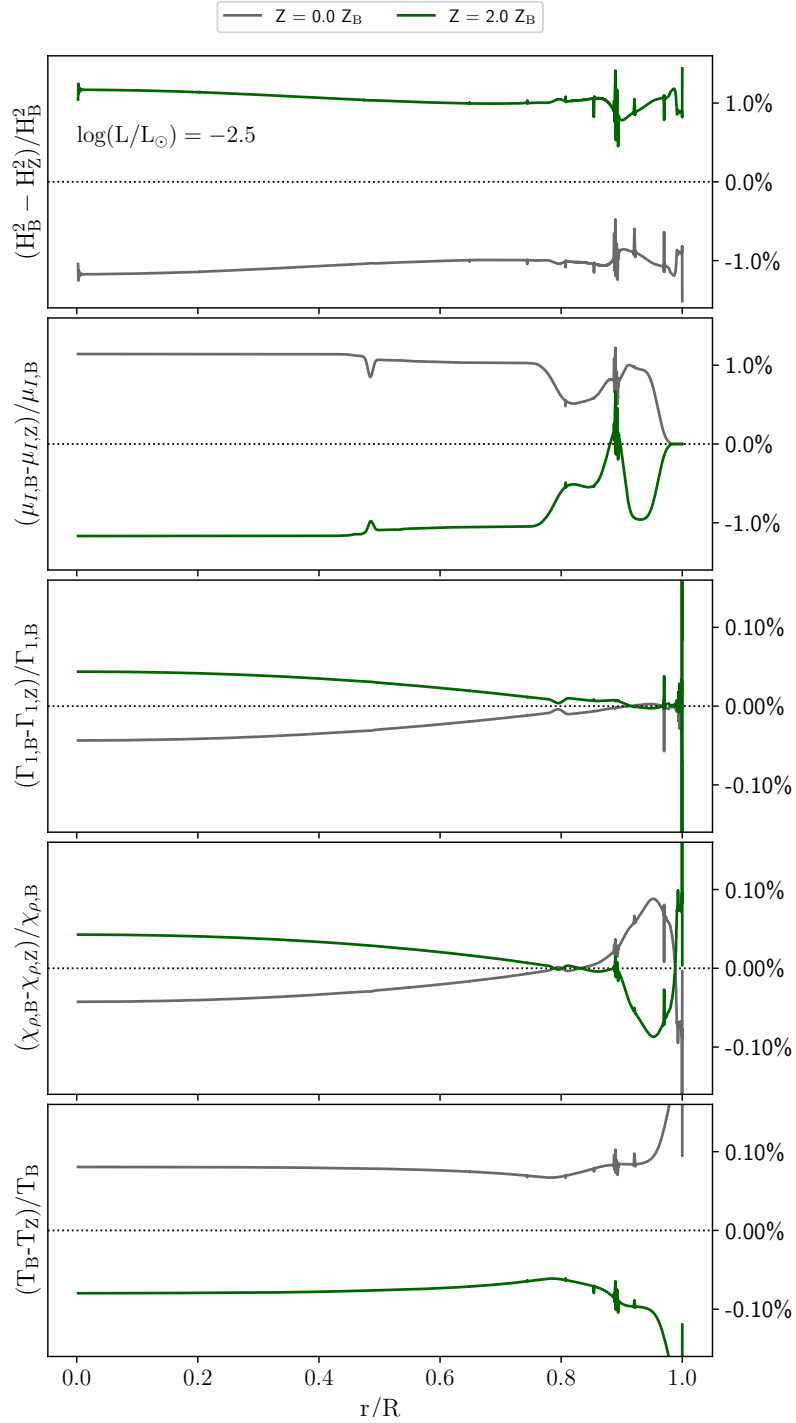


Figure 2.11: Top to Bottom: Relative differences in the H^2 , μ_I , Γ_1 , χ_ρ , and T contributions to N^2 in Equation 2.6. Subscript B represents the baseline model, and subscript Z represents the zero-metallicity models (gray curves) and super-solar metallicity models (green curves).

slopes at $T_{\text{eff}} \simeq 20,000$ K is due to plasmon neutrino emission becoming insignificant, and thus the luminosity becoming proportional to the enclosed mass, $L_r \propto M_r$.

What drives these g-mode period changes? Replacing an isotope which has a larger mass number with an isotope which has a smaller mass number decreases μ_I . This replacement also increases H through the mechanical structure and equation of state of the CO WD. Figure 2.8 shows the relative differences in the H^2 , μ_I , Γ_1 , χ_ρ and T contributions to N^2 in Equation 2.6. These changes collectively determine the magnitude and sign of the period change relative to the baseline model. For this $X(^{22}\text{Ne}) \rightarrow X(^{14}\text{N})$ model, the overall positive changes in μ_I and T are counteracted by the negative changes from H^2 , Γ_1 , and χ_ρ . The magnitude of the relative difference in H^2 drives the net result of a smaller N^2 and thus longer g-mode periods. The nearly uniform negative change in H^2 imply a change in the radius of the WD model. We find $(R_B - R_{14N})/R_B \simeq -0.4\%$, meaning the $X(^{22}\text{Ne}) \rightarrow X(^{14}\text{N})$ model has a larger radius than the model with ^{22}Ne . This is expected given differences in the electron fraction of a WD.

Figure 2.9 compares the weight functions of the baseline model with ^{22}Ne and the model where the ^{22}Ne has been replaced with ^{14}N . Following Kawaler *et al.* (1985), the weight function is

$$\frac{d\zeta}{dr} = \frac{[C(\mathbf{y}, r) + N(\mathbf{y}, r) + G(\mathbf{y}, r)]\rho r^2}{\int_{r=0}^{r=R} T(\mathbf{y}, r)\rho r^2 dr} , \quad (2.7)$$

where $C(\mathbf{y}, r)$ varies with the Lamb frequency, $N(\mathbf{y}, r)$ contains the Brunt-Väisälä frequency, $G(\mathbf{y}, r)$ involves the gravitational eigenfunctions, $T(\mathbf{y}, r)$ is proportional to the kinetic energy density, and $\mathbf{y} = (y_1, y_2, y_3, y_4)$ are the Dziembowski (1971) variables. The frequency of an adiabatic mode is then

$$\nu^2 = \zeta = \int_{r=0}^{r=R} \frac{d\zeta}{dr} \cdot dr . \quad (2.8)$$

The weight function for the two models is dominated by the $N(\mathbf{y}, r)$ term except for the surface layers. Figure 2.9 shows that the net effect of the $^{22}\text{Ne} \rightarrow ^{14}\text{N}$ composition change is a shift in ζ , the area under the weight function curves, towards smaller frequencies of the low-order g-modes. The subpanels in Figure 2.9 illustrate the relative percent differences between the weight function curves. Most of the changes in ζ occur at the CO transition region ($r/R \simeq 0.45$, see Figure 2.5), ^{12}C bump ($r/R \simeq 0.8$), and at the transition to a He-dominated atmosphere ($r/R \simeq 0.9$). The changes in these regions get as large as $\sim 10\%$. We identify the dipole g-mode of radial order $n=2$ as being more sensitive to the location and gradient of μ_I at the CO transition ($r/R \simeq 0.5$) than other low-order g-modes.

2.4.2 Zero-Metallicity and Super-Solar Metallicity

Replacing $X(^{14}\text{N})$ with $X(^4\text{He})$ and $X(^{22}\text{Ne})$ with $X(^{12}\text{C})$ is a model for ignoring the birth metallicity of the ZAMS star, CNO burning on the main-sequence, and the $^{14}\text{N}(\alpha, \gamma)^{18}\text{F}, (e^+ \nu_e)^{18}\text{O}(\alpha, \gamma)^{22}\text{Ne}$ reaction sequence during He-burning. Most studies of the pulsation periods of observed WDs use zero-metallicity DBV WDs when deriving the interior mass fraction profiles, although see Camisassa *et al.* (2016) for a counterexample. Alternatively, doubling $X(^{14}\text{N})$ at the expense of $X(^4\text{He})$ and doubling $X(^{22}\text{Ne})$ at the expense of $X(^{12}\text{C})$ is a model for a super-solar metallicity DBV WD.

Figure 2.10 compares the relative change in the low-order g-mode pulsation periods of the zero and super-solar metallicity models. The period differences are negative for the zero-metallicity model and positive for the super-solar metallicity model. Zero-metallicity DBV WD models have longer periods than the baseline model, which in

turn has longer periods than the super-solar metallicity model. The relative period differences of the zero and super-solar metallicity models are mostly symmetric about the baseline model's $Z = 0.02$ metallicity. The period differences of the zero-metallicity models, averaged over the T_{eff} evolution, are $\Delta P(g_{1,1}) \simeq -0.57$ s, $\Delta P(g_{1,2}) \simeq -0.40$ s, $\Delta P(g_{2,1}) \simeq -0.52$ s, and $\Delta P(g_{2,2}) \simeq -0.40$ s. For the super-solar metallicity models the averaged absolute period differences are $\Delta P(g_{1,1}) \simeq 0.66$ s, $\Delta P(g_{1,2}) \simeq 0.45$ s, $\Delta P(g_{2,1}) \simeq 0.46$ s, and $\Delta P(g_{2,2}) \simeq 0.35$ s. Over the T_{eff} range of currently observed DBV WDs, the mean relative period change of the dipole modes is 0.57% and the maximum of relative period change is 0.88%. The relative period change of the quadrupole modes is smaller, with a mean of 0.33% and a maximum of 0.63%.

Figure 2.11 shows the relative differences in the H^2 , μ_I , Γ_1 , χ_ρ and T contributions to N^2 of Equation 2.6 for the zero and super-solar metallicity models. These changes collectively determine the magnitude and sign of the period change relative to the baseline model. For the zero-metallicity models, the combined positive changes in μ_I and T are counteracted by the collective negative changes from H^2 , Γ_1 , and χ_ρ . The net change is negative, resulting in smaller N^2 and longer g-mode periods. Similar reasoning for the super-solar metallicity models leads to a net positive change, resulting in larger N^2 and smaller g-mode periods. The magnitude of the difference in H^2 drives the overall result for both metallicity cases. The nearly uniform changes in H^2 imply changes in the radii, and we find $(R_B - R_Z)/R_B \simeq \pm 0.4\%$ with zero-metallicity models having smaller radii and super-solar metallicity models having larger radii.

Interrogating further the composition dependence, the top panels of Figure 2.12 compare the mass fraction profiles of the $X(^{22}\text{Ne}) \simeq 0.02$ baseline and zero-metallicity at 30,000 K, 15,000 K and 12,100 K as a function of mass coordinate. Element diffusion is operating in both models. The middle panels show the relative differences in these mass fraction profiles, with the ^{22}Ne and ^{14}N offsets zeroed out. The C and

O differences at $\log(1 - M_r/M) \simeq -0.25$, from Figure 2.5, correspond to the C/O transition at $r/R \simeq 0.5$. The He difference at $\log(1 - M_r/M) \simeq -1.0$ correlates to the rise of He at $r/R \simeq 0.75$. Similarly, the C, O and He differences at $\log(1 - M_r/M) \simeq -2.0$ maps to He dominating the composition at $r/R \simeq 0.9$. These relative differences are the largest at 30,000 K, reaching $\simeq 7.5\%$ for ^{16}O and $\simeq -6\%$ for ^4He . The relative differences at 15,000 K and 12,100 K have about the same magnitude, $\simeq 7.5\%$ for ^{16}O and $\simeq -1\%$ for ^4He . The relative mass fraction differences span a larger range of $\log(1 - M_r/M)$ as the models cool due to element diffusion. The bottom panels of Figure 2.12 show the corresponding relative difference in the μ_I profiles. As μ_I is calculated by dividing the mass fraction of a isotope by its atomic weight, the relative differences in the mass fraction profiles are reduced in the μ_I profiles. The μ_I profile for 12,100 K in terms of a mass coordinate is the same as the μ_I profile in Figure 2.11 in terms of a radial coordinate.

We also computed the relative period differences between the $X(^{22}\text{Ne}) \simeq 0.02$ baseline and zero-metallicity model with diffusion turned off to disentangle structural and diffusion effects. The results are shown in Figure 2.13. While there is a slight variation from the zero-metallicity gray curves shown in Figure 2.10, mostly in the higher order $g_{10,1}$ and $g_{10,2}$ modes, the magnitude of the relative differences remains the same. This further suggests that the period shifts are a direct consequence of the presence or absence of ^{22}Ne .

2.5 Trends in the Period Changes with the White Dwarf Mass

Using the same physics and numerical choices as for the 0.56 M_\odot baseline model, we evolved a $Z = 0.02$, 1.1 M_\odot ZAMS stellar model from the pre-main sequence to a 0.526 M_\odot DB WD, and a $Z = 0.02$, 3.6 M_\odot ZAMS model to a 0.729 M_\odot DB WD. This initial to final mass mapping is similar to Table 1 of Camisassa *et al.* (2016). Relative

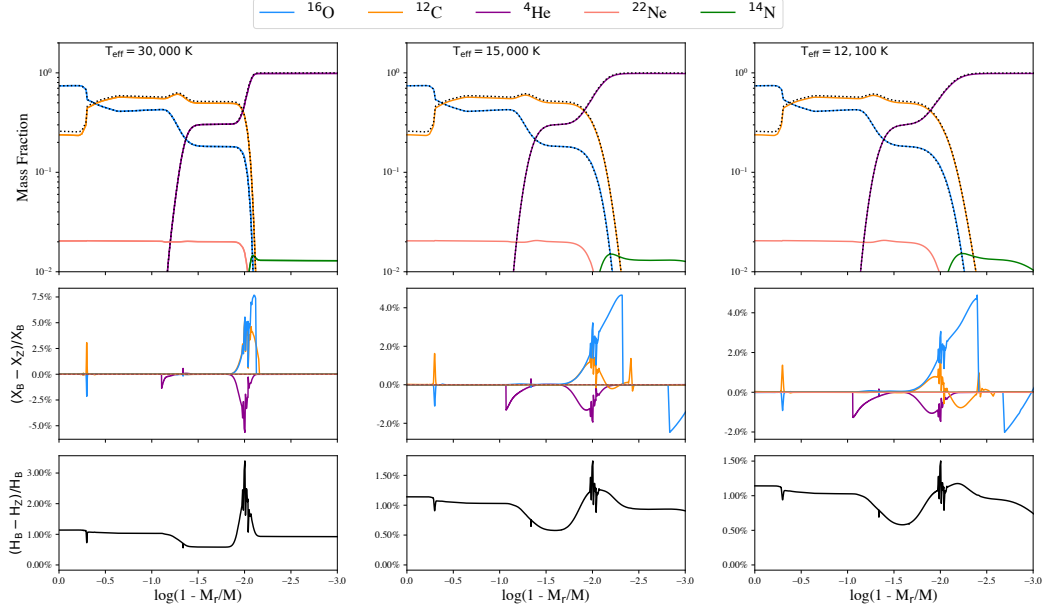


Figure 2.12: Top Panels: Mass fraction profiles for $0.56 M_{\odot}$ baseline (colored curves) and zero metallicity (black dashed curves) models at $T_{\text{eff}} \simeq 30,000 \text{ K}$, $15,000 \text{ K}$, and $12,100 \text{ K}$. Middle Panels: Relative differences in mass fraction profiles, where we have zeroed out the ^{22}Ne and ^{14}N offsets from ^{12}C and ^4He respectively. Bottom Panel: Relative differences in μ_I .

to the $0.56 M_{\odot}$ baseline model, the $0.526 M_{\odot}$ WD model has a thicker He-layer and a more abbreviated extent of $X(^{22}\text{Ne})$. Conversely, the $0.729 M_{\odot}$ WD model has a smaller ^{12}C bump, a thinner He-layer, and a more extended $X(^{22}\text{Ne})$ profile. These mass fraction profiles were imposed on $0.526 M_{\odot}$ and $0.729 M_{\odot}$ ab initio WD models, respectively.

Figure 2.14 shows the diffusion of these initial mass fraction profiles as the ab initio WD models cool to $T_{\text{eff}} \simeq 30,000 \text{ K}$, then $\simeq 15,000 \text{ K}$ and finally $\simeq 12,000 \text{ K}$ (corresponding to the termination at $\log(L/L_{\odot}) = -2.5$). Element diffusion is more pronounced for the more massive $0.729 M_{\odot}$ DB WD model due to its larger surface gravity. An enhancement forms in the $X(^{22}\text{Ne})$ profile at $\log(1 - M_r/M) \simeq -2.0$ by the time the $0.729 M_{\odot}$ model has cooled to $T_{\text{eff}} \simeq 30,000 \text{ K}$. As the model further cools, the $X(^{22}\text{Ne})$ bump grows in amplitude as it propagates inwards toward the center through the He-dominated outer layers. The $X(^{22}\text{Ne})$ bump generates an increase

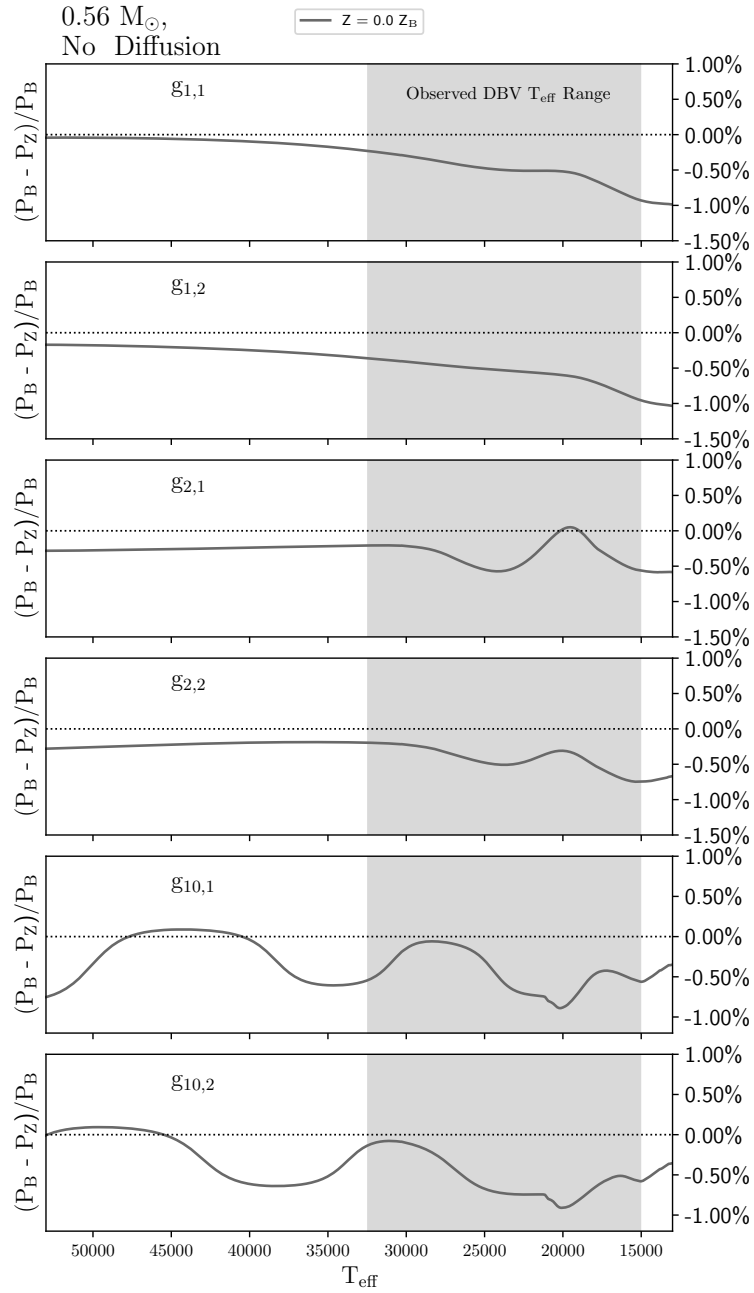


Figure 2.13: Top to Bottom: Relative period differences of the $g_{1,1}$, $g_{1,2}$, $g_{2,1}$, $g_{2,2}$, $g_{10,1}$ and $g_{10,2}$ modes between the baseline model, P_B , and the zero-metallicity WD model, P_Z , with diffusion turned off.

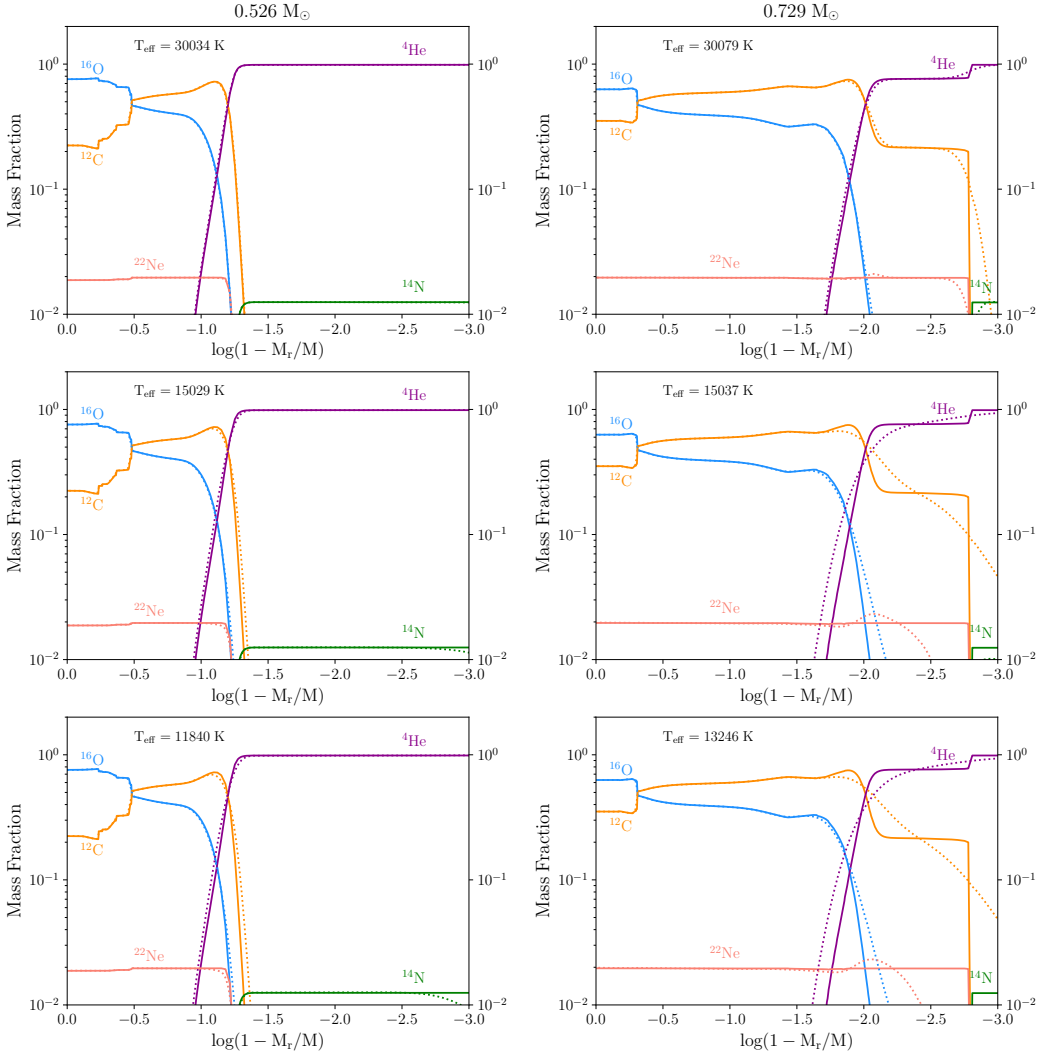


Figure 2.14: Mass fractions profiles for $0.52 M_{\odot}$ (left column) and $0.73 M_{\odot}$ (right column) ab initio DB WD models at $T_{\text{eff}} \simeq 30,000$ K (top), $15,000$ K (middle), and at the end of the evolution (bottom). Initial mass fraction profiles are shown as solid curves and the diffusing mass fraction profiles are shown as dotted curves.

in the local N^2 in the regions it propagates through from a locally larger μ_I and a smaller compensating H^2 . The regions trailing the $X(^{22}\text{Ne})$ bump are depleted of $X(^{22}\text{Ne})$, causing a decrease in the local N^2 in these regions.

We find longer low-order g-mode periods for the more massive WD, consistent with Camisassa *et al.* (2016). As was done for the $0.56 M_{\odot}$ baseline model, we replace $X(^{14}\text{N})$ with $X(^4\text{He})$ and $X(^{22}\text{Ne})$ with $X(^{12}\text{C})$ to generate a zero-metallicity ab

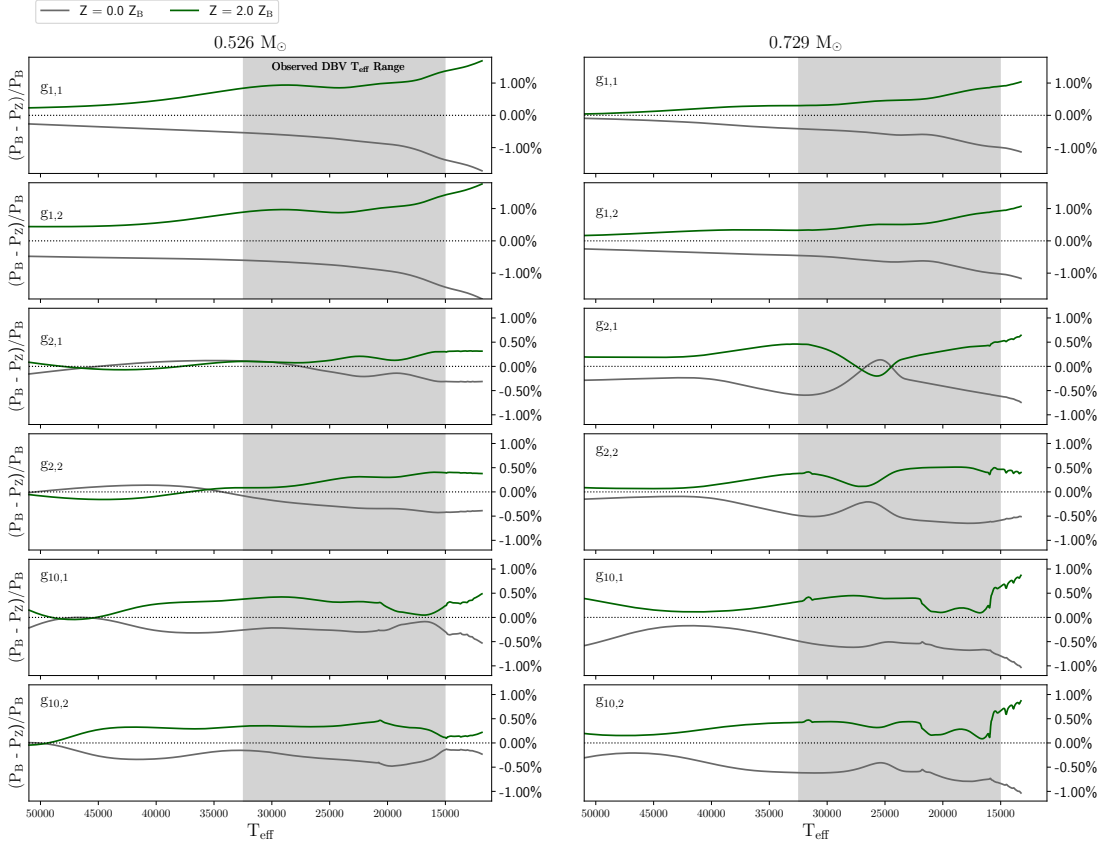


Figure 2.15: Relative period differences of the $g_{1,1}$, $g_{1,2}$, $g_{2,1}$, $g_{2,2}$, $g_{10,1}$ and $g_{10,2}$ modes for $0.526 M_{\odot}$ (left column) and $0.729 M_{\odot}$ (right column). Differences are between the baseline model, P_B , a zero-metallicity WD model (gray curves) where the ^{14}N and ^{22}Ne have been put into ^4He and ^{12}C respectively, and a super-solar metallicity model (green curves) where the ^{14}N and ^{22}Ne of the baseline model are doubled.

initio DB WD model. We also double $X(^{14}\text{N})$ at the expense of $X(^4\text{He})$ and double $X(^{22}\text{Ne})$ at the expense of $X(^{12}\text{C})$ to generate a super-solar metallicity DB WD.

Figure 2.15 compares the relative change in the low-order g-mode pulsation periods of the zero and super-solar metallicity $0.526 M_{\odot}$ and $0.729 M_{\odot}$ DB WD models. As for the $0.56 M_{\odot}$ baseline model, the relative period differences are mostly symmetric about the reference model's $Z = 0.02$ metallicity. For the $0.526 M_{\odot}$ models, over the T_{eff} range of currently observed DBV WDs, the mean relative period change of the dipole modes is 0.99% and the maximum of relative period change is 1.43%. The

relative period change of the quadrupole modes is smaller, with a mean of 0.25% and a maximum of 0.43%. For the $0.729 M_{\odot}$ models, the mean relative period change of the dipole modes is 0.65% and the maximum of relative period change is 1.02%. The relative period change of the quadrupole modes is again smaller, with a mean of 0.40% and a maximum of 0.65%. These values are commensurate with the mean and maximum relative period changes found for the $0.56 M_{\odot}$ baseline model.

There are a few trends in the relative period differences with respect to the WD mass. For the zero-metallicity $n = 2$ and $n = 10$ g-modes, the average relative differences in the observed T_{eff} range increase with increasing mass. For example, as the WD mass is increased from $0.526 M_{\odot}$ to $0.560 M_{\odot}$, we find the average relative period differences increase by factors of 1.74, 1.22, 2.43, and 1.46, for the $g_{2,1}$, $g_{2,2}$, $g_{10,1}$, and $g_{10,2}$ modes, respectively. As the WD mass is further increased from $0.560 M_{\odot}$ to $0.729 M_{\odot}$, we find additional magnification factors of 1.21, 1.29, 1.21, and 1.26, for g-modes $g_{2,1}$, $g_{2,2}$, $g_{10,1}$, and $g_{10,2}$ respectively. The absence of ^{22}Ne causes a greater deviation from the reference metallicity model as the WD mass increases.

The $g_{2,1}$ and $g_{2,2}$ g-modes show a trend in the local minimum as the WD mass increases. For the $0.526 M_{\odot}$ model, the $g_{2,1}$ g-mode has a local minimum at $T_{\text{eff}} \lesssim 20,000$ K. For the $0.526 M_{\odot}$ baseline model, this local minimum crosses zero at $T_{\text{eff}} \simeq 20,000$ K. For the $0.729 M_{\odot}$ model, the local minimum is deeper and crosses zero at $T_{\text{eff}} \simeq 25,000$ K. These trends with mass are due to when energy lost by the cooling WD is no longer dominated by neutrino cooling.

2.6 Discussion

We explored changes in the adiabatic low-order g-mode pulsation periods of 0.526, 0.560, and $0.729 M_{\odot}$ DB WD models due to the presence, absence, and enhancement

of ^{22}Ne as the models cool through the observed range of effective temperatures. We found mean relative period shifts of $\Delta P/P \simeq \pm 0.5\%$ for the low-order dipole and quadrupole g-mode pulsations within the observed effective temperature window, with a range of $\Delta P/P$ that depends on the specific g-mode, mass fraction of ^{22}Ne , effective temperature, and mass of the WD model. Shifts in the pulsation periods due to the presence, absence, or enhancement of $X(^{22}\text{Ne})$ mostly arise from a competition between the pressure scale height and ion mean molecular weight.

Low-mass DAV WDs, the ZZ Ceti class of stars, have pulsation periods in the 100–1500 s range (e.g., Vincent *et al.*, 2020). Comparing low-mass DAV WDs produced from stellar evolution models with and without diffusion of ^{22}Ne , Camisassa *et al.* (2016) find that the ^{22}Ne sedimentation induces mean period differences of $\simeq 3$ s, reaching maximum period differences of $\simeq 11$ s. For the more massive DAV WD models, where sedimentation of ^{22}Ne is stronger, they find mean period differences of $\simeq 15$ s between when diffusion is on and off, and a maximum period differences of $\simeq 47$ s. Comparatively, our article focuses on DBV WD models, the evolution of the pulsation periods as the DBV WD models cool, and the impact of ^{22}Ne being present, absent, or enhanced in the WD interior. Nevertheless, we conducted an experiment of turning element diffusion off in our $0.56 M_{\odot}$ baseline model. At $\log(L/L_{\odot}) = -2.5$, we find an absolute mean difference for $n = 1$ to $n = 11$ of $\simeq 16$ s, with a maximum period difference at $n = 9$ of $\simeq 56$ s. This maximum difference equates to a $\simeq 7\%$ relative difference between when diffusion is on and off. Our period changes are slightly higher than those found in Camisassa *et al.* (2016)'s $0.833 M_{\odot}$ model, and much larger than the differences found in their $0.576 M_{\odot}$ model. These differences could be a result of DAV versus DBV models, as DAV models have different cooling times than DBV models. In addition, Camisassa *et al.* (2016) computes their period differences at $\log(L/L_{\odot}) = -2.80$ and $\log(L/L_{\odot}) = -2.93$ for their 0.576 and $0.833 M_{\odot}$ models,

respectively. These are dimmer than the $\log(L/L_\odot) = -2.5$ used for our calculations. Our maximum radial order is found up to 11 at this luminosity, while Camisassa *et al.* (2016) uses more radial orders, with a maximum radial order of 50.

Giammichele *et al.* (2018) compares the g-mode pulsation periods of a pure oxygen core surrounded by a pure helium envelope with those from an oxygen-dominated core with $X(^{22}\text{Ne}) = 0.02$ surrounded by a pure helium envelope. They find including ^{22}Ne yields shorter periods, with mean period differences of $\simeq 0.1\%$. We find a mean period shift that is about 5 times larger in our $0.56 M_\odot$ baseline model. This difference may be caused by the contrast in the composition of the models, which in turn causes variances in the local mean molecular weight and pressure scale height scaling described by Equation 2.6.

Are 1% or less period differences important? The g-mode periods of observed DBV WD are found from a Fourier analysis of the photometric light curves and are typically given to 6–7 significant figures of precision. Usually zero-metallicity WD models (i.e., without ^{22}Ne) are fit to the observed g-mode periods and other properties (e.g., T_{eff} , $\log g$). The root-mean-square residuals to the $\simeq 150$ –400 s low-order g-mode periods are typically in the range $\sigma_{\text{rms}} \lesssim 0.3$ s (e.g., Bischoff-Kim *et al.*, 2014a), for a fit precision of $\sigma_{\text{rms}}/P \lesssim 0.3\%$. Our finding of a mean relative period shift of $\Delta P/P \simeq \pm 0.5\%$ induced by including ^{22}Ne in WD models suggests a systematic offset may be present in the fitting process of specific WDs when ^{22}Ne is absent. As part of the fitting process involves adjusting the composition profiles of the model WD, this study on the impact of ^{22}Ne can inform inferences about the derived interior mass fraction profiles. We encourage routinely including ^{22}Ne mass fraction profiles, informed by stellar evolution models, to future generations of DBV WD model fitting processes.

The adiabatic low-order g-mode pulsation periods of our DB WD models depend upon simplifying assumptions in the stellar evolution calculations (e.g., convective boundary layer mixing, shellular rotation), uncertainties (e.g., mass loss history, stripping of the residual thin H layer, thickness of the He-dominated atmosphere), and unknown inherent systematics. We hypothesize that these model dependencies and systematics could mostly cancel when dividing one model result by another model result, such as when calculating the relative period shifts $\Delta P/P$. We anticipate exploring a larger range of models, similar in approach to Fields *et al.* (2016), to test this conjecture in future studies.

ACKNOWLEDGEMENTS

The MESA project is supported by the National Science Foundation (NSF) under the Software Infrastructure for Sustained Innovation program grants (ACI-1663684, ACI-1663688, ACI-1663696). This research was also supported by the NSF under grant PHY-1430152 for the Physics Frontier Center “Joint Institute for Nuclear Astrophysics - Center for the Evolution of the Elements” (JINA-CEE). A.T. is a Research Associate at the Belgian Scientific Research Fund (F.R.S-FNRS). We acknowledge useful discussions at virtual Sky House 2020. This research made extensive use of the SAO/NASA Astrophysics Data System (ADS).

Software: MESA (Paxton *et al.*, 2011, 2013, 2015, 2018, 2019, <http://mesa.sourceforge.net>), MESASDK 20190830 (Townsend, 2019a,b), wd_builder https://github.com/jschwab/wd_builder, GYRE (Townsend and Teitler, 2013; Townsend *et al.*, 2018, <https://github.com/rhdtownsend/gyre>),
Montreal White Dwarf Database

(Dufour *et al.*, 2017, <http://www.montrealwhitedwarfdatabase.org>),
`matplotlib` (Hunter, 2007), and `NumPy` (van der Walt *et al.*, 2011).

Chapter 3

PROBING $^{12}\text{C}(\alpha, \gamma)^{16}\text{O}$ WITH TRAPPED MODES IN WDS

This is the content from the published work of Morgan T. Chidester et al 2022
ApJ 935 21.

3.1 Abstract

We seek signatures of the current experimental $^{12}\text{C}(\alpha, \gamma)^{16}\text{O}$ reaction rate probability distribution function in the pulsation periods of carbon-oxygen white dwarf models. We find that adiabatic g-modes trapped by the interior carbon-rich layer offer potentially useful signatures of this reaction rate probability distribution function. Probing the carbon-rich region is relevant because it forms during the evolution of low-mass stars under radiative helium burning conditions, mitigating the impact of convective mixing processes. We make direct quantitative connections between the pulsation periods of the identified trapped g-modes in variable white dwarf models and the current experimental $^{12}\text{C}(\alpha, \gamma)^{16}\text{O}$ reaction rate probability distribution function. We find an average spread in relative period shifts of $\Delta P/P \simeq \pm 2\%$ for the identified trapped g-modes over the $\pm 3\sigma$ uncertainty in the $^{12}\text{C}(\alpha, \gamma)^{16}\text{O}$ reaction rate probability distribution function — across the effective temperature range of observed DAV and DBV white dwarfs and for different white dwarf masses, helium shell masses, and hydrogen shell masses. The g-mode pulsation periods of observed white dwarfs are typically given to 6-7 significant figures of precision. This suggests that an astrophysical constraint on the $^{12}\text{C}(\alpha, \gamma)^{16}\text{O}$ reaction rate could, in principle, be extractable from the period spectrum of observed variable white dwarfs.

3.2 Introduction

Tens of thousands of nuclear reactions can participate during the evolution of a star, depending on the environmental conditions. Only a few of these reactions have a strong impact on the overall chemical evolution of the elements, with significant consequences for the chemistry and the subsequent molecular evolution of baryonic matter. In particular, the helium burning $^{12}\text{C}(\alpha,\gamma)^{16}\text{O}$ reaction plays a major role in the energy production and nucleosynthesis of stars (e.g., Iben, 1967; Fowler, 1984b; Arnett, 1996; Iliadis, 2015; deBoer *et al.*, 2017) and thus influences the $^{12}\text{C}/^{16}\text{O}$ ratio in the universe.

The difficulty in measuring the $^{12}\text{C}(\alpha,\gamma)^{16}\text{O}$ rate in nuclear experiments is due to the small cross section of the $^{12}\text{C}(\alpha,\gamma)^{16}\text{O}$ reaction at temperatures relevant for helium burning in stars. Nuclear experiments in terrestrial laboratories provide data for energies as low as about 2 MeV, with extrapolation to stellar conditions at $kT \simeq 20$ keV. At stellar conditions, two partial waves contribute, denoted by their spectroscopic E1 and E2 amplitudes in reaction and scattering theory (Fowler, 1984a). The challenge is measurement of the low energy angular distributions of the $^{12}\text{C}(\alpha,\gamma)^{16}\text{O}$ reaction, from which the E1 and E2 cross sections are extracted.

Decreasing the uncertainty in the $^{12}\text{C}(\alpha,\gamma)^{16}\text{O}$ reaction rate from low-energy nuclear experiments has markedly improved in recent years. For example, to obtain a comprehensive evaluation deBoer *et al.* (2017) considered the entirety of existing experimental data, aggregating about 60 years of experimental data consisting of more than 50 independent experimental studies. More than 10,000 data points were then incorporated into a complete multi-channel phenomenological R-matrix analysis. A main result was the characterization of the uncertainty in the reaction rate, which was accomplished through a Monte-Carlo uncertainty analysis of the data and the

extrapolation to low-energy using the R-matrix model. After finding an approximately Gaussian underlying probability distribution for the rate, there was statistical significance with the 1σ uncertainty of the reaction rate. A goal of forthcoming experiments is to further reduce the uncertainty in the $^{12}\text{C}(\alpha,\gamma)^{16}\text{O}$ reaction rate (e.g., Smith *et al.*, 2021).

Partnering with this laboratory astrophysics quest are astrophysical constraints on the $^{12}\text{C}(\alpha,\gamma)^{16}\text{O}$ reaction rate. For example, Weaver and Woosley (1993) find a permissible range of the reaction rate by requiring the integrated nucleosynthesis yields, from a set of massive star explosion models over plausible initial mass functions, agree with the observed solar abundances for the intermediate mass isotopes. They found this range was insensitive to the assumed slope of the initial mass function within observational limits, and relatively insensitive to some details of convective boundary mixing.

As another example of an astrophysical constraint, models for the evolution of single stars predicts the existence of a gap in the black hole mass distribution for high mass stars due to the high temperature effects of electron-positron pair production (Heger and Woosley, 2002). The location of the black hole mass gap is generally robust with respect to model uncertainties (Takahashi, 2018; Farmer *et al.*, 2019; Marchant and Moriya, 2020), but depends sensitively on the uncertain $^{12}\text{C}(\alpha,\gamma)^{16}\text{O}$ reaction rate (Farmer *et al.*, 2020). The location of the black hole mass gap, probed though LIGO/Virgo/Karga (LIGO Scientific Collaboration *et al.*, 2015; Acernese *et al.*, 2015; Akutsu *et al.*, 2021) gravitational wave determinations of the masses and spins of merging binary black holes, thus allows a constraint on the $^{12}\text{C}(\alpha,\gamma)^{16}\text{O}$ reaction rate (Farmer *et al.*, 2020; Woosley and Heger, 2021; Mehta *et al.*, 2022).

Seismology of hydrogen dominated atmosphere (DA class) and helium dominated atmosphere (DB class) carbon-oxygen white dwarfs (CO WDs) has also been used to

place constraints on the $^{12}\text{C}(\alpha,\gamma)^{16}\text{O}$ reaction rate (Metcalfe *et al.*, 2001, 2002). In this approach the central ^{16}O abundance and the location of the oxygen-to-carbon transition within the CO core are used as fitting parameters when minimizing the difference between the observed pulsations periods of specific WDs and the pulsation periods of WD models. The derived parameters can then imply a constraint on the $^{12}\text{C}(\alpha,\gamma)^{16}\text{O}$ reaction rate, but are sensitive to model choices (Metcalfe, 2003), diffusion (Fontaine and Brassard, 2002), and convective boundary mixing (Straniero *et al.*, 2003).

De Gerónimo *et al.* (2017) analyzed two CO WD models with masses 0.548 and 0.837 M_\odot derived from evolutionary calculations from the zero-age main sequence (ZAMS). They considered models that varied the number of thermal pulses, the amount of overshooting, and the $^{12}\text{C}(\alpha,\gamma)^{16}\text{O}$ reaction rate within the uncertainties known at the time. They found that independent variations of these quantities produced significant changes in the resulting DA WD chemical profiles and the pulsation period spectrum.

Pepper *et al.* (2022) calculated evolutionary models with initial masses in the range of $0.90 \leq M/\text{M}_\odot \leq 3.05$. They considered different $^{12}\text{C}(\alpha,\gamma)^{16}\text{O}$ reaction rates within the uncertainties known at the time. As expected, they found no changes in the evolution prior to the core He-burning stage. However, they found that the subsequent stages of evolution produced differences in the convective He core mass, the number of thermal pulses during the asymptotic giant branch phase of evolution, and broad trends in the chemical profiles.

The main novelty of this article is a new search for potential signatures of the current experimental $^{12}\text{C}(\alpha,\gamma)^{16}\text{O}$ reaction rate probability distribution function in the pulsation periods of CO WD models. Section 3.3 describes our models, Section 3.4

describes our results, Section 3.5 discusses sensitivities, and Section 3.6 summarizes the results of our new search.

3.3 Models

3.3.1 Updated $^{12}\text{C}(\alpha, \gamma)^{16}\text{O}$ Reaction Rates

Mehta *et al.* (2022) expanded the deBoer *et al.* (2017) tabulated reaction rate for $^{12}\text{C}(\alpha, \gamma)^{16}\text{O}$ to a finer temperature grid, from 52 to 2015 temperature points, to ensure that no temperature step results in variations in the rate of more than a factor of two. The recalculations also provided the formal $\pm 3\sigma$ uncertainties on the experimental reaction rate probability distribution function in steps of 0.5σ . σ_0 is the median rate consistent with an astrophysical S-factor of $S(300 \text{ keV}) = 140 \text{ keV b}$ with a $\pm 1\sigma = 21 \text{ keV b}$ uncertainty. By exploring $\pm 3\sigma$ we effectively explore the range $S(300 \text{ keV}) = (77, 203) \text{ keV b}$, where positive and negative σ indicate a stronger and weaker rate than the median value, respectively.

This probability distribution function is shown in Figure 3.1 over the $\pm 3\sigma$ region. Green bands represent positive σ_i while the gray bands represent negative σ_i . The 13 individual σ curves are depicted by respective dotted lines, with the $\pm 1, 2, 3\sigma$ lines labeled. The blue region shows the temperature range spanned by core and shell He burning in our evolutionary 2.1 M_\odot ZAMS mass models. These reaction rate files are available at doi:<https://doi.org/10.5281/zenodo.6779983>.

3.3.2 MESA wd_builder, and GYRE

We use **MESA** version r15140 (Paxton *et al.*, 2011, 2013, 2015, 2018, 2019) to evolve 2.1 M_\odot , $Z = 0.0151$ metallicity, non-rotating models from the ZAMS to the top of the WD cooling track in the Hertzsprung-Russell diagram. This results in 0.56 M_\odot

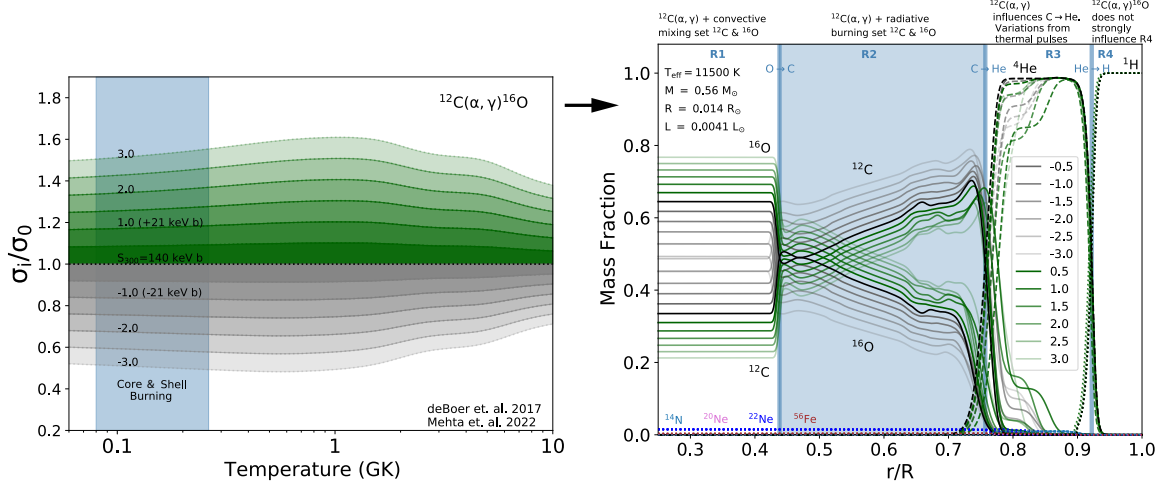


Figure 3.1: Left: $^{12}\text{C}(\alpha, \gamma)^{16}\text{O}$ reaction rate ratios, σ_i/σ_0 , as a function of temperature. For our models, σ_i spans -3.0 to 3.0 in 0.5 step increments, with σ_0 being the current nominal rate. Negative σ_i are gray curves and positive σ_i are green curves. The $\pm 1, 2, 3 \sigma_i$ curves are labeled. The blue band show the range of temperatures encountered during core and shell He burning. Right: Mass fraction profiles of the evolutionary DAV models resulting from the $^{12}\text{C}(\alpha, \gamma)$ reaction rate uncertainties σ_i after each model has cooled to $T_{\text{eff}}=11,500 \text{ K}$. The nominal $\sigma=0$ reaction rate is the black curve, negative σ_i are gray curves and positive σ_i are green curves. Solid curves are for ^{12}C and ^{16}O , dashed curves are for ^1H and ^4He . The trace isotopes ^{14}N , ^{20}Ne , ^{22}Ne , and ^{56}Fe are labeled. Key regions and transitions are also labeled (see text).

DA WDs with $\simeq 0.01 M_{\odot}$ He-rich mantles and $\simeq 10^{-3.5} M_{\odot}$ H-rich envelopes. One such evolutionary model is run for each 0.5σ step in the $^{12}\text{C}(\alpha, \gamma)^{16}\text{O}$ reaction rate probability distribution function. We refer to this set of models as the evolutionary DAVs. Each model used $\simeq 20,000$ cells with a 30 isotope nuclear reaction network and time resolution settings that consumed $\simeq 3$ months of wall-clock time on 16 cores to complete $\simeq 550,000$ time steps. Our models are similar to the lower resolution models used in Timmes *et al.* (2018b) and Chidester *et al.* (2021).

We also use `wd_builder` with `MESA` version r15140 to build ab initio WD models. By ab initio we mean calculations that begin with a hot WD model and an assumed chemical stratification, as opposed to a hot WD model that is the result of a stellar evolution calculation. The imposed initial ^1H , ^4He , ^{12}C , ^{14}N , ^{16}O , ^{22}Ne , and ^{56}Fe mass fraction profiles are taken from the evolutionary DAV models after the first

thermal pulse on the asymptotic giant branch, defined by the first time the luminosity $L > 10^4 L_\odot$. The H envelope is then thinned to mimic the H envelope thickness of the evolutionary DAVs, the mass fraction profiles are smoothed at chemical transitions, and mass location where ^{16}O and ^{12}C exchange dominance is taken to the average mass location for all σ_i . This initial conditions procedure is done for DAV and DBV `wd_builder` models. The DBV `wd_builder` models are then stripped of their H envelope.

We use ab initio WD models because they allow a more rapid exploration of the different WD classes, CO WD masses, and envelope masses needed to preliminary assess the robustness of our results. A potential disadvantage, or advantage, of ab initio WD models is that the imposed initial chemical stratification may not be attainable by a stellar model evolved from the ZAMS.

We use `GYRE` release 6.0 (Townsend and Teitler, 2013; Townsend *et al.*, 2018) embedded in `MESA` version r15140 to calculate the adiabatic pulsation properties as a WD model evolves. All the `MESA + GYRE` models begin from the top of the WD cooling track, terminate as cool WDs, and include the effects of element diffusion. Details of the `MESA` and `wd_builder` models are in the files to reproduce our results at doi: [<https://doi.org/10.5281/zenodo.6779983>].

We end this section by pointing out that we are not advocating for any specific model, or any specific setting used by an evolutionary model (e.g., convective mixing parameters). Rather our goal is to find, if there exists, potential signatures of the current experimental $^{12}\text{C}(\alpha, \gamma)^{16}\text{O}$ reaction rate probability distribution function in the pulsation periods of variable WD models. If such signatures exist and appear across the model space (including other researcher's variable WD models), then future uncertainty quantification studies could explore the impact of specific settings.

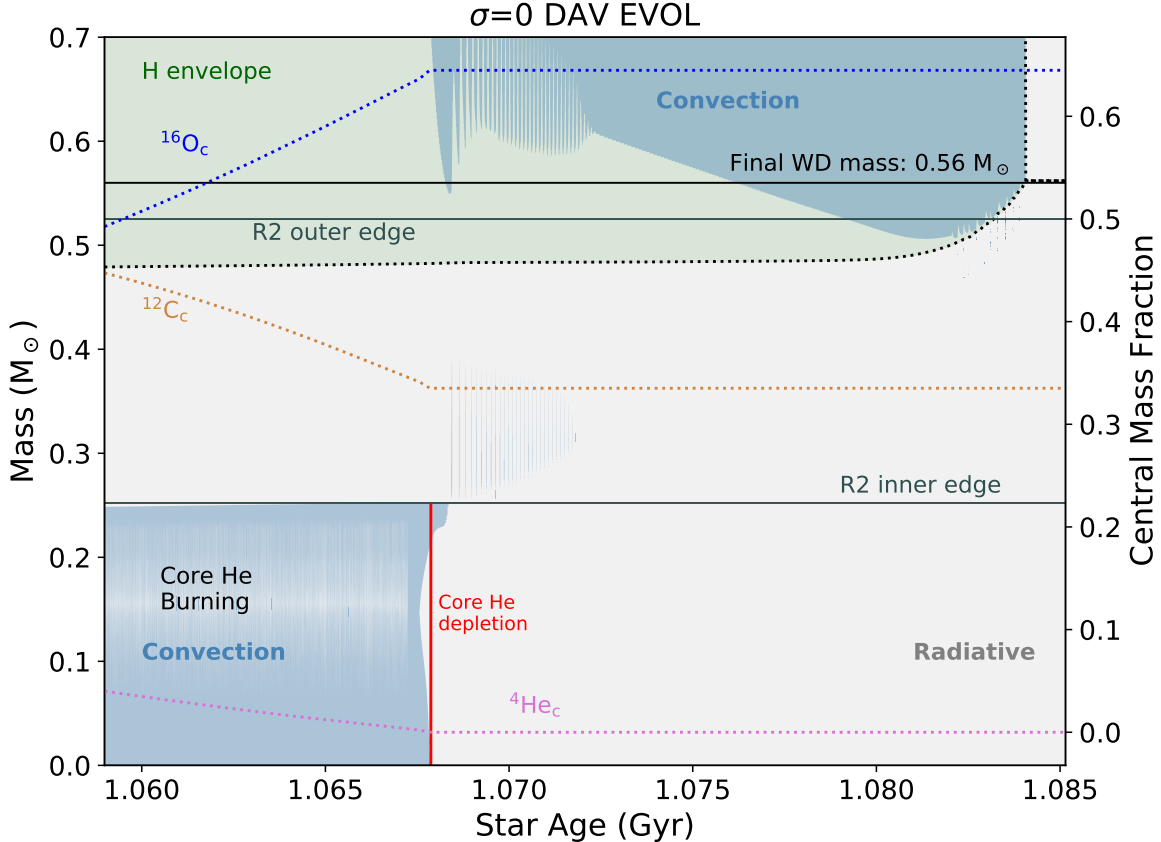


Figure 3.2: Kippenhahn diagram near core He depletion for the $\sigma=0$ evolutionary DAV model. Blue shading represents convective regions, gray the radiative regions, green the H envelope, and the red line marks core He depletion. Labeled are the eventual WD mass and the edges of radiative He burning region R2. Also shown is the evolution of the central ${}^4\text{He}$, ${}^{12}\text{C}$, and ${}^{16}\text{O}$ mass fractions.

3.4 Results

3.4.1 Evolutionary DAVs

Figure 3.1 shows the mass fraction profiles of the evolutionary DAV models for the 13 σ_i reaction rates. We describe the labeled regions and chemical transitions.

Region R1 extends from the center to the transition between ${}^{16}\text{O}$ and ${}^{12}\text{C}$ in the core, henceforth the O→C transition, encompassing the innermost $\simeq 0.3 \text{ M}_\odot$. The reaction rate uncertainties have a large impact in R1, with the central ${}^{16}\text{O}$ mass fraction ranging from 0.45 for $\sigma=-3.0$ to 0.77 for $\sigma=3.0$ in a regular pattern. The

^{16}O and ^{12}C mass fraction profiles are flat because this region forms during convective core He burning (see discussion of Figure 3.2). Deconvolving how much ^{16}O and ^{12}C is due to the $^{12}\text{C}(\alpha, \gamma)^{16}\text{O}$ reaction rate and how much is due to convective mixing processes, which has its own uncertainties, appears challenging (Straniero *et al.*, 2003; De Gerónimo *et al.*, 2017).

Region R2 extends from the O→C transition to the transition between ^{12}C and ^4He , henceforth the C→He transition, encompassing $\simeq 0.25 M_\odot$. The reaction rate uncertainties also have a large impact in R2, with the ^{12}C and ^{16}O mass fraction profiles showing a regular pattern with σ_i . This carbon-rich region forms during thick-shell He burning under radiative conditions (see Figure 3.2), mitigating the impact of convective mixing processes. The significant spread in the ^{16}O and ^{12}C mass fraction profiles is set by the $^{12}\text{C}(\alpha, \gamma)^{16}\text{O}$ reaction rate probability distribution function. The broad trend of the ^{12}C mass fraction increasing and the ^{16}O mass fraction decreasing with enclosed mass reflects the decreasing temperature and density in the radial direction during the formation of R2.

Region R3 extends from the C→He transition to the He→H transition. In the He-rich mantle of R3, the more irregular pattern of the ^{16}O , ^{12}C , and ^4He mass fraction profiles reflect variations in the thermal pulse histories. Region R4 extends from the He→H transition to the surface. The $^{12}\text{C}(\alpha, \gamma)^{16}\text{O}$ reaction rate does not have a strong role in R4. In addition, the four most abundant trace isotopes ^{22}Ne , ^{20}Ne , ^{14}N , and ^{56}Fe do not show a strong dependence on σ_i in any region.

Figure 3.2 shows the evolution of the $\sigma=0$ model near core He depletion and the onset of thick-shell He burning. Region R1 in the final WD model is formed during convective core He burning. The extent of the convective core does not intrude into region R2. Core convection ceases at core He depletion, marked by the red line. The O-rich R1 region then becomes radiative for the remainder of the evolution. Region

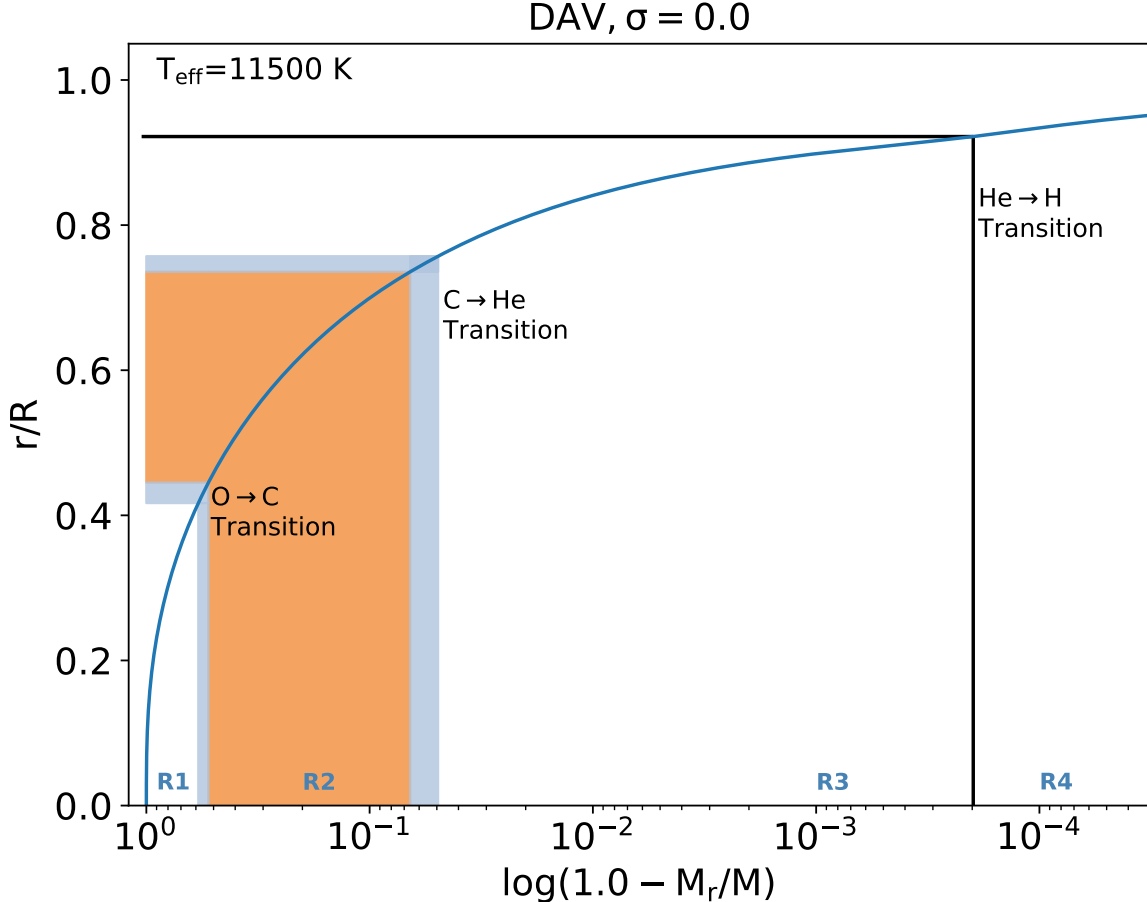


Figure 3.3: Mass-radius relation with key regions and chemical transitions annotated for the $\sigma=0$ evolutionary DAV model when it has cooled to $T_{\text{eff}}=11,500$ K. The shaded interiors highlight the regions that can most directly probe the $^{12}\text{C}(\alpha,\gamma)$ reaction rate.

R2 in the final WD model is formed after core He depletion during radiative thick-shell He burning. The resulting C-rich R2 region then remains radiative for the remainder of the evolution.

It is useful to reference features with respect to mass or radius. Figure 3.3 thus shows the mass-radius relation for the $\sigma=0$ model with regions and transitions labeled.

Some pulsation modes are more informative of these four regions than others. This can be due to a resonance, or near-resonance, between the mode's radial wavelength and thickness of one or more of the composition layers (Brassard *et al.*, 1991). As

these modes traverse a composition gradient within a local resonance region, they are partially reflected and become “trapped” within the local layer (Winget *et al.*, 1981). Such modes are identified by showing a local minima in a kinetic energy diagram. We choose to refer to any mode displaying a local minima in the kinetic energy diagram as a trapped mode, regardless of the resonant region’s location (e.g., upper or deeper layers). Modes trapped by the upper layers can reveal insights about WD envelopes (Kawaler and Weiss, 1990; Brassard *et al.*, 1992b; Kawaler, 1995; Costa *et al.*, 2008). Modes trapped deeper in the WD can be sensitive to the different regions, and thus reveal insights on the interior chemical profiles (Brassard *et al.*, 1992a; Córscico *et al.*, 2002; Giambicheli *et al.*, 2017b). In particular, g-modes trapped by R2 can probe the current experimental $^{12}\text{C}(\alpha, \gamma)$ reaction rate probability distribution function.

The Brunt-Väisälä frequency N is a characteristic frequency for pulsations, specifically the frequency of oscillation about an equilibrium position under gravity:

$$N^2 = \frac{g^2 \rho}{P} \frac{\chi_T}{\chi_\rho} (\nabla_{\text{ad}} - \nabla_T + B) , \quad (3.1)$$

where g is the gravitational acceleration, ρ is the mass density, P is the pressure, T is the temperature, χ_T is the temperature exponent $\partial(\ln P)/\partial(\ln \rho)|_{T,\mu_I}$, χ_ρ is the density exponent $\partial(\ln P)/\partial(\ln T)|_{\rho,\mu_I}$, ∇_{ad} is the adiabatic temperature gradient, ∇_T is the actual temperature gradient, and B is the Ledoux term that accounts for composition gradients (e.g., Hansen and Kawaler, 1994a; Fontaine and Brassard, 2008). The implementation of Equation 3.1 in **MESA** is described in Paxton *et al.* (2013).

Figure 3.4 shows the Brunt-Väisälä frequency and the Ledoux B term profiles as a function of fractional radius after the 13 σ_i evolutionary DAVs have cooled to $T_{\text{eff}} = 11,500$ K. The composition gradients in the O→C and C→He transition regions, highlighted by the blue bands, induce bumps in the Ledoux B term profile and thus bumps in the N^2 profile. The first peak is located at the O→C transition

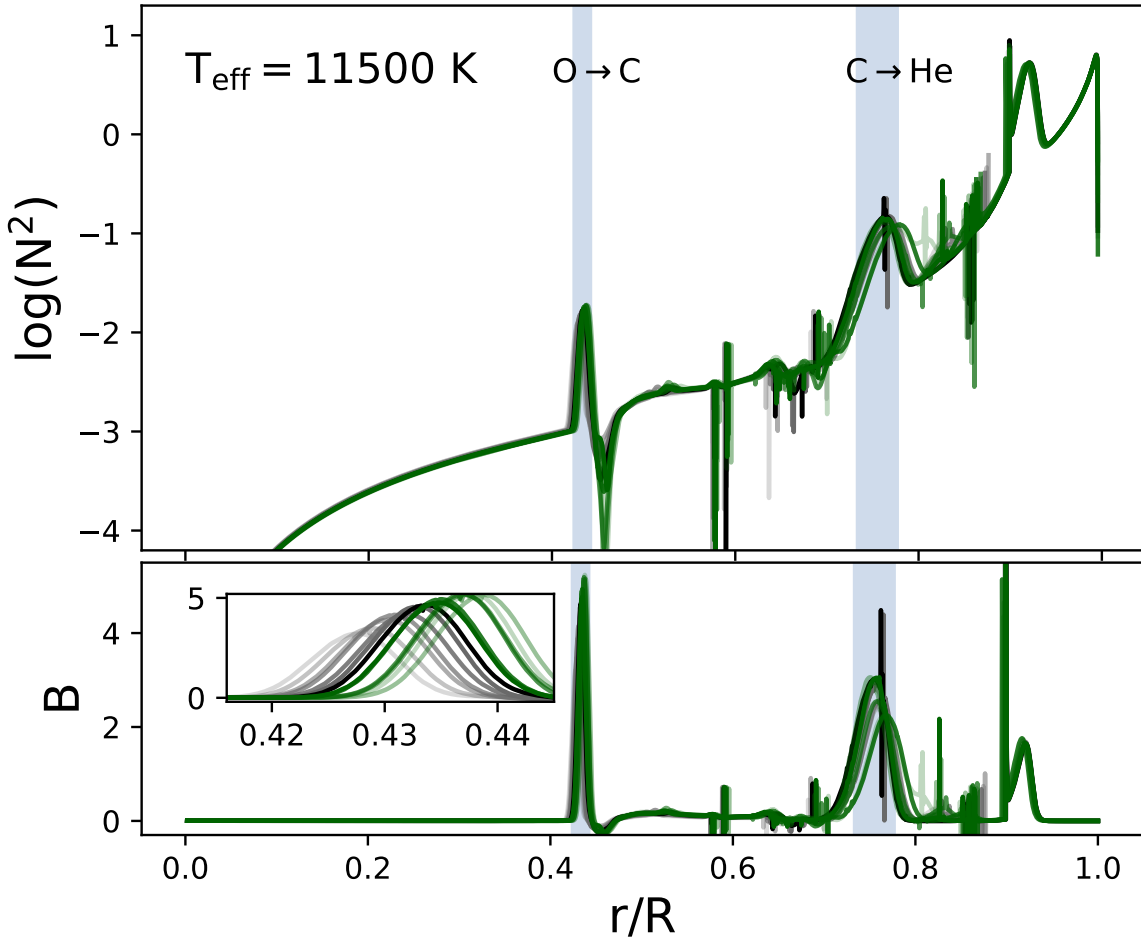


Figure 3.4: Top: Brunt-Väisälä frequency profiles as a function of fractional radius for the evolutionary DAVs after they have cooled to $T_{\text{eff}}=11,500$ K. As in Figure 3.1 the nominal $\sigma=0$ reaction rate is the black curve, positive σ_i are green curves, and negative σ_i are gray curves. Blue bands mark the $O \rightarrow C$ and $C \rightarrow He$ transition regions for all σ_i . Bottom: The Ledoux B term in Equation 3.1 as a function of fractional radius. An enlarged view of the first peak in B at the $O \rightarrow C$ transition is shown in the inset plot.

and magnified in the inset plot. As σ_i increases from -3.0 to 3.0, the location and magnitude of B increase with radius in a near-regular pattern.

The kinetic energy E_{kin} of each g-mode can be expressed as (Unno *et al.*, 1989; Córscico *et al.*, 2002)

$$E_{\text{kin}} = \frac{GMR^2}{2} \omega_n^2 \int_0^1 x^2 \rho \left[x^2 y_1^2 + x^2 \frac{\ell(\ell+1)}{(C_1 \omega_n^2)^2} y_2^2 \right] dx , \quad (3.2)$$

where n is the radial order, ℓ the spherical harmonic degree, G the gravitational constant, M the stellar mass, R the stellar radius, $\omega_n^2 = f_n^2(GM/R^3)^{-1}$ the dimensionless eigenfrequency, $f_n = 2\pi/P_n$ the frequency, P_n the period, $C_1 = x^3(M/M_r)$ the scaled density, r the radial distance from the center, M_r the stellar mass enclosed at radius r , $x = r/R$ the scaled radius, and y_1 and y_2 are the dimensionless Dziembowski (1971) eigenfunctions.

We numerically integrate Equation 3.2 for g-modes of radial orders $n = 1\text{--}19$ and harmonic degree $\ell = 1$. Unless otherwise specified, all g-modes considered have $\ell = 1$. Figure 3.5 shows the resulting E_{kin} and period spacing $\Delta P_n = P_{n+1} - P_n$ diagrams for the evolutionary DAVs when they have cooled to $T_{\text{eff}} = 11,500$ K. Trapped modes are identified by minima in E_{kin} and by a corresponding minima in the period spacing (e.g., Winget *et al.*, 1981; Brassard *et al.*, 1991). Figure 3.5 highlights two strong local minima, the g_5 and g_{10} trapped modes.

The frequency of an adiabatic g-mode is the area under a curve known as a weight function $d\zeta/dr$

$$f^2 = \zeta = \int_{r=0}^{r=R} \frac{d\zeta}{dr} \cdot dr , \quad (3.3)$$

where, following Kawaler *et al.* (1985),

$$\frac{d\zeta}{dr} = \frac{[C(\mathbf{y}, r) + N(\mathbf{y}, r) + G(\mathbf{y}, r)]\rho r^2}{\int_{r=0}^{r=R} T(\mathbf{y}, r)\rho r^2 dr} \quad (3.4)$$

and $C(\mathbf{y}, r)$ varies with the Lamb frequency, $N(\mathbf{y}, r)$ contains the Brunt-Väisälä frequency, $G(\mathbf{y}, r)$ involves the gravitational eigenfunctions, $T(\mathbf{y}, r)$ is proportional to the kinetic energy density, and $\mathbf{y} = (y_1, y_2, y_3, y_4)$ are the Dziembowski (1971) variables.

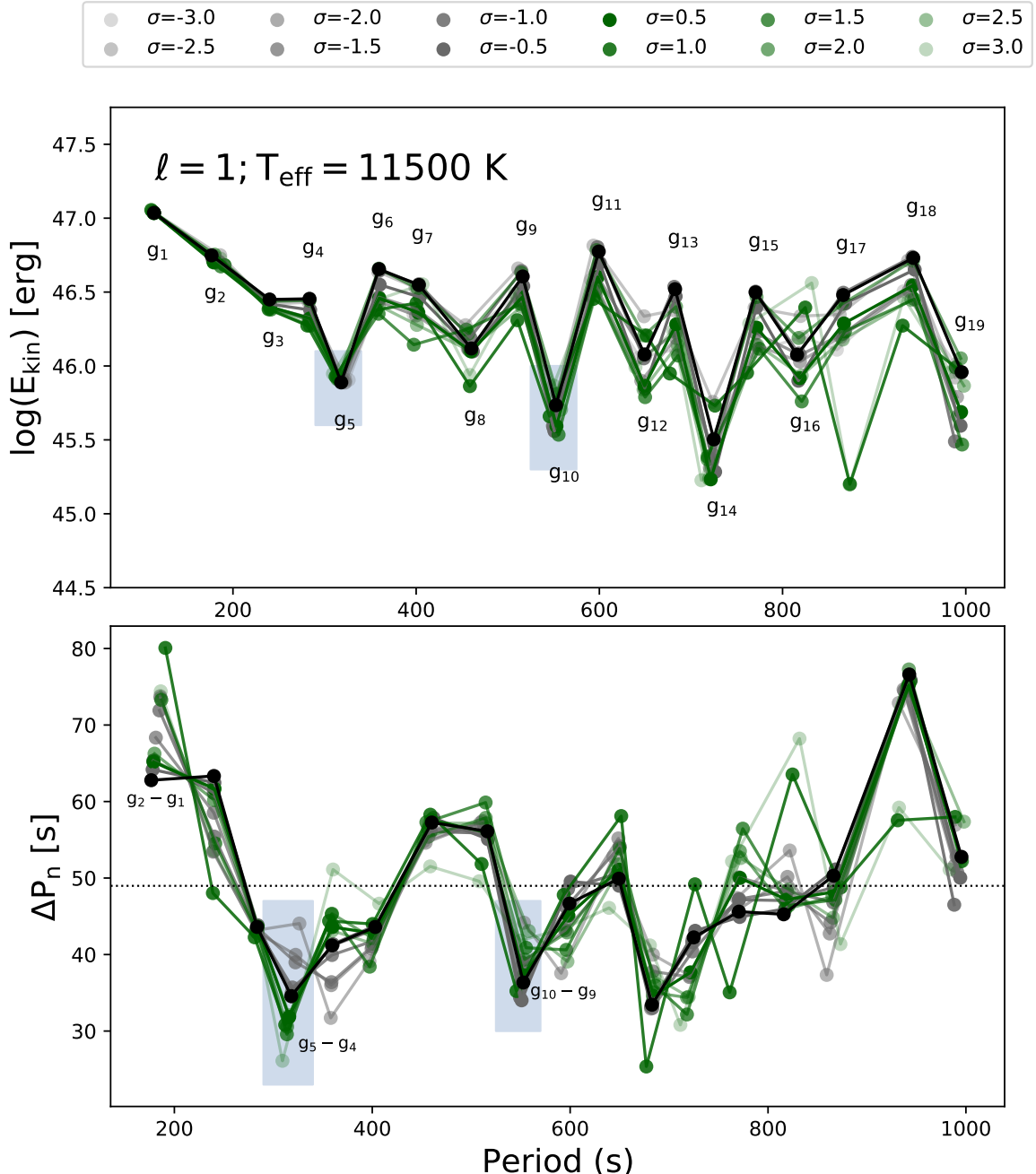


Figure 3.5: Top: Kinetic energy of adiabatic g-modes for radial orders $n = 1-19$ and harmonic degree $\ell = 1$ after the evolutionary DAVs have cooled to $T_{\text{eff}} = 11,500 \text{ K}$. The colors are as in Figure 3.1. Local minima identify trapped modes. The g_5 and g_{10} trapped modes are highlighted with blue bands. Bottom: Period spacing diagram with the local minima at g_5 and g_{10} highlighted by blue bands. The mean period spacing for $\sigma = 0$ model is marked by the dashed line.

Figure 3.6 shows the weight functions of the g_4 , g_5 , g_6 , and g_{10} modes. The g_5 and g_{10} trapped modes have larger weight functions in regions R1 and R2 compared to the g_4 and g_6 non-trapped modes. The frequency of the trapped modes is thus more strongly weighted by regions R1 and R2. The g_{10} weight function is more equally distributed than the g_5 weight function, and the peak at the O→C transition is about the same height as the other peaks. Both factors decrease the ability of g_{10} to probe the O→C transition and region R2. In contrast, the peak in the g_5 weight function at the O→C transition is the largest peak. About 35% of the g_5 frequency comes from the O→C transition, and $\simeq 67\%$ from the O→C transition and R2.

Taken together, these weight functions indicate that R2 contributes $\simeq 30\text{--}40\%$ and R1 contributes $\simeq 20\%$ to the periods of g_5 and g_{10} . This suggests that applying our results, conducted over the current experimental $\pm 3\sigma$ uncertainty in the $^{12}\text{C}(\alpha, \gamma)^{16}\text{O}$ reaction rate probability distribution function, to the derived pulsation spectrum of observed variable WD may face challenges obtaining precision constraints on the reaction rate.

Resonance regions can also be identified by checking when the width of a chemical stratification region is equal to an integer number of radial wavelengths, $\lambda_r = 2\pi/k_r$ where the wavenumber is

$$k_r^2 = \frac{\ell(\ell+1)}{r^2 f^2 S_\ell^2} (f^2 - N^2)(f^2 - S_l^2) \quad (3.5)$$

and S_ℓ is the Lamb frequency. Figure 3.7 shows integer multiples q of λ_r for the g_5 and g_{10} modes versus radius for σ_0 . When $q \cdot \lambda_r$ is near a black segment, the g-mode resonates, or nearly resonates, with the region's width. The $2 \cdot \lambda_r$ curve for g_5 lies close to the width of R2, identifying R2 as the resonant cavity for the g_5 mode. For the g_{10} mode the $4 \cdot \lambda_r$ curve is close to the widths of R1 and R2. We also verified $6 \cdot \lambda_r$ is close to the width of R3. Larger q values for g_{10} may resonate with R4. As g_{10} resonates

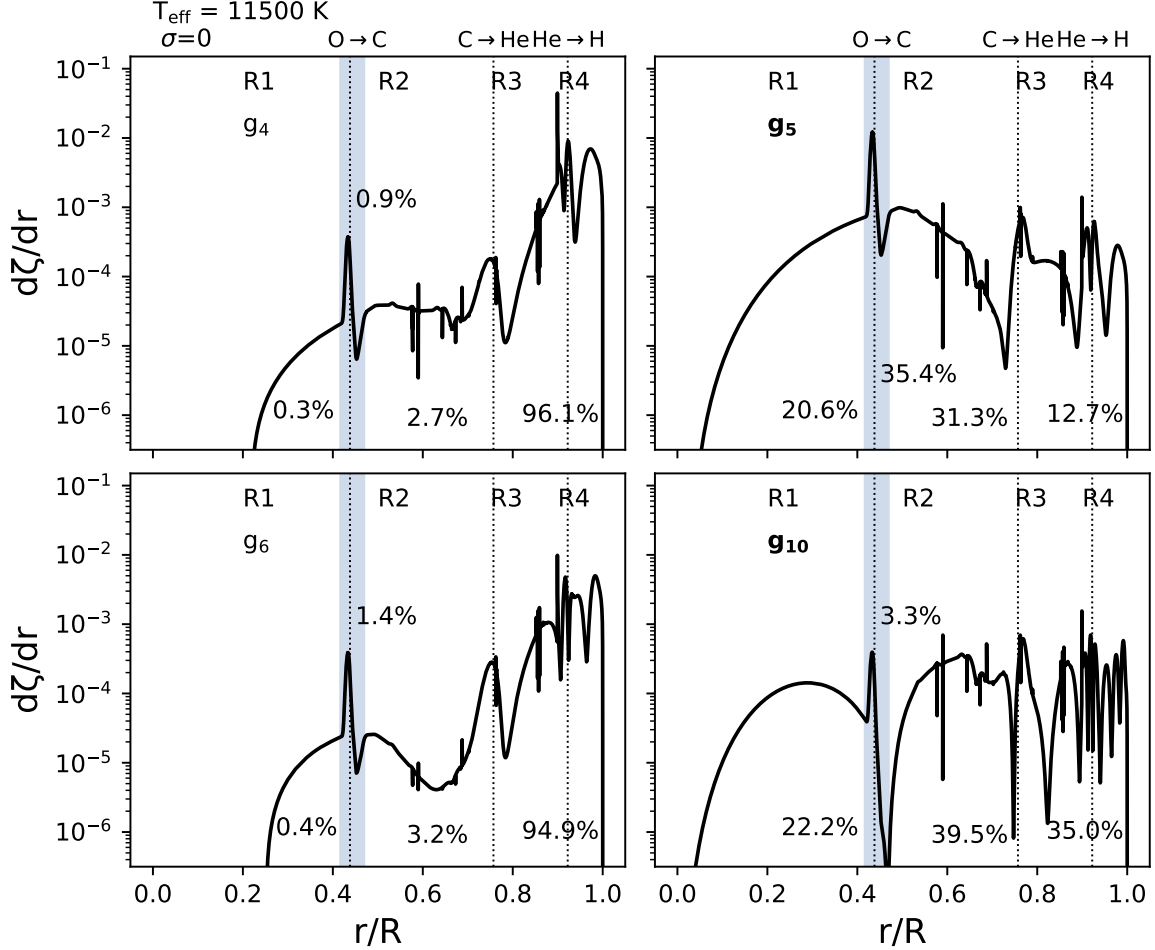


Figure 3.6: Weight functions of the g_4 , g_5 , g_6 , and g_{10} modes for the $\sigma=0$ model after it cools to $T_{\text{eff}} = 11,500 \text{ K}$. Trapped modes are in bold font. Weight functions returned by GYRE are normalized to have unit area under their curve. The fractional area under the curve of region R1, the O→C transition, region R2, and the sum of R3 and R4 are given.

with multiple regions, the mode is not uniquely trapped. This is commensurate with the more uniform distribution of peaks in the g_{10} weight function of Figure 3.6.

Figure 3.8 shows the history of the relative period differences for g_5 , g_6 , and g_{10} as the evolutionary DAVs cool. The g_5 trapped mode shows the most distinctive trend in the period with σ_i out of every g-mode in the range $1 \leq n \leq 20$. The relative period differences span $\simeq \pm 2\%$, with positive σ_i yielding shorter periods and negative σ_i yielding longer periods. The g_{10} trapped mode is not as distinctive, showing a

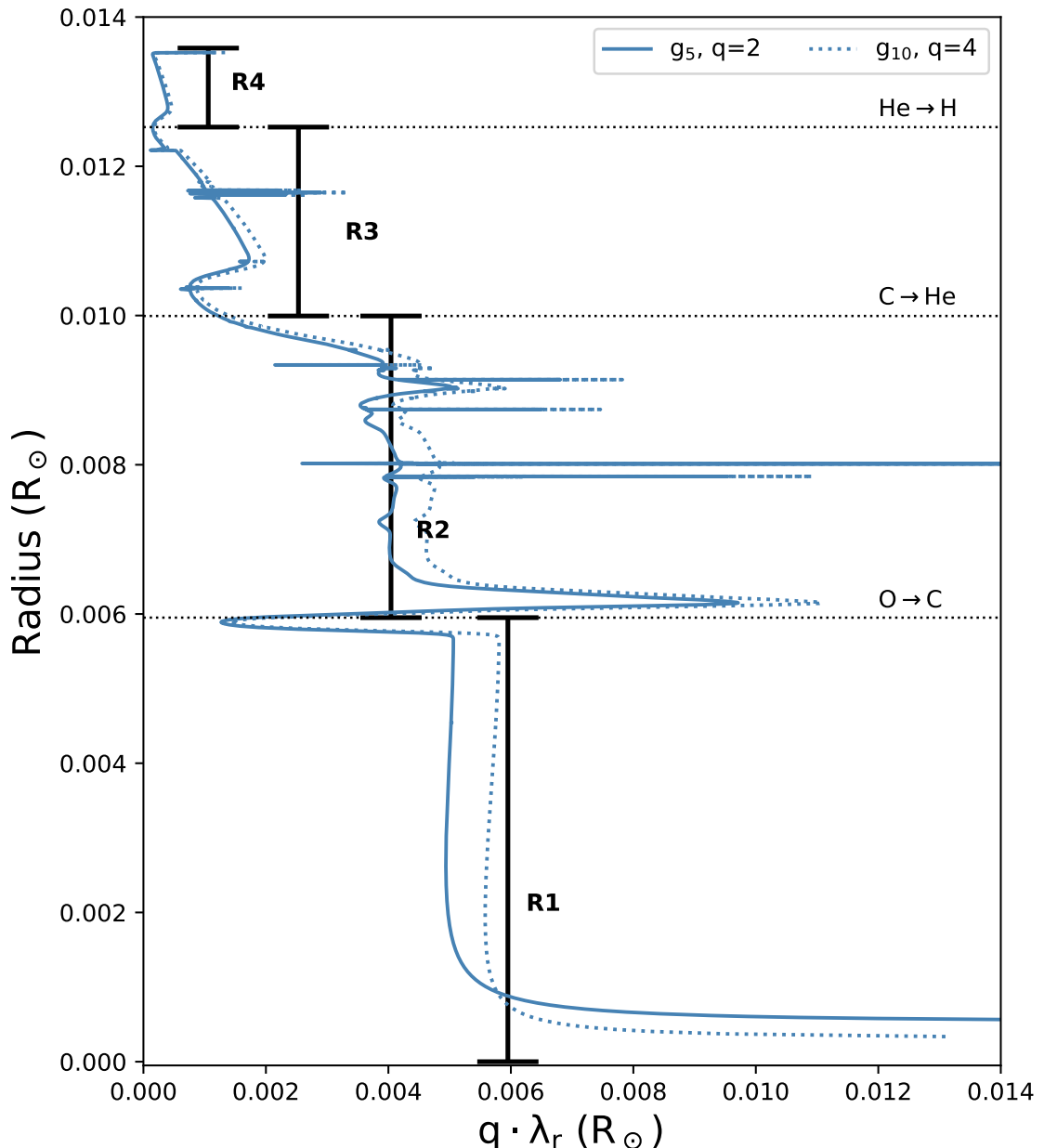


Figure 3.7: Integer multiples q of the radial wavelength λ_r profiles versus radius for the g_5 , and g_{10} modes, for σ_0 . The trapped g_5 mode is shown by the dark blue solid line, and the dotted curves depict the trapped g_{10} mode. Solid black segments depict the width of the regions R1, R2, R3, and R4, as defined by distance between labeled chemical transitions.

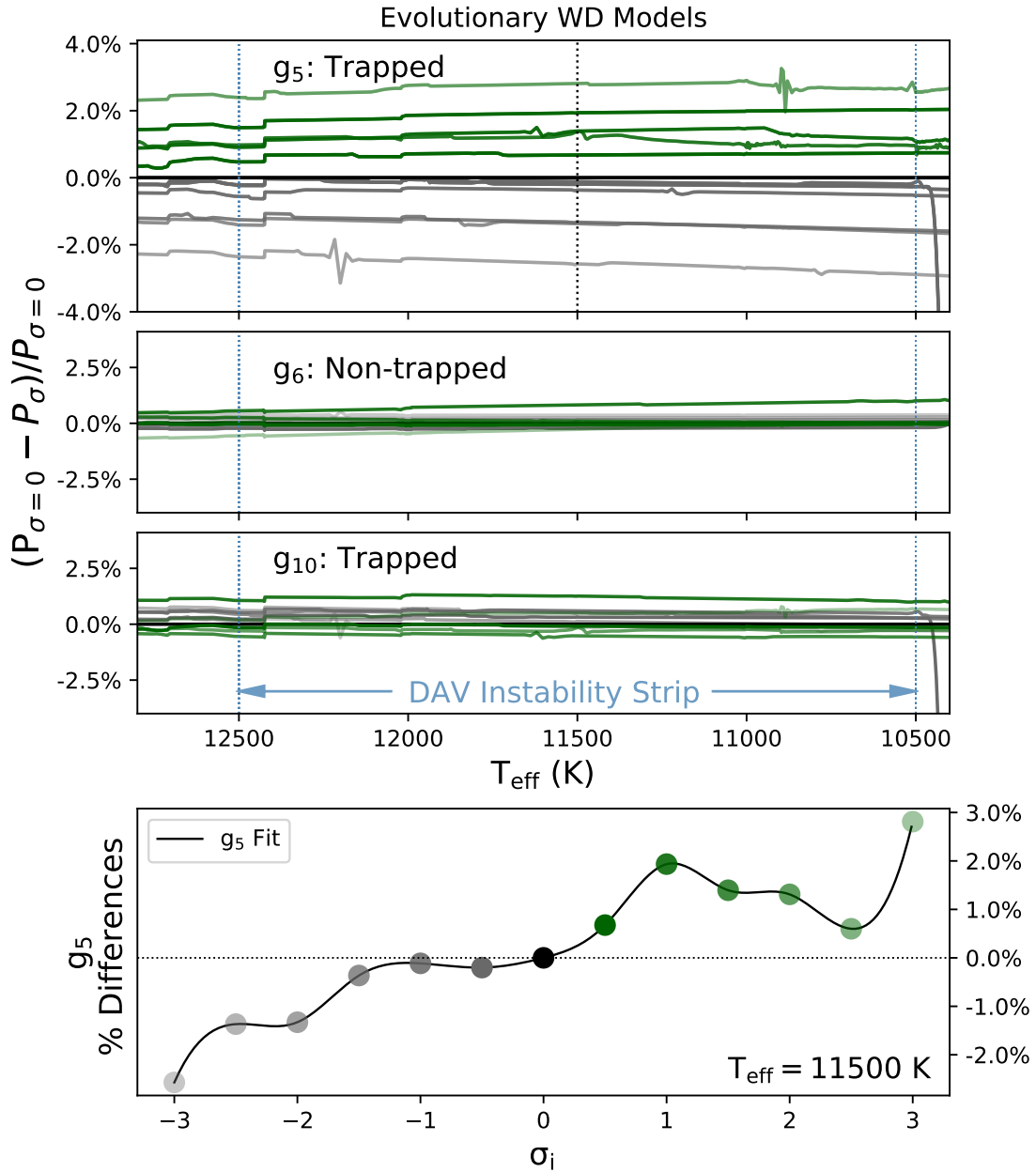


Figure 3.8: Top panels: Relative period differences from $\sigma = 0$ for the g_5 , g_6 , and g_{10} modes as the evolutionary DAVs cool. Colors for the σ_i follow Figure 3.1. The range of T_{eff} in observed DAV WDs is marked, with the vertical dashed black line selecting the $T_{\text{eff}} = 11,500$ K midpoint. Bottom panel: Relative period differences for g_5 versus the $^{12}\text{C}(\alpha,\gamma)^{16}\text{O}$ reaction rate uncertainties σ_i at $T_{\text{eff}} = 11,500$ K. Scatter points are the raw data values and the curve is a polynomial fit.

smaller spread in periods with σ_i . The g_6 non-trapped mode shows little spread with σ_i and no distinctive trend with period. While Figure 3.8 highlights g_6 and g_{10} , we emphasize that no other g-mode within $1 \leq n \leq 20$ shows any distinctive period pattern with σ_i .

Figure 3.8 also shows the relative period differences for g_5 with respect to σ_i at $T_{\text{eff}} = 11,500$ K. The relative period differences increase from $\simeq -2.0\%$ for $\sigma = -3.0$ to $\simeq 3.0\%$ for $\sigma = 3.0$. The relationship is non-monotonic due to variations in the location of the C \rightarrow He transition, which impacts the width of R2 where the g_5 trapped mode resonates. Minimizing variations in this location may increase the monotonicity of this relationship.

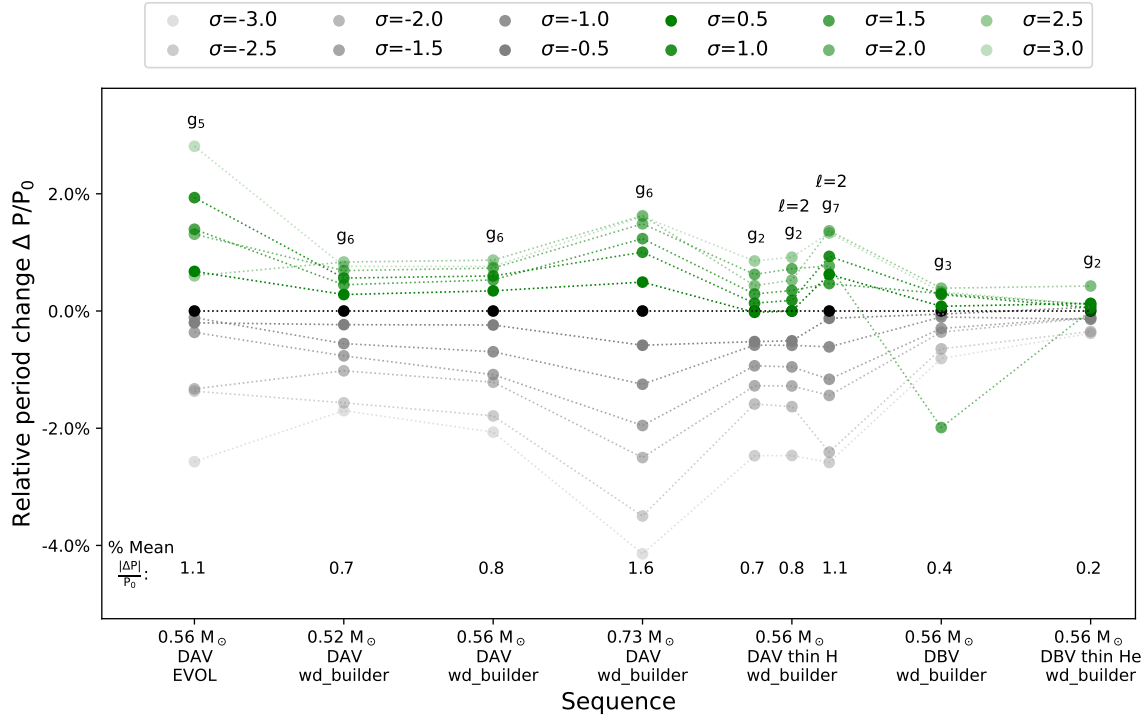


Figure 3.9: Relative period differences for model sequences of varying WD masses, shell masses, and classes. The `wd_builder` DAVs were measured at $T_{\text{eff}} = 11,500$ K for the `wd_builder` DBVs were measured at $T_{\text{eff}} = 25,000$ K. Labeled are the $\pm 3\sigma$ uncertainties on the experimental $^{12}\text{C}(\alpha, \gamma)^{16}\text{O}$ reaction rate in steps of 0.5σ , the trapped g-mode that most distinctly probes the radiatively-formed, carbon-rich region R2, and the mean relative period difference for each sequence.

3.4.2 Variations

We have presented evidence that adiabatic g-modes trapped by the radiatively formed carbon-rich layer in CO WD models offer potentially useful probes of the current experimental $^{12}\text{C}(\alpha, \gamma)^{16}\text{O}$ reaction rate probability distribution function. In this section we give a preliminary assessment of the robustness of this result by sampling different WD classes, masses, and shell masses. Each sequence contains 13 σ_i models. For each sequence, we verify the existence of a trapped or partially trapped mode that probes region R2 as indicated by the sequences's kinetic energy diagram and weight functions. We also confirm that the sequences's R2 trapped g-mode gives the most distinct $\Delta P/P_0$ versus σ_i relationship.

Figure 3.9 shows the results of this survey. The x-axis is the sequence and the y-axis is relative period difference $\Delta P/P_0$ for the labeled R2 trapped g-mode. Proceeding from left to right, the first sequence is the evolutionary DAVs which are analyzed in detail above.

The next three sequences explore the impact of the WD mass using `wd_builder` DAV models of 0.52, 0.56, and $0.73 M_\odot$, respectively. All three sequences show g_6 is the most distinctive adiabatic trapped g-mode that probes R2. The differences between the $0.56 M_\odot$ evolutionary DAVs and the $0.56 M_\odot$ `wd_builder` DAVs is due to their different composition profiles (see Section 3.3). This suggests that the most distinctive trapped g-mode depends on model details. The 0.52 and $0.56 M_\odot$ sequences are similar to one another, span a smaller $\Delta P/P_0 \simeq {}^{+1\%}_{-2\%}$ range than the evolutionary DAVs, and show non-monotonic spacings with σ_i . The $0.73 M_\odot$ sequence spans $\Delta P/P_0 \simeq {}^{+2\%}_{-4\%}$ and shows a monotonic spacing with σ_i . This suggests that more massive WDs may give stronger signals with this method.

The fifth sequence shows the impact of a H envelope that is 10 times thinner than the $0.56 M_{\odot}$ `wd_builder` DAVs. One dipole $\ell=1$ and two quadruple $\ell=2$ trapped g-modes are shown. The g_2 trapped mode with $\ell=1$ shows a regular pattern with σ_i over the range $\Delta P/P_0 \simeq {}^{+1}_{-2.5}\%$. The g_2 trapped mode with $\ell=2$ is similar to its $\ell=1$ counterpart, and the g_7 trapped mode with $\ell=2$ shows a larger $\Delta P/P_0 \simeq {}^{+1.5}_{-2.5}\%$ range. This sequence suggests that harmonic degrees $\ell=1$ and/or $\ell=2$ can have R2 trapped modes that distinguish σ_i .

The next sequence shows the `wd_builder` DBVs. A regular pattern with σ_i for the g_3 trapped mode emerges, and the sequence spans $\Delta P/P_0 \simeq {}^{+0.5}_{-1}\%$. The $\sigma=2.0$ point in this sequence is an outlier that we cannot explain. The last sequence shows the impact of a He envelope that is 10 times thinner than the $0.56 M_{\odot}$ `wd_builder` DBVs. A regular pattern with σ_i persists at the $\Delta P/P_0 \simeq {}^{+0.5}_{-0.5}\%$ level for the g_2 trapped mode.

For all the sequences, the positive σ_i have shorter periods than the $\sigma=0$ model. Following Chidester *et al.* (2021), the main contributors to period differences are changes in the local pressure scale height H , mean molecular weight μ_i , temperature, density exponent χ_{ρ} , and first adiabatic index Γ_1 . Changes in these parameters compete with one another to drive the overall period difference. Models with larger mass fractions of ${}^{22}\text{Ne}$ give shorter periods due to a smaller H . As increasing the ${}^{12}\text{C}(\alpha, \gamma){}^{16}\text{O}$ increases the ${}^{16}\text{O}$ content in R2, smaller H drive shorter periods. Similar logic applies to negative σ_i models showing longer periods.

3.5 Sensitivities

There are many potential sensitivities that we have not investigated. We highlight four and the edges of R2 that they affect.

3.5.1 Width of the O→C Transition

Mode trapping by R2 may depend on the width of the O→C transition. Increasing the O→C transition width decreases the μ_i gradient, which in turn may decrease the trapping ability of R2. The width of the O→C transition in our models is relatively narrow, in agreement with the MESA models of Pepper *et al.* (2022), while the O→C transition in Córscico *et al.* (2002) is considerably wider. Córscico *et al.* (2002) also find that their adiabatic g_5 mode depends on the O→C transition and R2. However, their g_5 mode is a local maximum in their E_{kin} diagram, meaning it is not a trapped mode. With mode trapping suppressed for a wide enough O→C transition, the kinetic energy from trapped modes in R2 is released. As Equation 3.2 is weighted with the density, a non-trapped g-mode sensitive to R2 may appear as a local maximum in E_{kin} , as found by Córscico *et al.* (2002). Relative extrema in E_{kin} , not just minima, might find g-modes that probe R2 and thus also reveal inferences on σ_i . Region R2 still exists, because it forms under thick-shell radiative He-burning conditions. We caution that its trapping abilities, and thus our relative period shifts may change with the width of the O→C transition.

3.5.2 3α Reaction Rate Probability Distribution Function

The 3α process, the fusion of three ^4He nuclei into one ^{12}C nucleus, impacts the innermost and outermost edges of R2. The 3α process is followed by the subsequent α -capture reaction $^{12}\text{C}(\alpha, \gamma)^{16}\text{O}$. The final mass fractions of ^{12}C and ^{16}O , under radiative burning conditions, is determined by the competition between the 3α and $^{12}\text{C}(\alpha, \gamma)^{16}\text{O}$ reaction rates at a given temperature. The feeding of ^{12}C , driven by the 3α process, occurs early in the evolution when the mass fraction of ^{12}C is low and ^4He is high (the carbon bump at the outermost edge of R2). Oxygen production occurs

later by α -capture on the freshly produced ^{12}C (the O \rightarrow C transition at the innermost edge of R2). Current estimates of the uncertainty in the 3α reaction rate are $\simeq 30\%$ over the regions of typical astrophysical interest (Kibédi *et al.*, 2020). However, at lower temperatures ($\lesssim 0.1$ GK), the uncertainty is likely much larger, because other reaction mechanisms become significant (Suno *et al.*, 2016). Region R2 again still exists, and we again caution that the period shifts we find from the $^{12}\text{C}(\alpha, \gamma)^{16}\text{O}$ probability distribution may change when a 3α reaction rate probability distribution function is considered.

3.5.3 Mixing During Core He-Depletion

Mixing in low- and intermediate-mass stars during core He-burning is particularly challenging to model (Salaris and Cassisi, 2017; Jermyn *et al.*, 2022) and impacts the innermost edge of R2. The radiative gradient profile within a He core convection region develops a local minimum at some point during its evolution (e.g., see Figure 6 of Paxton *et al.*, 2018). With further outward propagation of the convective boundary, or the action of overshooting, the mixing of fresh He into the core can lower the radiative gradient throughout the core to such an extent that it equals the adiabatic gradient at the local minimum of the radiative gradient. When this happens, the convective region interior to the minimum becomes decoupled from the region exterior to the minimum: the convective core splits (Eggleton, 1972). In addition, even small amounts of He added to the convective core enhances the rate of energy production by the $^{12}\text{C}(\alpha, \gamma)^{16}\text{O}$ reaction. The resulting increase in the radiative gradient can lead to rapid growth in the convective He core boundary (a “breathing pulse”). The enhanced nuclear burning also increases the central ^{16}O mass fraction. A concensus on breathing pulses being physical or numerical has not yet been reached (Caputo *et al.*, 1989; Cassisi *et al.*, 2003; Farmer *et al.*, 2016; Constantino *et al.*, 2017; Paxton

et al., 2019). Region R2 persists, and we caution that the absolute period shifts we find may change with different treatments of core He-depletion in evolutionary models.

De Gerónimo *et al.* (2017) found that overshooting during the core He burning leaves imprints on the Brunt-Väisälä frequency that result in absolute period differences of $\simeq 2\text{--}5$ s on average, relative to models with zero overshooting. Models that included overshooting had a larger central ^{16}O mass fraction and an extended R1. They found that these results are, on average, independent of the ZAMS mass. De Gerónimo *et al.* (2017) concluded their $^{12}\text{C}(\alpha, \gamma)^{16}\text{O}$ reaction rate uncertainties were less relevant than their uncertainties from overshooting. The Kunz *et al.* (2002) reaction rate adopted in De Gerónimo *et al.* (2017) is different in shape over the relevant temperature range than the deBoer *et al.* (2017) reaction rate; see Figure 29 in deBoer *et al.* (2017). A simple scaling of the Kunz *et al.* (2002) reaction rate is not the same as adopting a modern reaction rate sourced from a probability distribution function (Mehta *et al.*, 2022). We suspect the De Gerónimo *et al.* (2017) result is partially due to using a $^{12}\text{C}(\alpha, \gamma)^{16}\text{O}$ reaction rate that is $\simeq 10\%$ larger than their base reaction rate, as the highest rate considered. In contrast our $^{12}\text{C}(\alpha, \gamma)^{16}\text{O}$ rate probability distribution function spans $\simeq 0.5\text{--}1.5$ times our nominal $\sigma = 0$ reaction rate (see Figure 3.1). Therefore, we find larger overall average period differences from the $^{12}\text{C}(\alpha, \gamma)^{16}\text{O}$ reaction rate. Future uncertainty quantification studies could explore a potential coupling between simultaneous variations in overshooting and the adopted $^{12}\text{C}(\alpha, \gamma)^{16}\text{O}$ reaction rate. It is possible that a strong coupling could alter the R2 trapped mode properties of our models.

3.5.4 Number of Thermal Pulses

The thermal pulse phase of evolution impacts the outermost edge of R2. For the case of a fixed number of thermal pulses, De Gerónimo *et al.* (2017) found period differences of $\simeq 5\text{--}10$ s for their $0.548 M_{\odot}$ model and $\simeq 2\text{--}3$ s for their $0.837 M_{\odot}$ model. This effect is mainly due to the C \rightarrow He transition being less pronounced in their more massive WD models. The impact of the thermal pulses in our evolutionary models is shown in Figure 3.1. Each of our 13 σ_i models experienced $\simeq 14$ thermal pulses, with the onset of each thermal pulse defined by the photon luminosity exceeding $10^4 L_{\odot}$. In contrast, our `wd_builder` models were inferred from the chemical profiles at the first thermal pulse, fixing the number of thermal pulses for those sequences. The sensitivity of our results to the number of thermal pulses can thus be estimated by comparing the g_5 trapped mode periods of our $0.56 M_{\odot}$ evolutionary and `wd_builder` models.

We find a standard deviation of $\simeq 2.3$ for the thermal pulses and a standard deviation of $\simeq 4.5$ for the $^{12}\text{C}(\alpha, \gamma)^{16}\text{O}$. This suggests that variations from the number of thermal pulses in our models is smaller than the variations from the $^{12}\text{C}(\alpha, \gamma)^{16}\text{O}$ reaction rate probability distribution function. In contrast, De Gerónimo *et al.* (2017) found larger variations from thermal pulses than the $^{12}\text{C}(\alpha, \gamma)^{16}\text{O}$ reaction rate. We speculate this difference is again due to our larger span of $^{12}\text{C}(\alpha, \gamma)^{16}\text{O}$ reaction rates. Our $\simeq 14:1$ thermal pulse ratio is also larger than the 10:3 thermal pulse ratio of De Gerónimo *et al.* (2017), which may strengthen our result that variations from the $^{12}\text{C}(\alpha, \gamma)^{16}\text{O}$ reaction rate probability distribution function have a larger impact than the number of thermal pulses. In addition, Pepper *et al.* (2022) found the number of thermal pulses is dependent on the $^{12}\text{C}(\alpha, \gamma)^{16}\text{O}$ reaction rate, which Figure 3.1 confirms. Also in agreement with Pepper *et al.* (2022), we find that smaller

σ_i increases the number of thermal pulses as smaller reaction rates have larger He-shell masses at the onset of each pulse.

3.6 Summary

We conducted a new search for signatures of the current experimental $^{12}\text{C}(\alpha, \gamma)^{16}\text{O}$ reaction rate probability distribution function in the pulsation periods of CO WD models. We found that adiabatic g-modes trapped or partially trapped by the interior C-rich layer (region R2 in Figure 3.1) offer the most direct probe of this reaction rate because this region forms under radiative He burning conditions, mitigating the impact of uncertainties from convective mixing processes. We found an average spread in relative period shifts of $\Delta P/P \simeq \pm 2\%$ for the identified trapped g-modes over the experimental $\pm 3\sigma$ probability distribution function of the $^{12}\text{C}(\alpha, \gamma)^{16}\text{O}$ reaction rate. We found the effect persists across the observed T_{eff} window of DAV and DBV WDs, and for different WD masses and smaller H/He shell masses. Figures 3.1, 3.8, and 3.9 make the first direct quantitative connection between the pulsation periods of variable WD models and the current, experimental $^{12}\text{C}(\alpha, \gamma)^{16}\text{O}$ reaction rate probability distribution function.

The C-rich layer is a “sweet spot” in DAV and DBV WD models for probing the $^{12}\text{C}(\alpha, \gamma)^{16}\text{O}$ reaction rate probability distribution function. Figure 3.9 suggests a corresponding “sweet spot” of g-modes with radial orders $2 \lesssim n \lesssim 7$ can investigate R2. This suggestion is complemented by an analysis from Córscico *et al.* (2002), who found that all g-mode periods $\gtrsim 500$ –600 s were trapped (or nearly trapped) in the H-rich envelope. They found the weight functions of those modes were low in amplitude, and similar to one another, and concluded that mode trapping vanishes for long periods (higher radial orders). Thus, inferences from trapped modes such

as R2 are limited to g-modes with periods $\lesssim 500\text{--}600$ s. This confines our models to have g-modes $n \lesssim 10$.

In every model sequence explored, the g-mode that best distinguishes the $^{12}\text{C}(\alpha, \gamma)^{16}\text{O}$ reaction rate follows five specific patterns:

1. The g-mode is trapped, as confirmed by its local minimum in E_{kin} .
2. The g-mode best resonates with the R2 region; it has a $q \cdot \lambda_r$ matching best with the R2 region width, and gives a weight function substantially weighted in the R2 region.
3. The g-mode is within a radial order “sweet spot” of $2 \lesssim n \lesssim 7$.
4. The g-mode period is shorter for positive σ_i , and longer for negative σ_i .
5. The g-mode shifts are within the detectable range.

The signatures persist because R2 forms under radiative helium burning conditions, but could be sensitive to the couplings with other uncertainties (see Section 3.5). Out of the entire g-mode spectrum, only one, the R2 trapped g-mode, consistently showed an identifiable trace to the $^{12}\text{C}(\alpha, \gamma)^{16}\text{O}$ reaction rate probability distribution function. Moreover, the R2 trapped mode consistently followed the 5 patterns listed above, irrespective of model type, WD class, WD mass, and envelope thickness. Thus, the trapped R2 g-mode signature found is the most direct information at tracing the $^{12}\text{C}(\alpha, \gamma)^{16}\text{O}$ reaction rate probability distribution function using WD seismology.

The g-mode periods of observed variable WD are derived from a Fourier analysis of the photometric light curves and are typically given to 6–7 significant figures of precision (e.g., Duan *et al.*, 2021). Usually WD composition profile templates are

fit to the extracted g-mode period spectrum and other observed constraints (e.g., T_{eff} , $\log g$) of a specific WD. The root-mean-square residuals to the $\simeq 150$ –400 s low-order g-mode periods are typically in the range $\sigma_{\text{rms}} \lesssim 0.3$ s (e.g., Bischoff-Kim *et al.*, 2014b), for a fit precision of $\sigma_{\text{rms}}/P \lesssim 0.3\%$. Lower root-mean-square residuals using ab initio WD models are possible (Charpinet *et al.*, 2019; Giannicchele *et al.*, 2022), although see De Gerónimo *et al.* (2019).

Our finding of relative period shifts of $\Delta P/P \simeq \pm 2.0\%$ suggests that an astrophysical constraint on the $^{12}\text{C}(\alpha, \gamma)^{16}\text{O}$ reaction rate probability distribution function could, in principle, be extractable from the derived period spectrum of observed variable WD. Our results can inform future inferences, including those from machine-learning (e.g., Bellinger *et al.*, 2016), on the interior mass fraction profiles and the reaction rates that produce those chemical profiles.

ACKNOWLEDGEMENTS

We thank James Deboer for sharing the $^{12}\text{C}(\alpha, \gamma)^{16}\text{O}$ probability distribution function, Josiah Schwab for sharing `wd_builder`, and Pablo Marchant for sharing `mkipp`. This research is supported by NASA under the Astrophysics Theory Program grant NNH21ZDA001N-ATP, by the NSF under grant PHY-1430152 for the “Joint Institute for Nuclear Astrophysics - Center for the Evolution of the Elements”, and by the NSF under the Software Infrastructure for Sustained Innovation grants ACI-1663684, ACI-1663688, and ACI-1663696 for the MESA Project. This research made extensive use of the SAO/NASA Astrophysics Data System (ADS).

Software: MESA (Paxton *et al.*, 2011, 2013, 2015, 2018, 2019, <https://docs.mesastar.org/>), MESASDK 20190830 (Townsend, 2019a,b), `wd_builder` https://github.com/jschwab/wd_builder, GYRE (Townsend and Teitler, 2013; Townsend

et al., 2018, <https://github.com/rhdtownsend/gyre>), `mkipp` <https://github.com/orlox/mkipp>, `matplotlib` (Hunter, 2007), and `NumPy` (van der Walt *et al.*, 2011).

Chapter 4

HOW OVERSHOOTING IMPACTS WD PULSATION SIGNATURES OF $^{12}\text{C}(\alpha, \gamma)^{16}\text{O}$

This is the content from the submitted work of Morgan T. Chidester et al 2023 to the ApJ.

4.1 Abstract

We consider the combined effects that overshooting and the $^{12}\text{C}(\alpha, \gamma)^{16}\text{O}$ reaction rate has on variable white dwarf stellar models. We find that carbon-oxygen white dwarf models continue to yield pulsation signatures of the current experimental $^{12}\text{C}(\alpha, \gamma)^{16}\text{O}$ reaction rate probability distribution function when overshooting is included in the evolution. These signatures hold because the resonating mantle region, encompassing $\simeq 0.2 M_{\odot}$ in a typical $\simeq 0.6 M_{\odot}$ white dwarf model, still undergoes radiative helium burning during the evolution to a white dwarf. Our specific models show two potential low-order adiabatic g-modes, g_2 and g_6 , that signalize the $^{12}\text{C}(\alpha, \gamma)^{16}\text{O}$ reaction rate probability distribution function. Both g-mode signatures induce average relative period shifts of $\Delta P/P = 0.44\%$ and $\Delta P/P = 1.33\%$ for g_2 and g_6 respectively. We find that g_6 is a trapped mode, and the g_2 period signature is inversely proportional to the $^{12}\text{C}(\alpha, \gamma)^{16}\text{O}$ reaction rate. The g_6 period signature generally separates the slower and faster reaction rates, and has a maximum relative period shift of $\Delta P/P = 3.45\%$. We conclude that low-order g-mode periods from carbon-oxygen white dwarfs may still serve as viable probes for the $^{12}\text{C}(\alpha, \gamma)^{16}\text{O}$ reaction rate probability distribution function when overshooting is included in the evolution.

4.2 Introduction

Helium burning is primarily the fusion of helium into carbon by the triple-alpha (3α) process. All stars born with more than $\simeq 0.5 M_\odot$ go through this stage of energy production as they evolve beyond the main-sequence (e.g., Hansen *et al.*, 2004). Helium burning also plays a key role in transients such as Type I X-ray bursts (Weinberg *et al.*, 2006; Guichandut and Cumming, 2023), Type Ia supernovae (Shen *et al.*, 2018; Collins *et al.*, 2022), and He-rich subdwarf O stars (Werner *et al.*, 2022; Miller Bertolami *et al.*, 2022). Helium burning also impacts several classes of distribution functions, such as the black hole mass distribution function (Fryer and Kalogera, 2001; Sukhbold *et al.*, 2018; Sajadian and Sahu, 2023) including any mass gaps based on the pair-instability mechanism in the evolution of massive stars (Fowler and Hoyle, 1964; Woosley *et al.*, 2002; Farmer *et al.*, 2019, 2020; Renzo *et al.*, 2020; Marchant and Moriya, 2020; Farag *et al.*, 2022).

He burning is triggered by the 3α process releasing 7.5 MeV in fusion energy and producing ^{12}C (Hoyle, 1954; Eriksen *et al.*, 2020; Kibédi *et al.*, 2020; Cook *et al.*, 2021). This is a unique process, setting stringent conditions for helium ignition. The 3α process is followed by the α capture reaction $^{12}\text{C}(\alpha, \gamma)^{16}\text{O}$, converting the ^{12}C into ^{16}O (deBoer *et al.*, 2017; Mehta *et al.*, 2022; Shen *et al.*, 2023). These two isotopes are the principal products of He burning. In addition, nearly all of a star's initial CNO abundances in the stellar interior are converted to ^{22}Ne at the onset of He burning (Timmes *et al.*, 2003; Howell *et al.*, 2009; Bravo *et al.*, 2010; Blondin *et al.*, 2022; Meng *et al.*, 2023). This marks the first time in a star's life where the core becomes neutron rich. We follow the convention that ^{22}Ne is the “metallicity” of a carbon-oxygen (CO) white dwarf (WD).

The interiors of CO WDs are, in principle, the best probe of the ashes of He burning. A goal of WD seismology is to characterize the chemical profiles of principal products of He burning (Metcalfe *et al.*, 2001, 2002; Fontaine and Brassard, 2002; Straniero *et al.*, 2003; Metcalfe, 2003; Giammichele *et al.*, 2017b; De Gerónimo *et al.*, 2017; Giammichele *et al.*, 2018; De Gerónimo *et al.*, 2019; Córscico *et al.*, 2019; Pepper *et al.*, 2022; Giammichele *et al.*, 2022; Córscico *et al.*, 2022; Romero *et al.*, 2023) and the chemical profile of the trace ^{22}Ne metallicity (Camisassa *et al.*, 2016; Giammichele *et al.*, 2018; Chidester *et al.*, 2021; Althaus and Córscico, 2022).

Furthermore, regions within a CO WD model that burn helium radiatively during its prior evolution can offer potential constraints on the He burning nuclear reaction rates. For example, Chidester *et al.* (2022, hereafter C22) found that certain trapped adiabatic g-modes in WD models may provide a pulsation signature that constrains the experimental $^{12}\text{C}(\alpha, \gamma)^{16}\text{O}$ reaction rate probability distribution function. These signature g-modes were shown to resonate with the region of the CO WD model that underwent radiative He burning during its previous evolution. The innermost boundary of this resonant cavity corresponds to the molecular weight gradient at O→C chemical transition, and the outermost boundary to the molecular weight C→He chemical transition. The resonating region encompasses $\simeq 0.2 \text{ M}_\odot$ of a typical $\simeq 0.6 \text{ M}_\odot$ WD model. C22 cautioned that the chemical structure and resulting pulsation spectrum is sensitive to the width of the O→C transition (Córscico *et al.*, 2002; Salaris and Cassisi, 2017; Pepper *et al.*, 2022), the experimental 3α reaction rate probability distribution functions (deBoer *et al.*, 2017; Kibédi *et al.*, 2020; Schatz *et al.*, 2022), convective boundary mixing processes during core He depletion (Salaris and Cassisi, 2017; Anders *et al.*, 2022), and the number of thermal pulses during the Asymptotic Giant Branch (AGB) phase of evolution (De Gerónimo *et al.*, 2017; Pepper *et al.*, 2022).

Modeling convective boundary mixing processes at the convective-radiative interface during core He burning in low- and intermediate-mass stellar models is currently uncertain (Herwig, 2000; Salaris and Cassisi, 2017; Jermyn *et al.*, 2022; Anders *et al.*, 2022; Blouin *et al.*, 2023). Convective overshoot occurs because the convective boundary is not the location where convective velocities are zero, but the location where the buoyant acceleration of the fluid is zero. An order-of-magnitude expression $\Delta x = u\Delta t$ provides an estimate for how far convective motions overshoot (Anders *et al.*, 2022). Here Δx is the overshoot distance, u is the convective velocity, and $\Delta t \simeq 1/N$ where N is the Brunt-Väisälä frequency in the stable region. There is disagreement on how to calculate Δx , but this estimate broadly shows $\Delta x \ll H_P$ in stellar environments, where H_P is the pressure scale height. The exponential overshoot parameterization (e.g., Herwig, 2000) is frequently implemented in 1D models to describe this convective boundary mixing process, treating Δx as a free parameter. The values of Δx needed to match the gravity modes found in Slowly Pulsating B-type stars (Pedersen *et al.*, 2021) suggest $\Delta x/H_P \simeq 0.1$, which is larger than 3D hydrodynamical simulations of low Mach number flows at stable interfaces indicate (Korre *et al.*, 2019; Blouin *et al.*, 2023).

The injection of fresh He into the convective core enhances the rate of energy production by the $^{12}\text{C}(\alpha, \gamma)^{16}\text{O}$ reaction rate, increases the central ^{16}O mass fraction De Gerónimo *et al.* (e.g., 2017), and modifies the lifetime through this phase of evolution. The resulting increase in the radiative gradient can also lead to rapid growth in the convective He core boundary (a “breathing pulse”). A consensus on breathing pulses being physical or numerical has not yet been reached (Caputo *et al.*, 1989; Cassisi *et al.*, 2003; Farmer *et al.*, 2016; Constantino *et al.*, 2017; Paxton *et al.*, 2019).

C22 found a pulsation signature of the $^{12}\text{C}(\alpha, \gamma)^{16}\text{O}$ reaction rate probability distribution function using evolutionary models that purposely excluded overshooting. This article is novel in analyzing whether or not pulsation signals of the $^{12}\text{C}(\alpha, \gamma)^{16}\text{O}$ reaction rate probability distribution function still exist when overshooting at the inner convective-radiative interface during core He burning (CHeB) is included in the models' evolution history. Here, the inner convective-radiative interface is the transition from the convective core to the exterior radiative layer. Section 4.3 describes our models, §4.4 analyzes our models, §4.5 discusses our results, and we summarize our findings in §4.6. Appendix C lists the microphysics used, and Appendix C discusses variations with the number of isotopes in the reaction network and with the temporal resolution of our models.

4.3 Stellar Evolutionary Models

We define the term “model” to mean an evolutionary sequence that begins at the pre-main sequence, progresses through CHeB, and terminates as a cold WD. We define the term “snapshot” to mean a specific instance in time or phase of evolution within a model, and the term “set” to mean a suite of models or snapshots that have identical input physics except for the value of the $^{12}\text{C}(\alpha, \gamma)^{16}\text{O}$ reaction rate.

We use MESA version r15140 (Paxton *et al.*, 2011, 2013, 2015, 2018, 2019; Jermyn *et al.*, 2023) to build $2.1\,\text{M}_\odot$, $Z = 0.0151$ metallicity, $Y = 0.266$ He mass fraction, nonrotating models at the pre-main sequence. We adopt the AGSS09 (Asplund *et al.*, 2009) abundances and use a 23 isotope nuclear reaction network with ^{22}Ne being the heaviest isotope¹. Our models employ MESA’s Henyey mixing-length theory (MLT) of convection option, with an MLT parameter of $\alpha = 1.5$. We are not advocating that this is the best or correct value to use. Rather, we are using a representative value

¹A comparison to a 30 isotope network is given in Appendix C

that is also consistent with the value used in C22. We use the Ledoux criterion, and the predictive mixing scheme. Additional details of the MESA microphysics are listed in Appendix C.

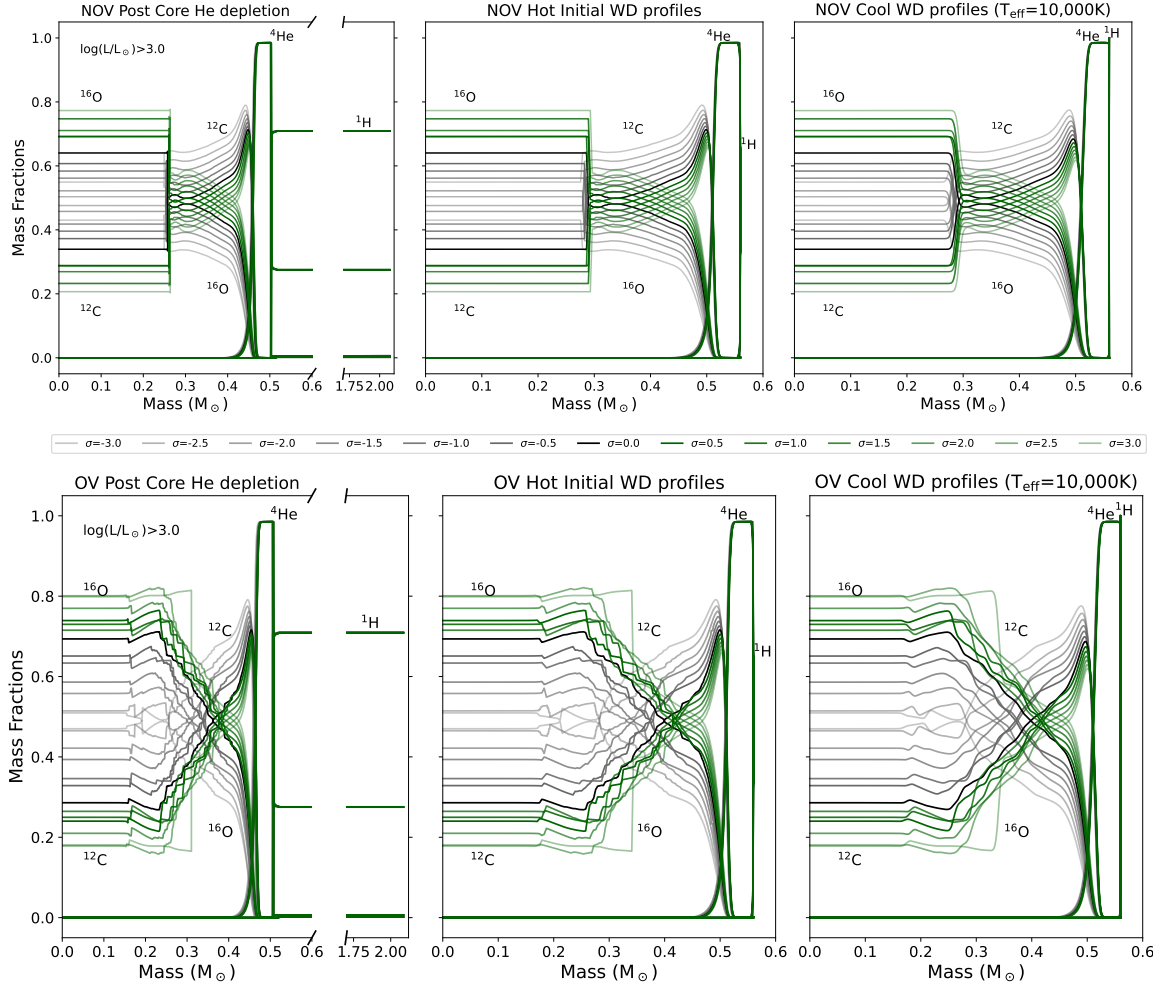


Figure 4.1: Top: Mass fraction profiles without overshooting (NOV) during the CHeB phase. Left: Mass fraction profiles after core He-depletion, terminated prior to the first thermal pulse at $\log(L/L_{\odot}) > 3.0$. Middle: Mass Fraction profiles at the first `wd_builder` model step. These profiles have been shaved of their excess H envelope prior to running on the WD cooling track. These are the initial hot WD profiles. Right: Mass fraction profiles when the models have cooled to $T_{\text{eff}} = 10,000 \text{ K}$. The smoothness in the profiles reflects the element diffusion processes included in the calculation. Bottom: Mass fraction profiles with core overshooting (OV) during the CHeB phase, in the same format as above. Green curves represent positive σ_i $^{12}\text{C}(\alpha, \gamma)^{16}\text{O}$ reaction rates, grey curves represent negative σ_i $^{12}\text{C}(\alpha, \gamma)^{16}\text{O}$ reaction rates. For both positive and negative σ_i , the shading grows fainter the further σ is from the standard rate ($\sigma = 0$; black curve).

As in C22, we span the current experimental $^{12}\text{C}(\alpha, \gamma)^{16}\text{O}$ reaction rate probability distribution function (deBoer *et al.*, 2017; Mehta *et al.*, 2022) from $\sigma = -3.0$ to $\sigma = +3.0$ in 0.5σ steps, totaling to $13 \sigma_i$ reaction rates; each model is prescribed one such σ_i $^{12}\text{C}(\alpha, \gamma)^{16}\text{O}$ reaction rate value for its evolution. We calculate one set of models without overshooting (NOV), and a second set with overshooting (OV) at the inner radiative-convective interface during the CHeB phase. Hence, each evolutionary model differs only in its σ_i $^{12}\text{C}(\alpha, \gamma)^{16}\text{O}$ reaction rate, and NOV or OV mixing prescription. This yields 26 individual stellar evolutionary models; 13 for the NOV set and 13 for the OV set. For $i = (-3.0, -2.5, \dots, +2.5, +3.0)$, we use σ_i and $\sigma = i$ interchangeably to reference a given σ from the $^{12}\text{C}(\alpha, \gamma)^{16}\text{O}$ reaction rate probability distribution function.

After CHeB, the models evolve until $\log(L/L_\odot) = 3.0$, prior to the first thermal pulse on the AGB. At this snapshot, we interrupt the evolution of each model. All models at this snapshot thus have a C \rightarrow He transition at nearly the same mass location. We use this snapshot to construct H-dominated atmosphere (DA) WDs by removing the H envelopes until $\log(M_H/M_*) < -3.5$. The resulting composition profile structures are used to build $0.56 M_\odot$ ab-initio WD models with `wd_builder`, as done in C22. These WD models evolve until $T_{\text{eff}} = 10,000$ K. We discuss the reasoning for constructing the WDs from the post-CHeB $\log(L/L_\odot) = 3.0$ snapshot in the following section.

We utilized version 6.0.1 of the `GYRE` code (Townsend and Teitler, 2013; Townsend *et al.*, 2018) to compute the adiabatic pulsations of our WD models throughout their respective cooling tracks (from $\sim 50,000$ K to $10,000$ K). The inlist parameters were set to search for modes of harmonic degrees $\ell = 1, 2$ and radial orders $n \leq 25$, where our models were assumed to be non-rotating, hence only $m = 0$ azimuthal orders were present. For the adiabatic mode analysis, we employed the fourth-order

Gauss-Legendre collocation difference equation scheme (?Townsend and Teitler, 2013; Townsend *et al.*, 2018).

Details of the MESA models and GYRE oscillation parameters are in the files to reproduce our results at doi:[<https://doi.org/10.5281/zenodo.6779983>. Next we summarize the overshooting prescription used for the OV set.

4.3.1 Core Overshooting Prescription During the CHeB

During the CHeB phase, we use the following core overshooting parameters in the MESA inlist for the OV set:

```
! overshoot
min_overshoot_q = 1d-3
overshoot_scheme(1) = 'exponential'
overshoot_zone_type(1) = 'any'
overshoot_zone_loc(1) = 'core'
overshoot_f(1) = 0.016
overshoot_f0(1) = 0.008
overshoot_mass_full_on(1) = 0.01
overshoot_mass_full_off(1) = 0.4
```

Details of the specific parameters are described in the MESA documentation ². We choose the conventional Herwig (2000) value of `overshoot_f(1)=0.016`. This parameter sets the fractional distance of H_p to overshoot at the $\nabla_{ad} = \nabla_{rad}$ interface, for the order of magnitude estimate given in the introduction, $\Delta x = f_0 \cdot H_p$.

We are not advocating that our choice for the value of the overshooting parameter (or even the underlying exponential overshooting model itself) is the best or correct one to use. Rather, we are using a representative value to assess whether or not

²<https://docs.mesastar.org/en/latest/>

pulsation signals of the $^{12}\text{C}(\alpha, \gamma)^{16}\text{O}$ reaction rate probability distribution functions still exist when overshooting at the inner convective-radiative interface during CHeB is included in the models' evolution history. Future uncertainty quantification studies could explore the impact of a set of overshooting values.

The trapped mode seismic signatures found in C22 were resonating most with the region that underwent radiative He burning, defined as R2. Their inner boundary of R2 is near the molecular weight gradient at the O→C transition (the “O drop”) and their outer boundary is near the C→He transition. Mode trapping is sensitive to the location of both of these boundaries because they define the width of the resonant cavity.

One approach to analyzing the sensitivity of the R2 trapped mode signatures is to fix one boundary and vary the other boundary. We fix the R2 outer boundary by excluding variations imposed from the thermal pulse history, hence the interruption at the post-CHeB $\log(L/L_\odot) = 3.0$ snapshot for all models. The phenomena that happens during the AGB phase is another source of model uncertainty. Gautschy (2023) found that early post-AGB pulsations can cause rapid growth of an instability that drives a super-wind which can shed much of the outer layers in a few years. Further, their 2.0 M_\odot , $Z=0.02$ model shows a dynamic evolutionary track, especially during the AGB, that is similar to the models in this article. Gautschy (2023) summarizes that while the preliminary results show promise on future AGB and post-AGB phenomenon, there are currently more questions than answers. We therefore leave the thermal pulse history and the particular envelope ejection phenomena on the AGB to future studies, and freeze the outermost R2 boundary before the first thermal pulse occurs. In this vein, we isolate the sensitivity of the R2 region to its inner boundary, and specifically address how core overshooting influences the pulsation signatures for the $^{12}\text{C}(\alpha, \gamma)^{16}\text{O}$ reaction rate probability distribution function.

We end this section by stating we are not advocating for a specific evolutionary model or overshooting scheme. Rather, we are exploring one approach to quantifying the coupled uncertainty between the $^{12}\text{C}(\alpha, \gamma)^{16}\text{O}$ reaction rate probability distribution function and a common overshooting model.

4.4 Results

4.4.1 Evolution of Composition Profiles

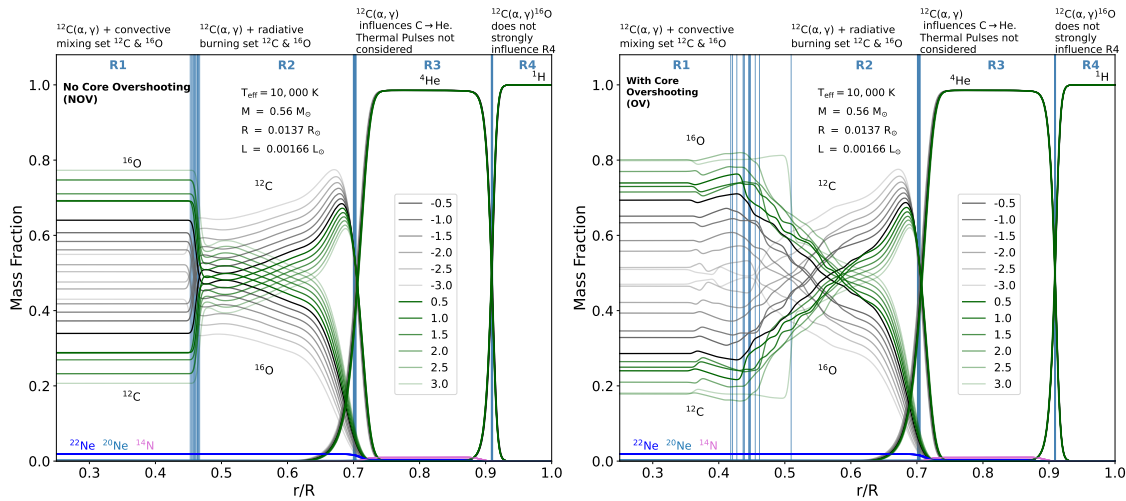


Figure 4.2: Composition profiles after the NOV (top) and OV (bottom) models cool to $T_{\text{eff}} = 10,000$ K. Region boundaries are indicated by vertical blue lines, and the σ_i colors are the same as in Figure 4.1.

Figure 4.1 shows the mass fraction profiles for both sets at three evolutionary snapshots. The top row shows the mass fraction profiles for the NOV set and the bottom row shows the mass fraction profiles for the OV set. The left most column shows the mass fraction profiles at the post-CHeB $\log(L/L_{\odot}) > 3.0$ snapshot. At this point, our models have not lost much mass and are all $\sim 2.1 M_{\odot}$. The middle column shows the mass fraction profiles after removing the H envelopes until $\log(M_H/M_*) < -3.5$. This snapshot shows the initial hot WD profiles, after completing one model step in `wd_builder`. The profiles shift slightly in mass location, but the overall composition

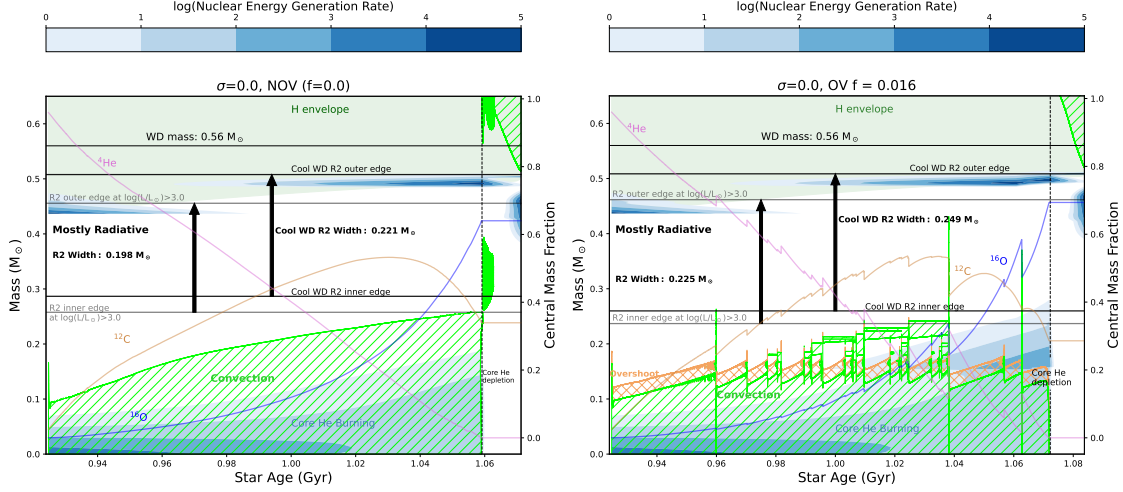


Figure 4.3: Kippenhahn diagrams for the NOV (left) and OV ($\sigma = 0.0$) models. The x-axis is the respective stellar model’s age, the left y-axis is the mass coordinate, the right y-axis is the central mass fraction of the isotopes. Bright green areas represent convection, blue shaded regions depict nuclear burning (see colorbar), white areas represent radiation, and yellow-gold areas represent overshooting (right figure). The light green area shows the hydrogen envelope. The solid pink curve is the central ${}^4\text{He}$ mass fraction, the solid dark blue curve is the central ${}^{16}\text{O}$ mass fraction, and the dark yellow curve is the central ${}^{12}\text{C}$ mass fraction. The dashed line shows core helium depletion. The evolution was terminated when $\log(L/L_\odot) > 3.0$ for all stellar models, and the figures are plotted until that point. Annotated is the radiative R2 region’s edges and widths. An interactive figure is provided in the online version. Its functionality compares the NOV and OV Kippenhahn diagrams for any given σ_i ${}^{12}\text{C}(\alpha, \gamma){}^{16}\text{O}$ reaction rate. To use the interactive figure, click on the ‘sigma’ slider at the top, and slide through the indices 0 through 12. Sliding through each index provides the user the side by side comparison of the Kippenhahn diagrams for the respective σ_i ${}^{12}\text{C}(\alpha, \gamma){}^{16}\text{O}$ reaction rate used in the evolution. Index 0 starts at $\sigma_{-3.0}$ and index 12 ends at $\sigma_{3.0}$.

structure only differs from the left panel in the thickness of the H envelope. The right column is the final snapshot of the mass fraction profiles, when the models reach $T_{\text{eff}} = 10,000$ K. Diffusion was included on the WD cooling track and leads to the smoothness of the profiles in this column.

Figure 4.2 accentuates the differences between the NOV (top) and OV (bottom) mass fraction profiles for the final WD structures (right column of Figure 4.1). Here, we show the abundance in mass fraction with respect to fractional radius r/R . We

partition the WDs' composition profiles into four regions: R1, R2, R3, and R4. This is similar to that done in C22. The regions are defined to estimate trapping (resonant) zones. Boundaries for mode trapping are typically near composition transitions because they generally have large mean molecular weight gradients. This may lead to partial reflections for a resonant mode(s), “trapping” it within the local cavity (Brassard *et al.*, 1991; Winget *et al.*, 1981). The Ledoux B profile (henceforth B) captures composition gradients and can estimate trapping regions. We use B as our primary guide to define the region boundaries for a given model. The R1-R2 boundary is set at the first local maximum in B that occurs after reaching peak ^{16}O in a given model's chemical profile. The R2-R3 boundary is set at the second local maximum in B . The R3-R4 boundary is set at the location where $\text{X}(^1\text{H}) > \text{X}(^4\text{He})$.

In both NOV and OV sets, σ_i impacts the magnitude of the ^{16}O and ^{12}C profiles in R1. Core overshooting changes the structure of these profiles, especially at $r/R \sim 0.37$ where the flatness of the profiles becomes disrupted. This is due to additional He fuel ingested during CHeB, from overshooting and/or convection. The fuel ingestion from overshooting and convection is a coupled effect and specific to each σ_i model. After $r/R \sim 0.37$, there is some overlap in the profiles that perturbs the proportional trend with σ_i .

For both sets, the first group of vertical blue lines marks the R1-R2 boundary, with each line representing a given σ_i . The NOV set shows a steep composition gradient at the R1-R2 boundary, and the R1-R2 location is nearly the same for all σ_i . There is greater variance in the R1-R2 location for the OV set. Further, core overshooting has softened the ^{16}O and ^{12}C gradients, and the disruption of the profiles' regularity with σ_i continues into the start of the R2 region. At $r/R \sim 0.6$, the proportionality of σ_i to the ^{12}C and ^{16}O profiles is restored.

By design from stopping at the first thermal pulse, the R3 and R4 regions are almost identical between the NOV and OV sets. These regions are least affected from mixing processes in the core (e.g. overshooting).

In Figures 4.1 and 4.2, the OV chemical profiles show a non-constant structure from overshooting during CHeB in the O dominated central core (below $\simeq 0.4 M_{\odot}$). While element diffusion is included during the white dwarf cooling phase, these chemical profiles may be further flattened by mixing processes not considered in this study such as time-dependent convection (Jermyn *et al.*, 2023), rotationally induced mixing, semiconvection, or thermohaline mixing.

4.4.2 Evolutionary Differences After the Main-Sequence

How do the final WD profiles for the NOV and OV sets in Figure 4.2 relate to their respective CHeB evolution histories? Figure 4.3 shows the Kippenhahn diagrams for the $\sigma = 0.0$ models for NOV (left) and OV (right). This figure shows the CHeB phase until the $\log(L/L_{\odot}) > 3.0$ termination point, spanning $\simeq 0.93$ – 1.10 Gyr. During this period the total mass of our models is $\simeq 2.1 M_{\odot}$, but we show only the innermost $\simeq 0.65 M_{\odot}$ to capture the evolution history that ultimately defines the CO WDs.

There are immediate differences between the NOV and OV CHeB evolution histories for the $\sigma = 0.0$ models. These differences are similar for any given σ_i models, and a link to an interactive figure is provided in the online journal to see each rate’s OV vs. NOV comparison in greater detail.

For the NOV set, we see gradual growth of the convective core throughout the CHeB phase; the noted central mass fraction isotopes smoothly deplete/grow to reach their final mass fractions; the convective cores have no apparent splitting during the CHeB phase. Further, there is a pure radiative zone throughout the CHeB history. In comparison, the OV set shows convective cores that ebb and flow in their extent,

in a saw-tooth like manner; overshooting extends past the inner convective core in a fairly consistent mass length; the OV central mass fraction isotopes ebb and flow symmetrically with the mixing phenomena at any given time.

We also see splittings of the convective core in the OV set. These splittings were not observed in any of the NOV models during the CHeB phase. We presume they are a result of overshoot inclusion. This introduces “pollution” to the pureness of the radiative burning zone, which becomes the R2 region of the WD. The pollution is seen by observing that some of the split-convection zone surpasses the $\log(L/L_\odot) > 3.0$ R2 inner edge boundary. This boundary becomes the inner edge of R2 in the cool WDs. The amount of convective pollution within the OV set is minor for $\sigma_{0.0}$, but varies with σ_i . Figure 4.3 qualifies R2 as “Mostly Radiative” for the NOV set due to localized, short-lived, subtle convective occurrences between $\simeq 0.30\text{--}0.35 M_\odot$ near core He depletion energetics. Composition profiles are less sensitive to mixing after CHeB is complete. Any convective pollution from these brief convective periods in the NOV set are insignificant compared to the convective pollution introduced in the OV set.

For both sets, nuclear burning primarily takes place within the convective core. Both sets also show similar burning regions in the mantle outside the core, in the radiative zone. Near the end of core He depletion, nuclear burning in the core extends past the convective and overshooting core regions in the OV set, and burns into the radiative zone. This is not seen in the NOV set.

4.4.3 WD Adiabatic Pulsation Analysis

How do these evolutionary and WD structural differences impact the WD $^{12}\text{C}(\alpha, \gamma)^{16}\text{O}$ reaction rate pulsation signatures? We first stress the importance of the NOV models’ R2 pure radiative zone during the CHeB. The trapped mode σ_i sig-

nature found in C22 resonates the most with this region. We want to determine if this signature, or any other σ_i pulsation signature, exists when overshooting is considered at the inner R2 boundary during CHeB. First we compare the NOV WD pulsation signatures in this work to those in C22.

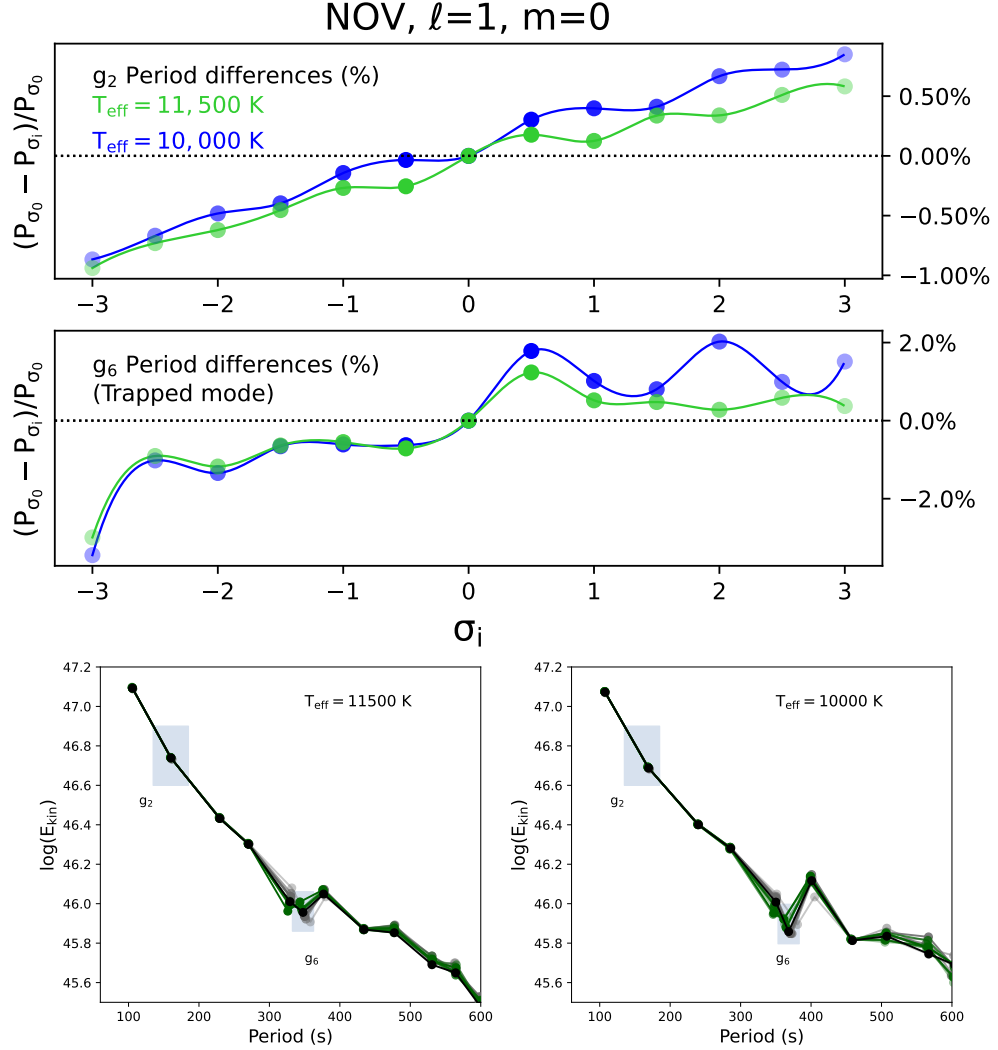


Figure 4.4: Top two: NOV set's signature adiabatic pulsation modes shown at $T_{eff} = 11,500$ (bright green), and $T_{eff} = 10,000$ K respectively. The first panel shows the signal from the g_2 mode; the second shows the signal from the g_6 trapped mode. Bottom: The kinetic energy diagrams for all σ_i at $T_{eff} = 11,500$ K (left) and $T_{eff} = 10,000$ K (right) respectively. The green dots/lines represent E_{kin} for $\sigma_i > 0$; grey for $\sigma_i < 0$; black for $\sigma = 0$. The shading of color gets fainter the further away from $\sigma = 0$.

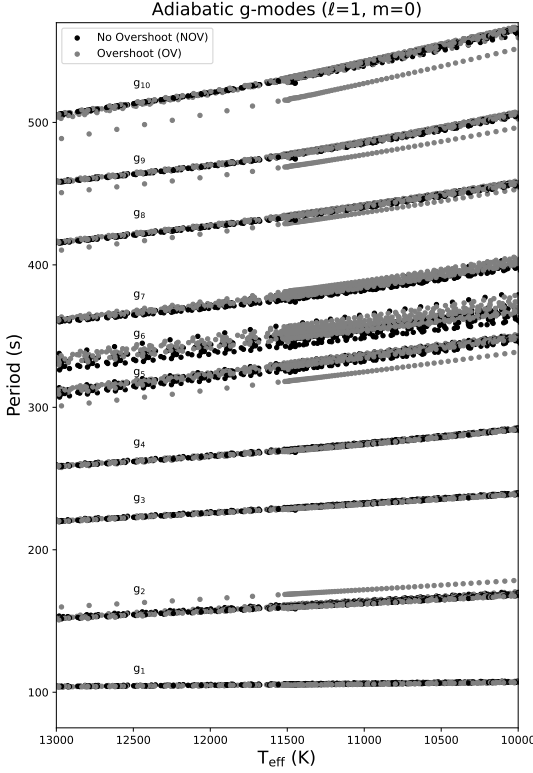


Figure 4.5: Pulsation periods as function of T_{eff} for the NOV (black) and OV (grey) model sets.

4.4.4 NOV Set vs. C22

The models in C22 are nearly the same as the NOV models in this article, but we briefly state the main differences. The models in C22 used a 30 isotope chemical network compared to the 23 isotope network used here. See Appendix C for a comparison. Also, the temporal resolution was greater in C22, especially through CHeB. The most important difference in the NOV models is that we terminated the evolution prior to the first thermal pulse; the models in C22 continued the evolution through the thermal pulse phase of evolution. The overall composition structure of the R1 and R2 regions in our NOV models are quite similar to those in C22.

The NOV set of models in this work found two WD g-mode signals for σ_i rather than one. This is shown in the top two panels of Figure 4.4. Both panels show

snapshots of the percent period differences as a function of σ_i , at $T_{\text{eff}} = \mathbf{11,500}$ K (bright green) and $T_{\text{eff}} = \mathbf{10,000}$ K (blue) respectively. The y-axis label defines the period differences as $(P_{\sigma_0} - P_{\sigma_i})/P_{\sigma_0}$. That is, they are normalized to the pulsation periods of the $\sigma = 0$ NOV model. The first panel is the signal from g_2 and the second is the signal from g_6 . In C22, the g-mode signature was a trapped mode. Trapped modes are identified from local minima in the kinetic energy diagram (Winget *et al.*, 1981; Brassard *et al.*, 1991). The NOV kinetic energy diagrams for all σ_i at these snapshots are shown in the bottom left and right panels of Figure 4.4, following Equation 2 in C22 (Unno *et al.*, 1989; Córscico *et al.*, 2002). The figure caption explains the coloring for σ_i . At $T_{\text{eff}} = 11,500$ K (bottom left panel), the first apparent trapped mode occurs at g_6 for all σ_i , with the exception of $\sigma = 0.5$, which has its first local minimum of E_{kin} at g_5 . By $T_{\text{eff}} = 10,000$ K (bottom right panel), all σ_i have the first local minimum in E_{kin} at g_6 , including $\sigma = 0.5$. This is important as g_6 is one of our signature modes for σ_i . These findings are in overall agreement with C22. The trapped g_6 mode signature is not linear with σ_i , but overall shows $\sigma_i < 0$ to have longer periods than $\sigma = 0.0$, and $\sigma_i > 0$ to have shorter periods than $\sigma = 0.0$. The R2 contribution to the g_6 period in our NOV models was $\sim 25\%$. Other regions equally contributed between $\sim 20 - 30\%$, meaning that the trapped mode from our NOV set is more equitably trapped among the four regions. Thus, its credibility from R2 isn't as strong as in C22. Nonetheless, it is not a negligible contribution and can still serve as a viable probe for σ_i .

Our other g-mode signal, g_2 , does not appear to be trapped by definition (see other highlighted mode in bottom of Figure 4.4). However, the g_2 period differences are directly proportional to σ_i (first panel of Figure 4.4). This suggests that g_2 is likely distinguishing CO features in the inner regions better than other g-modes. The additional g_2 signal was either recovered or contrived as a consequence of excluding

the thermal pulse history in the evolution. This was the only procedural difference between our models and those in C22. The direct impact of this procedural difference is expressed by the nearly uniform ^{12}C and ^4He profiles after the $\text{C} \rightarrow \text{He}$ transition (see Figure 4.1). C22 showed variations in these profiles that stemmed from variations in the thermal pulse histories. Eliminating such chemical variations near the R2-R3 interface can placate the g-modes' sensitivity to the R3 and R4 regions, especially for low-order g-modes such as g_2 . Figure 9 in C22 shows g_2 distinguishes σ_i in their thinner atmosphere sequence of models. Thinner atmospheres may also lessen sensitivities to outer regions, allowing lower-order g-modes like g_2 to probe deeper into the CO interior. We therefore suspect g_2 is a viable probe for σ_i if there are uniform composition profiles at the R2-R3 boundary, and/or thinner WD atmosphere models.

We conclude that our NOV pulsation signature results are overall consistent with C22; we find certain low-order adiabatic WD g-modes which probe the $^{12}\text{C}(\alpha, \gamma)^{16}\text{O}$ reaction rate probability distribution function. With our two signature modes established, we now discuss the impact that overshoot inclusion has on these pulsation signatures.

4.4.5 Detailed Analysis of Differences

We first show the pulsation periods as a function of surface temperature for all σ_i models in Figure 4.5. Black dots mark the NOV periods and grey dots mark the OV periods. G-modes with radial orders $n = 1 - 10$ are annotated, all for $\ell = 1$. Figure 4.5 shows that there are differences in the periods between the NOV and OV sets, but there is no global systematic offset; the differences between the OV and NOV periods for any given g-mode is random. This is the case even when σ_i is constant. We find that g_6 shows the largest spread in the periods of the models. Further, the kinetic energy diagrams for all models show that g_6 was a trapped mode by $T_{\text{eff}} = 10,000$

K for every model, regardless of the σ_i , NOV/OV prescription. Since g_6 is one of the signals for σ_i in the NOV models, we point out this feature in Figure 4.5. We will touch on the cause of the larger spread later, but now focus our attention on the detailed pulsation properties of the signature g_2 and g_6 modes.

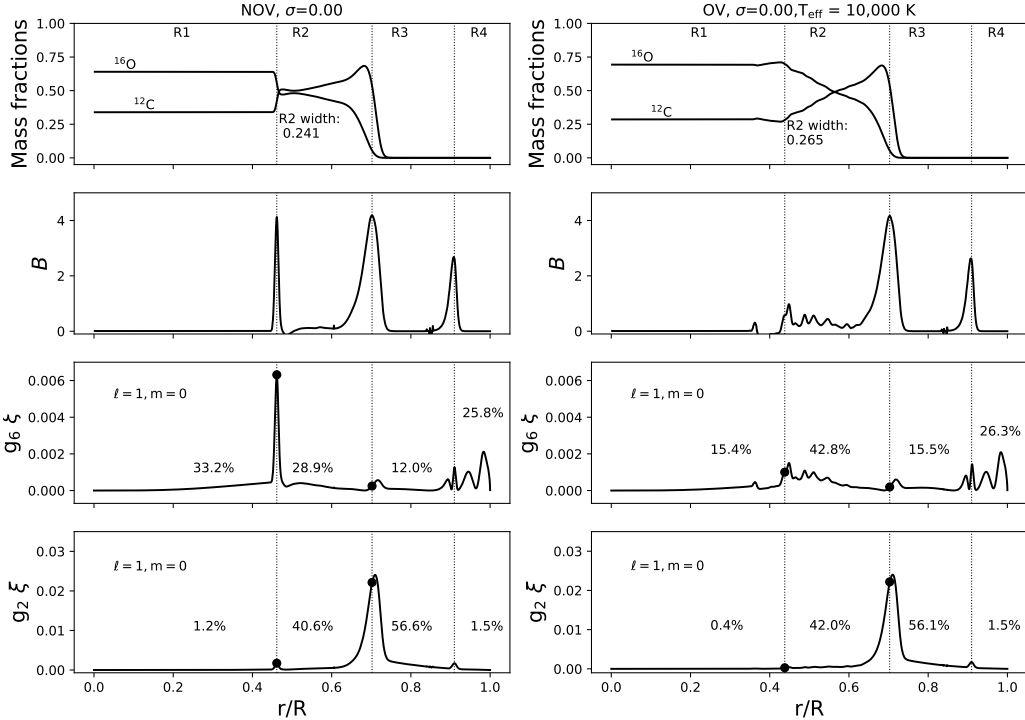


Figure 4.6: Top to bottom: Mass fractions of ^{12}C and ^{16}O ; B profile; normalized weight function profile for the g_6 mode; normalized weight function profile for the g_2 mode. The left column shows the NOV results and the right column shows the OV results. Both figures are for $\sigma = 0.0$, $T_{\text{eff}} = 10,000$ K. The R1-R4 region boundaries are indicated by dashed vertical lines. An interactive figure is provided in the online version. Its functionality compares the NOV and OV diagrams, as structured in this figure, for any given σ_i $^{12}\text{C}(\alpha, \gamma)^{16}\text{O}$ reaction rate. To use the interactive figure, click on the ‘sigma’ slider at the top, and slide through indices 0 through 12. Sliding through each index provides the user the side by side comparison of the diagrams for the respective σ_i $^{12}\text{C}(\alpha, \gamma)^{16}\text{O}$ reaction rate used in the evolution.

Index 0 starts at $\sigma_{-3.0}$ and index 12 ends at $\sigma_{3.0}$.

Figure 4.6 shows, from top to bottom, the mass fraction profiles, B , and the g_6 and g_2 mode weight functions ζ for the final WDs at $T_{\text{eff}} = 10,000$ K. The left and right

columns are the NOV and OV results respectively. Here, we show the comparison for $\sigma = 0.0$, but an interactive figure link is provided in the online article to compare these properties for any σ_i . For all σ_i , NOV/OV comparisons, the dotted vertical lines mark the region boundary locations in each panel. This is useful to compare where the boundary locations are across multiple profile properties. For instance, the R1-R2 boundary marks the C→O transition region, the first most prominent peak in B , and the first peak-like features in $g_6 \zeta$ and $g_2 \zeta$ in the NOV case. Comparing the OV column to the NOV column, we see the global impacts from overshooting. Overall, prominent features in the NOV set are lessened in magnitude in the OV set. The C→O transition is more gradual, lessening the composition gradient at the defined boundary. This remarkably impacts the shape of B . The first prominent peak after $\max(O)$ is much less in magnitude for all σ_i , and is not the only outstanding peak near the boundary. There are now multiple, smaller peaks in B and the $g_6 \zeta$ near the R1-R2 boundary as opposed to one. There are slight deviations between NOV and OV in these profiles for the R3 and R4 regions of the WD, but the R1→R2 region in these profiles was affected most.

The $g_6 \zeta$ and $g_2 \zeta$ panels in Figure 4.6 note the weight percentages per region in the WD. This tells each region's contribution to the overall mode period (frequency). An interesting result for all σ_i is that both the g_2 and g_6 modes decrease the amount of weight in R1 when overshoot is included, and increase the amount of weight in R2. There is also a slight decrease in the weight of R3 for g_2 for all σ_i when overshoot is included. These results are important. The R2 region is the most reliable region in terms of extracting the σ_i rate signature. When overshoot is included, the R2 contribution to the overall pulsation modes in g_2 and g_6 are accentuated, implying that these modes more reliably distinguish σ_i than the NOV set. A quantitative analysis of each region's weight percentage contribution per σ_i is given for both sets

Table 4.1: g_2 Weight Function Percentages Per WD Region

σ_i	R1		R2		R3		R4	
	NOV	OV	NOV	OV	NOV	OV	NOV	OV
-3.0	0.91	0.75	40.6	41.3	57.0	56.4	1.47	1.47
-2.5	1.14	0.99	40.2	44.2	57.2	52.9	1.43	1.94
-2.0	1.05	0.52	40.2	41.1	57.2	56.9	1.54	1.53
-1.5	1.18	0.53	39.5	41.7	57.9	56.2	1.50	1.50
-1.0	1.16	0.27	40.4	41.5	56.9	56.8	1.48	1.46
-0.5	1.15	0.18	38.8	42.1	58.6	56.3	1.43	1.49
0.0	1.25	0.38	40.6	42.0	56.6	56.1	1.52	1.47
0.5	1.44	0.49	40.8	41.9	56.2	56.2	1.52	1.47
1.0	1.28	0.31	40.4	41.4	56.9	56.7	1.49	1.58
1.5	1.32	0.28	39.9	41.4	57.2	56.8	1.50	1.51
2.0	1.35	0.19	39.4	40.8	57.8	57.5	1.50	1.49
2.5	1.25	0.42	38.3	41.6	58.9	56.6	1.47	1.45
3.0	1.39	2.06	40.2	39.6	56.9	56.8	1.59	1.52

in Table 4.1 and Table 4.2 for g_2 and g_6 respectively. Overall, Table 4.1 shows that R2 and R3 are the most heavily weighted regions for g_2 's period. G_6 has more equitable weight dispersed across regions, but the combined weight of R1 and R2 accounts for $\sim 50\%$ of the g_6 period for any given model. As identified in Figure 4.2 and Figure 4.6, R1 and R2 are the most impacted regions in this study. A g-mode with about half its weight from those regions may pick up the detailed differences more so than modes weighted more in outer regions. This may explain why Figure 4.5 shows a larger spread in the g_6 periods as this g-mode is likely picking up the R1 and R2 contributions to its period better than other g-modes.

Table 4.2: g_6 Weight Function Percentages Per WD Region

σ_i	R1		R2		R3		R4	
	NOV	OV	NOV	OV	NOV	OV	NOV	OV
-3.0	25.5	20.1	25.6	32.4	21.1	19.8	27.8	27.8
-2.5	33.1	19.1	29.5	33.5	13.1	20.2	24.2	24.2
-2.0	32.3	16.6	30.8	36.3	13.9	19.7	23.0	23.0
-1.5	33.5	17.3	29.6	39.1	12.6	17.3	24.4	24.4
-1.0	33.8	13.4	30.0	43.1	12.9	17.4	23.3	23.3
-0.5	33.5	11.7	29.8	47.5	12.8	14.9	23.9	23.9
0.0	33.2	15.4	28.9	42.8	12.0	15.5	25.9	25.9
0.5	26.6	16.4	22.5	41.0	13.8	14.0	37.1	37.1
1.0	31.2	14.1	27.1	43.8	12.4	16.1	29.3	29.3
1.5	32.2	13.7	27.4	46.7	12.2	14.7	28.3	28.3
2.0	25.5	11.7	23.0	48.1	14.1	14.3	37.3	37.3
2.5	30.9	14.2	28.0	42.5	12.5	13.8	28.6	28.6
3.0	30.1	32.0	25.5	26.2	12.4	13.8	32.0	32.0

When an integer multiple q of the local radial wavelength λ_r for a given g-mode nearly matches the width of a certain region(s) in a star, the g-mode resonates with that region(s). Figure 4.7 shows $q \cdot \lambda_r(R_\odot)$ as a function of radius R (R_\odot) for the g_2 and g_6 modes. The NOV set doesn't show any particular close matches for any region. But the closest matches to the R2 width were the λ_r curves of $g_2, q = 1$, and $g_6, q = 2$. Further, the $g_2, q = 2$ and $g_6, q = 3$ modes were best at resonating with R3. Larger q values may show stronger resonance with R4. The resonance with R2 is enhanced in the OV set. The $g_2, q = 1$ and $g_6, q = 2$ λ_r curves match much more closely to the R2 width in the OV set. This implies that overshoot has enhanced the

g-mode resonance for our signature modes in the region that was constructed mainly from radiative burning (Figure 4.3). We also see stronger resonance within the R1 region with the $g_2, q = 1 \lambda_r$ curve.

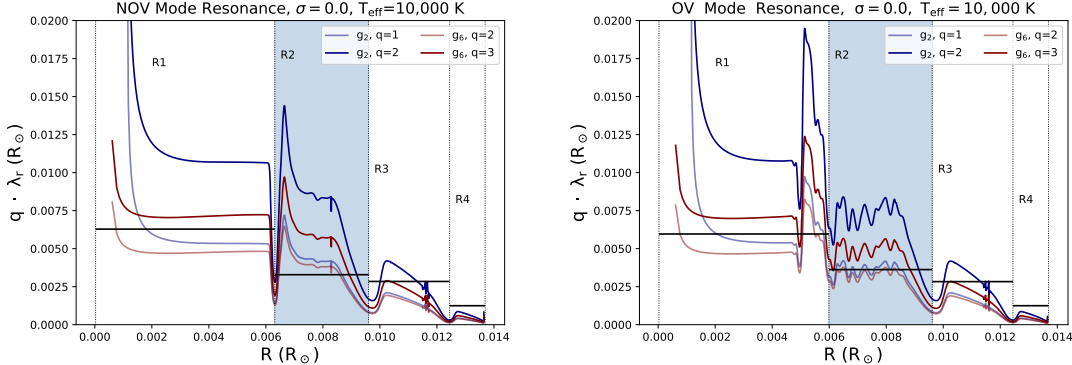


Figure 4.7: Integer multiples of the local radial wavelengths $q \cdot \lambda_r$ for g_2 and g_6 as a function of the star's radius R . Mode resonance occurs when $q \cdot \lambda_r$ closely matches the width of a certain region(s) in the star. The left panel is the NOV set's mode resonance and the right panel is the OV set's mode resonance. In both panels, the black horizontal lines mark the respective region widths. Blue curves show $q \cdot \lambda_r$ for g_2 and maroon curves show $q \cdot \lambda_r$ for g_6 . The q values are stated in the legend.

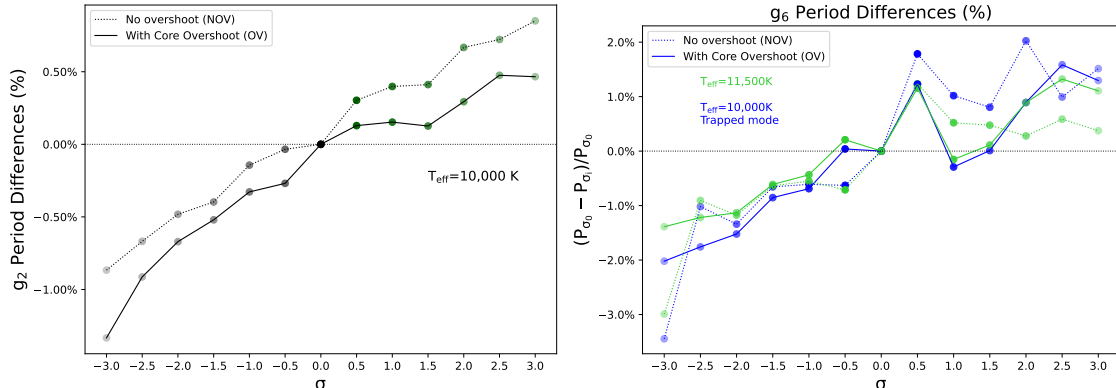


Figure 4.8: Adiabatic g_2 (left) and g_6 (right) mode signatures for the NOV and OV sets, at $T_{\text{eff}} = 11,500$ (bright green) and $T_{\text{eff}} = 10,000$ K (blue) respectively.

Will the differences between the NOV and OV sets in Figure 4.6 impact the WD $^{12}\text{C}(\alpha, \gamma)^{16}\text{O}$ σ_i pulsation signatures shown in Figure 4.4? Figure 4.8 shows the resulting relative period percent differences, as a function of σ_i at $\mathbf{T}_{\text{eff}} = 11,500$ K (bright green) and $\mathbf{T}_{\text{eff}} = 10,000$ K (blue). The period differences are negative for

σ_i with longer periods than the $\sigma = 0$ model, and are positive for σ_i with shorter periods than the $\sigma = 0$ model for the given NOV or OV set. The left of this figure shows the period differences for g_2 , and the right shows the period differences for g_6 . The NOV set is indicated by the dotted lines and the OV set is the solid lines.

Looking at g_2 , the period differences between NOV and OV at $T_{\text{eff}} = \mathbf{11,500}$ K are minimal; both sets show a trend of decreasing period with increasing σ_i . At $T_{\text{eff}} = \mathbf{10,000}$ K, the OV set shows an overall decrease in the percent differences, and a slightly greater variation in the overall σ_i vs. g_2 period difference shape. However, at both temperatures, the same pattern of the g_2 period decreasing with increasing σ_i is sustained with overshoot inclusion. Further, the magnitude of percent differences, ranging from $\simeq -1.5$ to $+1.0$, is within the detectable threshold (Chidester *et al.*, 2021).

The OV set shows greater deviation from the NOV line of period percent differences in g_6 more-so than g_2 . This is most likely because g_6 is more sensitive to changes from R1 than g_2 . Nonetheless, despite the $\sigma_{-0.5}$ and $\sigma_{+1.0}$ outliers, the overall trend remains: $\sigma_i < 0$ generally have longer periods than σ_0 and $\sigma_i > 0$ generally have shorter periods than σ_0 . Once again, the magnitude of the relative period percent differences surpass the observable threshold.

An interesting note is that for both g_2 ad g_6 signals, the percent differences change more in the NOV set as the models cool from $T_{\text{eff}} = \mathbf{11,500}$ to $T_{\text{eff}} = \mathbf{10,000}$ K than the OV set. The OV set showed nearly the same period differences at both temperatures.

4.5 Discussion

C22 found pulsation signature(s) for the experimental $^{12}\text{C}(\alpha, \gamma)^{16}\text{O}$ reaction rate probability distribution function. They describe four sensitivities that may impact

this result: width of the O→C transition, mixing during CHeB, thermal pulse history on the AGB, and the 3α reaction rate. This work investigated the impact that overshoot inclusion had on the $^{12}\text{C}(\alpha, \gamma)^{16}\text{O}$ reaction rate pulsation signature(s). Doing so, we address the width of the O→C transition and mixing during CHeB. Further, by ignoring the thermal pulse history in our models, we also address the sensitivity to the number of thermal pulses, albeit, the trivial case when the number of thermal pulses is zero. In the following paragraphs, we discuss how these three sensitivities impacted our results. We further caution how our results could be impacted from further sensitivity investigations.

Including overshooting overall increased the width of the O→C transition for all σ_i cool WDs. This lessened the sharp peak in B at the O→C transition, and decreased the peak in $g_6 \zeta$ at the O→C transition. While the transition peak was lessened and dispersed into R2, widening the O→C transition shows an *enhancement* of both the weight contribution to the R2 region for g_2 and g_6 , and the R2 resonance with λ_r for g_2 and g_6 . The widening of the O→C transition was from the combined effects of overshoot inclusion and the σ_i prescription. We conclude that widening the O→C transition imposes differences in B , ζ , and the pulsation periods. Despite these changes, we still find the g_2 and g_6 relative period differences in the NOV and OV sets to distinguish the $^{12}\text{C}(\alpha, \gamma)^{16}\text{O}$ reaction rate probability distribution function. Namely, the pattern of decreasing period with increasing σ_i persisted in both NOV and OV sets. By itself, the inclusion of overshooting does not destroy the seismic signatures of the $^{12}\text{C}(\alpha, \gamma)^{16}\text{O}$ reaction rate in our WD models – which was the primary question of this study.

We caution that increasing (decreasing) the width of the O→C transition in CO WD models could potentially yield different results. Our CO WD models were informed from their evolution history, with the stated model parameters. Thus, an

increase (decrease) of the width of the O→C transition may come from choosing different mixing processes, prescriptions and parameters, such as for convection and overshooting. A change in the width of the O→C transition may also come from mixing processes not considered in this study such as time-dependent convection (Jermyn *et al.*, 2023), rotationally induced mixing, semiconvection, or thermohaline mixing.

Ignoring the thermal pulse history gave an additional low-order adiabatic g-mode signature for σ_i , namely the g_2 signal. This signal was not found in C22, where the thermal pulse history was included. Future studies on the thermal pulse phase of evolution with different temporal and spatial resolutions are needed to determine the sustainability of the g_2 signal as a probe for σ_i . Concurrently, future studies could also explore the interaction, if any, between the thermal pulses and overshooting during CHeB on the chemical profiles.

The CO cores of WDs are the result of the competition between 3α and $^{12}\text{C}(\alpha, \gamma)^{16}\text{O}$ during CHeB.

An experimental 3α reaction rate probability distribution function, similar to the existing one for $^{12}\text{C}(\alpha, \gamma)^{16}\text{O}$ (deBoer *et al.*, 2017; Mehta *et al.*, 2022; Farag *et al.*, 2022, C22), does not yet exist to our knowledge, although a probability distribution function could be constructed using the STARLIB reaction rate library (?Fields *et al.*, 2016, 2018). Estimates of the uncertainty in the 3α reaction rate range from $\simeq 15\%$ accuracy (?) through $\simeq 10\%$ accuracy (??) to $\simeq 30\%$ accuracy (Kibédi *et al.*, 2020) over the regions of typical astrophysical interest. However, at temperatures $\lesssim 10^8 \text{ K}$, the uncertainty is likely larger because other reaction mechanisms become significant (Suno *et al.*, 2016).

Future studies involving both reaction rate probability distribution functions could probe properties of DAV WD models in the 3α rate - $^{12}\text{C}(\alpha, \gamma)^{16}\text{O}$ rate plane. For example, the 3α reaction rate is likely to slowly modulate the central ^{16}O mass frac-

tion at any $^{12}\text{C}(\alpha, \gamma)^{16}\text{O}$ reaction rate because 3α controls the production of ^{12}C . The $^{12}\text{C}(\alpha, \gamma)^{16}\text{O}$ reaction rate will likely modulate the central ^{16}O mass fraction more strongly at any 3α reaction rate. We predict that the radiative region R2 will exist in all such models. We also predict that all such models, whether terminated at the first thermal pulse or evolved through the thermal pulse phase, will show a trapped mode, with substantial trapping from R2, that best probes the reaction rates (i.e. g_6 in this work, and see Figure 9 in C22). Future studies could also explore why the g_2 mode found in this work does not apparently survive the thermal pulse phase of evolution, as this low-order adiabatic g-mode was not found in C22. We caution that the relative period shifts we find in this work from considering the $^{12}\text{C}(\alpha, \gamma)^{16}\text{O}$ probability distribution and overshooting may change when a 3α reaction rate probability distribution function is also considered.

De Gerónimo *et al.* (2017) found that including overshooting impacted ensuing WD pulsations by $\sim 2 - 5$ s. Their results were independent of their $^{12}\text{C}(\alpha, \gamma)^{16}\text{O}$ reaction rate uncertainty evaluation. We combined the effects of overshooting and the $^{12}\text{C}(\alpha, \gamma)^{16}\text{O}$ reaction rate sensitivities in our pulsation analysis, and likewise find period differences of similar magnitudes. Our $^{12}\text{C}(\alpha, \gamma)^{16}\text{O}$ reaction rate analysis spanned the current experimental probability distribution function, which analyzed different rate values than those explored in De Gerónimo *et al.* (2017). They concluded that the $^{12}\text{C}(\alpha, \gamma)^{16}\text{O}$ uncertainty was less relevant than overshooting. In this study, we find that the combined effects from overshooting and the $^{12}\text{C}(\alpha, \gamma)^{16}\text{O}$ reaction rate probability distribution function yields remarkable differences in the structure of the CO WDs, and pulsation differences. Despite these differences, we still find pulsation signatures for σ_i .

4.6 Summary

We conducted a search for signatures of the current experimental $^{12}\text{C}(\alpha, \gamma)^{16}\text{O}$ reaction rate probability distribution function in the pulsation periods of CO WD models with the inclusion of overshooting. We found two signature adiabatic g-modes that show period differences with the reaction rate probability distribution function σ_i trend regardless of whether or not overshoot is included. We find a g_2 period difference signature is inversely proportional to σ_i . Without overshoot, the g_2 relative period differences span $\pm 0.9\%$. With overshoot, the g_2 relative period differences range from -1.33% to 0.47%. The average magnitude of the relative period differences for g_2 were 0.46% and 0.44% respectively. The g_6 period differences were larger in magnitude, spanning from -3.44% to 1.78% for NOV and -2.02% to 1.58% for OV. The average magnitude of the g_6 period differences were 1.21% and 0.95% respectively. The average magnitudes of the g_2 and g_6 period differences were slightly decreased from the NOV set.

We found that the R2 weight contribution to these g-modes was enhanced with overshoot inclusion. The R2 region remains the best identifying region for tracing the $^{12}\text{C}(\alpha, \gamma)^{16}\text{O}$ reaction rate probability distribution function. This is because even with overshoot inclusion, it is predominantly constructed by radiative burning during CHeB. Regardless of whether or not overshooting is considered, we find:

1. two signature g-modes, g_2 and g_6 probe σ_i
2. g_2 is inversely proportional to σ_i and g_6 is a trapped mode
3. the g_2 and g_6 periods are generally shorter for positive σ_i and longer for negative σ_i
4. both signatures have period deviations within the detectable regime

These findings suggest that an astrophysical constraint on the $^{12}\text{C}(\alpha, \gamma)^{16}\text{O}$ reaction rate probability distribution function remains, in principle, extractable from the period spectrum of observed variable WDs.

4.7 Acknowledgements

We thank James Deboer for sharing the $^{12}\text{C}(\alpha, \gamma)^{16}\text{O}$ probability distribution function, Josiah Schwab for sharing `wd_builder`, and Pablo Marchant for sharing `mkipp`. We acknowledge using ChatGPT (OpenAI, 2023) to polish the language of one paragraph (Vishniac, 2023). This research is supported by NASA under the Astrophysics Theory Program grant NNH21ZDA001N-ATP, and in part by the National Science Foundation under Grant No. NSF PHY-1748958. This research made extensive use of the SAO/NASA Astrophysics Data System (ADS).

Software: MESA (Paxton *et al.*, 2011, 2013, 2015, 2018, 2019; Jermyn *et al.*, 2023, <https://docs.mesastar.org/>), MESASDK 20190830 (Townsend, 2019a,b), `wd_builder` https://github.com/jschwab/wd_builder, GYRE (Townsend and Teitler, 2013; Townsend *et al.*, 2018, <https://github.com/rhdtownsend/gyre>), `mkipp` <https://github.com/orlox/mkipp>, `matplotlib` (Hunter, 2007), NumPy (van der Walt *et al.*, 2011), and ChatGPT (OpenAI, 2023).

Chapter 5

HOW SPREADSHEET AND GRAPH COACHING IMPACTS STUDENT PERFORMANCE IN HABWORLDS COURSE

This work is the draft of educational research I've done during my P.h.D. We intend to submit this work by Dec. 2023.

5.1 Abstract

Background: Stronger partnerships between learning analytics (LA) and learning design (LD) have the potential to significantly improve student learning, however understanding how to unite these fields effectively is still a growing effort. Recent systematic literature reviews call for research to examine which learning design choices impact success in learning, and apply learning analytics when making deliberate decisions to improve various aspects of learning. This study analyzes a recent LA↔LD collaboration through a framework informed by these reviews. The learning designers in this collaboration made a number of changes to an existing astrobiology course (*Habitable Worlds*) that were intended to improve either spreadsheet use or graph reading. LA researchers worked with the learning designers to identify the modified portions of the course and to catalog the nature of those changes. LA researchers then performed the pre-/post-modification comparisons and shared the results back to the learning designers to inform future practice. The collaborative framework demonstrates LD↔LA synergy, showing how to apply learning analytics tools when evaluating deliberate design decisions intended to improve aspects of learning.

Results: We find that overall student performance was consistently improved following the spreadsheet and graph learning design modifications. Namely, the num-

ber of attempts to correctly answer questions on modified screens in the course was reduced in almost all cases. Spreadsheet learning design changes led to larger effects than graph learning design changes. We also find substantial indirect positive effects on near transfer task scores, which were unmodified during the studied period.

Conclusions: Our results provide direct efficacy data for each of the learning design changes made to the *Habitable Worlds* course. This helps learning designers in their practice and could serve as a foundation for controlled research into the relative efficacy of different digital learning design approaches. Our study as a whole serves as an example of a productive LA↔LD partnership. We hope this example will spur similar partnerships and draw continued attention from researchers interested in improving the synergy between learning analytics and learning design.

5.2 Introduction

5.2.1 *The Learning Analytics↔Learning Design Connection*

The field of learning analytics (LA) collects and analyzes data about learners with the goal of optimizing and improving student learning from the information gathered. While common uses for LA can predict student success or identify students at risk of failure SOLAR (2021), learning analytics cannot be maximally effective unless it is coupled with learning design (LD) (Hernández-Leo *et al.* (2018); Bos and Brand-Gruwel (2016); Lockyer *et al.* (2013a); Blumenstein (2020)). The field of LD exists to create and refine techniques and strategies that promote student learning Macfadyen *et al.* (2020). The promise of aligning LA with LD is for learning designers to be able to extract actionable information from LA that could support reflective practice and move the discipline toward empirically-grounded best-practices (Mangaroska and

Giannakos (2018), Hernández-Leo *et al.* (2018)). At the same time, it would also ensure that LA research is better grounded in meaningful learning outcomes.

5.2.2 Related Work

Schneider & Preckel Schneider and Preckel (2017) conducted a systematic review of more than 100 instructional variables and their empirical effects on student achievement in higher education. This review found that social interaction, stimulation of meaningful learning, and using conceptually demanding learning tasks had a close relationship to achievement Schneider and Preckel (2017). Blumenstein Blumenstein (2020) built on this work and others to review the synergistic effects of LA and LD on student outcomes in higher education. Blumenstein's review focused on the impacts of LD on learning outcomes and student performance as seen through an LA lens Blumenstein (2020). Like Schneider & Preckel, Blumenstein found that designs fostering socio-collaborative and independent learning skills (time management, self regulation, meaningful learning, etc.) resulted in large positive effects on student outcomes Blumenstein (2020).

Knobabout & Stappen Knobabout and Van Der Stappen (2020) performed a systematic study that focused on evaluating LA interventions to assess the ways in which LA improve learning. From their analysis, the authors recommend that future researchers should be clear and transparent on which operational definitions are used to measure learning affected by LA interventions. They further recommend that researchers include performance measurements that relate to learning processes and learning environments Knobabout and Van Der Stappen (2020). This is an example of where LD expertise can enhance LA-based research.

Another systematic review of LA for LD was done by Mangaroska et. al., 2019 Mangaroska and Giannakos (2018) and included 43 research articles. Their study

focused on analytics-driven design decisions, or, learning analytics *for* learning design. The study centered on investigating the current status of LA for LD, classifying what LA indicators have been used to inform LD decisions, and providing a synopsis of existing work regarding the alignment of LD and LA Mangaroska and Giannakos (2018). The authors' research questions were to 1) determine the current status of LA for LD research and 2) find what LA have been used to inform LD decisions, and the extent that LA has been used to support dynamic and data-driven LD decisions.

Regarding their first research question, the authors found benefits of LA for both teachers and students. For teachers, LA helped them manage time better, identify problems in the course design, and utilize real-time tracking and provide instant corrective feedback Mangaroska and Giannakos (2018). Teachers also became more knowledgeable about their students' learning behaviors and progress. Students became more knowledgeable about their learning behaviors and progress as well, which led them to improve their decision making skills and appreciate their own skill growth. However, the authors also highlight a key limitation in that none of the included studies clearly report any measurement of learning gains. Further, although there is evidence of changes in students' self-monitoring, there is not evidence that speaks directly to what, if any, changes in behavior followed from that self-monitoring. In turn, they suggest that the research community could benefit from a taxonomy of LA techniques that are likely to create an impact on user's behavior, whether positive or negative Mangaroska and Giannakos (2018).

From their findings, Mangaroska and co-authors conclude there is a misalignment between LA tools and LD objectives, particularly a lack of metrics which are pedagogically valuable and a failure to tie LA metrics to learners' goals and expectations. The authors recommend the development of a framework on how to capture and systematize LD data grounded in LA and learning theory in order to more effectively

study how LD choices influence learner performance. Further, the authors provide a checklist for future LA↔LD work (Section V. D, pg 530 Mangaroska and Giannakos (2018)). A few particularly important checklist items are: to indicate how LA metrics offer insight into the learning process, thus yielding meaningful interpretation to inform LD; evaluate and compare which LD patterns/phenomena make learning effective; evaluate and denote the impact of LA outcomes on LD decisions and experiences. These speak to the varied synergies between LA and LD. Our study provides examples of these in practice.

Hernandez-Leo et. al. Hernández-Leo *et al.* (2018) proposed a framework that closely aligns with Mangoroska et. al.'s suggestion, particularly the use of LA to understand learning. The framework, *Analytics Layers for Learning Design* (AL4LD) Hernández-Leo *et al.* (2018), articulates layers of data analytics aimed to support informed decision-making in LD. AL4LD offers different data analytics perspectives that support LD processes. We refer the reader to Hernández-Leo *et al.* (2018) for an extensive review of how AL4LD conceptualizes the role of analytics in the LD space. As we will describe in the next section, our study gives a practical example of interactions across the different layers within the AL4LD model.

Another framework was proposed in Lockyer 2013 Lockyer *et al.* (2013b). It is broadly categorized into *checkpoint analytics* and *process analytics*. The framework closely aligns with Mangoroska et. al.'s recommendations to evaluate LD with LA Mangaroska and Giannakos (2018). This framework also relates to Blumenstein's work (assessing the impact of LD through an LA lens) Blumenstein (2020) as mentioned previously. We refer the reader to Lockyer *et al.* (2013b) for a full understanding of their framework. Simply, the focus particularly follows Knobabout & Stappen's Knobabout and Van Der Stappen (2020) suggestion to use appropriate performance measurements and analytics that relate to the LD process or environment under eval-

uation. The broad categories help guide educators and researchers to know which analytics to use for various evaluation scenarios. For example, *checklist analytics* could check if students are logging into an online portal regularly, and help measure student engagement of the LD space, whereas *process analytics* could evaluate how students are performing on a specific learning activity or assignment.

The research literacy has identified two important areas for improvement related to LA↔LD collaborations. First is the need for LA work to be clearly grounded in the specific outcomes of interest for learning designers. Second, is the need for LD work to be more consistently and more thoroughly informed by LA. And yet, despite several proposed frameworks for how LA↔LD collaborations can function more effectively, there remains a need for applied work that puts these ideas into practice for the benefit of both the LA and LD communities.

5.2.3 A Simplified Framework

Informed by the research-based recommendations of Knobbout & Stappen and Mangaroska et al. (Knobbout and Van Der Stappen (2020); Mangaroska and Giannakos (2018)) and drawing on framework concepts from both AL4LD (Hernández-Leo *et al.* (2018)) and *checklist analytics/process analytics* (Lockyer *et al.* (2013b)), we present a simplified framework representing the iterative loop of LA and LD practices employed in the present study. In short, LD work is informed by current practices and LA/LD products are evaluated through appropriate LA tools. The results then re-inform subsequent LD work, and the cycle repeats. This process is shown in Figure 5.1. In addition to the practical steps taken, our proposed model also highlights the expertise that is drawn on at each step in the loop, as indicated by the color legend in the figure.

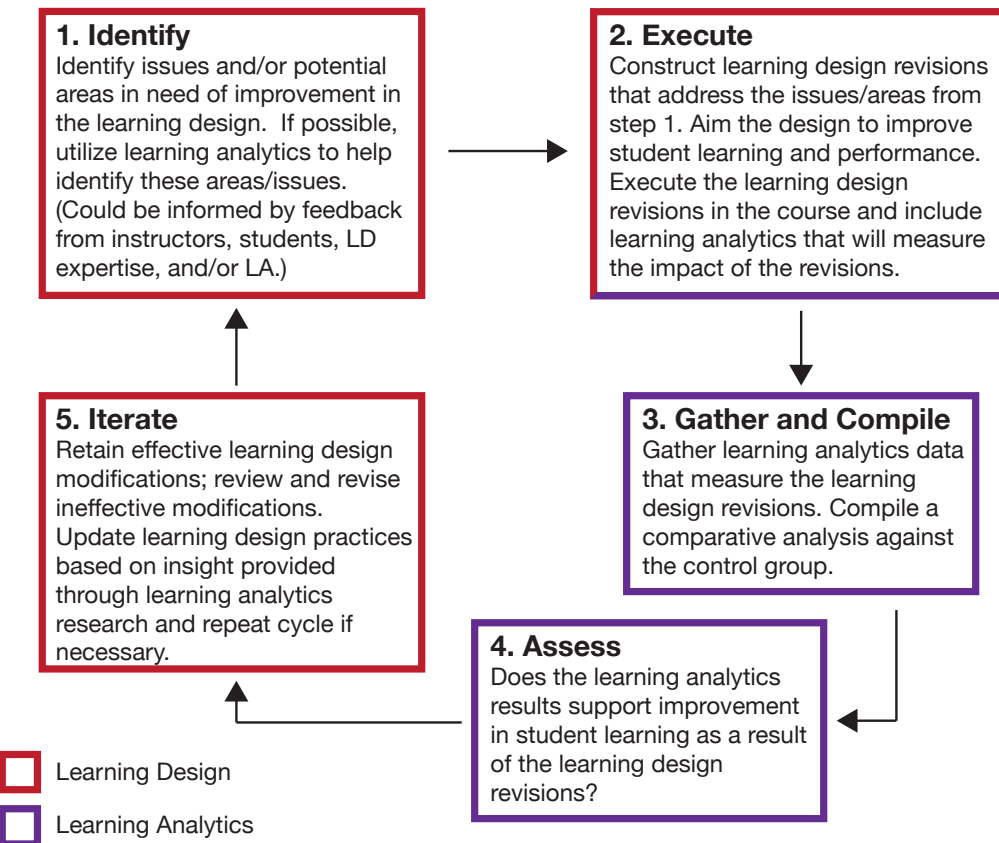


Figure 5.1: General framework to successfully unite LD with LA, aimed to enhance student learning and performance.

The first step is to *Identify* areas in the course in need of improvement. This may be informed solely by LD expertise, it may be guided by input from LA-based examination of the course, and/or may be driven by input from educators or direct learner input. Figure 1 presents an iterative loop, and this initial step need not rely on previous LA guidance. However, maximizing the amount of expertise involved in supplying information for this step may reduce the need for future iterations of the process. The identification step also implicitly serves to document and define the scope of work and by extension the nature and focus of the LA data.

The *Execute* step is where revisions are done to the learning design of the course. Revisions should address the identified issues in the *Identify* step as directly as pos-

sible. Work in the *Execute* step is conducted by learning designers and reflects their current LD expertise. In other words, the LD revisions represent the designers' best effort at enhancing student learning, performance, engagement, or whichever specific goal was defined in the *Identify* step. Although work in this step is performed by learning designers, ideally the work is done in close coordination with LA experts in order to facilitate subsequent steps in the loop.

Steps 3 and 4, *Gather and Compile* and *Assess*, primarily call for LA expertise. Here, LA researchers collect the appropriate LA data and analyze these data with respect to the goals which were defined in the *Identify* step. These results should determine whether or not the LD revisions supported those initial goals, whether student learning, performance, engagement, interest, or other outcomes.

Finally, the *Iterate* step is where the LD team decides what actions are necessary based on the information from the *Assess* step. Regarding the course or lesson itself, they may decide to retain effective modifications, review, revise, or discard ineffective modifications. Regarding the professional expertise of the learning designers, they may also reflect on their own practices and heuristics and update these based on insight gained from the LA findings. The process then returns to Step 1, as appropriate.

5.2.4 Novelty of this Work

Previous studies have called for closer LA↔LD partnerships, including a better alignment of LA metrics and the ultimate goals of specific learning design work. In the present study, we describe the results of a novel collaborative project, drawing on both LD and LA, following the framework outlined in Figure 5.1. We address some of the important limitations highlighted by the reviews previously described, including the need for closer and more practically-minded collaboration between the domains

of LD and LA, and the continued need for research that is grounded in meaningful learning outcomes data.

Our work specifically responds to several calls for improvement in LA↔LD researching, including:

- Rooting LA measurements in outcomes that are meaningful to LD and leveraging LA to help learning designers make deliberate decisions (Knobabout and Van Der Stappen (2020), Mangaroska and Giannakos (2018))
- Tying LA metrics to the designers' goals and expectations (Mangaroska and Giannakos (2018))
- Accounting for successive semesters after the changes were implemented, thus tracking learning performance over time (Mangaroska and Giannakos (2018))
- Addressing a gap in reviews such as Blumenstein (Blumenstein (2020)) which examined lesson- or course-level outcomes.
- Evaluating and comparing our LD revisions effectiveness on learning, measured by our LA outcomes (Mangaroska and Giannakos (2018))

5.2.5 Research Questions

In this study we pose two main research questions:

RQ1: Do learning analytics in *Habitable Worlds* indicate that the learning design changes for spreadsheet use or graph interpretation were effective in improving student performance on training lessons?

RQ2: Do the learning design changes to the training lessons result in an overall improvement in student performance?

These questions help guide the LA↔LD synergy we intend to demonstrate.

5.3 Methodology

5.3.1 Course Context

Habitable Worlds is a 7.5 week online course in astrobiology that is offered at a large public research university in the Southwestern U.S. Like many U.S. universities, undergraduate students are required to complete a four credit laboratory science course as part of their degree. *Habitable Worlds* is one course that meets this requirement and it is commonly taken by non-science majors. Therefore, for many students, this course is a means to an end and may be the last formal science background for the rest of their lives. Often, these introductory science courses leave students with a misleading perception of science; the typical lecture-lab setting teaches decontextualized facts of science more so than the actual practice of science Horodyskyj *et al.* (2018). *Habitable Worlds* is intended to enhance students' perception of science and teach students how qualitative science is performed.

Habitable Worlds has two parts to each lesson. The first portion is a training lesson. The training lessons are designed to introduce new material. Students are allowed to retry questions without penalty until they answer correctly. The second portion is an application lesson. These lessons are quiz-like, and students are penalized for incorrect answers. The application lessons are designed to assess the mastery of the skills and knowledge from the previous lesson. We will not discuss the science content of the course, because it is not directly relevant to our focus on LA and LD. However, we will adopt the course's internal nomenclature when referring to specific lessons. After the Introductory unit, the lesson name prefixes are (in order) **R***, **fp**, and **ne**. Interested readers may see Horodyskyj *et al.* (2018) for details about the content of these units.

Habitable Worlds was built on the adaptive eLearning platform *Smart Sparrow* Ben-Naim (2010). *Smart Sparrow* has three features that significantly impact our work. First, by delivering adaptive feedback, the platform allows the LD to design the lesson to intelligently respond to a variety of student actions, both correct and incorrect. Second, it allows non-specialists to quickly make changes to lessons through the web-based author. The LD changes in this study were only possible through this accessible authoring. Third, the platform stores detailed analytics beyond overall grades Dror *et al.* (2018), including the time spent on each screen, the number of attempts taken to get the correct answer, and the specific responses and other actions submitted. This allows educators, learning designers, and LA researchers to examine the learning process in fine-grained detail.

5.3.2 Learning Design Objective: Better Teaching of 21st Century Skills

As our society incorporates more technology in jobs, careers, and daily life, it's important for our classrooms to focus on skill development commensurate with the 21st century. The National Research Council (NRC) addressed 21st century skills in 2012. They reported that business, political, and educational leaders are urging schools to integrate the development of problem solving, critical thinking, and collaboration skills in learning environments NRC (2012). The NRC constructed three levels of 21st century skills, which are cognitive, intrapersonal, and interpersonal. These levels provide a broad framework for the type of skills educators should consider. How can we directly hone in on teaching 21st Century Skills in our curricula so students will be prepared for their respective futures? One example is to teach students how to interpret graph data in math and science courses. Graphs are important for learning, technical occupations, and public discourse Donnelly-Hermosillo *et al.* (2020). Donnelly et. al Donnelly-Hermosillo *et al.* (2020) illustrated that graph technologies at the

K-12 level improve student learning, and are comparatively better than conventional approaches.

A second important and versatile 21st century skill is knowing how to use a spreadsheet. Uses for spreadsheets include modelling and planning, finance planning, budgeting business accounts, organizing data, computing calculations, creating graphs and charts, etc. McNally (2015). These uses are advantageous to anyone, no matter their career path. If used correctly, spreadsheets are reliable and efficient. The calculations are correct and automatic. Information can be easily sorted and readily analyzed. Data can also be visualized for easy interpretation. Introducing this 21st century skill in an undergraduate science course should provide far reaching benefits outside the course.

The *Habitable Worlds* course, which is the focus of this study, was designed to incorporate 21st century skill development. The LD modifications studied were intended to specifically improve students' graph reading and spreadsheet use.

5.3.3 Summary of LA↔LD Collaboration

Steps 1 and 2 in Figure 5.1 were completed by the ASU LD team. They decided the spreadsheet and graph LD changes aimed to enhance the course (Step 1), and performed the LD revisions necessary to meet their course improvement goals (Step 2). We are not aware that the issues identified during Step 1 were motivated by prior LA measurements. Further, we note that the LA metrics we chose for evaluating the impact of the LD revisions were not necessarily schemed out in Step 2 by the ASU LD team. They were consequently included by the *Smart Sparrow* platform, and measure the LD revisions nonetheless. We caution future researchers to intentionally include suitable LA metrics if they are not already built into the course's platform or learning design.

In short, the ASU LD team implemented the modifications regarding spreadsheet and graph questions for the Spring 2020, Fall 2020, and Spring 2021 courses. The Fall 2019 course was used as a pre-modification comparison. The remainder of this section describes the student sample, the nature of the LD changes, and our analytical approach which follows Steps 3 and 4 in Figure 5.1.

5.3.4 Initial Spreadsheet LD Modifications

Overall, the largest change, with respect to the spreadsheet use LD implementations, was a new introductory lesson segment which taught students how to use spreadsheets. Like all other *Habitable Worlds* training lessons, this new material took advantage of the adaptive platform to provide students feedback in response to their specific mistakes. Unlike the subsequent LD changes, which modify existing questions, this material was entirely new. Thus, our analysis cannot directly study the impact of the added introductory material. However, the subsequent LD changes trace back to what students learn from the added material to this lesson. The lesson covers:

- the benefits of using a spreadsheet
- common operator symbols
- how to use columns as input/output
- how to interpret a given formula
- practice questions for using spreadsheets
- formula examples

The remaining LD changes related to spreadsheets were interspersed throughout the course. In the lesson immediately following the introduction, two screens were

added to demonstrate how to use a spreadsheet in the context of calculating a distance. The next lesson had modified questions with directions to include “using the formula in your spreadsheet...”. The subsequent lessons had less direct spreadsheet instructions. These included help buttons with spreadsheet tips, splitting screens up into separate calculations, and adjusting the adaptive feedback to ask students to double check the formulas in their spreadsheet. As an example, Figure 5.2 shows a question from the *R*1: Calculate Distance* lesson as seen in the Fall 2019 semester (top), and the same question as seen in the subsequent semesters (bottom). Both screens ask the same question, but the screen in the post-Fall 2019 semesters show adjusted text in the prompt that supports using a spreadsheet instead of having a help button suggesting to use a spreadsheet, as in the Fall 2019 screen. The sample calculation icon was also removed in the post-Fall 2019 semesters. These and other studied LD changes are summarized and categorized in Table 5.1.

5.3.5 Graph LD Implementations Post-Fall 2019

The post-Fall 2019 semester courses also included an introductory lesson on various graph types. The lesson introduces several specific types of graphs (i.e. bar graphs, scatter plots, etc.); teaches students how to read these types of graphs; and covers relevant mathematical terminology such as “inversely proportional”, “proportional to a power”, and “inversely proportional to a power”. As with the spreadsheet changes, the other LD modifications related to graphs were interspersed throughout the course. These changes include adding interpretation questions, clarifying the graph questions, replacing the graph images themselves, and providing feedback when a question is answered incorrectly.

Parallax

Stellar parallax is so small that it remained undetected until the advent of powerful telescopes in the 19th century. Today, we can measure the parallax of distant stars and use some trigonometry to calculate how far away they are.

How far away are all these objects?

Object Name	Parallax Angle	Distance
Atreyu	0.217"	<input type="text"/> light years
Crab Nebula	0.000502"	<input type="text"/> light years
Alpha Centauri	0.747"	<input type="text"/> light years

$$\text{distance (light years)} = \frac{3.26 \text{ ly}}{\text{parallax angle}}$$

Sample Calculation

A star moves through a parallax angle of 0.00438". How far away is it?
 $\text{distance} = 3.26 \text{ light years} / 0.00438"$
 $\text{distance} = 744.29 \text{ light years}$

If you calculate a value more than twice, it may be a good idea to set up a spreadsheet to do the work for you! Many of the calculations that you repeat in the coming lessons will be useful in the assessments and project.

10

Parallax

Now is the easy part! All you have to do is enter these parallax values in column A and then click and drag down column B to perform the calculation on all the new values.

How far away are all these objects?

Object Name	Parallax Angle	Distance
Atreyu	0.187"	<input type="text"/> light years
Gaius	0.0387"	<input type="text"/> light years
Nyota	0.0049"	<input type="text"/> light years

$$\text{distance (light years)} = \frac{3.26 \text{ ly}}{\text{parallax angle}}$$

Figure 5.2: Top: Fall 2019 question in *R*1: Calculate Distance* lesson that suggests ease of spreadsheet use for computation in the left help button. Bottom: Same question in the post-Fall 2019 semesters (through Spring 2021), modified to give support for spreadsheet use in the prompt. The help buttons were also removed. Note that the numerical values shown are randomly generated for each student to prevent cheating. The underlying calculation shown was not modified as part of the LD changes.

5.3.6 Additional LD Modifications Post-Spring 2020

There were two Spreadsheet screens that were further modified for use in the Fall 2020 and Spring 2021 semesters. The first screen was further modified by splitting the calculations into two screens, and adding a question in-between the calculations. The second screen was updated by adding feedback for students who answered incorrectly. These additional changes are noted in our results. Aside from these two modified Spreadsheet screens in Fall 2020 and Spring 2021, the rest of the Spreadsheet screens in Spring 2020, Fall 2020, and Spring 2021 were identical to one another.

Additional revisions were made to 11 of the Graph screens after the Spring 2020 semester. These changes were all minor wording changes, including single word changes like replacing the word “degrees” with “Kelvin”, or replacing “flux” with “intensity” and other re-phrasings of questions or instructions. All of the changes made after Spring 2020 are noted in the results section. Here again, the studied LD changes are shown in Table 5.1.

5.3.7 Categorizing LD Change Types

In Table 5.1, we have grouped the LD changes into several categories based on the nature of each change. This categorization is very much specific to *Habitable Worlds* and this project. Therefore, we do not intend to claim that our categorization will be generalizable to other courses or to LD broadly. Such a general model would require data from multiple courses. Yet we hope that our limited examination of differences in impact based on LD change type will inform future work in this area.

5.3.8 Population and Sample Sizes

The *Habitable Worlds* course enrollment is split evenly between undergraduates enrolled in an in-person degree program and undergraduates enrolled in a fully online degree program. The course is identical and is delivered fully online to students from both populations. As a course that fulfills a general education requirement, students are most often non-science majors. For the respective Fall 2019 - Spring 2021 semesters, the number of enrolled students was $n_s = 332, 341, 320, 422$. This gives a total of 1415 students in this study. The number of students per semester *per lesson* was usually less than the semesters' values because not all students attempted each lesson. However, for all the reported lessons across all semesters, $n_s > 300$. All student work was analyzed anonymously and this research was conducted under an approved human subjects research protocol (study #3679).

5.3.9 Data Sources and Statistical Analyses

The spreadsheet and graph LD modifications were implemented in the training lessons. As mentioned before, the training lessons allow students to retry questions without penalty until they answer correctly. *Smart Sparrow* tracks each student's number of attempts until reaching the correct answer on each question. This data is indicative of how quickly students are able to progress through learning new material. By comparing the number of attempts in the Fall 2019 course to the post-Fall 2019 courses, we can directly measure student performance on the modified questions.

Each training lesson is paired with an application lesson that is intended to assess what students have just learned. Application lesson scores are, thus, a measure of near transfer (Perkins *et al.* (1992)), indicating how well students grasp the material they learned in the prior training lesson. It is also important to note that the application

lessons were not changed, making these scores a stable metric prior to and following the learning design changes.

A student's college GPA provides additional information about how they are likely to perform in the course. As such, GPA is a ubiquitous control variable in educational evaluation and research.

In the sections that follow, we use these data sources to measure the impact of the spreadsheet and graph LD revisions, and show how we followed Steps 3 and 4 from Figure 5.1.

5.3.10 Statistical Analysis

After converting the *Smart Sparrow* data to .json files for each semester, we processed and analyzed the data in R: A Language and Environment for Statistical Computing R Core Team (2020). This included isolating the data from screens that were modified, matching screens across semesters, and computing the number of attempts per student for each of these screens.

Our ultimate research goal is to determine the impact of the spreadsheet and graph LD modifications between the Fall 2019 and post-Fall 2019 semesters. We hypothesize that students should generally have fewer attempts on the modified screens in the post-Fall 2019 semesters compared to the Fall 2019 semester. To test this, we perform a Wilcoxon Rank Sum test (also known as Mann-Whitney U test) (Mann and Whitney (1947);Wilcoxon (1945)) with the student attempt numbers on the modified screens. This is a non-parametric statistical test (i.e. assumes no underlying parent distribution) which determines if two groups are equal (supporting the null hypothesis) or not equal (supporting the research hypothesis). We use the Wilcoxon Rank Sum test as opposed to a t-test because our data is not normally distributed, which

would violate the assumptions of the t-test. The test statistic is $W = \min(W_1, W_2)$, where Mann and Whitney (1947):

$$\begin{cases} W_1 = n_1 n_2 + \frac{n_1(n_1+1)}{2} - R_1, \\ W_2 = n_1 n_2 + \frac{n_2(n_2+1)}{2} - R_2 \end{cases}$$

R_1 is the sum of the ranks for the first group and R_2 is the sum of the ranks for the second group. For our study, W_1 is the Fall 2019 semester, and W_2 is the Spring 2020, Fall 2020, or Fall 2021 semester, respectively.

The Wilcoxon effect size r Fritz *et al.* (2011) measures the magnitude of the difference between groups. It's defined as $r = W/\sqrt{N}$, where N is the total population ($n_1 + n_2$). Using the **wilcox_effsize** function in the **rstatix** package Kassambara (2020), we computed the r values for each modified screen on each of the three post-Fall 2019 semesters. We then computed the weighted average and standard deviation of the r values for each modified screen to 1) report a single r value per change, and 2) asses the consistency across semesters.

We report the impacts of the LD changes studied using effect sizes. The benefit of effect sizes is they provide a standardized way to compare findings across studies that use different outcome measures. The magnitude of effect sizes are often described as being “small”, “medium”, or “large” based on convention (Cohen, 1988). Although these categories can be useful as a rule of thumb, it is good practice to also compare the results of new research to effect sizes within the subfield of study (Schäfer & Schwarz, 2019). The novelty of our approach means that there is not a directly comparable study. Instead we refer to the Cheung & Slavin meta-analysis that reviewed research on the use of educational technology Cheung and Slavin (2013). Prior reviews had reported a “small” effect size on average ($d = 0.31$), while Cheung & Slavin’s analysis concludes that the effect is actually just below the “small” effect threshold ($d = 0.16$).

This is important context for interpreting our results and we will return to this point in the discussion.

To test our second research question, we used linear regression to examine differences in application lesson scores among students who used the modified training lessons relative to scores from students in the comparison section who used the unmodified training lessons. The model predicted application lesson percentage score based on condition (pre-/post-modification), controlled for variations in student academic ability using GPA, and included a dummy variable indicating whether the student was majoring in Earth and Space Science. GPAs were taken from the end of the semester, but excluded the Habitable Worlds course grade. This ensured that all students, even first-semester students, would have a valid GPA.

5.4 Results

In the following sections, we show the mean r (effect size) values of the individual spreadsheet and graph modifications from the training lessons, as well as the overall mean application scores from the testing lessons. We adopt the convention as given in Cohen (1992), where $0.1 \leq r < 0.3$ is small, $0.3 \leq r < 0.5$ is medium, and $r \geq 0.5$ is large. Positive r values support our research hypothesis, that the LD changes resulted in fewer attempts in the post-Fall 2019 semesters. Negative effects indicate the opposite, where more attempts were needed in the semesters after Fall 2019. All r values use the Fall 2019 semester attempt numbers for the base comparison.

5.4.1 Spreadsheet Changes and Their Effect Sizes

Panel A of Figure 5.3 shows the weighted mean r values for the number of attempts on screens with spreadsheet LD changes. The x-axis is categorical, with lessons grouped by the type of change. The x-axis categories are defined in Table 5.1, and

we refer the reader to Table 5.1 for the detailed descriptions. The y-axis shows the effect size, r . Each blue circle in Figure 5.3 is the weighted mean r value (from the Spring 2020, Fall 2020, and Spring 2021 semesters) for an individual modified screen. They are annotated with the corresponding lesson prefix.

The three screens that have r values with error bars represent an LD change that split the original question across two screens. These changes were intended to break a set of calculations into more manageable parts. This complicates our comparison of attempt values with the Fall semesters' single screen. The reason being that on the original (single screen) version, a student who makes multiple errors will receive adaptive feedback that helps them to correct all of these mistakes. Thus they may only need one additional question attempt to correct these multiple mistakes. Assuming this same student made the same errors in the revised (multiple screen) version, they would likely make one additional question attempt on both of the new screens. Because it is impossible to perfectly compare these two versions, we have plotted an upper and lower bound to capture the most likely “true” effect size. By convention, the attempts data are zero indexed, thus a student who answered correctly on their first attempt will have an attempt count of 0. When accounting for these split questions, we simply sum each student's attempts on the two screens. For students who make no mistakes or who make only a single mistake across the two screens, no correction factor is needed. For students who make two or more mistakes in total, we define the lower bound as being one attempt less than their actual total of attempts across the two screens. The upper bound is the actual attempt total. We postulate that the “true” attempt number lies within the maximum and minimum values. The error bars on the r values of these screens thus span the r range given by the maximum and minimum attempt score values.

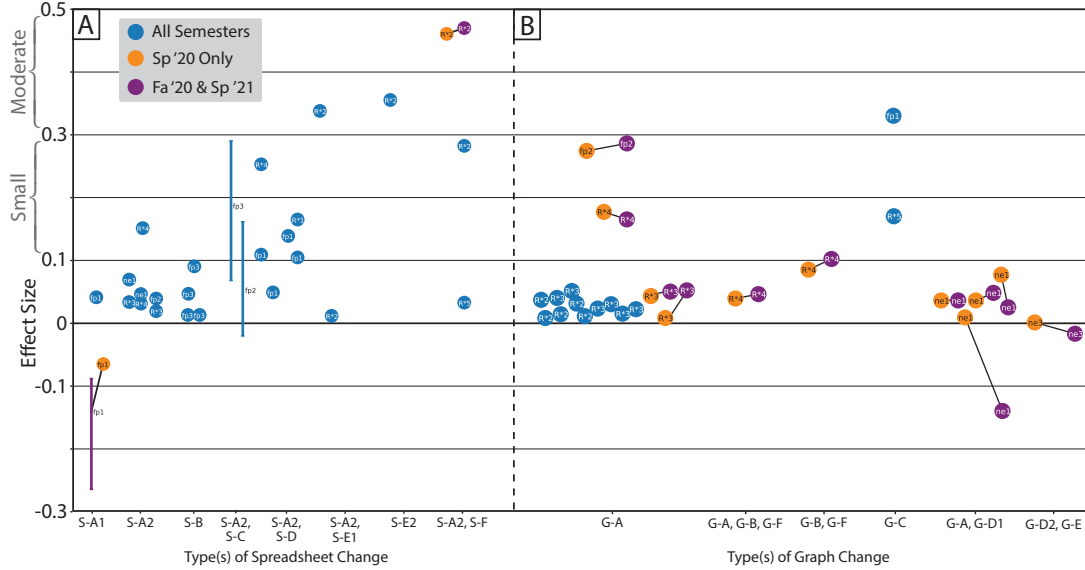


Figure 5.3: A: Wilcox Effects for screens with spreadsheet changes. Effects with error bars indicate screens with split screens. B: Wilcox Effect sizes for screens with graph changes. For both panels, blue circles are the weighted means of the Spring 2020, Fall 2020, and Spring 2021 semesters. Orange circles are for Spring 2020 only, while the purple circles are the weighted means of Fall 2020 and Spring 2021 effect sizes. The x-axis is categorized by the type of change as indexed in Table 5.1. Please refer to Table 5.1 for the detailed descriptions.

The two purple and orange pairs in Panel A represent instances with a second LD modification after the Spring 2020 semester. Orange circles are the **r** values of the screen with the first change only (Spring 2020 semester) and the purple **r** value includes both LD changes on the screen (Fall 2020 and Spring 2021 semesters). The additional changes are noted in Table 5.1 (indicated by the “a” superscript). We treated the screens with an additional change independently, i.e., there is not a corresponding blue **r** for the purple-orange pairs.

Table D.1 in Appendix D provides the semester-by-semester effect sizes, weighted means, and standard deviations for each modified screen. The table also lists the lesson and screen names and the type of change made for each screen.

5.4.2 Graph Changes and Their Effect Sizes

Panel B of Figure 5.3 shows the weighted mean r values for screens with graph changes. Again, blue circles indicate the weighted mean r values for questions that were modified only once, whereas paired orange and purple circles show the r values for Spring 2020 only (orange) and the weighted means for Fall 2020 and Spring 2021 (purple), indicating additional changes after the Spring 2020 semester.

As mentioned in Section 5.3.6, the additional revisions for the graph screens intuitively seemed minor compared to the original change (i.e. replacing “degrees” with “Kelvin” after Spring 2020 vs. adding interpretation questions after Fall 2019). For full transparency, Panel B includes all additional changes made after Spring 2020. The specific changes are depicted by the x-axis label categories which are described in Table 5.1. We point out that while most of the additional changes initially seemed trivial, changing the wording of a question in a screen from the **ne1** lesson gave a considerably negative impact on the effect size. Comparatively, the other post-Spring 2020 revisions show less significant deviations from the Spring 2020 r values. As with the spreadsheet analysis, we provide the detailed semester-by-semester data in Table D.2 in Appendix D.

5.4.3 Application Scores

Figure 5.4 shows the weighted mean scores on application lessons in the Fall 2019 semester and the average across the three modified semesters. This reveals a clear pattern of higher application scores in the modified semesters. This is confirmed by our regression model results in Table 5.2, which show the modified semesters to be associated with an increase of about six percentage points after controlling for the

effects of GPA and student major. This increase is substantial, being equivalent to roughly half a GPA point.

All of the results presented in Section 5.4 is our completion of Step 3 in Figure 5.1.

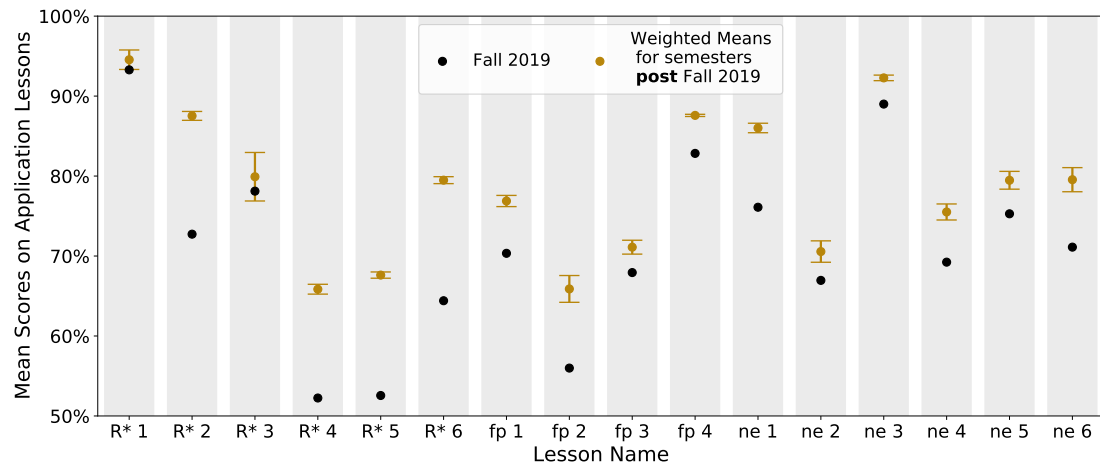


Figure 5.4: Mean scores on application lessons (quizzes) following each lesson. The x-axis is the lesson name and the y axis is the mean percentage score. Black dots represent the Fall 2019 mean percentage scores; gold dots are the weighted mean values of the post-Fall 2019 semester percentage scores. Error bars show one standard error and represent the variability among the three treatment semesters.

5.5 Discussion and Conclusions

5.5.1 Demonstrating $LA \leftrightarrow LD$ Partnership

We examined the impact spreadsheet and graph LD modifications had on student performance in the *Habitable Worlds* course. This work is a practical demonstration of the $LA \leftrightarrow LD$ synergy, following the general framework outlined in Figure 5.1. By tracking a single course before and after making LD modifications, we were able to analyze how targeted LD changes on individual screens directly impacted the students' performance on that screen. We hypothesized that students would generally take fewer attempts on the screens with LD changes in the post-Fall 2019 semesters compared to the Fall 2019 semester, and that the overall student performance would

be enhanced as a result of the LD modifications. The rest of this section demonstrates how we performed the *Assess Step* (Step 4) in Figure 5.1.

5.5.2 Spreadsheet LD Changes Analysis

Overall, our results show that the LD changes for spreadsheet questions enhanced students' ability to answer correctly with fewer attempts in the post-Fall 2019 semesters. This is readily observed in Panel A of Figure 5.3. While most of the r values are very small ($|r| < 0.1$), all but one screen produced a positive mean r value, which is in support of our hypothesis. 40.7% of the spreadsheet LD changes had at least a small effect ($r > 0.1$), with 29.6% small effects and 11.1% moderate effects. These effect sizes are comparable to those reported previously for educational technology Cheung and Slavin (2013).

The magnitude of the effects is scattered among the type of LD changes, but we can still gain some insight from Panel A regarding how effective certain spreadsheet changes were. For instance, the least effective changes with positive effects ($0.0 < r < 0.1$) were adding spreadsheet tips to a help button icon (with no additional changes) and providing feedback when answering incorrectly. Adjusting the text on the screen and adding spreadsheet tips to a help button icon was the largest contributor to positive small effects. Other changes that produced small effects were the addition of spreadsheet tips, splitting the calculation into 2 screens with added tips, and having an example/tutorial with added tips. Changes that produced moderate effects were directions to use a formula in the spreadsheet, an example/tutorial with spreadsheet tips, and a combination of directions to use a formula in the spreadsheet, a pre-question on the screen, and added tips.

The change that resulted in a small negative effect was an added icon without spreadsheet hints. The additional LD change implemented after the Spring 2020

semester (splitting the calculation and adding a question in-between the calculations) proved to worsen the effect.

We note that the larger, moderate effects were all from the **R*2** lesson. **R*2** was only 2 lessons after the **intro** lesson on how to use spreadsheets and graphs, so it's possible that the impact of the **intro** lesson was stronger at this earlier stage in the course. At the same time, **R*2**, **R*4**, **fp1**, and **fp3** had more screens with spreadsheet questions than the other lessons. At least half the **r** values from **R*2**, **R*4**, and **fp1** were greater than 0.1. Therefore, it is possible that the magnitude of **r** for a given screen may be influenced not only by the type of change, but by the recentness after the **intro** lesson and the frequency/quantity of spreadsheet questions in a given lesson.

5.5.3 Graph LD Changes Analysis

The collective effect sizes from graph LD changes in Panel B of Figure 5.3 were also nearly uniformly positive, with the exceptions being two screens giving small or very small negative effects. Most screens had the change of added interpretation questions earlier in the lesson, and that type of LD change yielded very small ($r < 0.1$) positive effects. There were not enough graph-related screens with small or moderate effects to suggest a pattern with respect to LD change type. The clarified direction in the **fp1** lesson was the only graph LD change that gave a moderate effect and the other instance of this type was also a small effect size. The strategy of adding interpretation questions earlier in the lesson generally led to very small effects, yet two of the larger effects were also of this type.

5.5.4 Application Scores

Our analysis of application lesson scores showed significant and substantial increases following the lesson modifications. The mean application scores depicted in Figure 5.4 provide an additional measurement of student performance across the 4 semesters. Most of the lessons had improved application scores in the semesters post-Fall 2019, with more noteworthy improvements in the **R*2, R*4, R*5, R*6, fp2, and ne4** lessons.

Because the application lessons demand that students apply what they learned in the training lessons in a slightly different context, they are an example of near-transfer. In addition, the application lessons were not modified during the study period, thus, increases in these scores are strong evidence of learning. Between the mostly positive, small effects on the modified training screens, and the consistent improved application scores, we have greater confidence that these changes were overall beneficial.

5.5.5 Limitations

It is important to acknowledge that the post-Fall 2019 courses occurred during the COVID-19 pandemic. This complicates our comparisons and, in fact, a separate study has shown that students at the studied university earned slightly higher grades on average in the Spring 2020 semester than in previous Spring semesters (Supriya *et al.* (2021)). In spite of this, we are confident that the reported effects are driven by the LD changes and not external factors related to the pandemic. The most important reason for this is that the course was offered fully online across all four semesters. Also important is that neither the course content itself nor the number or grading of required activities are changed by the instructor. Thus, apart from the LD changes, the level of difficulty of the course was constant in all observed semesters. Finally,

our analysis relied on the number of question attempts on each changed screen and the scores on specific lessons, rather than relying on course grades. Thus, our results would not be effected by decisions that the course instructors made with respect to letter grade cutoffs or similar discretionary actions.

As an online course, it is necessary to consider the potential of cheating. The *Habitable Worlds* course is designed to prevent cheating Horodyskyj *et al.* (2018) through the use of randomized numerical values on questions. But it would be possible for one student to create a spreadsheet and share it, allowing other students to insert their own question-given values. This would still require the students to understand the spreadsheet enough to know where to change the values. Cheating in this manner may not be much less difficult than to honestly perform the spreadsheet task. Moreover, this kind of cheating was possible in the pre-modification Fall 2019 semester as well. We consider it unlikely that cheating impacted our findings, however, we cannot fully exclude the possibility.

Another uncertainty stems from variability in students' GPA among the semesters studied. The average student GPA varies from term to term. In this case, we find that the Fall 2019 semester students had lower GPAs on average than the subsequent semesters ($M_{Fall2019} = 3.04, SD_{Fall2019} = 0.83; M_{post2019} = 3.24, SD_{post2019} = 0.78$). In part to address this potential confounder, our regression analysis of application lesson scores found a significant increase in scores in the treatment semesters, after accounting for student GPA. Thus, although the comparison semester did have the lowest average student GPA, this difference cannot account for the observed gains in scores.

Another potentially confounding factor is that Earth and Space science majors began to enroll in *Habitable Worlds* in greater numbers starting in Fall 2020. This was related to the creation of a new degree program. Previously, the course did not

fulfill any STEM degree program requirements, thus the course enrollment was almost entirely non-science students taking the course for a general education requirement. It is possible that the new Earth and Space majors might earn higher scores due to greater motivation or prior knowledge. As shown in Table 5.2, these students did in fact perform slightly better. However, the regression coefficient associated with Earth and Space majors was half that of the modified lessons and the overall effect from the modified lessons remained significant even accounting for these students.

Finally, it is important to note two other contextual factors that could lead to student performance differences in any given semester. First, the course instructor alternates each semester, with one instructor teaching each Fall term and a second teaching in the Spring terms. Although these instructors do not modify the lessons themselves, it is possible that the nature of their communication with students via email or the course discussion board may systematically influence student performance and thus the data analyzed in this study. Further, there may be differences between student performance in Fall terms and Spring terms generally. We have attempted to minimize the possibility that the differences observed between the comparison and treatment semesters are caused by a difference in instructor or season by studying the treatment effect across three different semesters. The consistency in results as observed in both Fall and Spring semesters suggests that the observed effects are due to the course modifications.

5.5.6 Conclusions

With these limitations acknowledged, our results demonstrate that the LD changes were effective in improving student performance in the *Habitable Worlds* course. In regard to *RQ1*, we saw that for both spreadsheet and graph modified screens, the effects, while small, were consistently positive. We also found the spreadsheet LD

changes to be consistently more effective than the graph LD changes. Although our analysis of relating the magnitude of \mathbf{r} as a function of the type of LD change suggests a possible correlation, there were too many uncontrolled factors within this single course study to make strong claims. However, we deem this interesting and worthy of future study.

In regard to *RQ2*, the improved application scores suggest that the LD changes in the training lessons led to students being more prepared to succeed on these assessments.

These results inform the *Habitable Worlds* course designers of the positive (and negative) impacts of their LD refinement to the Fall 2019 semester. It enables them to keep the LD changes that proved helpful, and revisit the LD changes that produced negative effects, following Step 5 in Figure 5.1, and thus completing one cycle of the LD \leftrightarrow LA loop.

In conjunction with completing one cycle of the framework in Figure 5.1, we applied several recommendations from the literature to improve the LA \leftrightarrow LD synergy, as listed in Section 5.2.4. On a broader scale, this study exemplifies how to use the LD \leftrightarrow LD syntheses beyond overall student success such as grades and failure/drop-out prediction. The detailed nature of this work charts another direction for practitioners to gain insight to a joint LA \leftrightarrow LD approach in their courses.

5.5.7 Future Work

Our results regarding differences in impact based on type of LD change are far from conclusive, but suggest an area for more careful study. Namely, future work should seek to establish a more robust set of categories for LD changes than what we were able to work with in the current study. In addition, replication of this analytical approach with larger and more varied datasets would provide insight into whether

there are generalizable trends in which types of LD changes lead to the largest benefits to student learning.

As previously stated, this work represents one cycle of Figure 5.1's LD↔LA loop. We have shared our findings with the *Habitable Worlds* learning designers. Step 5 in the cycle is for the designers to consider these effects and perform the *Iterate* step by updating LD practices based on the results from step 4 in our LD↔LA loop. We suggest retaining the LD modifications with positive effects, revising the two screens that showed negative effects, and perhaps extend beneficial LD modifications to relevant screens. This would fulfill Knobabout & Stappen's recommendation Knobabout and Van Der Stappen (2020) to apply LA when making deliberate decisions to improve various aspects of learning. Future work could examine the dynamics of these collaborations through multiple iterations.

Like virtually all LA research, this work is quantitative. Valenzuela et. al. 2021 Guzmán-Valenzuela *et al.* (2021) expresses how the growing field of LA should include a qualitative analysis in order to truly focus on students' learning. One of their key concerns for LA in higher education is the extent at which LD facilitates student learning Guzmán-Valenzuela *et al.* (2021). They suggest that students be involved in the learning design environment by asking for their perceptions of various learning processes in the course. Student interviews could be used alongside a LA-based study to paint a fuller picture of the improvements to student learning following from specific LD changes.

Finally, we encourage other LD practitioners and LA researchers to work closely in ways that are mutually beneficial, and adhere to the recommendations within the literature, such as those mentioned in this article. In particular, it would benefit the research community for more practitioners to record what LD choices impact

succeeding learning activities and performances over time and apply LA when making deliberate decisions to improve various aspects of learning.

5.6 List of Abbreviations

As defined in the text, here is the following list of abbreviations used in the manuscript:

- learning analytics (LA)
- learning design (LD)

5.7 Declarations

5.7.1 Availability of Data and Materials

We choose to not make our data publicly available due to the possibility of compromising student privacy. The interested reader may contact the corresponding author at mtaylo60@asu.edu for questions about the data or requests for data reproduction. We emphasize that any shared information must maintain student privacy and would need to be carefully filtered prior to any sharing.

5.7.2 Competing Interests

The authors declare that they have no competing interests in this section.

5.7.3 Funding

This project was supported by the National Science Foundation (Award #1936656). MTC was also supported through funding from the NSF under the Software Infrastructure for Sustained Innovation program grants (ACI-1663684, ACI-1663688, ACI-1663696), as well as grant PHY-1430152 for the Physics Frontier Center

”Joint Institute for Nuclear Astrophysics - Center for the Evolution of the Elements” (JINA-CEE).

5.7.4 Authors’ Contributions

ADA secured the funding for this project. ADA and CM contributed to the design and conceptualization. CM gathered and constructed the metadata files (.json files holding each semesters’ data regarding number of attempts, student ID, quiz scores, etc), and obtained the documentation of the specific LD modifications. CM also performed the regression analysis for the application scores. MTC performed the data analysis. This involved sorting through each lesson to determine the screens associated with the documented changes, and obtaining the effect sizes on the number of attempts for those screens. This further entailed compiling the data into the figures and tables in the manuscript. MTC wrote the initial manuscript draft. All authors contributed to the writing of the final manuscript.

5.8 Acknowledgements

We would like to thank Heather Fischer, Kimberley Preston, Nancy Staus, Martin Storksdieck, and Katy Borner for their contributions to the learning design process. We would also like to acknowledge Siobhan Sackey, Miasha Bodin for the LD work that formed the basis of this project and Judd Bowman as one of the instructors of *Habitable Worlds*.

Category	Name (ID)	Description	Lessons
Spreadsheet	S-A1	Added a help button to encourage use of a spreadsheet; ^a Split calculation to 2 screens and added question in-between calculations	fp1
	S-A2	Added spreadsheet use tips to help button.	R*3, R*4, ne1, fp2
	S-B	Feedback if wrong answer	fp3
	S-C	Split calculation into 2 screens	fp2, fp3
	S-D	Adjusted text on screen	R*1, R*4, fp1
	S-E1	Directions to use formula in spreadsheet & added pre-question to screen	R*2
	S-E2	Directions to use formula in spreadsheet	R*2
	S-F	Example/tutorial; ^a Added feedback if wrong answer	R*2, R*5
Graph	G-A	Interpretation questions prior to screen	R*2, R*3, R*4, fp2
	G-B	New HR diagram	R*4
	G-C	Clarified Directions	R*5, fp1
	G-D1	Changed question phrasing and only one answer box	ne1
	G-D2	Changed question phrasing	ne3
	G-E	feedback if wrong on first try	ne3
	G-F	Corrected "degrees" to "Kelvin"	R*4

Table 5.1: Categorization of LD Changes Studied.

^a Additional changes after the Spring 2020 semester.

Variable	Beta	SE ¹	p-value
(Intercept)	0.35	0.013	< 0.001
Modified Lessons	0.06	0.006	< 0.001
GPA	0.11	0.004	<0.001
Earth & Space Major	0.03	0.011	0.013

¹ SE=Standard Error

Table 5.2: Regression Output.

Chapter 6

SUMMARY

The stellar evolution history of a star is baked into its interior chemical stratification. White dwarfs are the end fate of most stars. The interior structure of a white dwarf is the end result of its entire evolutionary past: probing white dwarf interiors yield important implications for stellar evolution theory and observation.

The focus of my thesis centered on such implications from white dwarf seismology. I showed that white dwarf pulsations are sensitive to ^{22}Ne , within the detectable threshold, informing modelers of a systematic offset in the fitting process. This should be considered in future fitting efforts because such an offset is representative of neglecting the star's birth metallicity, and/or certain nuclear reactions that occur during stellar evolution. I then showed that certain trapped modes from variable white dwarfs may yield a potential signature for probing the $^{12}\text{C}(\alpha, \gamma)^{16}\text{O}$ reaction rate, a new probe that may help constrain the rate. I then follow this work by addressing the sensitivity of the seismic signature(s) when core overshooting is considered. Two potential pulsation signature g-modes were found to probe the $^{12}\text{C}(\alpha, \gamma)^{16}\text{O}$ reaction rate both when overshoot is or is not accounted for.

Each of these results show important considerations for stellar evolution theory and fitting to observed white dwarf pulsation data. Such considerations are important components to large scale questions, as they relate to the stellar evolution processes that ultimately form life.

This thesis also includes the educational research I was part of regarding the Habitable Worlds course offered at ASU. The results from this work inform learning designers that spreadsheet and graph coaching appears to be effective in the online

STEM course, and demonstrates a way to amplify the synergy between learning analytics and learning design.

REFERENCES

- Abbott, R., T. D. Abbott, S. Abraham, F. Acernese, K. Ackley, C. Adams, R. X. Adhikari, V. B. Adya, C. Affeldt, M. Agathos and et al., “Properties and Astrophysical Implications of the 150 M_\odot Binary Black Hole Merger GW190521”, *ApJ* **900**, 1, L13 (2020).
- Acernese, F., M. Agathos, K. Agatsuma, D. Aisa, N. Allemandou, A. Allocca, J. Amarni, P. Astone, G. Balestri, G. Ballardin and et al., “Advanced Virgo: a second-generation interferometric gravitational wave detector”, *Classical and Quantum Gravity* **32**, 2, 024001 (2015).
- Akutsu, T., M. Ando, K. Arai, Y. Arai, S. Araki, A. Araya, N. Aritomi, H. Asada, Y. Aso, S. Bae and et al., “Overview of KAGRA: Calibration, detector characterization, physical environmental monitors, and the geophysics interferometer”, *Progress of Theoretical and Experimental Physics* **2021**, 5, 05A102 (2021).
- Alsing, J., H. Peiris, J. Leja, C. Hahn, R. Tojeiro, D. Mortlock, B. Leistedt, B. D. Johnson and C. Conroy, “SPECULATOR: Emulating Stellar Population Synthesis for Fast and Accurate Galaxy Spectra and Photometry”, *ApJS* **249**, 1, 5 (2020).
- Althaus, L. G. and O. G. Benvenuto, “Evolution of Helium White Dwarfs of Low and Intermediate Masses”, *ApJ* **477**, 1, 313–334 (1997).
- Althaus, L. G. and A. H. Córscico, “New DA white dwarf models for asteroseismology of ZZ Ceti stars”, *A&A* **663**, A167 (2022).
- Althaus, L. G., P. Gil Pons, A. H. Córscico, M. Miller Bertolami, F. De Gerónimo, M. E. Camisassa, S. Torres, J. Gutierrez and A. Rebassa-Mansergas, “The formation of ultra-massive carbon-oxygen core white dwarfs and their evolutionary and pulsational properties”, arXiv e-prints p. arXiv:2011.10439 (2020).
- Anders, E. H., A. S. Jermyn, D. Lecoanet, J. R. Fuentes, L. Korre, B. P. Brown and J. S. Oishi, “Convective Boundary Mixing Processes”, *Research Notes of the American Astronomical Society* **6**, 2, 41 (2022).
- Angulo, C., M. Arnould, M. Rayet, P. Descouvemont, D. Baye, C. Leclercq-Willain, A. Coc, S. Barhoumi, P. Aguer, C. Rolfs, R. Kunz, J. Hammer, A. Mayer, T. Paradellis, S. Kossionides, C. Chronidou, K. Spyrou, S. Degl’Innocenti, G. Fiorentini, B. Ricci, S. Zavatarelli, C. Providencia, H. Wolters, J. Soares, C. Grama, J. Rahighi, A. Shotter and M. L. Rachti, “A compilation of charged-particle induced thermonuclear reaction rates”, *Nuclear Physics A* **656**, 1, 3 – 183, URL <http://www.sciencedirect.com/science/article/pii/S0375947499000305> (1999).
- Arcones, A., D. W. Bardayan, T. C. Beers, L. A. Bernstein, J. C. Blackmon, B. Messer, B. A. Brown, E. F. Brown, C. R. Brune, A. E. Champagne, A. Chieffi, A. J. Couture, P. Danielewicz, R. Diehl, M. El-Eid, J. E. Escher, B. D. Fields, C. Fröhlich, F. Herwig, W. R. Hix, C. Iliadis, W. G. Lynch, G. C. McLaughlin, B. S. Meyer, A. Mezzacappa, F. Nunes, B. W. O’Shea, M. Prakash, B. Pritychenko,

- S. Reddy, E. Rehm, G. Rogachev, R. E. Rutledge, H. Schatz, M. S. Smith, I. H. Stairs, A. W. Steiner, T. E. Strohmayer, F. X. Timmes, D. M. Townsley, M. Wiesscher, R. G. T. Zegers and M. Zingale, “White paper on nuclear astrophysics and low energy nuclear physics Part 1: Nuclear astrophysics”, *Progress in Particle and Nuclear Physics* **94**, 1–67 (2017).
- Arnett, D., *Supernovae and Nucleosynthesis: An Investigation of the History of Matter, from the Big Bang to the Present* (Princeton University Press, 1996).
- Asplund, M., N. Grevesse, A. J. Sauval and P. Scott, “The Chemical Composition of the Sun”, *ARA&A* **47**, 1, 481–522 (2009).
- Baines, P. G. and A. E. Gill, “On thermohaline convection with linear gradients”, *Journal of Fluid Mechanics* **37**, 289–306 (1969).
- Balona, L. A. and D. Ozuyar, “Pulsation among TESS A and B stars and the Maia variables”, *MNRAS* **493**, 4, 5871–5879 (2020).
- Bauer, E. B. and L. Bildsten, “Increases to Inferred Rates of Planetesimal Accretion due to Thermohaline Mixing in Metal-accreting White Dwarfs”, *ApJ* **859**, L19 (2018).
- Bauer, E. B., J. Schwab, L. Bildsten and S. Cheng, “Multi-Gigayear White Dwarf Cooling Delays from Clustering-Enhanced Gravitational Sedimentation”, arXiv e-prints p. arXiv:2009.04025 (2020).
- Becker, S. A. and I. Iben, Jr., “The asymptotic giant branch evolution of intermediate-mass stars as a function of mass and composition. I - Through the second dredge-up phase”, *ApJ* **232**, 831–853 (1979).
- Becker, S. A. and I. Iben, Jr., “The asymptotic giant branch evolution of intermediate-mass stars as a function of mass and composition. II - Through the first major thermal pulse and the consequences of convective dredge-up”, *ApJ* **237**, 111–129 (1980).
- Bell, K. J., A. H. Córscico, A. Bischoff-Kim, L. G. Althaus, P. A. Bradley, L. M. Calcaferro, M. H. Montgomery, M. Uzundag, A. S. Baran, Z. Bognár, S. Charpinet, H. Ghasemi and J. J. Hermes, “TESS first look at evolved compact pulsators. Asteroseismology of the pulsating helium-atmosphere white dwarf TIC 257459955”, *A&A* **632**, A42 (2019).
- Bellinger, E. P., G. C. Angelou, S. Hekker, S. Basu, W. H. Ball and E. Guggenberger, “Fundamental Parameters of Main-Sequence Stars in an Instant with Machine Learning”, *ApJ* **830**, 31 (2016).
- Ben-Naim, D., *A software architecture that promotes pedagogical ownership in intelligent tutoring systems.*, Ph.D. thesis, University of New South Wales, Sydney, Australia (2010).
- Bethe, H. A., “Energy production in stars”, *Phys. Rev.* **55**, 434–456, URL <http://link.aps.org/doi/10.1103/PhysRev.55.434> (1939).

- Bildsten, L. and D. M. Hall, “Gravitational Settling of ^{22}Ne in Liquid White Dwarf Interiors”, *ApJ***549**, L219–L223 (2001).
- Bischoff-Kim, A. and M. H. Montgomery, “WDEC: A Code for Modeling White Dwarf Structure and Pulsations”, *AJ***155**, 187 (2018).
- Bischoff-Kim, A., R. H. Østensen, J. J. Hermes and J. L. Provencal, “Seven-period Asteroseismic Fit of the Kepler DBV”, *ApJ***794**, 1, 39 (2014a).
- Bischoff-Kim, A., R. H. Østensen, J. J. Hermes and J. L. Provencal, “Seven-period Asteroseismic Fit of the Kepler DBV”, *ApJ***794**, 39 (2014b).
- Bischoff-Kim, A., J. L. Provencal, P. A. Bradley, M. H. Montgomery, H. L. Shipman, S. T. Harrold, B. Howard, W. Strickland, D. Chandler, D. Campbell, A. Arredondo, R. Linn, D. P. Russell, D. Doyle, A. Brickhouse, D. Peters, S. L. Kim, X. J. Jiang, Y. N. Mao, A. V. Kusakin, A. V. Sergeev, M. Andreev, S. Velichko, R. Janulis, E. Pakstiene, F. Aliçavuş, N. Horoz, S. Zola, W. Ogłozna, D. Koziel-Wierzbowska, T. Kundera, D. Jableka, B. Debski, A. Baran, S. Meingast, T. Nagel, L. Loebling, C. Heinitz, D. Hoyer, Z. Bognár, B. G. Castanheira and A. Erdem, “GD358: Three Decades of Observations for the In-depth Asteroseismology of a DBV Star”, *ApJ***871**, 1, 13 (2019).
- Blöcker, T., “Evolution on the AGB and beyond: on the formation of H-deficient post-AGB stars”, *Ap&SS***275**, 1–14 (2001).
- Bloecker, T., “Stellar evolution of low- and intermediate-mass stars. II. Post-AGB evolution.”, *A&A***299**, 755 (1995a).
- Bloecker, T., “Stellar evolution of low and intermediate-mass stars. I. Mass loss on the AGB and its consequences for stellar evolution.”, *A&A***297**, 727 (1995b).
- Blondin, S., E. Bravo, F. X. Timmes, L. Dessart and D. J. Hillier, “Stable nickel production in type Ia supernovae: A smoking gun for the progenitor mass?”, *A&A***660**, A96 (2022).
- Blouin, S., H. Mao, F. Herwig, P. Denissenkov, P. R. Woodward and W. R. Thompson, “3D hydrodynamics simulations of internal gravity waves in red giant branch stars”, arXiv e-prints p. arXiv:2303.07332 (2023).
- Blouin, S., N. R. Shaffer, D. Saumon and C. E. Starrett, “New Conductive Opacities for White Dwarf Envelopes”, *ApJ***899**, 1, 46 (2020).
- Blumenstein, M., “Synergies of learning analytics and learning design: A systematic review of student outcomes”, *Journal of Learning Analytics* **7**, 3, 13–32, URL <https://learning-analytics.info/index.php/JLA/article/view/7004> (2020).
- Borexino Collaboration, M. Agostini, K. Altenmüller, S. Appel, V. Atroshchenko, Z. Bagdasarian, D. Basilico, G. Bellini, J. Benziger, D. Bick, G. Bonfini, D. Bravo, B. Caccianiga, F. Calaprice, A. Caminata, S. Caprioli, M. Carlini, P. Cavalcanete, A. Chepurnov, K. Choi, L. Collica, D. D’Angelo, S. Davini, A. Derbin,

X. F. Ding, A. Di Ludovico, L. Di Noto, I. Drachnev, K. Fomenko, A. Formozov, D. Franco, F. Gabriele, C. Galbiati, C. Ghiano, M. Giammarchi, A. Goretti, M. Gromov, D. Guffanti, C. Hagner, T. Houdy, E. Hungerford, A. Ianni, A. Ianni, A. Jany, D. Jeschke, V. Kobylev, D. Koralev, G. Korga, D. Kryn, M. Laubenstein, E. Litvinovich, F. Lombardi, P. Lombardi, L. Ludhova, G. Lukyanchenko, L. Lukyanchenko, I. Machulin, G. Manuzio, S. Marcocci, J. Martyn, E. Meroni, M. Meyer, L. Miramonti, M. Misiaszek, V. Muratova, B. Neumair, L. Oberauer, B. Opitz, V. Orekhov, F. Ortica, M. Pallavicini, L. Papp, Ö. Penek, N. Pilipenko, A. Pocar, A. Porcelli, G. Raikov, G. Ranucci, A. Razeto, A. Re, M. Redchuk, A. Romani, R. Roncin, N. Rossi, S. Schönert, D. Semenov, M. Skorokhvatov, O. Smirnov, A. Sotnikov, L. F. F. Stokes, Y. Suvorov, R. Tartaglia, G. Testera, J. Thurn, M. Toropova, E. Unzhakov, F. L. Villante, A. Vishneva, R. B. Vogelaar, F. von Feilitzsch, H. ang, S. Weinz, M. Wojcik, M. Wurm, Z. Yokley, O. Zaimidoroga, S. Zavatarelli, K. Zuber and G. Zuzel, “Comprehensive measurement of pp-chain solar neutrinos”, *Nature***562**, 7728, 505–510 (2018).

Borexino Collaboration, M. Agostini, K. Altenmüller, S. Appel, V. Atroshchenko, Z. Bagdasarian, D. Basilico, G. Bellini, J. Benziger, D. Bick, G. Bonfini, D. Bravo, B. Caccianiga, F. Calaprice, A. Caminata, S. Caprioli, M. Carlini, P. Cavalcalante, A. Chepurnov, K. Choi, L. Collica, D. D’Angelo, S. Davini, A. Derbin, X. F. Ding, A. Di Ludovico, L. Di Noto, I. Drachnev, K. Fomenko, A. Formozov, D. Franco, F. Gabriele, C. Galbiati, C. Ghiano, M. Giammarchi, A. Goretti, M. Gromov, D. Guffanti, C. Hagner, T. Houdy, E. Hungerford, A. Ianni, A. Ianni, A. Jany, D. Jeschke, V. Kobylev, D. Koralev, G. Korga, D. Kryn, M. Laubenstein, E. Litvinovich, F. Lombardi, P. Lombardi, L. Ludhova, G. Lukyanchenko, L. Lukyanchenko, I. Machulin, G. Manuzio, S. Marcocci, J. Martyn, E. Meroni, M. Meyer, L. Miramonti, M. Misiaszek, V. Muratova, B. Neumair, L. Oberauer, B. Opitz, V. Orekhov, F. Ortica, M. Pallavicini, L. Papp, Ö. Penek, N. Pilipenko, A. Pocar, A. Porcelli, G. Raikov, G. Ranucci, A. Razeto, A. Re, M. Redchuk, A. Romani, R. Roncin, N. Rossi, S. Schönert, D. Semenov, M. Skorokhvatov, O. Smirnov, A. Sotnikov, L. F. F. Stokes, Y. Suvorov, R. Tartaglia, G. Testera, J. Thurn, M. Toropova, E. Unzhakov, F. L. Villante, A. Vishneva, R. B. Vogelaar, F. von Feilitzsch, H. ang, S. Weinz, M. Wojcik, M. Wurm, Z. Yokley, O. Zaimidoroga, S. Zavatarelli, K. Zuber and G. Zuzel, “Experimental evidence of neutrinos produced in the CNO fusion cycle in the Sun”, *Nature***587**, 7728, 577–582 (2020).

Bos, N. and S. Brand-Gruwel, “Student differences in regulation strategies and their use of learning resources: Implications for educational design”, in “Proceedings of the Sixth International Conference on Learning Analytics & Knowledge”, LAK ’16, p. 344–353 (Association for Computing Machinery, New York, NY, USA, 2016), URL <https://doi.org/10.1145/2883851.2883890>.

Boulanger, J., N. Clementel, A. J. van Marle, L. Decin and A. de Koter, “Developing a self-consistent AGB wind model - I. Chemical, thermal, and dynamical coupling”, *MNRAS***482**, 4, 5052–5077 (2019).

- Brassard, P., G. Fontaine, F. Wesemael and C. J. Hansen, “Adiabatic properties of pulsating DA white dwarfs. II - Mode trapping in compositionally stratified models”, *ApJS***80**, 369–401 (1992a).
- Brassard, P., G. Fontaine, F. Wesemael, S. D. Kawaler and M. Tassoul, “Adiabatic properties of pulsating DA white dwarfs. I - The treatment of the Brunt-Vaisala frequency and the region of period formation”, *ApJ***367**, 601–611 (1991).
- Brassard, P., G. Fontaine, F. Wesemael and M. Tassoul, “Adiabatic Properties of Pulsating DA White Dwarfs. IV. an Extensive Survey of the Period Structure of Evolutionary Models”, *ApJS***81**, 747 (1992b).
- Bravo, E., I. Domínguez, C. Badenes, L. Piersanti and O. Straniero, “Metallicity as a Source of Dispersion in the SNIa Bolometric Light Curve Luminosity-Width Relationship”, *ApJ***711**, L66–L70 (2010).
- Bravo, E., J. Isern, R. Canal and J. Labay, “On the contribution of Ne-22 to the synthesis of Fe-54 and Ni-58 in thermonuclear supernovae”, *A&A***257**, 534–538 (1992).
- Brown, J. M., P. Garaud and S. Stellmach, “Chemical Transport and Spontaneous Layer Formation in Fingering Convection in Astrophysics”, *ApJ***768**, 34 (2013).
- Burbidge, E. M., G. R. Burbidge, W. A. Fowler and F. Hoyle, “Synthesis of the elements in stars”, Rev. Mod. Phys. **29**, 547–650, URL <https://link.aps.org/doi/10.1103/RevModPhys.29.547> (1957a).
- Burbidge, E. M., G. R. Burbidge, W. A. Fowler and F. Hoyle, “Synthesis of the elements in stars”, Rev. Mod. Phys. **29**, 547–650, URL <http://link.aps.org/doi/10.1103/RevModPhys.29.547> (1957b).
- Camisassa, M. E., L. G. Althaus, A. H. Córscico, N. Vinyoles, A. M. Serenelli, J. Isern, M. M. Miller Bertolami and E. García-Berro, “The Effect of ^{22}Ne Diffusion in the Evolution and Pulsational Properties of White Dwarfs with Solar Metallicity Progenitors”, *ApJ***823**, 2, 158 (2016).
- Caputo, F., V. Castellani, A. Chieffi, L. Pulone and J. Tornambe, A., “The “Red Giant Clock” as an Indicator for the Efficiency of Central Mixing in Horizontal-Branch Stars”, *ApJ***340**, 241 (1989).
- Cassisi, S., A. Y. Potekhin, A. Pietrinferni, M. Catelan and M. Salaris, “Updated Electron-Conduction Opacities: The Impact on Low-Mass Stellar Models”, *ApJ***661**, 1094–1104 (2007).
- Cassisi, S., M. Salaris and A. W. Irwin, “The Initial Helium Content of Galactic Globular Cluster Stars from the R-Parameter: Comparison with the Cosmic Microwave Background Constraint”, *ApJ***588**, 2, 862–870 (2003).
- Chandrasekhar, S., “The Maximum Mass of Ideal White Dwarfs”, *ApJ***74**, 81 (1931).

- Charpinet, S., P. Brassard, N. Giammichele and G. Fontaine, “Improved seismic model of the pulsating DB white dwarf KIC 08626021 corrected from the effects of neutrino cooling”, *A&A***628**, L2 (2019).
- Cheng, S., J. D. Cummings and B. Ménard, “A Cooling Anomaly of High-mass White Dwarfs”, *ApJ***886**, 2, 100 (2019).
- Cheung, A. C. and R. E. Slavin, “The effectiveness of educational technology applications for enhancing mathematics achievement in k-12 classrooms: A meta-analysis”, *Educational Research Review* **9**, 88 – 113, URL <http://www.sciencedirect.com/science/article/pii/S1747938X13000031> (2013).
- Chidester, M. T., E. Farag and F. X. Timmes, “On Trapped Modes in Variable White Dwarfs as Probes of the $^{12}\text{C}(\alpha, \gamma)^{16}\text{O}$ Reaction Rate”, *ApJ***935**, 1, 21 (2022).
- Chidester, M. T., F. X. Timmes, J. Schwab, R. H. D. Townsend, E. Farag, A. Thoul, C. E. Fields, E. B. Bauer and M. H. Montgomery, “On the impact of 22ne on the pulsation periods of carbon–oxygen white dwarfs with helium-dominated atmospheres”, *The Astrophysical Journal* **910**, 1, 24, URL <http://dx.doi.org/10.3847/1538-4357/abdec4> (2021).
- Choi, J., A. Dotter, C. Conroy, M. Cantiello, B. Paxton and B. D. Johnson, “Mesa Isochrones and Stellar Tracks (MIST). I. Solar-scaled Models”, *ApJ***823**, 102 (2016).
- Chugunov, A. I., H. E. DeWitt and D. G. Yakovlev, “Coulomb tunneling for fusion reactions in dense matter: Path integral MonteCarlo versus mean field”, *Phys. Rev. D***76**, 2, 025028 (2007).
- Cohen, J., “Statistical power analysis”, *Current Directions in Psychological Science* **1**, 3, 98–101, URL <https://doi.org/10.1111/1467-8721.ep10768783> (1992).
- Collins, C. E., S. Gronow, S. A. Sim and F. K. Röpke, “Double detonations: variations in Type Ia supernovae due to different core and He shell masses - II. Synthetic observables”, *MNRAS***517**, 4, 5289–5302 (2022).
- Constantino, T., S. W. Campbell, J. Christensen-Dalsgaard, J. C. Lattanzio and D. Stello, “The treatment of mixing in core helium burning models - I. Implications for asteroseismology”, *MNRAS***452**, 123–145 (2015).
- Constantino, T., S. W. Campbell and J. C. Lattanzio, “The treatment of mixing in core helium-burning models - III. Suppressing core breathing pulses with a new constraint on overshoot”, *MNRAS***472**, 4900–4909 (2017).
- Constantino, T., S. W. Campbell, J. C. Lattanzio and A. van Duijneveldt, “The treatment of mixing in core helium burning models - II. Constraints from cluster star counts”, *MNRAS***456**, 4, 3866–3885 (2016).
- Cook, K. J., A. Chevis, T. K. Eriksen, E. C. Simpson, T. Kibédi, L. T. Bezzina, A. C. Berriman, J. Buete, I. P. Carter, M. Dasgupta, D. J. Hinde, D. Y. Jeung, P. McGlynn, S. Parker-Steele, B. M. A. Swinton-Bland, T. Tanaka and W. Wojtaczka, “High-precision proton angular distribution measurements of $^{12}\text{C}(\text{p}, \text{p}')$ for

the determination of the E 0 decay branching ratio of the Hoyle state”, *Phys. Rev. C***104**, 2, 024620 (2021).

Córsico, A. H., L. G. Althaus, O. G. Benvenuto and A. M. Serenelli, “The mode trapping properties of full DA white dwarf evolutionary models”, *A&A***387**, 531–549 (2002).

Córsico, A. H., L. G. Althaus, M. M. Miller Bertolami and S. O. Kepler, “Pulsating white dwarfs: new insights”, *The Astronomy and Astrophysics Review***27**, 1, 7 (2019).

Córsico, A. H., M. Uzundag, S. O. Kepler, R. Silvotti, L. G. Althaus, D. Koester, A. S. Baran, K. J. Bell, A. Bischoff-Kim, J. J. Hermes, S. D. Kawaler, J. L. Provencal, D. E. Winget, M. H. Montgomery, P. A. Bradley, S. J. Kleinman and A. Nitta, “Pulsating hydrogen-deficient white dwarfs and pre-white dwarfs observed with TESS. III. Asteroseismology of the DBV star GD 358”, *A&A***659**, A30 (2022).

Costa, J. E. S., S. O. Kepler, D. E. Winget, M. S. O’Brien, S. D. Kawaler, A. F. M. Costa, O. Giovannini, A. Kanaan, A. S. Mukadam, F. Mullally, A. Nitta, J. L. Provençal, H. Shipman, M. A. Wood, T. J. Ahrens, A. Grauer, M. Kilic, P. A. Bradley, K. Sekiguchi, R. Crowe, X. J. Jiang, D. Sullivan, T. Sullivan, R. Rosen, J. C. Clemens, R. Janulis, D. O’Donoghue, W. Ogloza, A. Baran, R. Silvotti, S. Marinoni, G. Vauclair, N. Dolez, M. Chevreton, S. Dreizler, S. Schuh, J. Deetjen, T. Nagel, J. E. Solheim, J. M. Gonzalez Perez, A. Ulla, M. Barstow, M. Burleigh, S. Good, T. S. Metcalfe, S. L. Kim, H. Lee, A. Sergeev, M. C. Akan, Ö. Çakırlı, M. Paparo, G. Viraghalmay, B. N. Ashoka, G. Handler, Ö. Hürkal, F. Johannessen, S. J. Kleinman, R. Kalytis, J. Krzesinski, E. Klumpe, J. Larrison, T. Lawrence, E. Meištas, P. Martinez, R. E. Nather, J. N. Fu, E. Pakštienė, R. Rosen, E. Romero-Colmenero, R. Riddle, S. Seetha, N. M. Silvestri, M. Vučković, B. Warner, S. Zola, L. G. Althaus, A. H. Córsico and M. H. Montgomery, “The pulsation modes of the pre-white dwarf PG 1159-035”, *A&A***477**, 2, 627–640 (2008).

Cyburt, R. H., A. M. Amthor, R. Ferguson, Z. Meisel, K. Smith, S. Warren, A. Heger, R. D. Hoffman, T. Rauscher, A. Sakharuk, H. Schatz, F. K. Thielemann and M. Wiesscher, “The JINA REACLIB Database: Its Recent Updates and Impact on Type-I X-ray Bursts”, *ApJS***189**, 240–252 (2010).

D’Antona, F. and I. Mazzitelli, “Cooling of white dwarfs.”, *ARA&A***28**, 139–181 (1990).

Das, U. and B. Mukhopadhyay, “New mass limit for white dwarfs: Super-chandrasekhar type ia supernova as a new standard candle”, *Phys. Rev. Lett.* **110**, 071102, URL <https://link.aps.org/doi/10.1103/PhysRevLett.110.071102> (2013).

De Gerónimo, F. C., L. G. Althaus, A. H. Córsico, A. D. Romero and S. O. Kepler, “Asteroseismology of ZZ Ceti stars with fully evolutionary white dwarf models. I. The impact of the uncertainties from prior evolution on the period spectrum”, *A&A***599**, A21 (2017).

- De Gerónimo, F. C., T. Battich, M. M. Miller Bertolami, L. G. Althaus and A. H. Cársico, “On the recent parametric determination of an asteroseismological model for the DBV star KIC 08626021”, *A&A***630**, A100 (2019).
- deBoer, R. J., J. Görres, M. Wiescher, R. E. Azuma, A. Best, C. R. Brune, C. E. Fields, S. Jones, M. Pignatari, D. Sayre, K. Smith, F. X. Timmes and E. Uberseder, “The $^{12}\text{C}(\alpha,\gamma)^{16}\text{O}$ reaction and its implications for stellar helium burning”, *Reviews of Modern Physics* **89**, 3, 035007 (2017).
- Deloye, C. J. and L. Bildsten, “Gravitational Settling of ^{22}Ne in Liquid White Dwarf Interiors: Cooling and Seismological Effects”, *ApJ***580**, 1077–1090 (2002).
- Demarque, P. and J. G. Mengel, “Advanced Evolution of Population II Stars. I. Red Giants and the Helium Flash”, *ApJ***164**, 317 (1971).
- Denissenkov, P. A., F. Herwig, J. W. Truran and B. Paxton, “The C-flame Quenching by Convective Boundary Mixing in Super-AGB Stars and the Formation of Hybrid C/O/Ne White Dwarfs and SN Progenitors”, *ApJ***772**, 37 (2013).
- Descouvemont, P., “Nuclear reactions of astrophysical interest”, *Frontiers in Astronomy and Space Sciences* **7**, URL <https://www.frontiersin.org/articles/10.3389/fspas.2020.00009> (2020).
- Donnelly-Hermosillo, D. F., L. F. Gerard and M. C. Linn, “Impact of graph technologies in k-12 science and mathematics education”, *Computers & Education* **146**, 103748, URL <http://www.sciencedirect.com/science/article/pii/S036013151930301X> (2020).
- Dotter, A., “MESA Isochrones and Stellar Tracks (MIST) 0: Methods for the Construction of Stellar Isochrones”, *ApJS***222**, 8 (2016).
- Dror, B.-N., H. Shaowei, B. Zack and S. Ariel, “About smart sparrow”, <https://www.smartsparrow.com/technology/> (2018).
- Duan, R. M., W. Zong, J. N. Fu, Y. H. Chen, J. J. Hermes, Z. P. Vanderbosch, X. Y. Ma and S. Charpinet, “EPIC 228782059: Asteroseismology of What Could Be the Coolest Pulsating Helium-atmosphere White Dwarf (DBV) Known”, *ApJ***922**, 1, 2 (2021).
- Dufour, P., S. Blouin, S. Coutu, M. Fortin-Archambault, C. Thibeault, P. Bergeron and G. Fontaine, “The montreal white dwarf database: a tool for the community”, (2016).
- Dufour, P., S. Blouin, S. Coutu, M. Fortin-Archambault, C. Thibeault, P. Bergeron and G. Fontaine, “The Montreal White Dwarf Database: A Tool for the Community”, in “20th European White Dwarf Workshop”, edited by P. E. Tremblay, B. Gaensicke and T. Marsh, vol. 509 of *Astronomical Society of the Pacific Conference Series*, p. 3 (2017).
- Dupree, A. K., “Mass loss from cool stars”, *ARA&A***24**, 377–420 (1986).

- Dziembowski, W. A., “Nonradial Oscillations of Evolved Stars. I. Quasiadiabatic Approximation”, *Acta Astron.***21**, 289–306 (1971).
- Eggleton, P. P., “Composition changes during stellar evolution”, *MNRAS***156**, 361 (1972).
- Endal, A. S. and S. Sofia, “The evolution of rotating stars. II - Calculations with time-dependent redistribution of angular momentum for 7- and 10-solar-mass stars”, *ApJ***220**, 279–290 (1978).
- Eriksen, T. K., T. Kibédi, M. W. Reed, A. E. Stuchbery, K. J. Cook, A. Akber, B. Alshahrani, A. A. Avaa, K. Banerjee, A. C. Berriman, L. T. Bezzina, L. Bignell, J. Buete, I. P. Carter, B. J. Coombes, J. T. H. Dowie, M. Dasgupta, L. J. Evitts, A. B. Garnsworthy, M. S. M. Gerathy, T. J. Gray, D. J. Hinde, T. H. Hoang, S. S. Hota, E. Ideguchi, P. Jones, G. J. Lane, B. P. McCormick, A. J. Mitchell, N. Palalani, T. Palazzo, M. Ripper, E. C. Simpson, J. Smallcombe, B. M. A. Swinton-Bland, T. Tanaka, T. G. Tornyi and M. O. de Vries, “Improved precision on the experimental E 0 decay branching ratio of the Hoyle state”, *Phys. Rev. C***102**, 2, 024320 (2020).
- Farag, E., M. Renzo, R. Farmer, M. T. Chidester and F. X. Timmes, “Resolving the Peak of the Black Hole Mass Spectrum”, *ApJ***937**, 2, 112 (2022).
- Farag, E., F. X. Timmes, M. Taylor, K. M. Patton and R. Farmer, “On Stellar Evolution in a Neutrino Hertzsprung-Russell Diagram”, *ApJ***893**, 2, 133 (2020).
- Farmer, R., C. E. Fields, I. Petermann, L. Dessart, M. Cantiello, B. Paxton and F. X. Timmes, “On Variations Of Pre-supernova Model Properties”, *ApJS***227**, 22 (2016).
- Farmer, R., C. E. Fields and F. X. Timmes, “On Carbon Burning in Super Asymptotic Giant Branch Stars”, *ApJ***807**, 184 (2015).
- Farmer, R., M. Renzo, S. de Mink, M. Fishbach and S. Justham, “Constraints from gravitational wave detections of binary black hole mergers on the $^{12}\text{C}(\alpha, \gamma)^{16}\text{O}$ rate”, arXiv e-prints p. arXiv:2006.06678 (2020).
- Farmer, R., M. Renzo, S. E. de Mink, P. Marchant and S. Justham, “Mind the Gap: The Location of the Lower Edge of the Pair-instability Supernova Black Hole Mass Gap”, *ApJ***887**, 1, 53 (2019).
- Ferguson, J. W., D. R. Alexander, F. Allard, T. Barman, J. G. Bodnarik, P. H. Hauschildt, A. Heffner-Wong and A. Tamai, “Low-Temperature Opacities”, *ApJ***623**, 1, 585–596 (2005a).
- Ferguson, J. W., D. R. Alexander, F. Allard, T. Barman, J. G. Bodnarik, P. H. Hauschildt, A. Heffner-Wong and A. Tamai, “Low-Temperature Opacities”, *ApJ***623**, 1, 585–596 (2005b).
- Fields, C. E., *Multidimensional Hydrodynamic Simulations of Massive Stars and Their Explosions*, Ph.D. thesis, Michigan State University (2021).

- Fields, C. E., R. Farmer, I. Petermann, C. Iliadis and F. X. Timmes, “Properties of Carbon-Oxygen White Dwarfs From Monte Carlo Stellar Models”, *ApJ***823**, 46 (2016).
- Fields, C. E., F. X. Timmes, R. Farmer, I. Petermann, W. M. Wolf and S. M. Couch, “The Impact of Nuclear Reaction Rate Uncertainties on the Evolution of Core-collapse Supernova Progenitors”, *ApJS***234**, 19 (2018).
- Fontaine, G. and P. Brassard, “Can White Dwarf Asteroseismology Really Constrain the $^{12}\text{C}(\alpha, \gamma)^{16}\text{O}$ Reaction Rate?”, *ApJ***581**, L33–L37 (2002).
- Fontaine, G. and P. Brassard, “The Pulsating White Dwarf Stars”, *PASP***120**, 1043 (2008).
- Fontaine, G., P. Brassard and P. Bergeron, “The Potential of White Dwarf Cosmochronology”, *PASP***113**, 409–435 (2001).
- Fowler, W. A., “Experimental and theoretical nuclear astrophysics: the quest for the origin of the elements”, *Reviews of Modern Physics* **56**, 2, 149–179 (1984a).
- Fowler, W. A., “The Quest for the Origin of the Elements”, *Science* **226**, 4677, 922–935 (1984b).
- Fowler, W. A. and F. Hoyle, “Neutrino Processes and Pair Formation in Massive Stars and Supernovae.”, *ApJS***9**, 201–+ (1964).
- Fritz, C., P. Morris and J. Richler, “Effect size estimates: Current use, calculations, and interpretation”, *Journal of experimental psychology. General* **141**, 2–18 (2011).
- Fryer, C. L. and V. Kalogera, “Theoretical Black Hole Mass Distributions”, *ApJ***554**, 1, 548–560 (2001).
- Fuller, G. M., W. A. Fowler and M. J. Newman, “Stellar weak interaction rates for intermediate-mass nuclei. IV - Interpolation procedures for rapidly varying lepton capture rates using effective log (ft)-values”, *ApJ***293**, 1–16 (1985).
- Garaud, P., “Double-Diffusive Convection at Low Prandtl Number”, *Annual Review of Fluid Mechanics* **50**, 1, 275–298 (2018).
- García-Berro, E., C. Ritossa and I. Iben, Jr., “On the Evolution of Stars that Form Electron-Degenerate Cores Processed by Carbon Burning. III. The Inward Propagation of a Carbon-Burning Flame and Other Properties of a 9 Msun Model Star”, *ApJ***485**, 2, 765, URL <http://stacks.iop.org/0004-637X/485/i=2/a=765> (1997).
- Gautschy, A., “Helium Ignition in the Cores of Low-Mass Stars”, ArXiv e-prints (2012).
- Gautschy, A., “On an Early - Post-AGB Instability”, arXiv e-prints p. arXiv:2303.11374 (2023).

- Giacobbo, N. and M. Mapelli, “The progenitors of compact-object binaries: impact of metallicity, common envelope and natal kicks”, *MNRAS***480**, 2, 2011–2030 (2018).
- Giammichele, N., S. Charpinet and P. Brassard, “Seismic Cartography of White-Dwarf Interiors From the Toulouse-Montréal Optimal-Design Approach”, *Frontiers in Astronomy and Space Sciences* **9**, 879045 (2022).
- Giammichele, N., S. Charpinet, P. Brassard and G. Fontaine, “The potential of asteroseismology for probing the core chemical stratification in white dwarf stars”, *A&A***598**, A109 (2017a).
- Giammichele, N., S. Charpinet, G. Fontaine and P. Brassard, “Toward High-precision Seismic Studies of White Dwarf Stars: Parametrization of the Core and Tests of Accuracy”, *ApJ***834**, 136 (2017b).
- Giammichele, N., S. Charpinet, G. Fontaine, P. Brassard, E. M. Green, V. Van Grootel, P. Bergeron, W. Zong and M.-A. Dupret, “A large oxygen-dominated core from the seismic cartography of a pulsating white dwarf”, *Nature***554**, 73–76 (2018).
- Guichandut, S. and A. Cumming, “The imprint of convection on Type I X-ray bursts: Pauses in photospheric radius expansion lightcurves”, arXiv e-prints p. arXiv:2301.08769 (2023).
- Guzmán-Valenzuela, C., C. Gómez-González, A. Rojas-Murphy Tagle and A. Lorca-Vyhmeister, “Learning analytics in higher education: a preponderance of analytics but very little learning?”, *International Journal of Educational Technology in Higher Education* **18** (2021).
- Hansen, C. J. and S. D. Kawaler, *Stellar Interiors. Physical Principles, Structure, and Evolution.* (New York: Springer-Verlag, 1994a).
- Hansen, C. J. and S. D. Kawaler, *Stellar Interiors. Physical Principles, Structure, and Evolution.* (Springer New York, NY, 1994b).
- Hansen, C. J., S. D. Kawaler and V. Trimble, *Stellar interiors : physical principles, structure, and evolution* (New York: Springer-Verlag, 2004).
- Heger, A., N. Langer and S. E. Woosley, “Presupernova Evolution of Rotating Massive Stars. I. Numerical Method and Evolution of the Internal Stellar Structure”, *ApJ***528**, 368–396 (2000).
- Heger, A. and S. E. Woosley, “The Nucleosynthetic Signature of Population III”, *ApJ***567**, 532–543 (2002).
- Heger, A., S. E. Woosley and H. C. Spruit, “Presupernova Evolution of Differentially Rotating Massive Stars Including Magnetic Fields”, *ApJ***626**, 350–363 (2005).
- Hekker, S. and J. Christensen-Dalsgaard, “Giant star seismology”, *The Astronomy and Astrophysics Review***25**, 1, 1 (2017).

- Hermes, J. J., S. D. Kawaler, A. Bischoff-Kim, J. L. Provencal, B. H. Dunlap and J. C. Clemens, “A Deep Test of Radial Differential Rotation in a Helium-atmosphere White Dwarf. I. Discovery of Pulsations in PG 0112+104”, *ApJ***835**, 2, 277 (2017).
- Hernández-Leo, D., R. Martínez-Maldonado, A. Pardo, J. Muñoz-Cristóbal and M. Rodríguez-Triana, “Analytics for learning design: a layered framework and tools”, *British Journal of Educational Technology* **50**, 1, 139–152 (2018).
- Herwig, F., “The evolution of agb stars with convective overshoot”, URL <https://arxiv.org/abs/astro-ph/0007139> (2000).
- Herwig, F., “The evolution of AGB stars with convective overshoot”, *A&A***360**, 952–968 (2000).
- Herwig, F., “Evolution of Asymptotic Giant Branch Stars”, *ARA&A***43**, 435–479 (2005).
- Hon, M., D. Stello and J. C. Zinn, “Detecting Solar-like Oscillations in Red Giants with Deep Learning”, *ApJ***859**, 1, 64 (2018).
- Horodyskyj, L. B., C. Mead, Z. Belinson, S. Buxner, S. Semken and A. D. Anbar, “Habitable worlds: Delivering on the promises of online education”, *Astrobiology* **18**, 1, 86–99, URL <https://doi.org/10.1089/ast.2016.1550>, pMID: 29345987 (2018).
- Howell, D. A., M. Sullivan, E. F. Brown, A. Conley, D. LeBorgne, E. Y. Hsiao, P. Astier, D. Balam, C. Balland, S. Basa, R. G. Carlberg, D. Fouchez, J. Guy, D. Hardin, I. M. Hook, R. Pain, K. Perrett, C. J. Pritchett, N. Regnault, S. Baumont, J. LeDu, C. Lidman, S. Perlmutter, N. Suzuki, E. S. Walker and J. C. Wheeler, “The Effect of Progenitor Age and Metallicity on Luminosity and ^{56}Ni Yield in Type Ia Supernovae”, *ApJ***691**, 661–671 (2009).
- Hoyle, F., “On Nuclear Reactions Occuring in Very Hot STARS.I. the Synthesis of Elements from Carbon to Nickel.”, *Astrophys. J. Suppl. Ser.* **1**, 121 (1954).
- Hunter, J. D., “Matplotlib: A 2d graphics environment”, *Computing In Science & Engineering* **9**, 3, 90–95 (2007).
- Iben, I., Jr., “Stellar Evolution.VI. Evolution from the Main Sequence to the Red-Giant Branch for Stars of Mass 1 M_{sun} , $1.25 \text{ M}_{\text{sun}}$, and $1.5 \text{ M}_{\text{sun}}$ ”, *ApJ***147**, 624 (1967).
- Iben, I., Jr. and A. Renzini, “Asymptotic giant branch evolution and beyond”, *ARA&A***21**, 271–342 (1983).
- Iglesias, C. A. and F. J. Rogers, “Radiative Opacities for Carbon- and Oxygen-rich Mixtures”, *ApJ***412**, 752 (1993).
- Iglesias, C. A. and F. J. Rogers, “Updated Opal Opacities”, *ApJ***464**, 943– (1996).
- Iliadis, C., *Nuclear Physics of Stars* (Wiley-VCH Verlag, 2015).

- Irwin, A., “The freeeos code for calculating the equation of state for stellar interiors i: An improved eff-style approximation for the fermi-dirac integrals”, (2004).
- Isern, J., M. Hernanz, R. Mochkovitch and E. Garcia-Berro, “The role of the minor chemical species in the cooling of white dwarfs”, *A&A***241**, L29–L32 (1991).
- Itoh, N., H. Hayashi, A. Nishikawa and Y. Kohyama, “Neutrino Energy Loss in Stellar Interiors. VII. Pair, Photo-, Plasma, Bremsstrahlung, and Recombination Neutrino Processes”, *ApJS***102**, 411–+ (1996).
- Itoh, N., H. Totsuji, S. Ichimaru and H. E. DeWitt, “Enhancement of thermonuclear reaction rate due to strong screening. II - Ionic mixtures”, *ApJ***234**, 1079–1084 (1979).
- Jermyn, A. S., E. H. Anders, D. Lecoanet and M. Cantiello, “Convective Penetration in Early-type Stars”, *ApJ***929**, 2, 182 (2022).
- Jermyn, A. S., E. B. Bauer, J. Schwab, R. Farmer, W. H. Ball, E. P. Bellinger, A. Dotter, M. Joyce, P. Marchant, J. S. G. Mombarg, W. M. Wolf, T. L. Sunny Wong, G. C. Cinquegrana, E. Farrell, R. Smolec, A. Thoul, M. Cantiello, F. Herwig, O. Toloza, L. Bildsten, R. H. D. Townsend and F. X. Timmes, “Modules for Experiments in Stellar Astrophysics (MESA): Time-dependent Convection, Energy Conservation, Automatic Differentiation, and Infrastructure”, *ApJS***265**, 1, 15 (2023).
- Jones, S., R. Hirschi, K. Nomoto, T. Fischer, F. X. Timmes, F. Herwig, B. Paxton, H. Toki, T. Suzuki, G. Martínez-Pinedo, Y. H. Lam and M. G. Bertolli, “Advanced Burning Stages and Fate of 8-10 M_⊙ Stars”, *ApJ***772**, 150 (2013).
- Kalirai, J. S., B. M. S. Hansen, D. D. Kelson, D. B. Reitzel, R. M. Rich and H. B. Richer, “The initial-final mass relation: Direct constraints at the low-mass end”, *The Astrophysical Journal* **676**, 1, 594–609, URL <https://doi.org/10.1086/2F527028> (2008).
- Kalita, S., B. Mukhopadhyay and T. R. Govindarajan, “Significantly super-chandrasekhar mass-limit of white dwarfs in noncommutative geometry”, *International Journal of Modern Physics D* **30**, 05, 2150034, URL <https://doi.org/10.1142%2Fs0218271821500346> (2021).
- Karakas, A. I. and J. C. Lattanzio, “The Dawes Review 2: Nucleosynthesis and stellar yields of low and intermediate-mass single stars”, ArXiv e-prints (2014).
- Kassambara, A., *rstatix: Pipe-Friendly Framework for Basic Statistical Tests*, URL <https://CRAN.R-project.org/package=rstatix>, r package version 0.6.0 (2020).
- Kawaler, S. D., “Probing the Extraordinary Ends of Ordinary Stars: White Dwarf Seismology with the Whole Earth Telescope”, in “IAU Colloq. 155: Astrophysical Applications of Stellar Pulsation”, edited by R. S. Stobie and P. A. Whitelock, vol. 83 of *Astronomical Society of the Pacific Conference Series*, p. 81 (1995).

- Kawaler, S. D. and P. Weiss, "Mode Trapping in Pulsating White Dwarfs", in "Progress of Seismology of the Sun and Stars", edited by Y. Osaki and H. Shiba-hashi, vol. 367, p. 431 (Springer-Verlag: Berlin, 1990).
- Kawaler, S. D., D. E. Winget and C. J. Hansen, "Evolution of the pulsation properties of hot pre-white dwarf stars", *ApJ***295**, 547–560 (1985).
- Kibédi, T., B. Alshahrani, A. E. Stuchbery, A. C. Larsen, A. Görgen, S. Siem, M. Gut-tormsen, F. Giacoppo, A. I. Morales, E. Sahin, G. M. Tveten, F. L. B. Garrote, L. C. Campo, T. K. Eriksen, M. Klintefjord, S. Maharramova, H. T. Nyhus, T. G. Tornyi, T. Renstrøm and W. Paulsen, "Radiative Width of the Hoyle State from γ -Ray Spectroscopy", *Phys. Rev. L.***125**, 18, 182701 (2020).
- Knobabout, J. and E. Van Der Stappen, "Where is the learning in learning analytics? a systematic literature review on the operationalization of learning-related constructs in the evaluation of learning analytics interventions", *IEEE Transactions on Learning Technologies* **13**, 3, 631–645 (2020).
- Koester, D., "White dwarf spectra and atmosphere models", *Mem. Societa Astronomica Italiana***81**, 921–931 (2010).
- Korre, L., P. Garaud and N. H. Brummell, "Convective overshooting and penetration in a Boussinesq spherical shell", *MNRAS***484**, 1, 1220–1237 (2019).
- Kunz, R., M. Fey, M. Jaeger, A. Mayer, J. W. Hammer, G. Staudt, S. Harissopoulos and T. Paradellis, "Astrophysical Reaction Rate of $^{12}\text{C}(\alpha, \gamma)^{16}\text{O}$ ", *ApJ***567**, 1, 643–650 (2002).
- Kutter, G. S. and M. P. Savedoff, "Evolution of Initially Pure ^{12}C Stars and the Production of Planetary Nebulae", *ApJ***156**, 1021 (1969).
- Langanke, K. and G. Martínez-Pinedo, "Shell-model calculations of stellar weak interaction rates: II. Weak rates for nuclei in the mass range /A=45-65 in supernovae environments", *Nuclear Physics A* **673**, 481–508 (2000).
- Lecoanet, D., J. Schwab, E. Quataert, L. Bildsten, F. X. Timmes, K. J. Burns, G. M. Vasil, J. S. Oishi and B. P. Brown, "Turbulent Chemical Diffusion in Convectively Bounded Carbon Flames", *ApJ***832**, 71 (2016).
- LIGO Scientific Collaboration, J. Aasi, B. P. Abbott, R. Abbott, T. Abbott, M. R. Abernathy, K. Ackley, C. Adams, T. Adams, P. Addesso and et al., "Advanced LIGO", *Classical and Quantum Gravity* **32**, 7, 074001 (2015).
- Lockyer, L., E. Heathcote and S. Dawson, "Informing pedagogical action aligning learning analytics with learning design", *American Behavioral Scientist* **57**, 1439–1459 (2013a).
- Lockyer, L., E. Heathcote and S. Dawson, "Informing pedagogical action: Aligning learning analytics with learning design", *American Behavioral Scientist* **57**, 10, 1439–1459 (2013b).

- Macfadyen, L. P., L. Lockyer and B. Rienties, “Learning design and learning analytics: Snapshot 2020”, *Journal of Learning Analytics* **7**, 3, 6–12, URL <https://learning-analytics.info/index.php/JLA/article/view/7389> (2020).
- Maeder, A. and G. Meynet, “Stellar evolution with rotation and magnetic fields. I. The relative importance of rotational and magnetic effects”, *A&A* **411**, 543–552 (2003).
- Maeder, A. and G. Meynet, “Stellar evolution with rotation and magnetic fields. II. General equations for the transport by Tayler-Spruit dynamo”, *A&A* **422**, 225–237 (2004).
- Mangaroska, K. and M. Giannakos, “Learning analytics for learning design: A systematic literature review of analytics-driven design to enhance learning”, *IEEE Transactions on Learning Technologies* **PP**, 1–1 (2018).
- Mann, H. B. and D. R. Whitney, “On a Test of Whether one of Two Random Variables is Stochastically Larger than the Other”, *The Annals of Mathematical Statistics* **18**, 1, 50 – 60, URL <https://doi.org/10.1214/aoms/1177730491> (1947).
- Marchant, P. and T. J. Moriya, “The impact of stellar rotation on the black hole mass-gap from pair-instability supernovae”, *A&A* **640**, L18 (2020).
- McNally, R., “Investigate common uses for spreadsheets”, https://www.fess.ie/images/stories/ResourcesForTutors/Resource_Lists_Level_5/InvestigateCommonUsesForSpreadsheets.pdf (2015).
- Mehta, A. K., A. Buonanno, J. Gair, M. C. Miller, E. Farag, R. J. deBoer, M. Wijscher and F. X. Timmes, “Observing Intermediate-mass Black Holes and the Upper Stellar-mass gap with LIGO and Virgo”, *ApJ* **924**, 1, 39 (2022).
- Meng, X.-C., J.-J. Zhang, X. Zhao, L.-P. Li and X.-F. Wang, “Environments of Type Ia Supernovae with Different Relative Equivalent Widths of the Si II Feature in Their Spectra”, *ApJ* **943**, 2, 159 (2023).
- Metcalfe, T. S., “White Dwarf Asteroseismology and the $^{12}\text{C}(\alpha,\gamma)^{16}\text{O}$ Rate”, *ApJ* **587**, L43–L46 (2003).
- Metcalfe, T. S., M. H. Montgomery and S. D. Kawaler, “Probing the core and envelope structure of DBV white dwarfs”, *MNRAS* **344**, L88–L92 (2003).
- Metcalfe, T. S., M. Salaris and D. E. Winget, “Measuring $^{12}\text{C}(\alpha, \gamma)^{16}\text{O}$ from White Dwarf Asteroseismology”, *ApJ* **573**, 803–811 (2002).
- Metcalfe, T. S., D. E. Winget and P. Charbonneau, “Preliminary Constraints on $^{12}\text{C}(\alpha,\gamma)^{16}\text{O}$ from White Dwarf Seismology”, *ApJ* **557**, 2, 1021–1027 (2001).
- Meynet, G. and A. Maeder, “Stellar evolution with rotation. I. The computational method and the inhibiting effect of the μ -gradient.”, *A&A* **321**, 465–476 (1997).

- Miles, B. J., D. R. van Rossum, D. M. Townsley, F. X. Timmes, A. P. Jackson, A. C. Calder and E. F. Brown, “On Measuring the Metallicity of a Type Ia Supernova’s Progenitor”, *ApJ***824**, 1, 59 (2016).
- Miller Bertolami, M. M., T. Battich, A. H. Córscico, L. G. Althaus and F. C. Wachlin, “An evolutionary channel for CO-rich and pulsating He-rich subdwarfs”, *MNRAS***511**, 1, L60–L65 (2022).
- Moll, R., C. Raskin, D. Kasen and S. E. Woosley, “Type Ia Supernovae from Merging White Dwarfs. I. Prompt Detonations”, *ApJ***785**, 2, 105 (2014).
- Mukhopadhyay, M., C. Lunardini, F. X. Timmes and K. Zuber, “Presupernova Neutrinos: Directional Sensitivity and Prospects for Progenitor Identification”, *ApJ***899**, 2, 153 (2020).
- NRC, “Education for life and work developing transferable knowledge and skills in the 21st century”, https://www.nap.edu/resource/13398/dbasse_070895.pdf (2012).
- Oda, T., M. Hino, K. Muto, M. Takahara and K. Sato, “Rate Tables for the Weak Processes of sd-Shell Nuclei in Stellar Matter”, *Atomic Data and Nuclear Data Tables* **56**, 231–403 (1994).
- OpenAI, “GPT-4 Technical Report”, arXiv e-prints p. arXiv:2303.08774 (2023).
- Parsons, S. G., A. Rebassa-Mansergas, M. R. Schreiber, B. T. Gänsicke, M. Zorotovic and J. J. Ren, “The white dwarf binary pathways survey - I. A sample of FGK stars with white dwarf companions”, *MNRAS***463**, 2, 2125–2136 (2016).
- Patton, K. M., C. Lunardini, R. J. Farmer and F. X. Timmes, “Neutrinos from Beta Processes in a Presupernova: Probing the Isotopic Evolution of a Massive Star”, *ApJ***851**, 1, 6 (2017).
- Paxton, B., “EZ to Evolve ZAMS Stars: A Program Derived from Eggleton’s Stellar Evolution Code”, *PASP***116**, 699–701 (2004).
- Paxton, B., L. Bildsten, A. Dotter, F. Herwig, P. Lesaffre and F. Timmes, “Modules for Experiments in Stellar Astrophysics (MESA)”, *ApJS***192**, 3 (2011).
- Paxton, B., M. Cantiello, P. Arras, L. Bildsten, E. F. Brown, A. Dotter, C. Mankovich, M. H. Montgomery, D. Stello, F. X. Timmes and R. Townsend, “Modules for Experiments in Stellar Astrophysics (MESA): Planets, Oscillations, Rotation, and Massive Stars”, *ApJS***208** (2013).
- Paxton, B., P. Marchant, J. Schwab, E. B. Bauer, L. Bildsten, M. Cantiello, L. Dessart, R. Farmer, H. Hu, N. Langer, R. H. D. Townsend, D. M. Townsley and F. X. Timmes, “Modules for Experiments in Stellar Astrophysics (MESA): Binaries, Pulsations, and Explosions”, *ApJS***220**, 15 (2015).

- Paxton, B., J. Schwab, E. B. Bauer, L. Bildsten, S. Blinnikov, P. Duffell, R. Farmer, J. A. Goldberg, P. Marchant, E. Sorokina, A. Thoul, R. H. D. Townsend and F. X. Timmes, “Modules for Experiments in Stellar Astrophysics (MESA): Convective Boundaries, Element Diffusion, and Massive Star Explosions”, *ApJS***234**, 34 (2018).
- Paxton, B., R. Smolec, J. Schwab, A. Gautschy, L. Bildsten, M. Cantiello, A. Dotter, R. Farmer, J. A. Goldberg, A. S. Jermyn, S. M. Kanbur, P. Marchant, A. Thoul, R. H. D. Townsend, W. M. Wolf, M. Zhang and F. X. Timmes, “Modules for Experiments in Stellar Astrophysics (MESA): Pulsating Variable Stars, Rotation, Convective Boundaries, and Energy Conservation”, *ApJS***243**, 1, 10 (2019).
- Pedersen, M. G., C. Aerts, P. I. Pápics, M. Michielsen, S. Gebruers, T. M. Rogers, G. Molenberghs, S. Burssens, S. Garcia and D. M. Bowman, “Internal mixing of rotating stars inferred from dipole gravity modes”, *Nature Astronomy* **5**, 715–722 (2021).
- Pedersen, M. G., S. Chowdhury, C. Johnston, D. M. Bowman, C. Aerts, G. Handler, P. De Cat, C. Neiner, A. David-Uraz, D. Buzasi, A. Tkachenko, S. Simón-Díaz, E. Moravveji, J. Sikora, G. M. Mirouh, C. C. Lovekin, M. Cantiello, J. Daszyńska-Daszkiewicz, A. Pigulski, R. K. Vanderspek and G. R. Ricker, “Diverse Variability of O and B Stars Revealed from 2-minute Cadence Light Curves in Sectors 1 and 2 of the TESS Mission: Selection of an Asteroseismic Sample”, *ApJ***872**, 1, L9 (2019).
- Pepper, B. T., A. G. Istrate, A. D. Romero and S. O. Kepler, “The impact of the uncertainties in the $^{12}\text{C}(\alpha, \gamma)^{16}\text{O}$ reaction rate on the evolution of low- to intermediate-mass stars”, *MNRAS***513**, 1, 1499–1512 (2022).
- Perkins, D. N., G. Salomon and P. Press, “Transfer of learning”, in “International Encyclopedia of Education (2nd)”, (Pergamon Press, 1992).
- Pinsonneault, M. and B. Ryden, *Stellar Structure and Evolution* (Cambridge University Press, 2023).
- Pinsonneault, M. H., S. D. Kawaler, S. Sofia and P. Demarque, “Evolutionary models of the rotating sun”, *ApJ***338**, 424–452 (1989).
- Placco, V. M., R. M. Santucci, Z. Yuan, M. K. Mardini, E. M. Holmbeck, X. Wang, R. Surman, T. T. Hansen, I. U. Roederer, T. C. Beers, A. Choplín, A. P. Ji, R. Ezzeddine, A. Frebel, C. M. Sakari, D. D. Whitten and J. Zepeda, “The R-Process Alliance: The Peculiar Chemical Abundance Pattern of RAVE J183013.5-455510”, arXiv e-prints p. arXiv:2006.04538 (2020).
- Pols, O. R., C. A. Tout, P. P. Eggleton and Z. Han, “Approximate input physics for stellar modelling”, *MNRAS***274**, 964–974 (1995).
- Potekhin, A. Y. and G. Chabrier, “Thermodynamic Functions of Dense Plasmas: Analytic Approximations for Astrophysical Applications”, *Contributions to Plasma Physics* **50**, 1, 82–87 (2010a).

- Potekhin, A. Y. and G. Chabrier, “Thermodynamic Functions of Dense Plasmas: Analytic Approximations for Astrophysical Applications”, Contributions to Plasma Physics **50**, 82–87 (2010b).
- Poutanen, J., “Rosseland and Flux Mean Opacities for Compton Scattering”, *ApJ* **835**, 2, 119 (2017).
- Prada Moroni, P. G. and O. Straniero, “Very low-mass white dwarfs with a C-O core”, *A&A* **507**, 3, 1575–1583 (2009).
- R Core Team, *R: A Language and Environment for Statistical Computing*, R Foundation for Statistical Computing, Vienna, Austria, URL <https://www.R-project.org/> (2020).
- Rauscher, T. and F.-K. Thielemann, “Astrophysical Reaction Rates From Statistical Model Calculations”, Atomic Data and Nuclear Data Tables **75**, 1–351 (2000).
- Reimers, D., “Circumstellar absorption lines and mass loss from red giants”, Memoires of the Societe Royale des Sciences de Liege **8**, 369–382 (1975).
- Renzo, M., R. Farmer, S. Justham, Y. Götberg, S. E. de Mink, E. Zapartas, P. Marchant and N. Smith, “Predictions for the hydrogen-free ejecta of pulsational pair-instability supernovae”, *A&A* **640**, A56 (2020).
- Rogers, F. J. and A. Nayfonov, “Updated and Expanded OPAL Equation-of-State Tables: Implications for Helioseismology”, *ApJ* **576**, 1064–1074 (2002a).
- Rogers, F. J. and A. Nayfonov, “Updated and Expanded OPAL Equation-of-State Tables: Implications for Helioseismology”, *ApJ* **576**, 2, 1064–1074 (2002b).
- Romero, A. D., G. O. da Rosa, S. O. Kepler, P. A. Bradley, M. Uzundag, K. J. Bell, J. J. Hermes and G. R. Lauffer, “Asteroseismology of PG 1541 + 651 and BPM 31594 with TESS”, *MNRAS* **518**, 1, 1448–1458 (2023).
- Rose, B. M., D. Rubin, A. Cikota, S. E. Deustua, S. Dixon, A. Fruchter, D. O. Jones, A. G. Riess and D. M. Scolnic, “Evidence for Cosmic Acceleration Is Robust to Observed Correlations between Type Ia Supernova Luminosity and Stellar Age”, *ApJ* **896**, 1, L4 (2020).
- Rosenfield, P., P. Marigo, L. Girardi, J. J. Dalcanton, A. Bressan, B. F. Williams and A. Dolphin, “Evolution of thermally pulsing asymptotic giant branch stars. v. constraining the mass loss and lifetimes of intermediate-mass, low-metallicity agb stars*”, The Astrophysical Journal **822**, 2, 73, URL <https://dx.doi.org/10.3847/0004-637X/822/2/73> (2016).
- Sajadian, S. and K. C. Sahu, “Detecting Isolated Stellar-mass Black Holes with the Roman Telescope”, *AJ* **165**, 3, 96 (2023).
- Salaris, M. and S. Cassisi, “Chemical element transport in stellar evolution models”, Royal Society Open Science **4**, 8, 170192 (2017).

Saumon, D., G. Chabrier and H. M. van Horn, “An Equation of State for Low-Mass Stars and Giant Planets”, *ApJS***99**, 713–+ (1995).

Schatz, H., A. D. Becerril Reyes, A. Best, E. F. Brown, K. Chatzioannou, K. A. Chipps, C. M. Deibel, R. Ezzeddine, D. K. Galloway, C. J. Hansen, F. Herwig, A. P. Ji, M. Lugaro, Z. Meisel, D. Norman, J. S. Read, L. F. Roberts, A. Spyrou, I. Tews, F. X. Timmes, C. Travaglio, N. Vassh, C. Abia, P. Adsley, S. Agarwal, M. Aliotta, W. Aoki, A. Arcones, A. Aryan, A. Bandyopadhyay, A. Banu, D. W. Bardayan, J. Barnes, A. Bauswein, T. C. Beers, J. Bishop, T. Boztepe, B. Côté, M. E. Caplan, A. E. Champagne, J. A. Clark, M. Couder, A. Couture, S. E. de Mink, S. Debnath, R. J. deBoer, J. den Hartogh, P. Denissenkov, V. Dexheimer, I. Dillmann, J. E. Escher, M. A. Famiano, R. Farmer, R. Fisher, C. Fröhlich, A. Frebel, C. Fryer, G. Fuller, A. K. Ganguly, S. Ghosh, B. K. Gibson, T. Gorda, K. N. Gourgouliatos, V. Graber, M. Gupta, W. C. Haxton, A. Heger, W. R. Hix, W. C. G. Ho, E. M. Holmbeck, A. A. Hood, S. Huth, G. Imbriani, R. G. Izzard, R. Jain, H. Jayatissa, Z. Johnston, T. Kajino, A. Kankainen, G. G. Kiss, A. Kwiatkowski, M. La Cognata, A. M. Laird, L. Lamia, P. Landry, E. Laplace, K. D. Launey, D. Leahy, G. Leckenby, A. Lennarz, B. Longfellow, A. E. Lovell, W. G. Lynch, S. M. Lyons, K. Maeda, E. Masha, C. Matei, J. Merc, B. Messer, F. Montes, A. Mukherjee, M. R. Mumpower, D. Neto, B. Nevins, W. G. Newton, L. Q. Nguyen, K. Nishikawa, N. Nishimura, F. M. Nunes, E. O’Connor, B. W. O’Shea, W. J. Ong, S. D. Pain, M. A. Pajkos, M. Pignatari, R. G. Pizzone, V. M. Placco, T. Plewa, B. Pritychenko, A. Psaltis, D. Puentes, Y. Z. Qian, D. Radice, D. Rapagnani, B. M. Rebeiro, R. Reifarth, A. L. Richard, N. Rijal, I. U. Roederer, J. S. Rojo, J. S. K., Y. Saito, A. Schwenk, M. L. Sergi, R. S. Sidhu, A. Simon, T. Sivarani, Á. Skúladóttir, M. S. Smith, A. Spiridon, T. M. Sprouse, S. Starrfield, A. W. Steiner, F. Strieder, I. Sultana, R. Surman, T. Sziucs, A. Tawfik, F. Thielemann, L. Trache, R. Trappitsch, M. B. Tsang, A. Tumino, S. Upadhyayula, J. O. Valle Martínez, M. Van der Swaelmen, C. Viscasillas Vázquez, A. Watts, B. Wehmeyer, M. Wiescher, C. Wrede, J. Yoon, R. G. T. Zegers, M. A. Zermane and M. Zingale, “Horizons: nuclear astrophysics in the 2020s and beyond”, *Journal of Physics G Nuclear Physics* **49**, 11, 110502 (2022).

Schneider, M. and F. Preckel, “Variables associated with achievement in higher education: A systematic review of meta-analyses”, *Psychological Bulletin* **143**, 565–600 (2017).

Schwab, J., R. Farmer and F. X. Timmes, “Laminar Flame Speeds in Degenerate Oxygen-Neon Mixtures”, arXiv e-prints p. arXiv:2001.07733 (2020).

Serenelli, A. M. and M. Fukugita, “Burst Neutrinos from the Nitrogen Flash”, *ApJ***632**, 1, L33–L36 (2005).

Shen, K. J., D. Kasen, B. J. Miles and D. M. Townsley, “Sub-Chandrasekhar-mass White Dwarf Detonations Revisited”, *ApJ***854**, 52 (2018).

Shen, Y., B. Guo, R. J. deBoer, E. Li, Z. Li, Y. Li, X. Tang, D. Pang, S. Adhikari, C. Basu, J. Su, S. Yan, Q. Fan, J. Liu, C. Chen, Z. Han, X. Li, G. Lian, T. Ma, W. Nan, W. Nan, Y. Wang, S. Zeng, H. Zhang and W. Liu, “New Determination

of the $^{12}\text{C}(\alpha, \gamma)^{16}\text{O}$ Reaction Rate and Its Impact on the Black-hole Mass Gap”, *ApJ***945**, 1, 41 (2023).

Simón-Díaz, S., C. Aerts, M. A. Urbaneja, I. Camacho, V. Antoci, M. Fredslund Andersen, F. Grundahl and P. L. Pallé, “Low-frequency photospheric and wind variability in the early-B supergiant HD 2905”, *A&A***612**, A40 (2018).

Simpson, C., K. Abe, C. Bronner, Y. Hayato, M. Ikeda, H. Ito, K. Iyogi, J. Kameda, Y. Kataoka, Y. Kato, Y. Kishimoto, L. Marti, M. Miura, S. Moriyama, T. Mochizuki, M. Nakahata, Y. Nakajima, S. Nakayama, T. Okada, K. Okamoto, A. Orii, G. Pronost, H. Sekiya, M. Shiozawa, Y. Sonoda, A. Takeda, A. Takenaka, H. Tanaka, T. Yano, R. Akutsu, T. Kajita, K. Okumura, R. Wang, J. Xia, D. Bravo-Berguño, L. Labarga, P. Fernandez, F. d. M. Blaszczyk, C. Kachulis, E. Kearns, J. L. Raaf, J. L. Stone, L. Wan, T. Wester, S. Sussman, S. Berkman, J. Bian, N. J. Grishevich, W. R. Kropp, S. Locke, S. Mine, M. B. Smy, H. W. Sobel, V. Takhistov, P. Weatherly, K. S. Ganezer, J. Hill, J. Y. Kim, I. T. Lim, R. G. Park, B. Bodur, K. Scholberg, C. W. Walter, A. Coffani, O. Drapier, M. Gonin, J. Imber, T. A. Mueller, P. Paganini, T. Ishizuka, T. Nakamura, J. S. Jang, K. Choi, J. G. Learned, S. Matsuno, R. P. Litchfield, A. A. Sztuc, Y. Uchida, M. O. Wascko, V. Berardi, N. F. Calabria, M. G. Catanesi, R. A. Intonti, E. Radicioni, G. De Rosa, G. Collazuol, F. Iacob, L. Ludovici, Y. Nishimura, S. Cao, M. Friend, T. Hasegawa, T. Ishida, T. Kobayashi, T. Nakadaira, K. Nakamura, Y. Oyama, K. Sakashita, T. Sekiguchi, T. Tsukamoto, K. Abe, M. Hasegawa, Y. Isobe, H. Miyabe, Y. Nakano, T. Shiozawa, T. Sugimoto, A. T. Suzuki, Y. Takeuchi, A. Ali, Y. Ashida, T. Hayashino, S. Hirota, M. Jiang, T. Kikawa, M. Mori, K. Nakamura, T. Nakaya, R. A. Wendell, L. H. V. Anthony, N. McCauley, A. Pritchard, K. M. Tsui, Y. Fukuda, Y. Itow, M. Murrase, T. Niwa, M. Taani, M. Tsukada, P. Mijakowski, K. Frankiewicz, C. K. Jung, X. Li, J. L. Palomino, G. Santucci, C. Vilela, M. J. Wilking, C. Yanagisawa, D. Fukuda, M. Harada, K. Hagiwara, T. Horai, H. Ishino, S. Ito, Y. Koshio, M. Sakuda, Y. Takahira, C. Xu, Y. Kuno, L. Cook, D. Wark, F. Di Lodovico, S. Molina Sedgwick, B. Richards, S. Zsoldos, S. B. Kim, R. Tacik, M. Thiesse, L. Thompson, H. Okazawa, Y. Choi, K. Nishijima, M. Koshiba, M. Yokoyama, A. Goldsack, K. Martens, M. Murdoch, B. Quilain, Y. Suzuki, M. R. Vagins, M. Kuze, Y. Okajima, M. Tanaka, T. Yoshida, M. Ishitsuka, R. Matsumoto, K. Ohta, J. F. Martin, C. M. Nantais, H. A. Tanaka, T. Towstego, M. Hartz, A. Konaka, P. de Perio, S. Chen, B. Jamieson, J. Walker, A. Minamino, K. Okamoto, G. Pintaudi and Super-Kamiokande Collaboration, “Sensitivity of Super-Kamiokande with Gadolinium to Low Energy Antineutrinos from Pre-supernova Emission”, *ApJ***885**, 2, 133 (2019).

Smith, R., M. Gai, S. R. Stern, D. K. Schweitzer and M. W. Ahmed, “Precision measurements on oxygen formation in stellar helium burning with gamma-ray beams and a Time Projection Chamber”, *Nature Communications* **12**, 5920 (2021).

SOLAR, “Society for learning analytics research”, <https://www.solaresearch.org/about/what-is-learning-analytics/> (2021).

Spruit, H. C., “Dynamo action by differential rotation in a stably stratified stellar interior”, *A&A***381**, 923–932 (2002).

- Stanton, L. G. and M. S. Murillo, “Ionic transport in high-energy-density matter”, *Phys. Rev. E***93**, 4, 043203 (2016).
- Straniero, O., I. Domínguez, G. Imbriani and L. Piersanti, “The Chemical Composition of White Dwarfs as a Test of Convective Efficiency during Core Helium Burning”, *ApJ***583**, 878–884 (2003).
- Suijs, M. P. L., N. Langer, A.-J. Poelarends, S.-C. Yoon, A. Heger and F. Herwig, “White dwarf spins from low-mass stellar evolution models”, *A&A***481**, L87–L90 (2008).
- Sukhbold, T., S. E. Woosley and A. Heger, “A High-resolution Study of Presupernova Core Structure”, *ApJ***860**, 93 (2018).
- Suno, H., Y. Suzuki and P. Descouvemont, “Precise calculation of the triple- α reaction rates using the transmission-free complex absorbing potential method”, *Phys. Rev. C***94**, 5, 054607 (2016).
- Supriya, K., C. Mead, A. D. Anbar, J. L. Caulkins, J. P. Collins, K. M. Cooper, P. C. LePore, T. Lewis, A. Pate, R. A. Scott and S. E. Brownell, “Undergraduate biology students received higher grades during covid-19 but perceived negative effects on learning”, *Frontiers in Education* **6**, URL <https://www.frontiersin.org/articles/10.3389/feduc.2021.759624> (2021).
- Taghiniyarami, K., *Rotational Evolution of Low-Mass stars in close binaries*, Ph.D. thesis (2016).
- Takahashi, K., “The Low Detection Rate of Pair-instability Supernovae and the Effect of the Core Carbon Fraction”, *ApJ***863**, 2, 153 (2018).
- Thoul, A. A., J. N. Bahcall and A. Loeb, “Element Diffusion in the Solar Interior”, *ApJ***421**, 828 (1994).
- Timmes, F. X., E. F. Brown and J. W. Truran, “On Variations in the Peak Luminosity of Type Ia Supernovae”, *ApJ***590**, L83–L86 (2003).
- Timmes, F. X. and F. D. Swesty, “The Accuracy, Consistency, and Speed of an Electron-Positron Equation of State Based on Table Interpolation of the Helmholtz Free Energy”, *ApJS***126**, 501–516 (2000).
- Timmes, F. X., R. H. D. Townsend, E. B. Bauer, A. Thoul, C. E. Fields and W. M. Wolf, “The Impact of White Dwarf Luminosity Profiles on Oscillation Frequencies”, *ApJ***867**, L30 (2018a).
- Timmes, F. X., R. H. D. Townsend, E. B. Bauer, A. Thoul, C. E. Fields and W. M. Wolf, “The Impact of White Dwarf Luminosity Profiles on Oscillation Frequencies”, *ApJ***867**, L30 (2018b).
- Townsend, R. H. D., “MESA SDK for Linux”, URL <https://doi.org/10.5281/zenodo.2669541> (2019a).

- Townsend, R. H. D., “Mesa sdk for mac os”, URL <http://doi.org/10.5281/zenodo.2669543> (2019b).
- Townsend, R. H. D., J. Goldstein and E. G. Zweibel, “Angular momentum transport by heat-driven g-modes in slowly pulsating B stars”, *MNRAS***475**, 879–893 (2018).
- Townsend, R. H. D. and S. A. Teitler, “GYRE: an open-source stellar oscillation code based on a new Magnus Multiple Shooting scheme”, *MNRAS***435**, 3406–3418 (2013).
- Unno, W., Y. Osaki, H. Ando, H. Saio and H. Shibahashi, *Nonradial oscillations of stars* (Tokyo: University of Tokyo Press, 1989).
- van der Walt, S., S. C. Colbert and G. Varoquaux, “The numpy array: A structure for efficient numerical computation”, *Computing in Science Engineering* **13**, 2, 22–30 (2011).
- Van Grootel, V., Dupret, M.-A., Fontaine, G., Brassard, P., Grigahcène, A. and Quirion, P.-O., “The instability strip of zz ceti white dwarfs - i. introduction of time-dependent convection”, *A&A* **539**, A87, URL <https://doi.org/10.1051/0004-6361/201118371> (2012).
- van Horn, H. M., “Cooling of White Dwarfs”, in “White Dwarfs”, edited by W. J. Luyten, vol. 42 of *IAU Symposium*, p. 97 (Dordrecht: Springer, 1971).
- Vila, S. C., “Pre-White-Dwarf Evolution. I”, *ApJ***146**, 437 (1966).
- Vincent, O., P. Bergeron and D. Lafrenière, “Searching for ZZ Ceti White Dwarfs in the Gaia Survey”, *AJ***160**, 6, 252 (2020).
- Vishniac, E. T., “Editorial: On the Use of Chatbots in Writing Scientific Manuscripts”, in “Bulletin of the American Astronomical Society”, vol. 55, p. 016 (2023).
- Weaver, T. A. and S. E. Woosley, “Nucleosynthesis in massive stars and the $^{12}\text{C}(\alpha, \gamma)^{16}\text{O}$ reaction rate”, *Phys. Reports***227**, 65–96 (1993).
- Weidemann, V., “Revision of the initial-to-final mass relation”, *A&A***363**, 647–656 (2000).
- Weinberg, N. N., L. Bildsten and H. Schatz, “Exposing the Nuclear Burning Ashes of Radius Expansion Type I X-Ray Bursts”, *ApJ***639**, 1018–1032 (2006).
- Werner, K., N. Reindl, S. Geier and M. Pritzkuleit, “Discovery of hot subdwarfs covered with helium-burning ash”, *MNRAS***511**, 1, L66–L71 (2022).
- Wilcoxon, F., “Individual comparisons by ranking methods”, *Biometrics Bulletin* **1**, 6, 80–83, URL <http://www.jstor.org/stable/3001968> (1945).
- Willson, L. A., “Mass Loss From Cool Stars: Impact on the Evolution of Stars and Stellar Populations”, *ARA&A***38**, 573–611 (2000).

- Winget, D. E., D. J. Sullivan, T. S. Metcalfe, S. D. Kawaler and M. H. Montgomery, “A Strong Test of Electroweak Theory Using Pulsating DB White Dwarf Stars as Plasmon Neutrino Detectors”, *ApJ***602**, L109–L112 (2004).
- Winget, D. E., H. M. van Horn and C. J. Hansen, “The nature of the ZZ Ceti oscillations - Trapped modes in compositionally stratified white dwarfs”, *ApJ***245**, L33–L36 (1981).
- Woosley, S. E. and A. Heger, “The Pair-instability Mass Gap for Black Holes”, *ApJ***912**, 2, L31 (2021).
- Woosley, S. E., A. Heger and T. A. Weaver, “The evolution and explosion of massive stars”, Rev. Mod. Phys. **74**, 1015–1071, URL <http://link.aps.org/doi/10.1103/RevModPhys.74.1015> (2002).
- Young, P., “Star formation, review”, University Lectures on Canvas (2020).
- Zahn, J.-P., “Circulation and turbulence in rotating stars”, *A&A***265**, 115–132 (1992).

APPENDIX

APPENDIX A

CO-AUTHOR PERMISSIONS

The papers published in this dissertation have the full acknowledgement and approval of all co-authors.

APPENDIX B

APPENDIX FOR CHAPTER 2

Convergence Studies In this appendix we demonstrate that the pulsation periods of the baseline model are only weakly dependent on the details of the mass and temporal resolution of the **MESA + GYRE** calculations.

A MESA parameter controlling the mass resolution is `max_dq`, the maximum fraction a model’s mass in one cell. That is, the minimum number of cells in a model is $N_{\min \text{ cells}} = 1/\text{max_dq}$. We use $N_{\min \text{ cells}} = 5,000$ for all the results reported. MESA can also adaptively refines its mesh based on a set of mesh functions. The maximum cell-to-cell variation of these functions is maintained around the value of the control `mesh_delta_coeff`. We use `mesh_delta_coeff` = 1 for all the results reported. Primarily as a result of these two mesh parameters, the total number of cells in the baseline model is $\simeq 8,000$ cells.

A MESA parameter controlling the time resolution is the largest change in the central temperature allowed over a timestep, `delta_lgT_cntr_limit`. For all the reported results, we use `delta_lgT_cntr_limit` = 0.001. MESA can also adaptively adjusts the timestep based on other criteria, but this setting dominates the size of every timestep as the baseline WD model cools. The total number of timesteps in the baseline model is $\simeq 1,000$ and varies roughly linearly with `delta_lgT_cntr_limit`.

Figure B.1 shows changes in the low-order g-mode periods for different $N_{\min \text{ cells}}$ as the models cool. The time resolution is held fixed at `delta_lgT_cntr_limit` = 0.001. Our standard $N_{\min \text{ cells}} = 5,000$ baseline model is the basis of the comparison and shown as the horizontal lines. A model with 10 times less mass resolution than our standard mass resolution, $N_{\min \text{ cells}} = 500$, induces maximum relative period changes of $\simeq 0.05\%$ at $\simeq 30,000$ K for $g_{1,1}$, $\simeq 0.07\%$ at $\simeq 35,000$ K for $g_{1,2}$, $\simeq 0.07\%$ at $\simeq 45,000$ K for $g_{2,1}$, and $\simeq 0.07\%$ at $\simeq 45,000$ K for $g_{2,2}$. A model with 5 times less mass resolution than our standard mass resolution, $N_{\min \text{ cells}} = 1,000$, reduces these maximum relative period changes by $\simeq 20\%$. A model with 5 times more mass resolution than our standard mass resolution, $N_{\min \text{ cells}} = 25,000$ causes maximum relative period changes of 0.000022% at $g_{1,1}$ to 0.028% at $g_{10,1}$. These maximum relative period changes are, respectively, a factor of $\simeq 20,000$ to 20 smaller than the relative period change caused by including or excluding ^{22}Ne .

Figure B.2 shows changes in the low-order g-mode periods for different `delta_lgT_cntr_limit` as the models cool. The mass resolution is held fixed at $N_{\min \text{ cells}} = 5,000$. Our standard `delta_lgT_cntr_limit` = 0.001 baseline model is the basis of the comparison and shown as the horizontal lines. A model with 10 times less time resolution, `delta_lgT_cntr_limit` = 0.01, causes maximum relative period changes of $\simeq -0.05\%$ at $\simeq 50,000$ K for $g_{1,1}$, $\simeq 0.02\%$ at $\simeq 50,000$ K for $g_{1,2}$, $\simeq -0.06\%$ at $\simeq 40,000$ K for $g_{2,1}$, $\simeq -0.05\%$ at $\simeq 45,000$ K for $g_{2,2}$, $\simeq -0.25\%$ at $\simeq 45,000$ K for $g_{10,1}$, and $\simeq -0.25\%$ at $\simeq 50,000$ K for $g_{10,2}$. A model with 5 times less time resolution than our standard mass resolution, `delta_lgT_cntr_limit` = 0.005, reduces these maximum relative period changes by $\simeq 10\%$. A model with 5 times more time resolution, `delta_lgT_cntr_limit` = 0.0002, has average period changes of 0.00061 s for $g_{1,1}$, -0.00077 s for $g_{1,2}$, 0.0034 s for $g_{2,1}$, 0.0010 s for $g_{2,2}$, 0.0021 s for $g_{10,1}$, and

0.0014 s for $g_{10,2}$. The average period changes are a factor of $\simeq 1000$ smaller than the average period changes caused by including or excluding ^{22}Ne .

Input Physics Details

In this appendix we briefly discuss the salient physics used in our **MESA** models.

Thermodynamics

The **MESA** r12115 equation of state (EOS) is a blend of the OPAL (Rogers and Nayfonov, 2002a), SCVH (Saumon *et al.*, 1995), PTEH Pols *et al.* (1995), HELM (Timmes and Swesty, 2000), and PC (Potekhin and Chabrier, 2010b) EOSes. The **MESA** EOS also covers the late stages of WD cooling where the ions in the core crystallize (e.g., Bauer *et al.*, 2020). WD interiors lie in the PC region of the **MESA** EOS, which provides a semi-analytic EOS treatment for arbitrary composition. The default in **MESA** version 12115 is to account for each species of ion with mass fraction greater than 10^{-3} when calling the PC EOS. Therefore changing the interior composition in a WD model, such as including or excluding ^{22}Ne , self-consistently changes the thermodynamics.

Opacities

MESA r12115 divides the radiative opacity tables into two temperature regimes, low ($T \lesssim 10^4$ K) and high ($T \gtrsim 10^4$ K). For the stellar evolution calculations from the pre-MS to a WD we use the Ferguson *et al.* (2005a) low-temperature regions, and for the high-temperature regions we use the OPAL Type I opacities (Iglesias and Rogers, 1996), smoothly transitioning to the OPAL Type II opacities (Iglesias and Rogers, 1996) starting at the end of core H-burning. In our WD models, the radiative opacities are provided by the OPAL Type 2 tables, which are functions of the hydrogen mass fraction X, metal mass fraction Z, and the C/O-enhancements. Thus for the same temperature and density, our $X(^{22}\text{Ne}) \rightarrow X(^{14}\text{N})$ replacement in Section 2.4.1 does not change the radiative opacities. Our $X(^{14}\text{N}) \rightarrow X(^4\text{He})$ and $X(^{22}\text{Ne}) \rightarrow X(^{12}\text{C})$ replacements to generate zero-metallicity ab initio DB WD in Section 2.4.2 decreases Z in the He-dominated envelope and increases the C enhancement in the interior. Conversely, our doubling $X(^{14}\text{N})$ at the expense of $X(^4\text{He})$ and doubling $X(^{22}\text{Ne})$ at the expense of $X(^{12}\text{C})$ to generate a super-solar metallicity ab initio DB WD in Section 2.4.2 increases Z in the He-dominated envelope and decreases the C enhancement in the interior. Electron conduction opacities are from Cassisi *et al.* (2007), which are the relevant opacity in the WD interior. The conduction opacities are a function of the mean atomic number \bar{Z} , which **MESA** evaluates using the full composition vector in each cell.

Nuclear Reaction Networks

We use **MESA**'s `mesa_49.net`, a nuclear reaction network that follows 49 isotopes from ^1H to ^{34}S , including ^{22}Ne . This impact of this reaction network on properties of CO WDs from Monte Carlo stellar models is discussed by Fields *et al.* (2016). All forward thermonuclear reaction rates are from the JINA reaclib version V2.2 2017-10-20 (Cyburt *et al.*, 2010). Inverse rates are calculated directly from the forward

rates (those with positive Q -value) using detailed balance, rather than using fitted rates. The nuclear partition functions used to calculate the inverse rates are from Rauscher and Thielemann (2000). Electron screening factors for both weak and strong thermonuclear reactions are from Chugunov *et al.* (2007) with plasma parameters from Itoh *et al.* (1979). All the weak rates are based (in order of precedence) on the tabulations of Langanke and Martínez-Pinedo (2000), Oda *et al.* (1994), and Fuller *et al.* (1985). Thermal neutrino energy losses are from Itoh *et al.* (1996).

Mass Loss

The implementations of mass loss in **MESA** r12115 are based on a number of observationally and theoretically motivated prescriptions, but uncertainties remain on line-driven and dust-driven winds (Dupree, 1986; Willson, 2000; Boulaquier *et al.*, 2019). We follow the mass loss settings used by the MIST isochrones (Dotter, 2016; Choi *et al.*, 2016), with a combination of the Reimer mass loss prescription (Reimers, 1975) with $\eta=0.1$ on the Red Giant Branch and a Blöcker mass loss prescription (Bloecker, 1995b) with $\eta=0.5$ on the AGB.

Rotation and Magnetic Fields

MESA r12115 implements the inherently 3D process of rotation by making the 1D shellular approximation (Zahn, 1992; Meynet and Maeder, 1997), where the angular velocity is constant over isobars. The transport of angular momentum and material due to rotationally induced instabilities is followed using a diffusion approximation (e.g., Endal and Sofia, 1978; Pinsonneault *et al.*, 1989; Heger *et al.*, 2000; Maeder and Meynet, 2003, 2004; Suijs *et al.*, 2008) for the dynamical shear instability, secular shear instability, Eddington-Sweet circulation, Goldreich-Schubert-Fricke instability, and Spruit-Tayler dynamo. See Heger *et al.* (2000) for a description of the different instabilities and diffusion coefficients.

Magnetic fields are implemented in **MESA** using the formalism of Heger *et al.* (2005), where a magnetic torque due to a dynamo (Spruit, 2002) allows angular momentum to be transported inside the star. The azimuthal and radial components of the magnetic field are modeled as $B_\phi \sim r\sqrt{(4\pi\rho)\omega_A}$ and $B_r \sim B_\phi/(rk)$ respectively, where r is the radial coordinate, ω_A the Alfvén frequency, and k the wavenumber. These magnetic fields provide a torque $S = B_r B_\phi/(4\pi)$ which slows down the rotation rate by decreasing the amount of differential rotation (Heger *et al.*, 2005).

We initialize rotation by imposing a solid body rotation law, $\Omega/\Omega_{\text{crit}} = 1.9 \times 10^{-4}$, at the ZAMS. ZAMS is defined as where the nuclear burning luminosity is 99% of the total luminosity, and the rotation rate is normalized by the surface critical rotation rate $\Omega_{\text{crit}} = \sqrt{(1 - L/L_{\text{edd}})cM/R^3}$, where c is the speed of light, M is the mass of the star, R the stellar radius, L the luminosity and L_{edd} the Eddington luminosity. The initial magnetic field is set to $B_r = B_\phi = 0$. Effects from rotationally induced mass loss are not included.

Element Diffusion

Element diffusion is implemented in **MESA** r12115 following Thoul *et al.* (1994), and described in Section 3 of Paxton *et al.* (2018). All isotopes in the reaction network

are categorized into classes according to their atomic masses, each of which has a representative member whose properties are used to calculate the diffusion velocities. Diffusion coefficients are calculated, by default, according to Stanton and Murillo (2016), whose formalism is based on binary collision integrals between each pair of species in the plasma. The diffusion equation is then solved using the total mass fraction within each class. From the ZAMS to the construction of the DB WD, we use the ten element classes ^1H , ^3He , ^4He , ^{12}C , ^{14}N ^{16}O , ^{20}Ne , ^{22}Ne , ^{24}Mg and ^{28}Si .

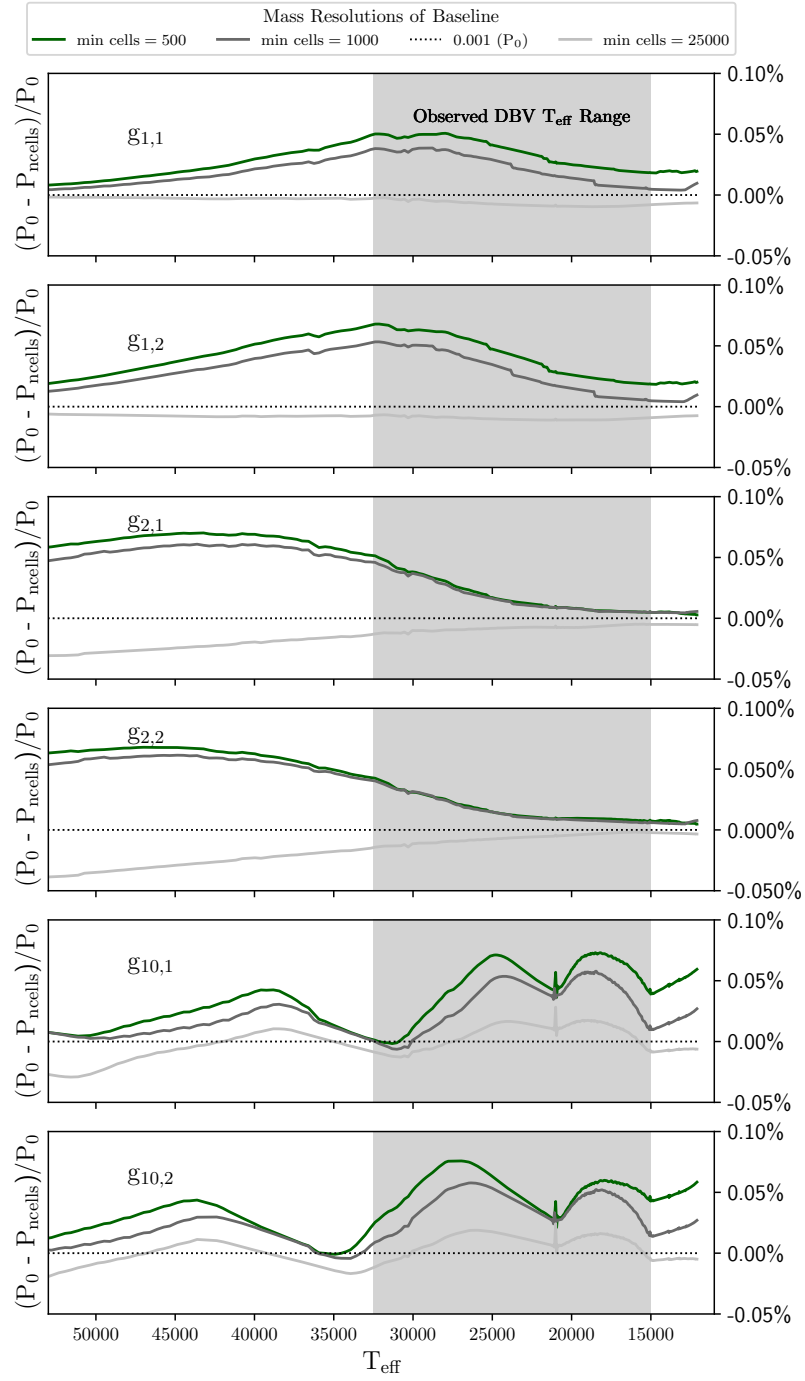


Figure B.1: Relative differences in the $g_{1,1}$, $g_{1,2}$, $g_{2,1}$, $g_{2,2}$, $g_{10,1}$, $g_{10,2}$ pulsation periods for different minimum mass resolutions as the baseline WD models cool. We use the notation $g_{n,\ell}$ for a g-mode of order n and degree ℓ . The minimum mass resolution of 5,000 cells, used for all the results reported, is shown by the black horizontal lines.

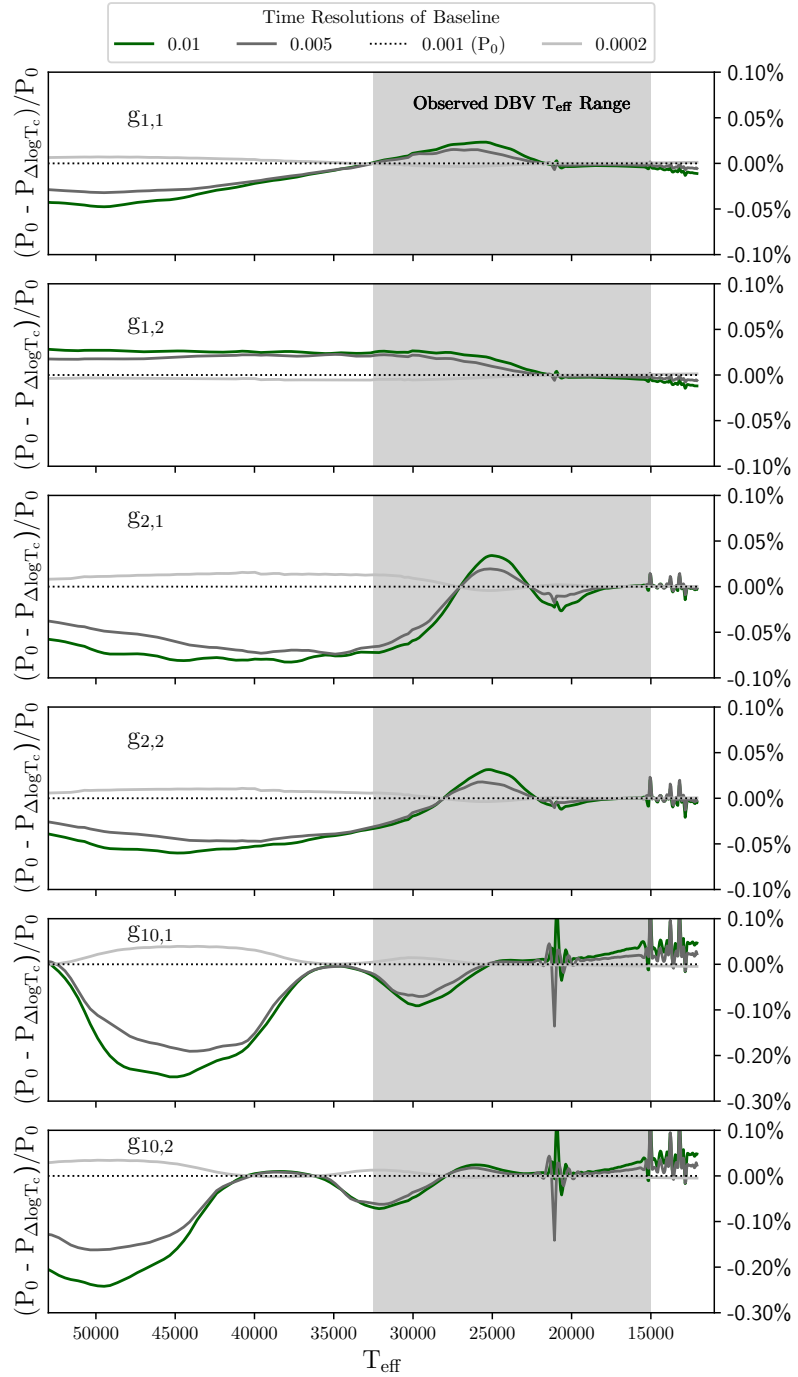


Figure B.2: Relative differences in the $g_{1,1}$, $g_{1,2}$, $g_{2,1}$, $g_{2,2}$, $g_{10,1}$, and $g_{10,2}$ pulsation period for different temporal resolutions as the baseline WD models cool. The largest change in the central temperature allowed over a timestep, $\text{delta_lgT_cntr_limit} = 0.001$, used for all the results reported, is shown by the black horizontal lines.

APPENDIX C

APPENDIX FOR CHAPTER 4

Microphysics in MESA The MESA EOS is a blend of the OPAL (Rogers and Nayfonov, 2002b), SCVH (Saumon *et al.*, 1995), FreeEOS (Irwin, 2004), HELM (Timmes and Swesty, 2000), PC (Potekhin and Chabrier, 2010a), and Skye (Jermyn *et al.*, 2022) EOSes.

Radiative opacities are primarily from OPAL (Iglesias and Rogers, 1993, 1996), with low-temperature data from Ferguson *et al.* (2005b) and the high-temperature, Compton-scattering dominated regime by Poutanen (2017). Electron conduction opacities are from Cassisi *et al.* (2007) and Blouin *et al.* (2020).

Nuclear reaction rates are from JINA REACLIB (Cyburt *et al.*, 2010), NACRE (Angulo *et al.*, 1999) and additional tabulated weak reaction rates Fuller *et al.* (1985); Oda *et al.* (1994); Langanke and Martínez-Pinedo (2000). Screening is included via the prescription of Chugunov *et al.* (2007). Thermal neutrino loss rates are from Itoh *et al.* (1996).

Model Optimization and Resolution Reduced Chemical Network

The nature of our evolutionary models is computationally expensive. This paper is concerned about overshooting and the $^{12}\text{C}(\alpha, \gamma)^{16}\text{O}$ reaction rate probability distribution function, which primarily dictate the evolutionary processes and consequences of the CHeB phase. The isotopes most impacted during CHeB are ^{12}C , ^{16}O , and ^4He . ^{14}N and ^{20}Ne are the next two most impacted isotopes during CHeB. We thus optimize the efficiency of our models by reducing the chemical network number of isotopes from 30 to 23. The eliminated isotopes are ^{21}Ne , $^{21,22,23}\text{Na}$, $^{23,24}\text{Mg}$, and ^{56}Fe . A comparison of the resulting inner mass fraction profiles for the 5 most abundant isotopes for both networks is shown in Figure C.1 for each chemical network. This figure shows the profiles at the completion of CHeB. both network models used the same temporal and spatial resolution during CHeB. The run-time was reduced from a few days to a few hours on 12 cores. All resolution studies were conducted with $\sigma = 0.0$ without overshoot (NOV).

Reducing the network impacted ^{22}Ne most, with an offset of $\sim 22\%$ more ^{22}Ne in the 23 isotope network. We note that C22 used a 30 network and our overall signature results persistent through variations in heavier isotopes.

Temporal Resolution

Several timestep limiters in **MESA** help optimize convergence studies. In this paper, we want to limit the timestep to achieve the temporal resolution that yields a smooth evolution of the central ^4He , ^{16}O , and ^{12}C abundances during CHeB. We first utilize the `delta_XC_cntr_limit` limiter. This limits the amount the central ^{12}C abundance can change in a given timestep. To help optimize computational run-time, we begin limiting the change in central ^{12}C during CHeB which the central helium abundance $X(^4\text{He}_c) < 0.6$. This is done by adding the following lines of code in the **MESA**

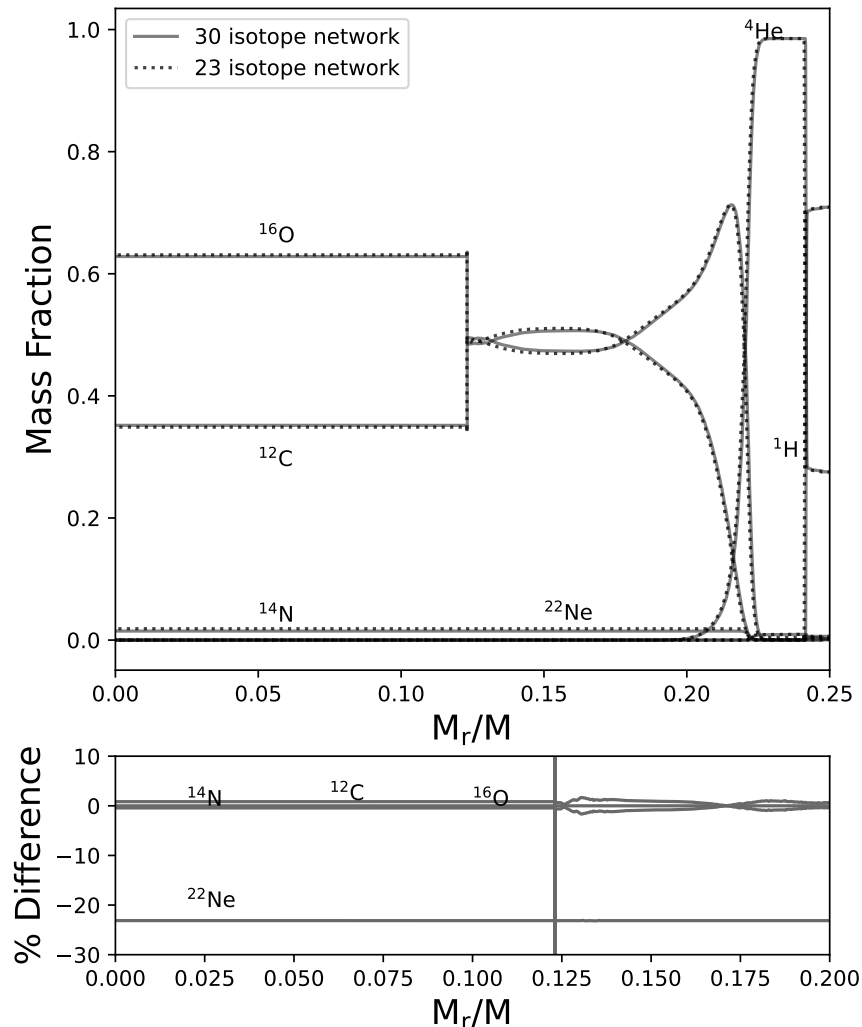


Figure C.1: Mass fraction profiles for the completion of CHeB for a 30 isotope (solid) and 23 isotope nuclear reaction network (dotted). Shown are the 5 most abundant isotopes for both networks.

`run_star_extras.f90` file:

```

if ((s% center_h1<1d-6).and.(s% center_he4 < 0.6).and.(s%
delta_XC_cntr_limit>0.001))then
s% delta_XC_cntr_limit = 0.0005d0
end if

```

This temporal resolution was used for the 30 and 23 isotope network models. We refer to it as resolution A. The remaining temporal resolution studies were performed using the 23 isotope chemical network.

The next iteration of increased temporal resolution modified the `run_star_extras.f90` file to include the following:

```
if ((s% center_h1<1d-6).and.(s% center_he4 < 0.5).and.(s%
delta_XC_cntr_limit>0.001))then
```

```
    s% delta_XC_cntr_limit = 0.0005d0
    s% delta_lgT_cntr_limit = 5d-4
    s% delta_lgT_cntr_hard_limit = 1d-3
    s% delta_lgRho_cntr_limit = 1d-3
    s% delta_lgRho_cntr_hard_limit = 5d-3
end if
```

This resolution is employed slightly earlier during CHeB, when $X(^4\text{He}_c) < 0.5$. We added limits to the change in central temperature and density from resolution A. This is resolution B.

Our third resolution iteration used the following limiter controls in the `run_star_extras.f90` file:

```
if ((s% center_h1<1d-6).and.(s% center_he4 < 0.999).and.(s%
delta_XC_cntr_limit>0.001))then  s% delta_XC_cntr_limit = 0.00025
    s% delta_X0_cntr_limit = 0.00025
    s% delta_lgT_cntr_limit = 2.5d-4
    s% delta_lgT_cntr_hard_limit = 0.5d-3
    s% delta_lgRho_cntr_limit = 0.5d-3
    s% delta_lgRho_cntr_hard_limit = 2.5d-3
end if
```

This is resolution C. We have set the limiters at the start of CHeB, and have decreased the limiter values from those in resolution B.

A comparison for resolutions A, B, and C are shown in Figure C.2. In each column, the solid light curves represent resolution A, the dotted curves B, and the dark solid curves C.

The left figure shows the evolution of central abundances of ^4He , ^{12}C , and ^{16}O during CHeB, starting when $X(^4\text{He}_c) \lesssim 0.6$ until the completion of CHeB. The central abundances for resolutions A and B are nearly identical. Resolution C varies slightly, with the final central ^{16}O abundance reaching a slightly larger amount than resolutions A and B. Further, all three resolutions show a smooth evolution of these central abundances throughout CHeB.

The middle plot in Figure C.2 shows the mass fraction profiles at the completion of CHeB. We show the 5 most abundant isotope profiles for each resolution. The ^{12}C and ^{16}O profiles for A are noticeably different than the profiles for B and C, especially after the O \rightarrow C transition. This is more apparent in the right plot of Figure C.2, which zooms in on the ^{16}O and ^{12}C profiles of the three resolutions. Resolution B follows A in the core, but then more closely aligns with C after the O \rightarrow C transition. Since resolutions B and C agree well, with only a slight difference in the central ^{12}C and

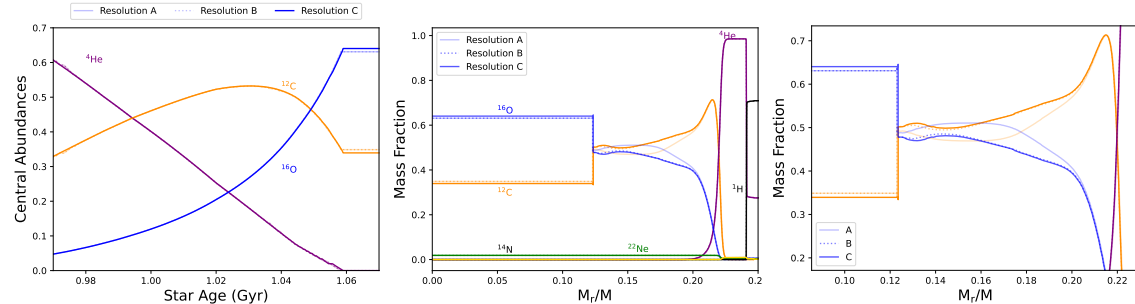


Figure C.2: Left: Evolution of central mass fractions during CHeB until $\log(L/L_\odot) = 3.0$ at three resolutions. Middle: Mass fraction profiles at $\log(L/L_\odot) = 3.0$ for the three resolutions. Right: Middle figure zoom-in to show differences.

${}^{16}\text{O}$ abundance, we set resolution C as the standard temporal resolution for our 13 models.

APPENDIX D

APPENDIX FOR CHAPTER 5

Tabular Data of LD Changes and Effect sizes

Here we tabulate the LD modifications made for each screen in finer detail. The tables show the screen lesson and name, the type of change made to post-Fall 2019 semesters, exact r values for each semester, the weighted r mean values, and the standard deviation. Yellow and green rows represent screens with changes that gave weighted mean rs above the small and moderate thresholds respectively ($r > 0.1; r > 0.3$). The red row in Table D.1 is a screen with a change that gave a negative r above the small threshold.

Spreadsheet LD Changes

This first table shows the spreadsheet LD changes for their corresponding screens and lessons, r values for each semester, weighted mean r values, and standard deviation. Yellow and green rows represent screens with changes that gave weighted mean rs above the small and moderate thresholds respectively ($r > 0.1; r > 0.3$). The red row is a screen with a change that gave a negative r above the small threshold.

Graph LD changes

The second table shows the graph LD changes for their corresponding screens and lessons, r values for each semester, weighted mean r values, and standard deviation. Yellow and green rows represent screens with changes that gave weighted mean rs above the small and moderate thresholds respectively ($r > 0.1; r > 0.3$).

Lesson and Screen	Change	Spring 2020 r	Fall 2020 r	Spring 2021 r	Weighted Mean	std
R1: Calculate Distance	Adjusted text on screen and added spreadsheet tips to icon	0.128	0.188	0.179	0.166	0.033
R2: Application	Combo: directions to use formula in spreadsheet	0.005	0.001	0.03	0.013	0.016
R2: Calculate Luminosity	Combo: directions to use formula in spreadsheet	0.335	0.352	0.327	0.337	0.013
R2: Calculate Lum w/meters	Example/tutorial and spreadsheet tips in icon,+added feedback (F20 & S21)	0.281	0.28	0.287	0.283	0.004
R2: Calculate Solar Luminosity Units	Example/tutorial and spreadsheet tips in icon	0.461	0.476	0.465	0.467	0.008
R2: Question Bank	Directions to use formula in spreadsheet	0.332	0.352	0.382	0.358	0.025
R3: Wien's Temp to Wave	Added spreadsheet tips to icon	0.019	0.052	0.03	0.033	0.017
R3: Wien's Wave to Temp	Added spreadsheet tips to icon	0.028	0.015	0.015	0.019	0.007
R4: Cool Flux	Added spreadsheet tips to icon	0.17	0.167	0.117	0.149	0.03
R4: Hot Flux	Added spreadsheet tips to icon	0.03	0.062	0.002	0.029	0.03
R4: Use HR	Adjusted text on screen and added spreadsheet tips to icon	0.268	0.229	0.262	0.254	0.021
R5: Lifetime Calculations	Example/tutorial and spreadsheet tips in icon	0.04	0.045	0.014	0.031	0.017
fp1: Fraction	Added icon, no spreadsheet hints	0.012	0.07	0.042	0.04	0.029
fp1: Calculate Populations/Calculate Field of View/Calculate Galaxy	Added icon, no spreadsheet hints+ (F20 & S21) split calculation into 2 screens, split icon tip, added prediction q before 2nd q	-0.065	-0.118	-0.157	-0.116	0.046
fp1: Calculate Radius	Adjusted text on screen and added spreadsheet tips to icon	0.007	0.151	0.171	0.112	0.09
fp1: Star 1	Adjusted text on screen and added spreadsheet tips to icon	0.03	0.186	0.202	0.142	0.095
fp1: Star 2	Adjusted text on screen and added spreadsheet tips to icon	0.117	0.115	0.083	0.103	0.019
fp1: Star 3	Adjusted text on screen and added spreadsheet tips to icon	0.067	0.029	0.052	0.05	0.019
fp2: Doppler to RV/Doppler Shift	Split calculation into 2 screens and added spreadsheet tips to icon	0.106	0.11	0.084	0.099	0.014
fp2: RV to Mass	Added spreadsheet tips to icon	0.021	0.057	0.04	0.039	0.018
fp3: Volume Calculations/Density Calculations	Split calculation into 2 screens and added spreadsheet tips to icon	0.225	0.251	0.225	0.233	0.015
fp3: Saturn Density	Feedback help if wrong answer	0.016	0.014	0.01	0.013	0.003
fp3: Neptune Density	Feedback help if wrong answer	0.016	0.014	0.01	0.013	0.003
fp3: Earth Density	Feedback help if wrong answer	0.072	0.043	0.026	0.046	0.023
fp3: Pluto Density	Feedback help if wrong answer	0.107	0.082	0.084	0.09	0.014
ne1: Calculating Flux	Added spreadsheet tips to icon	0.048	0.043	0.049	0.047	0.004
ne1: Calculating Temperatures	Added spreadsheet tips to icon	0.101	0.069	0.039	0.068	0.031

Table D.1: Detailed Spreadsheet LD Changes.

Lesson and Screen	Change	Spring 2020 r	Fall 2020 r	Spring 2021 r	Weighted Mean	Weighted Mean F20 S21 Only	std
R2: Method - Points	Interpretation questions earlier in lesson or before screen	0.012	0.024	-0.004	0.009	0.008	0.014
R2: Method - Distribution	Interpretation questions earlier in lesson or before screen	0.016	0.005	0.023	0.015	0.015	0.009
R2: Method - Do	Interpretation questions earlier in lesson or before screen	0.06	0.014	0.039	0.038	0.028	0.023
R2: Method - Differentiation 1	Interpretation questions earlier in lesson or before screen	0.024	0.002	0.009	0.012	0.006	0.011
R2: Method - Differentiation 2	Interpretation questions earlier in lesson or before screen	-0.03	0.057	0.065	0.032	0.061	0.053
R3: Tutorial 1	Interpretation questions earlier in lesson or before screen + flux-> intensity in popups (F20, S21)	0.044	0.048	0.054	0.049	0.051	0.005
R3: Tutorial 2	Interpretation questions earlier in lesson or before screen + flux-> intensity in popups (F20, S21)	0.009	0.054	0.052	0.039	0.053	0.026
R3: Sun Percentage	Interpretation questions earlier in lesson or before screen	0.034	0.012	0.025	0.024	0.019	0.011
R3: Blue Percentage	Interpretation questions earlier in lesson or before screen	0.028	0.027	0.037	0.031	0.033	0.006
R3: Red Percentage	Interpretation questions earlier in lesson or before screen	0.038	0.004	0.007	0.016	0.005	0.019
R3: Peak Wavelengths	Interpretation questions earlier in lesson or before screen	0.040	0.029	0.005	0.023	0.016	0.018
R3: Temps - Generic	Interpretation questions earlier in lesson or before screen	0.057	0.032	0.036	0.041	0.034	0.014
R3: Temps - Specific	Interpretation questions earlier in lesson or before screen	0.002	0.086	0.068	0.052	0.076	0.044
R4: Identify Outliers	Interpretation questions earlier in lesson or before screen + corrected degrees->kelvin (F20, S21)	0.178	0.148	0.180	0.170	0.166	0.018
R4: Label H-R Diagram	Previous interpretation questions and new HR diagram + corrected degrees->kelvin (F20, S21)	0.040	0.052	0.042	0.045	0.047	0.006
R4: H-R Question Bank	New HR Diagram + corrected degrees->kelvin (F20, S21)	0.086	0.098	0.107	0.097	0.103	0.011
R5: Time Assumption	Clarified Directions	0.098	0.259	0.164	0.171	0.205	0.081
Ip1: Passed Light	Clarified Directions	0.343	0.37	0.291	0.331	0.325	0.04
Ip2: New Observations	Interpretation questions earlier in lesson or before screen + modified directions (F20,S21))	0.275	0.297	0.280	0.284	0.287	0.011
ne1: Temp vs Luminosity	Interpretation questions earlier in lesson or before screen + q5 from prior screen remain, changed 3rd q wording only one box (F20, S21)	0.010	-0.030	-0.221	-0.091	-0.139	0.123
ne1: Temp vs Distance	Interpretation questions earlier in lesson or before screen+ changed 3rd q wording and only one box (F20, S21)	0.037		0.037	0.037	0.037	0.0
ne1: Temp vs Radius	Interpretation questions earlier in lesson or before screen+ changed 3rd q wording and only one box (F20, S21)	0.037		0.049	0.044	0.049	0.008
ne1: Temp vs Albedo	Interpretation questions earlier in lesson or before screen+ changed 3rd q wording and only one box (F20, S21)	0.078		0.026	0.050	0.026	0.036
ne3: Tutorial	Feedback if wrong on first try + wording changed in q (F20, S21)	0.002	0.039	-0.058	-0.010	-0.016	0.049

Table D.2: Detailed Graph LD Changes.